STUDY OF BUBBLY AND ANNULAR FLOW USING QUANTITATIVE FLOW VISUALIZATION

By

SHAHROUZ MOHAGHEGHIAN

Bachelor of Science in Mechanical Engineering
Shahrekord University
Shahrekord, Iran
2009

Master of Science in Mechanical Engineering
Yazd University
Yazd, Iran
2012

Submitted as partial requirement for the degree of
Doctor of Philosophy
School of Mechanical and Aerospace Engineering
May 2019

STUDY OF BUBBLY AND ANNULAR FLOW USING QUANTITATIVE FLOW VISUALIZATION

Dissertation Approved:

Dr. Brian R. Elbing

Dissertation Adviser

Dr. Afshin J. Ghajar

Dr. Jamey Jacob

Dr. Prem Bikkina

ACKNOWLEDGEMENTS

First I thank God for giving me the strength and opportunity to study the wonders of multiphase flows, without his blessing the successful accomplishement of my research would not have been possible. I would like to express my gratitude to my parents Mansour and Shahin for loving me, believing in me, and being my role models, I could not ask for better parents. I take this opportunity to express my most sincere appreciation to my advisor Dr. Brian R. Elbing who raised the expectations from me and gave me the unique opportunity to develop as an independent researcher. In addition, many thanks to Dr. Afshin J. Ghajar for donating the vibrating bubble column setup as well as giving me the opportunity to use the test facilities at OSU Multiphase Lab to accomplish my research. Thanks to graduated members of OSU Multiphase lab in particular Dr. Swanand M. Bhawgat for helping with annular flow test setup and Mr. Adam L. Still for helping me with the vibrating bubble column setup. Thanks to my dear friends, Milad Samaee, and Farmanesh family for love, support, and kindness. Also thanks to dear colleague Yasaman Farsiani and other student members of Experimental Flow Physics Lab (EFPL). Finally, many thanks to my best friend Khrystyna Khvorost for the encouragement and support.

Acknowledgments reflect the views of the author and are not endorsed by committee members or Oklahoma State University.

Name: SHAHROUZ MOHAGHEGHIAN
Date of Degree: MAY, 2019
Title of Study: STUDY OF BUBBLY AND ANNULAR FLOW USING QUANTITATIVE FLOW VISUALIZATION
Major Field: Mechanical Engineering

Abstract: Multiphase flow phenomena in bubble columns and annular pipe flow were experimentally studied using quantitative flow visualization. The bubble column work was divided between studies on the operation regime within a sparged bubble column, the effect of vibration on bubble size and void fraction, and the impact of vibration on bubble induced mixing. The operation regime study varied the gas superficial velocity and liquid phase properties and then analyzed the impact on the bubble size distribution and void fraction to identify operation regimes. This study showed that increasing the liquid viscosity enhances the regime transition from homogeneous to heterogeneous. In addition, bubble size was successfully scaled in the heterogeneous regime showing that it has an inverse power-law correlation with the scaled specific input power. The vibration study used a single point injector and measured the bubble size distribution and void fraction with high-amplitude (up to 10 mm), low-frequency (< 23 Hz) vibrations. A power-law correlation between the scaled bubble size and scaled specific input power was identified. The bubble induced mixing study tracked the distribution of a passive scalar within a sparged bubble column exposed to vibrations in the aforementioned range. These results show that vibration suppresses the liquid velocity agitations in the bubble swarm wake, which decelerates mixing, while also bubble clustering and aggregation produces void fraction gradients that induce a mean flow that accelerates mixing. Finally, the annular pipe flow work used planar laser induced fluorescence to study the sensitivity of the annular film thickness on the bottom of the pipe to inclination angle. The current measurements were first validated by comparing the results in horizontal (pipe) orientation with established data from the literature. The horizontal results also showed that the ratio of the film roughness to film thickness increases with increasing liquid flow rate. Then the pipe inclination angle was varied from –20 degrees (downward) to +60 degrees (upward). The downward results show the film thickness decreasing with increasing inclination angle, while the upward results have the film thickness remain relatively constant. However, the upward results did show that the film thickness had significant temporal fluctuations.

TABLE OF CONTENTS

LIST OF FIGURES ..... **viii**
LIST OF TABLES ..... **xx**
NOMENCLATURE ..... **xxii**

ABSTRACT ..... Error! Bookmark not defined.

CHAPTER I **1**
1. INTRODUCTION **1**
1.1 Background and Motivation 1
1.2 Vibrating Bubble Columns 3
1.2.1 Problem overview 3
1.2.2 Flow regimes (static and vibrating) 3
1.3 Gas-Liquid Annular Pipe Flow 6
1.3.1 Problem overview 6
1.3.2 Pipe flow regimes 7
1.4 Research Objectives 10
1.5 Summary of the Current Study 13

CHAPTER II **15**
2. LITERATURE REVIEW ..... Error! Bookmark not defined.
2.1 Vibrating Bubble Column Literature Review 15
2.1.1 Mass transfer and void fraction studies 16
2.1.2 Modeling the bubble dynamics 19
2.1.3 Modeling bubble size and void fraction 23
2.2 Review of Bubble Induced Mixing 25
2.3 Annular Flow Film Thickness Literature Review 31
2.3.1 Horizontal pipe 33
2.3.2 Vertical pipe 40
2.3.3 Inclined pipe 46
2.3.4 Triangular Relationship 48

CHAPTER III **51**
3. EXPERIMENTAL METHODS ..... Error! Bookmark not defined.
3.1 Vibrating Bubble Column Testing 52
3.1.1 Test facility 52
3.1.2 Bubble size measurement 62
3.1.3 Void fraction measurement 67

3.1.4 Liquid diffusion measurement 68
3.2 Inclined Gas-Liquid Pipe Setup 72
3.2.1 Test facility overview 72
3.2.2 Flow loop control and monitoring 74
3.2.3 Planar laser induced fluorescent 76

CHAPTER IV 79
4. CHARACTERIZATION OF STATIC BUBBLE COLUMN REGIMES. 79
4.1 Introduction 79
4.2 Characterization of Bubble Size Distribution 80
4.3 Bubble Size Scaling 90
4.4 Void Fraction Scaling 94
4.5 Conclusions 100

CHAPTER V 102
5. EFFECT OF VERTICAL VIBRATION ON BUBBLE SIZE AND VOID FRACITON 102
5.1 Introduction 102
5.2 Static Bubble Column 104
5.2.1 Bubble size measurement and scaling 104
5.2.2 Effect of gas injection rate 112
5.2.3 Effect of injector tube angle 114
5.2.4 Effect of injector tube diameter 115
5.2.5 Effect of column diameter 118
5.2.6 Higher order statistics 119
5.3 Vibrating Bubble Column 121
5.3.1 Bubble size measurement, scaling and statistics 121
5.3.2 Void fraction modeling 128
5.4 Conclusions and Remarks 138

CHAPTER VI 142
6. MIXING OF PASSIVE SCALAR IN VIBRATING BUBBLE COLUMN 142
6.1 Introduction 142
6.2 Results and Discussion 144
6.2.1 Static bubble column 144
6.2.2 Vibrating bubble column 152
6.3 Analysis 163
6.4 Conclusions 164

CHAPTER VII 166
7. DEPENDENCE OF INCLINATION ANGLE ON ANNULAR FLOW LIQUID FILM THICKNESS ..... Error! Bookmark not defined.
7.1 Introduction 166
7.2 Planar Laser Induced Fluorescent (PLIF) Setup 169

7.3 PLIF Processing 174
7.4 Test Setup Validation 177
7.5 Sensitivity to Inclination Angle 180
7.6 Conclusions and Remarks 186

CHAPTER VIII 188
8. CONCLUSIONS AND RECOMMENDATIONS 188
8.1 Conclusions 188
8.2 Recommendations 191

REFERENCES 193

APPENDICES 217
Appendix A: Calculations and Derivations 217
Image Macro for Analyzing Bubble Size Distribution 217
Image Macro for Analyzing the Dye Concentration 218
Appendix B: Uncertainty Analysis 219
Vibration frequency and amplitude 219
Gas superficial velocity 220
Bubble Size 221
Void fraction 222
Annular liquid film thickness 222

LIST OF FIGURES

FIGURE 1-1. FLOW PATTERNS IN STATIC BUBBLE COLUMNS (REPRODUCED FROM KANTARCI ET AL., 2005). 4

FIGURE 1-2. PROPOSED FLOW PATTERNS IN VIBRATING BUBBLE COLUMNS..... 6

FIGURE 1-3. FLOW PATTERNS IN A VERTICAL GAS-LIQUID PIPE FLOW (ADAPTED FROM BRENNEN, 2005). 8

FIGURE 1-4. FLOW PATTERNS IN A HORIZONTAL GAS-LIQUID PIPE FLOW (ADAPTED FROM BRENNEN, 2005). 10

FIGURE 2-1. VOID FRACTION AND MASS TRANSFER ENHANCEMENT WITH RESPECT TO A STATIONARY CASE; U_{SG} = 10.1MM/S AND A = 0.5MM (ADAPTED FROM KRISHNA & ELLENBERGER, 2002). 18

FIGURE 2-2. VOID FRACTION UNDER VIBRATION. (A) EFFECT OF FREQUENCY, (B) EFFECT OF AMPLITUDE (ADAPTED FROM KRISHNA & ELLENBERGER, 2003). 18

FIGURE 2-3. VOID FRACTION INTENSIFICATION WITH VIBRATION FREQUENCY; U_{SG} = 41MM/S, A = 0.3MM, H_0 = 0.85-1.35M (ADAPTED FROM ELLENBERGER ET AL., 2005). 19

FIGURE 2-4. COMPARISON BETWEEN THE PREDICTED STABILIZATION FREQUENCY (Ω_S) FROM EQUATION 2-1 AND THAT OF CUT-OUT FREQUENCY (Ω_C), (ADAPTED FROM ELBING ET AL., 2015). 21

FIGURE 2-5. B_J VERSUS BUBBLE REYNOLDS NUMBER AT LEVITATION CONDITION (ADAPTED FROM ELBING ET AL., 2015). 22

FIGURE 2-6. THE POWER SPECTRA OF NORMALIZED LIQUID VELOCITY AGITATIONS WITH WAVELENGTH IN THE BUOYANCY DIRECTION (ADAPTED FROM RIBOUX ET AL., 2010).27

FIGURE 2-7. TIME TRACE OF THE CONCENTRATION DISTRIBUTION OF A PASSIVE SCALAR IN A BUBBLE COLUMN (AIR AND WATER, D = 0.2M, U_{SG} = 20MM/S); (A) EXPERIMENTAL RESULTS, (B) NUMERICAL SIMULATION RESULTS (ADAPTED FROM WEIMANN & MEWES, 2005). 28

FIGURE 2-8. INSTANTANEOUS CONCENTRATION FIELD OF THE PASSIVE SCALAR (FLUORESCENT DYE) AT (A) E = 3.2%, AND (B) E = 7.5% (ADAPTED FROM BOUCHE ET AL., 2013). 29

FIGURE 2-9. SPECTRUM OF THE NORMALIZED CONCENTRATION FLUCTUATIONS, SLOPE OF -3 IS LOCATED WITHIN 5 TO 25 HZ (ADAPTED FROM ALMÉRAS ET AL., 2016). 30

FIGURE 2-10. SCHEMATIC OF LIQUID FILM IN ANNULAR FLOW (ADAPTED FROM BERNA ET AL., 2014). 33

FIGURE 2-11. CIRCUMFERENTIAL FILM THICKNESS MEASUREMENTS IN A 12.7MM PIPE (ADAPTED FROM SHEDD & NEWELL, 2004). 34

FIGURE 2-12. EXPERIMENTAL MEASUREMENT OF LIQUID FILM THICKNESS (Δ) IN A HORIZONTAL PIPE VERSUS LIQUID SUPERFICIAL VELOCITY (U_{SL}) AT DIFFERENT GAS SUPERFICIAL VELOCITIES (U_{SG}). PIPE DIAMETER D=8.8MM, AIR-WATER AT AMBIENT PRESSURE AND TEMPERATURE (ADAPTED AND REPRODUCED FROM SCHUBRING, 2008)..... 35

FIGURE 2-13. TRIANGULAR RELATIONSHIP IN ANNULAR FLOW (ADAPTED FROM BHAGWAT, 2015). 36

FIGURE 2-14. FILM THICKNESS (Δ) VERSUS SUPERFICIAL LIQUID VELOCITY (U_{SL}), COMPARISON BETWEEN EXPERIMENTAL DATA (HORIZONTAL CHANNEL FLOW, 0.305M X 0.025M, U_{SG} = 35M/S) FROM TATTERSON ET AL. (1977) AND AVAILABLE MODELS (ADAPTED AND REPRODUCED FROM BERNA ET AL., 2014). 39

FIGURE 2-15. FILM THICKNESS (Δ) VERSUS SUPERFICIAL LIQUID VELOCITY (U_{SG}), COMPARISON BETWEEN EXPERIMENTAL DATA (HORIZONTAL CHANNEL FLOW, D = 8.8 MM, U_{SL} = 0.192M/S) FROM SCHUBRING (2009) AND AVAILABLE MODELS (ADAPTED AND REPRODUCED FROM BERNA ET AL., 2014). 39

FIGURE 2-16. EFFECT OF GAS SUPERFICIAL VELOCITY AS WELL AS LIQUID SUPERFICIAL VELOCITY ON FILM THICKNESS IN VERTICAL ANNULAR FLOW (ADAPTED FROM ALAMU, 2010). 40

FIGURE 2-17. PROCESSED PLIF IMAGE OF VERTICAL ANNULAR FLOW; U_{SG} = 55.3M/S, U_{SL} = 0.127M/S, D = 23.4MM (ADAPTED FROM SCHUBRING & SHEDD, 2008)..... 41

FIGURE 2-18. EXPERIMENTAL MEASUREMENTS OF THE LIQUID FILM THICKNESS (Δ) IN A VERTICAL PIPE VERSUS GAS SUPERFICIAL VELOCITY (U_{SL}) AT DIFFERENT LIQUID SUPERFICIAL VELOCITIES (U_{SG}). PIPE DIAMETER D=23.4MM, AIR-WATER AT AMBIENT PRESSURE AND TEMPERATURE (ADAPTED AND REPRODUCED FROM SCHUBRING, 2008).42

FIGURE 2-19. FILM THICKNESS (Δ) VERSUS SUPERFICIAL LIQUID VELOCITY (U_{SL}), COMPARISON BETWEEN EXPERIMENTAL DATA (VERTICAL PIPE, D = 19MM, U_{SL} = 0.05M/S) FROM ALAMU (2010) AND AVAILABLE MODELS (ADAPTED AND REPRODUCED FROM BERNA ET AL, 2014). 45

FIGURE 2-20. FILM THICKNESS (Δ) VERSUS SUPERFICIAL LIQUID VELOCITY (U_{SG}), COMPARISON BETWEEN EXPERIMENTAL DATA (HORIZONTAL CHANNEL FLOW, D = 23.4 MM, U_{SG} = 71M/S) FROM SCHUBRING (2009) AND AVAILABLE MODELS (ADAPTED AND REPRODUCED FROM BERNA ET AL, 2014)..... 45

FIGURE 2-21. CIRCUMFERENTIAL LIQUID FILM THICKNESS DISTRIBUTION AT 0°, 45°, AND, 85° (FROM LEFT TO RIGHT); (A) U_{SG} =21.5M/S U_{SL} =0.007M/S, (B) U_{SG} =21.5M/S U_{SL} =0.011M/S, (C) U_{SG} =21.5M/S U_{SL} =0.028M/S (ADAPTED FROM GERACI ET AL., 2007).47

FIGURE 3-1. SHAKER TABLE; ECCENTRIC DRIVE MECHANISM AND BASE PLATE. 54

FIGURE 3-2. FROM LEFT TO RIGHT, AC MOTOR AND GEARBOX (INSIDE THE CARRIAGE), AND EDM (SHAKER)..... 54

FIGURE 3-3. COMPARISON OF SHAKER VIBRATION ACCELERATION IN LONGITUDINAL AND PLANAR DIRECTION, THE DASHED LINE REPRESENTS RMS (A_{XY}) / RMS (A_Z) = 33%.... 56

FIGURE 3-4. BUBBLE COLUMN MOUNTED ON THE SHAKER TABLE VIA VERTICAL BEAMS (THREADED RODS)..... 57

FIGURE 3-5. SCHEMATIC OF THE BUBBLE COLUMN ASSEMBLY AND THEECOMPRESSED AIR INJECTION MANIFOLD..... 59

FIGURE 3-6. COMPRESSED AIR INJECTION MANIFOLD..... 59

FIGURE 3-7. SINGLE POINT INJECTION OF AIR INSIDE OF THE COLUMN (D = 102MM, D_{INJ} = 1.6MM AT 90°, AND U_{SG} = 6.9MM/S AT P_M = 600 KPA). 60

FIGURE 3-8. POROUS BUBBLE SPARGER USED IN DIFFUSION EXPERIMENTS. (A) PLENUM AND PORE BUBBLE DIFFUSER AND (B) BUBBLE SPARGER IN OPERATION AT U_{SG} = 0.5MM/S.61

FIGURE 3-9. SPATIAL CALIBRATION USING A WATERBOX TO CORRECT FOR DISTORTIONS FROM EDGE EFFECTS, (A) ΔX = 5MM, D = 102MM. (B) SPATIAL VARIATION OF THE CALIBRATION COEFFICIENT ACROSS THE COLUMN MID-PLANE. 62

FIGURE 3-10. TOP VIEW OF THE BUBBLE COLUMN TEST FACILITY SHOWING THE CAMERA AND LIGHTING CONFIGURATION FOR BUBBLE IMAGING. 63

FIGURE 3-11. EFFECT OF COLUMN CURVATURE ON SPATIAL CALIBRATION, ΔX = 5MM, D = 102MM. (A) RAW IMAGE OF THE CALIBRATION PLATE, AND (B) SPATIAL VARIATION OF THE CALIBRATION COEFFICIENT ACROSS THE COLUMN MID-PLANE. 64

FIGURE 3-12. EXAMPLE IMAGE OF BUBBLE IDENTIFICATION (IDENTIFIED BUBBLES ARE OUTLINED). NOTE THAT OUT-OF-FOCUSED BUBBLES ARE NOT IDENTIFIED DUE TO BLURRED EDGES. 65

FIGURE 3-13. VOID FRACTION MEASUREMENT USING SURFACE DISPLACEMENT FROM TRACKING THE STYROFOAM AT U_{SG} OF (A) 0, (B) 4MM/S, AND (C) 10MM/S 68

FIGURE 3-14. CHANGE OF GRAYSCALE VALUE WITH THE INJECTED SOLUTION OF 10% DYE AND 90% WATER. 70

FIGURE 3-15. GRAYSCALE VALUE MEASUREMENT FROM THE BUBBLE IMAGES. (A) RAW IMAGE AND THE RESULTING (B) GRAYSCALE PROFILE ALONG THE COLUMN DIAMETER..... 71

FIGURE 3-16. GRAYSCALE MEASUREMENT FOR EVALUATION OF TEMPORAL EVOLUTION OF THE DYE CONCENTRATION IN BUBBLE MIXING. 71

FIGURE 3-17. SCHEMATIC OF THE VARIABLE INCLINATION FRAME MECHANISM AND RELATIVE POSITION OF THE TEST SECTION ADOPTED FROM BHAGWAT (2015). 73

FIGURE 3-18. SCHEMATIC OF THE IMPSF FLOW VISUALIZATION AND VOID FRACTION TEST SECTION, ADOPTED FROM BHAGWAT (2015)..... 74

FIGURE 3-19. SCHEMATIC OF THE INSTRUMENTED MULTIPHASE PIPE FLOW SETUP, ADOPTED FROM BHAGWAT (2015)..... 76

FIGURE 3-20. SCHEMATIC OF LASER POSITION IN PLIF MEASUREMENT OF LIQUID FILM THICKNESS AND ASSOCIATED MEASUREMENT UNCERTAINTY (Ξ_{FILM}) DUE TO PIPE CURVATURE. 77

FIGURE 3-21. OPTICAL CALIBRATION OF THE FIELD-OF-VIEW USING DAVIS8 (LAVISION). 78

FIGURE 3-22. FLOW VISUALIZATION OF HORIZONTAL ANNULAR FLOW USING PLIF WITH $\dot{M}_G$ = 0.5KG/MIN AND, $\dot{M}_L$ = 1.6KG/MIN..... 78

FIGURE 4-1. SPARGER SUBMERGED IN A FISH TANK FOR PRELIMINARY TESTING, A UNIFORM BUBBLE GENERATION FROM THE PORE DISK WAS OBSERVED..... 81

FIGURE 4-2. COMPARISON OF THE SAUTER MEAN DIAMETER FROM A SPARGER AND SINGLE POINT INJECTOR (D_{INJ}=1.6MM) USING AIR AND WATER. 83

FIGURE 4-3. BUBBLE SIZE DISTRIBUTION IN THE SPARGED BUBBLE COLUMN AT 3 DIFFERENT GAS SUPERFICIAL VELOCITIES. 84

FIGURE 4-4. SAUTER MEAN DIAMETER (D_{32}) MEASURED USING A SINGLE POINT INJECTOR (WATER) AND A SPARGER DISK (WATER AND AQUEOUS SOLUTION OF 85% GLYCERIN).86

FIGURE 4-5. BUBBLE SIZE DISTRIBUTION IN AQUEOUS SOLUTION; (A) 85% GLYCERIN AND (B) 60% GLYCERIN. MEASUREMENTS WERE CARRIED OUT AT TEN DIFFERENT GAS SUPERFICIAL VELOCITIES. 86

FIGURE 4-6. PROBABILITY DENSITY FUNCTION OF BUBBLE SIZE DISTRIBUTION, EFFECT OF LIQUID VISCOSITY ON THE DISTRIBUTION SHAPE AND OPERATION REGIME (U_{SG}=27.6MM/S). 88

FIGURE 4-7. THE BUBBLE SAUTER MEAN DIAMETER (D_{32}) PLOTTED VERSUS THE SPECIFIC INPUT POWER, (EQUATION 4-3) FOR BOTH SINGLE POINT INJECTOR (WATER) AND A SPARGER DISK (WATER AND AQUEOUS SOLUTIONS OF GLYCERIN). THESE RESULTS ARE COMPARED AGAINST HINZE BASED CORRELATIONS FOR THE MAXIMUM STABLE BUBBLE SIZE. 90

FIGURE 4-8. EFFECT OF LIQUID PHASE PROPERTIES AND SPECIFIC INPUT POWER ON SAUTER MEAN DIAMETER IN CHURN-TURBULENT REGIME. A NEW DIMENSIONLESS TERM S_I ($Mo.Ca$) PLOTTED VERSUS THE OHNESORGE NUMBER (BASED ON SAUTER MEAN DIAMETER). 91

FIGURE 4-9. AN IMPERICAL CORRELATION FOR BUBBLE SIZE SCALING IN HOMOGENOUS OPERTAION REGIME USING DIMENSIONAL ANALYSIS. 94

FIGURE 4-10. EFFECT OF GAS SUPERFICIAL VELOCITY AND LIQUID PHASE PROPERTIES ON VOID FRACTION IN A STATIC-SPARGED BUBBLE COLUMN. 95

FIGURE 4-11. SCHEMATIC OF ACTING FORCES ON A SINGLE BUBBLE AT TERMINAL VELOCITY. 97

FIGURE 4-12. A CORRELATION FOR SCALING THE VOID FRACTION IN THE HOMOGENOUS REGIME. 99

FIGURE 4-13. A CORRELATION FOR SCALING THE VOID FRACTION IN HETEROGENEOUS REGIME. 99

FIGURE 5-1. SAUTER MEAN DIAMETER (D_{32}) PLOTTED VERSUS THE SCALED VERTICAL DISTANCE ABOVE THE INJECTION LOCATION. EACH DATA POINT IS THE AVERAGE OF 10 REPETITIONS,

AND THE ERROR BARS ARE THE STANDARD DEVIATION OF THE MEAN (P_{ME} = 600 KPA, T_C = 21 ± 1 °C, D = 102 MM, D_{INJ} = 1.6 MM). 105

FIGURE 5-2. (**A**) PROBABILITY DENSITY FUNCTIONS (PDF) AND (B) CUMULATIVE DENSITY FUNCTION (CDF) OF BUBBLE SIZE (D_B) FOR THE SAME CONDITIONS SHOWN IN FIGURE 5-1. THE PDF/CDF FOR EACH U_{SG} WAS DETERMINED FROM COUNTING AT LEAST 10,000 BUBBLES. DASHED LINES IN (**A**) CORRESPOND TO THE D_{32} VALUES FOR EACH CONDITION (P_{ME} = 600 KPA, T_C = 21 ± 1 °C, D = 102 MM, D_{INJ} = 1.6 MM). 106

FIGURE 5-3. COMPARISON BETWEEN THE MOST FREQUENT BUBBLE SIZE (D_{MF}) AND THE SAUTER MEAN DIAMETER (D_{32}). THE DASHED LINE CORRESPONDS TO D_{MF} = D_{32}. OPEN AND CLOSED SYMBOLS CORRESPOND D_{INJ} = 0.8 AND 1.6 MM, RESPECTIVELY. 108

FIGURE 5-4. THE BUBBLE SAUTER MEAN DIAMETER (D_{32}) IN STATIC TEST CONDITIONS PLOTTED VERSUS THE INPUT POWER (SEE EQUATION 4-3). THESE RESULTS ARE COMPARED AGAINST HINZE (1955) SUGGESTION FOR SCALING THE MAXIMUM STABLE BUBBLE SIZE. 109

FIGURE 5-5. A POWER-LAW CORRELATION BETWEEN SCALED BUBBLE SIZE AND SCALED SPECIFIC INPUT POWER (EQUATION 5-1) IN STATIC TEST CONDITIONS. 110

FIGURE 5-6. PDFS FROM BIMODAL CONDITIONS (U_{SG} = 1.4, 3.5, 4.9 AND 6.9 MM/S). WHILE THE D_{MF} IS STILL DETERMINED FROM THE SMALLER BUBBLES, THERE IS A SECOND WEAKER PEAK NEAR 5 MM (D = 102 MM; D_{INJ} = 1.6 MM). 111

FIGURE 5-7. (**A**) SAUTER MEAN DIAMETER AND (**B**) MOST FREQUENT BUBBLE SIZE PLOTTED VERSUS THE SUPERFICIAL GAS VELOCITY. ERROR BARS REPRESENT THE STANDARD DEVIATION FOR THE GIVEN CONDITION (D = 102 MM; D_{INJ} = 1.6 MM; T_C = 21 ± 1 °C).113

FIGURE 5-8. STILL FRAMES IN THE D = 102 MM COLUMN WITH D_{INJ} = 1.6 MM WITH AN INJECTION CONDITION OF (**A**) P_{ME} = 260 KPA, U_{SG} = 3.5 MM/S; (**B**) P_{ME} = 600 KPA, U_{SG} = 6.9 MM/S AND (**C**) P_{ME} = 40 KPA, U_{SG} = 11.1 MM/S. 114

FIGURE 5-9. BUBBLE SIZES (D_{MF} AND D_{32}) PLOTTED VERSUS THE SUPERFICIAL GAS VELOCITY WITH THE INJECTOR TUBE ANGLED AT EITHER 45° OR 90° FROM HORIZONTAL (SEE INSERT SKETCH) (D = 102 MM; D_{INJ} = 0.8 MM; P_{ME} = 600 KPA). 115

FIGURE 5-10. BUBBLE SIZES (D_{MF} AND D_{32}) PLOTTED VERSUS THE SUPERFICIAL GAS VELOCITY VARYING THE INJECTOR TUBE DIAMETER (D = 102 MM; P_{ME} = 600 KPA). 117

FIGURE 5-11. BUBBLE SIZE PDF FOR THE TWO INJECTOR TUBE DIAMETERS (D_{INJ} = 0.8 OR 1.6 MM) TESTED AT (**A**) U_{SG} = 6.9 MM/S AND (**B**) U_{SG} = 27.6 MM/S (D = 102 MM; P_{ME} = 600 KPA; T_C = 21 ± 1 °C). 118

FIGURE 5-12. BUBBLE SIZES (D_{MF} AND D_{32}) PLOTTED VERSUS THE SUPERFICIAL GAS VELOCITY WITH DIFFERENT COLUMN DIAMETERS (D_{INJ} = 0.8 MM; P_{ME} = 600 KPA). 119

FIGURE 5-13. HIGHER ORDER STATISTICS FROM THE PDFS INCLUDING (**A**) UNWEIGHTED MEAN, (**B**) STANDARD DEVIATION Σ, (**C**) SKEWNESS S AND (**D**) KURTOSIS K OF THE BUBBLE DIAMETER. DASHED LINE ON THE KURTOSIS PLOT AT $K(D_B)$ = 3 CORRESPONDS TO THE KURTOSIS VALUE OF A NORMAL DISTRIBUTION. THE SAME LEGEND IS USED FOR ALL PLOTS. OPEN AND CLOSED SYMBOLS CORRESPOND TO D_{INJ} = 0.8 AND 1.6 MM, RESPECTIVELY.121

FIGURE 5-14. TEMPORAL RESPONSE OF THE BUBBLE SIZE (D_{32}) WITH VIBRATION (F = 10 HZ, A = 6 MM) STARTING AT TIME EQUALS ZERO. (H_0 = 85 CM, U_{SG} = 6.9 MM/S, P_0 = 1 ATM).123

FIGURE 5-15. PROBABILITY DENSITY FUNCTION OF BUBBLE SIZES (U_{SG} = 6.9MM/S, P_0 = 1 ATM) FOR THE (A) STATIC COLUMN AND (B) COLUMN VIBRATING AT F = 10 HZ WITH A = 6 MM. SYMBOLS FOR THE VIBRATION PHASE ϕ IN RADIANS IS PROVIDED IN THE LEGEND... 124

FIGURE 5-16. INSTANTANEOUS IMAGES ILLUSTRATING THE BUBBLE SIZE DISTRIBUTION ALONG THE COLUMN HEIGHT AT F = 10 HZ AND (FROM LEFT TO RIGHT) A = 1 MM, 2 MM, 6 MM AND 10 MM. (H_0 = 85 CM, U_{SG} = 5.0MM/S, P_0 = 1 ATM). 126

FIGURE 5-17. SAUTER MEAN DIAMETER (D_{32}) UNDER VIBRATION VERSUS THE INPUT POWER (SEE EQUATION 4-3). RESULTS ARE COMPARED AGAINST BUBBLE SIZE IN STATIC CONDITION (D_O). 127

FIGURE 5-18. A POWER-LAW CORRELATION BETWEEN SCALED BUBBLE SIZE AND SCALED SPECIFIC INPUT POWER (SEE EQUATION 5-1) IN STATIC AND VIBRATING TEST CONDITIONS. 127

FIGURE 5-19. EFFECT OF VIBRATION AMPLITUDE ON BUBBLE VELOCITY. 128

FIGURE 5-20. (A) VOID FRACTION VERSUS *M(H)*, (B) VOID FRACTION VERSUS THE SPECIFIC POWER INPUT (P_M). PLOT PRODUCED BY DATA FROM STILL (2012)..... 135

FIGURE 5-21. COMPARISON OF THE EXPERIMENTAL DATA FROM STILL (2012) WITH THE PREDICTED VOID FRACTION BY MODELS FROM THIS WORK AND WAGHMARE ET AL. (2007). RMS IS THE ROOT MEAN SQUARE OF E/E_0. 137

FIGURE 5-22. AIR-WATER INTERFACE AT F = 12.5 HZ, H_0 = 85 CM AND (FROM LEFT TO RIGHT) (A) A = 1.5 MM (*M(H)*=0.035), (B) A = 2.5 MM (*M(H)*=0.098), (C) A = 4.5 MM (*M(H)*=0.317), (D) A = 6.5 MM (*M(H)*=0.661) AND (E) A = 9.5 MM (*M(H)*=1.41) (ADOPTED FROM STILL ET AL., 2013). 138

FIGURE 6-1. DIFFUSION OF A PASSIVE SCALAR UNDER BUBBLE INDUCED MIXING VIA (A) TURBULENT WAKE TRANSPORT AND (B) BUBBLE INTERACTION..... 143

FIGURE 6-2. MEASUREMENT SECTION OF BUBBLE COLUMN, THE WATERBOX MITIGATED OPTICAL DISTORTION DUE TO REFRACTIVE INDEX MISS-MATCH. THE DYE INJECTOR NEEDLE WAS MOUNTED ON THE WALL, CENTERED, AND POINTED DOWNWARD IN THE COLUMN.146

FIGURE 6-3. MEASUREMENT SECTION (A) BEFORE AND (B) DURING DYE INJECTION, AS WELL AS (C) BEFORE AND (D) AFTER BUBBLE MIXING. 147

FIGURE 6-4. TIME EVOLUTION OF THE NORMAL CONCENTRATION OF A PASSIVE SCALAR UNDER BUBBLE INDUCED MIXING AT THE COLUMN MID-POINT. THE INITIAL TIME WAS BASED ON THE SUPPLY OF AIR TO THE SYSTEM. 148

FIGURE 6-5. TEMPORAL EVOLUTION OF THE NORMALIZED CONCENTRATION AND THE EFFECT OF GAS SUPERFICIAL VELOCITY ON MIXING TIME IN A BUBBLE SWARM. HERE THE TIME HAS BEEN ADJUSTED TO ACCOUNT FOR THE SYSTEM DELAY BETWEEN THE START OF AIR INJECTION AND MIXING. 149

FIGURE 6-6. INSTANTANEOUS IMAGES OF BUBBLE MIXING AT T = 8 SEC AND (A) U_{SG}=13.8MM/S, E = 2.5%. (B) U_{SG}=27.6MM/S, E = 3.3%. (C) U_{SG}=41.4MM/S, E = 4.2%. AND (D) U_{SG}=55.2MM/S, E = 5.9%. 150

FIGURE 6-7. A CORRELATION FOR TEMPORAL EVALUATION OF DYE CONCENTRATION UNDER BUBBLE INDUCED MIXING. 150

FIGURE 6-8. A COMPARISON BETWEEN THE MIXING TIME IN WATER (U_{SG}=27.6MM/S, E=3.4%) AND AQUEOUS SOLUTION OF GLYCERIN (85% GLYCERIN – 15% WATER) (U_{SG}=27.6MM/S, E=4.4%). 151

FIGURE 6-9. SAUTER MEAN DIAMETER FROM THE IN TABLE 6-2. 154

FIGURE 6-10. EFFECT OF VIBRATION AMPLITUDE ON BUBBLE SIZE AND VELOCITY USING SCALED AMPLITUDE AND FROUDE NUMBER. 154

FIGURE 6-11. MIXING TIME OF THE DYE IN STATIC AND VIBRATING SCENARIOS WITH MATCHING SPECIFIC POWER INPUT. 156

FIGURE 6-12. SAUTER MEAN DIAMETER FROM THE TESTED CONDITIONS IN FIGURE 6-11. 157

FIGURE 6-13. SAUTER MEAN DIAMETER FROM THE CONDITIONS TESTED (SEE FIGURE 6-11).157

FIGURE 6-14. INSTANTANEOUS IMAGES OF MIXING IN (TOP ROW) STATIC AND (BOTTOM ROW) VIBRATING BUBBLE COLUMN (P_M = 0.136 W/KG). 158

FIGURE 6-15. INSTANTANEOUS IMAGES OF MIXING IN (TOP ROW) STATIC AND (BOTTOM ROW) VIBRATING BUBBLE COLUMN (P_M = 0.667 W/KG). 158

FIGURE 6-16. EFFECT OF VIBRATION FREQUENCY ON MIXING TIME, A = 0.6MM AND U_{SG} = 11MM/S. 160

FIGURE 6-17. INSTANTANEOUS IMAGES OF MIXING AT T = 8 SEC (A= 0.68MM, U_{SG} = 11MM/S). 160

FIGURE 6-18. EFFECT OF VIBRATION AMPLITUDE ON MIXING TIME, F = 10 HZ AND U_{SG} = 9.6MM/S. 162

FIGURE 6-19. INSTANTANEOUS IMAGES OF MIXING AT T = 10 SEC (F= 10HZ, U_{SG} = 9.6MM/S). 162

FIGURE 6-20. SCALED MIXING TIME VERSUS SCALED SPECIFIC INPUT POWER, WITH EXPERIMENTAL DATA COMPARED TO A DIMENSIONALLY REASONED CURVE FIT. 164

FIGURE 7-1. FLOW PATTERN MAN FOR UPWARD INCLINED PIPE ORIENTATIONS, ADAPTED FROM BHAGWAT (2015). 170

FIGURE 7-2. LASER AND CAMERA POSITIONING ON THE VARIABLE INCLINATION MULTIPHASE PIPE FLOW SETUP, GREEN DASH LINES REPRESENT THE LASER BEAM PATH USED TO REACH THE TEST SECTION. 171

FIGURE 7-3. SPATIAL CALIBRATION FOR MAPPING THE PLIF IMAGES TO CORRECT FOR THE EFFECTS OF REFRACTIVE INDEX AND OPTICAL DISTORTIONS FROM THE NAVITAR ZOOM 7000 LENS. 174

FIGURE 7-4. FLOW VISUALIZATION OF HORIZONTAL ANNULAR FLOW USING PLIF, $\dot{M_G}$ = 0.48KG/MIN AND , $\dot{M_L}$ = 1.8KG/MIN. 174

FIGURE 7-5. (A) RAW PLIF IMAGE EXPORTED FROM DAVIS AND (B) PROCESSED PLIF IMAGE WITH THE FILM BOUNDARIES DETECTED AND MARKED WITH RED CONTOUR. 176

FIGURE 7-6. VALIDATION TEST CONDITIONS (RED SQUARE-DOTS) AGAINST THE BOUNDARIES OF ANNULAR FLOW (REPRODUCED FROM BHAWGAT, 2015). THE BLUE AND GRAY LINES ARE THE BOUNDARIES OF THE ANNULAR FLOW IN UPWARD AND DOWNWARD VERTICAL PIPE ORIENTATION. 177

FIGURE 7-7. COMPARISON OF THE BASE FILM HEIGHT FROM THE CURRENT WORK TO THAT OF SHEDD & NEWELL (2004). 179

FIGURE 7-8. RATIO OF THE STANDARD DEVIATION OF THE FILM THICKNESS (FILM ROUGHNESS) TO THE FILM THICKNESS PLOTTED VERSUS THE REYNOLDS NUMBER OF SUPERFICIAL LIQUID VELOCITY (Re_{SG}~20000). 180

FIGURE 7-9. ANNULAR LIQUID FILM THICKNESS IN DOWNWARD ORIENTATIONS; EFFECT OF GAS SUPERFICIAL VELOCITY. 181

FIGURE 7-10. ANNULAR LIQUID FILM THICKNESS IN UPWARD ORIENTATIONS; EFFECT OF GAS SUPERFICIAL VELOCITY. 182

FIGURE 7-11. ANNULAR LIQUID FILM THICKNESS IN DOWNWARD ORIENTATIONS; EFFECT OF LIQUID SUPERFICIAL VELOCITY. 184

FIGURE 7-12. ANNULAR LIQUID FILM THICKNESS IN UPWARD ORIENTATIONS; EFFECT OF LIQUID SUPERFICIAL VELOCITY. 185

FIGURE 7-13. FILM AVERAGE ROUGHNESS (RATIO OF FILM THICKNESS STANDARD DEVIATION TO THE AVERAGE FILM THICKNESS) 186

LIST OF TABLES

TABLE 2-1. SUMMARY OF CORRELATIONS FOR THE LIQUID FILM THICKNESS IN HORIZONTAL ANNULAR FLOW. 38

TABLE 2-2. SUMMARY OF CORRELATIONS FOR THE LIQUID FILM THICKNESS IN HORIZONTAL ANNULAR FLOW. 44

TABLE 4-1. TEST MATRIX FOR CHARACTERIZATION OF MULTIPHASE PARAMETERS IN THE SPARGED BUBBLE COLUMN 82

TABLE 4-2. SKEWNESS AND KURTOSIS FROM BUBBLE SIZE DISTRIBUTION IN THE SPARGED BUBBLE COLUMN..... 84

TABLE 4-3. BUBBLE SIZE AND HIGHER ORDER STATISTICS, BUBBLES WERE PRODUCED USING A SPARGER DISK IN WATER AND AQUEOUS SOLUTION OF 85% GLYCERIN. 87

TABLE 4-4. DIMENSIONLESS TERMS AND THE CORRELATION FOR BUBBLE SIZE SCALING IN HOMOGENEOUS BUBBLY FLOW..... 93

TABLE 4-5. DIMENSIONLESS TERMS AND THE CORRELATION FOR VOID FRACTION SCALING.98

TABLE 5-1. THE MAXIMUM MEASURED BUBBLES SIZE (D_{MAX}) SPANNING THE FLOW RATES TESTED WITH BOTH INJECTOR TUBE DIAMETERS..... 118

TABLE 6-1. A TEST MATRIX FOR MIXING TIME MEASUREMENTS IN A STATIC COLUMN 145

TABLE 6-2. SUMMARY OF ALL TEST CONDITIONS FOR BUBBLE SIZE AND VOID FRACTION MEASUREMENT. 153

TABLE 6-3. OPERATION SETTINGS EMPLOYED TO STUDY THE EFFECT OF SPECIFIC POWER INPUT ON MIXING TIME..... 156

TABLE 6-4. OPERATION SETTINGS EMPLOYED TO STUDY THE EFFECT OF VIBRATION FREQUENCY ON MIXING TIME. 159

TABLE 6-5. OPERATION SETTINGS EMPLOYED TO STUDY THE EFFECT OF VIBRATION AMPLITUDE ON MIXING TIME. 161

TABLE 7-1. ESTIMATION OF THE PLIF MEASUREMENT ERROR DUE TO THICKNESS OF THE LASER SHEET. 172

TABLE 7-2. FLOW CONDITIONS FOR THE DATA OBTAINED FOR VALIDATION OF THE TEST SETUP. 178

TABLE 7-3. FLOW CONDITIONS FOR THE STUDY OF LIQUID FLOW RATE ON ANNULAR FILM THICKNESS. 183

TABLE B-1. SUMMARY OF ACCELERATION ERROR FOR ALL POSSIBLE TEST CONDITIONS . 220

TABLE B-2. SUMMARY OF THE AIR FLOW RATE ERROR FOR ALL POSSIBLE TEST CONDITIONS221

NOMENCLATURE

Symbol	Description	Units
A	Vibration Amplitude	[mm]
A_{proj}	Projected Two-Dimensional Area	[mm^2]
AR	Aspect Ratio	[-]
A_{SC}	Column Cross Section Area	[mm^2]
a	Interfacial Surface Area	[mm^2]
Bj	Bjerknes Number	[-]
C	Dissolved Gas Concentration	[mgL^{-1}]
$C^{'}$	Normalized Instantaneous Gasd Concentration	[-]
C_D	Coefficient of Drag for a Bubble Swarm	[-]
$C_{D,\infty}$	Coefficient of Drag for a Single Isolated Bubble	[-]
C_0	Initial Dissolved Gas Concentration	[mgL^{-1}]
C_∞	Final State Concentration	[mgL^{-1}]
C^*	Dissolved Gas Concentration at Saturation or Equilibrium	[mgL^{-1}]
D	Column/Pipe Diameter	[mm]
d	Bubble Diameter	[mm]
d_{32}	Sauter Mean Diameter	[mm]
D_{Dif}	Molecular Diffusion Coefficient	[mm^2s^{-1}]
d_{eq}	Area Equivalent Bubble Diameter	[mm]
d_{inj}	Injector Tube Diameter	[mm]
d_0	Sauter Mean diameter in static column	[mm]
F	Buoyancy Force	[N]
f	Vibration Frequency	[Hz]
f_N	Bubble Resonance Frequency	[Hz]
g	Gravitational Acceleration	[ms^{-2}]
H	Static Gas-Liquid Interface Height	[m]
h	Liquid Height Above the Point of Interest	[m]

H_D	Dynamic Gas-Liquid Interface Height	[m]
K	Proportionality Coefficient in k_La Correlation	[-]
k	Proportionality Coefficient in Hinze Correlation	[-]
k_c	Linear Correlation Coefficient	[-]
k_L	Liquid Mass Transfer Coefficient	[m/s]
k_La	Volumetric Mass Transfer Coefficient	[s^{-1}]
k_La_0	Volumetric Mass Transfer Coefficient in static column	[s^{-1}]
$\dot{m}$	Mass Flow Rate	[kgs^{-1}]
$M(h)$	Transient Buoyancy Number	[-]
n_j	Number Count	[-]
P_0	External or Ambient Pressure	[Pa]
P_G	Gas Phase pressure at Injection Manifold	[Pa]
P_m	Specific Input Power	[m^2s^{-3}]
P_{me}	Metered Air Pressure	[Pa]
$\dot{P}_m(t)$	Transient Vibration Specific Power	[m^2s^{-3}]
$P(t)$	Transient Pressure from Vibration	[Pa]
P_v	Liquid Vapor Pressure	[Pa]
Q	Volumetric Flux	[mit/min]
R	Transient Bubble Radius	[mm]
r	Amplitude of Bubble Oscillation	[mm]
R_0	Transient Bubble Radius	[mm]
R^2	Initial Bubble Radius (in Static Column)	[mm]
R_{air}	Specific Ideal Gas Constant	[$KjKg^{-1}K^{-1}$]
$S()$	Skewness of ()	
T	Time	[s]
T_b	Mixing Time	[s]
t_c	Contact (Residence) Time	[s]
T_G	Gas Phase Temperature	[k]
U_b	Bubble Terminal Velocity	[m/s]

V	Bubble Volume	[mm^3]
x	Two-phase flow quality	[-]

Greek Letters and Symbols

<>	Longitudinal Average	
ΔH	Vertical Distance between Pressure Taps	[m]
ΔP	Differential Pressure	[Pa]
ε	Void Fraction	[-]
ε_0	Void Fraction in static column	[-]
κ	Adiabatic Index	[-]
$\kappa()$	Kurtosis of ()	
λ	Wavelength	[m]
μ	Dynamic Viscosity	[$kgm^{-1}s^{-1}$]
ν	Kinematic Viscosity	[m^2s^{-1}]
Ξ	Measuremet Uncertainty	
π	Non-dimensional Term	
ρ	Density	[kgm^{-3}]
σ	Gas-Liquid Surface Tension	[Nm^{-1}]
$\sigma()$	Standard deviation of ()	
τ	Interfacial Shear	[Nm^{-2}]
Φ	Scale of Segregation	[-]
ω	Vibration angular velocity	[$Rads^{-1}$]

Subscripts

∞	Final State
10	Arithmatic Mean
32	Sauter Mean
atm	Atmospheric
base	Base Film

c	Column
cap	Capilary
eq	Equvalent Quantity
f	Frictional
film	Annular Liquid Film
Fr	Parameter based on Froude Number
fr	Frictional Component
G	Gas
i	Interfacial
inj	Injector
L	Liquid
mani	Injection Manifold Readings
P	Pipe
proj	Projected
ps	Passive scalar
S	Superficial
sp	Sparger
TP	Two-phase
XY	Planar Componet of Acceletation
Z	Vertical (Longitudinal) Componet of Acceletation

Superscripts

`	Derivation with Respect to Time
+	Non-dimensional Turbulent Boundary Layer Parameter

CHAPTER I

INTRODUCTION

1.1 Background and Motivation

Multiphase flow describes the intricate combination of two or more phases that produces complex physical patterns. Understanding the phase interactions as well as the boundary conditions assist engineers to replicate any pattern of interest to the benefit of research and industrial applications (Brennen, 2005). Gas-liquid flow is one of the most prominent types of multiphase flows encountered in the oil and gas industry as well as chemical processing industry (Crowe, 2005; Helmig, 1997; Govier & Aziz, 1972). The current work focuses on gas-liquid studies (vibrating bubble column and annular pipe flow) using flow visualization techniques, which has numerous fundamental and industrial applications.

A gas-liquid contactor introduces a gas into a liquid for the purpose of heat transfer, mass transfer, and/or chemical processing (Kantarci, 2005). A batch bubble column is a gas-liquid contactor, widely used due to its simplicity and cost effectiveness. Increasing the phase interfacial area and the residence time are the two primary methods for enhancing the efficiency of a bubble column. It has been shown that mechanical vibration improves both the aforementioned aspects (Harbaum & Houghton, 1962; Houghton, 1963; Baird, 1963; Houghton, 1966; Bretsznajder, 1963; Jameson & Davidson, 1966; Jameson, 1966; Baird & Garstang, 1972; Marmur & Rubin, 1976; Rubin, 1968; Foster et al., 1968). An example of a

potential application for a vibrating bubble column is the liquefaction of coal slurries through the Fischer-Tropsch process, which is used in the production of synthetic fuel. It is worth mentioning that the civil air transport sector has led the demand for synthetic fuel (e.g. Airbus A380; Vogelaar, 2010). Thus the first part (chapters 4-6) of this work aims to understand the physical behavior of a gas-liquid system in a vibrating bubble column.

The second part (chapter 7) of this work also studies gas-liquid multiphase flows via flow visualization, but now within a pipe flow. Specifically, the dependence of film thickness on inclination angle within annular flow will be analyzed, which leverages established facilities at Oklahoma State University (OSU Muliphase Flow Lab). Two-phase gas-liquid pipe flow in inclined pipes exists in a broad spectra of industrial applications including oil-and-gas, refrigeration systems, and nuclear power plants (Crowe, 2005). The phase distribution across the pipe cross-section depends on the pipe geometry, orientation, and mass flow rate of each individual phase (Brennen, 2005). Given the potentially substantial difference in thermo-physical properties between phases, compressible nature of gases, turbulent mixing, and complex phase distribution; an analytical approach for calculating the multiphase parameters is beyond current methods. Therefore, empirical relationships derived from experimental studies of multiphase flows are required for prediction of flow parameters (e.g. void fraction, pressure drop). To author's knowledge studies on the effect pipe inclination on annular flow are scarce in the annular flow literature (Belt, 2007; Geraci et al. 2007; Al-Sarkhi et al. 2012). Thus, the current study aims to experimentally investigate the phase distribution specifically within the annular flow regime to understand the underlying physics.

1.2 Vibrating Bubble Columns

1.2.1 Problem overview

The vibrating bubble column research branches into the study of bubble size, bubble-retardation, void fraction, and mass transfer. The precise modeling of mass transfer requires the understanding of void fraction, which itself is governed by bubble size and velocity. Vibrating bubble column literature primarily focuses on investigating the effect of vibration frequency, but there is a dearth of results on the effect of amplitude on bubble behavior and void fraction. Moreover, the accuracy of the existing correlations for void fraction is uncertain due to the lack of experimental data in vibrating bubble columns. Hence, there is a gap in vibrating bubble column research for a systematic approach to predict the bubble size using dimensional analysis.

1.2.2 Flow regimes (static and vibrating)

The operation regime (i.e. flow pattern) addresses the physical behavior of the gas-liquid multiphase flow. That is classification of the physical structure and appearance of the flow patterns in a gas liquid flow. Regime demarcation in multiphase flow literature has been carried out by visual inspection; hence, an individual's perceptions of the definition and description of flow patterns can impact the regime identification.

Flow patterns are the physical manifestation of the coupling between gas and liquid phase. The flow patterns in bubble columns are a function of void fraction (global scale) and gas injection method (bubble scale). Considering the most general cases, four operation

regimes are distinguished with increasing gas superficial velocity in batch bubble columns, as shown in Figure 1-1. The description of flow patterns are as follows:

- **Perfect bubbly flow:** Perfect bubbly flow is characterized by a uniform distribution of equal size bubbles.
- **Imperfect bubbly flow:** This flow regime is characterized by the unstable flow field around the bubble and poly-dispersed bubble size distribution. Here bubble breakage and coalescence is rare.
- **Churn-turbulent flow:** Churn-turbulent flow is formed by the agglomeration of bubbles to form large bubbles. Regions of recirculation are notable near the wall and bubble size distribution is very broad.
- **Slug-flow:** Slug flow is characterized by the alternating between the flow of large bullet shape bubbles spanning the cross section of the column (slugs) and liquid plugs containing small bubbles.

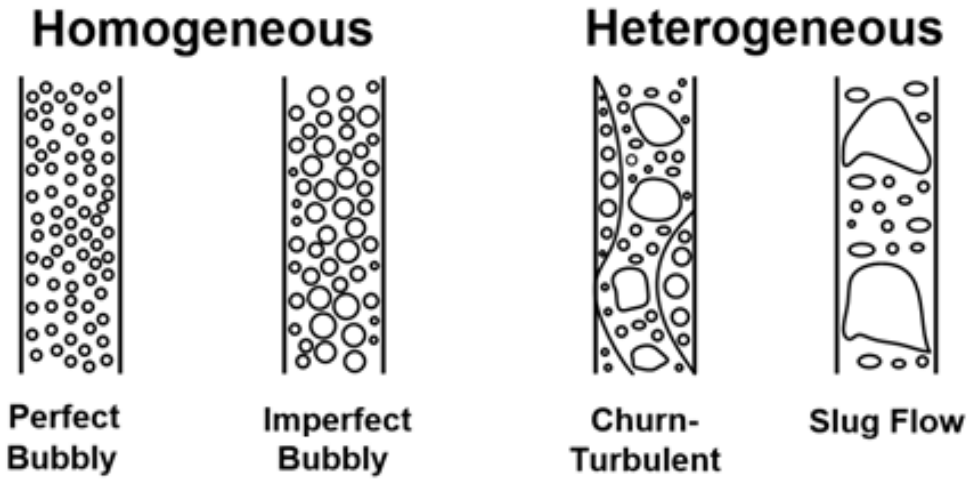

Figure 1-1. Flow patterns in static bubble columns (reproduced from Kantarci et al., 2005).

Due to the scarcity of literature on vibrating bubble columns, especially on the hydrodynamic behavior and flow patterns, an established definition of flow patterns and operation regimes is not readily available. Based on observations from the current work, three flow patterns are proposed based on the wavelength of the standing acoustic wave, which are illustrated in Figure 1-2. The definitions to these flow patterns are:

- **Solid body vibration:** Solid body vibration describes low power vibrations without liquid sloshing at the free surface and consequently no vibration-induced liquid velocity field. In the current experimental setup this regime occurs at relatively low vibration frequencies ($f < 8.5$ Hz).
- **Cyclic bubble migration:** This flow pattern features aggregated bubbles that migrate as a whole in a cyclic fashion towards the column bottom and vice versa. Here the liquid height in the column (H_0) is smaller than the standing acoustic wavelength (λ), $H_0 < \lambda$.
- **Modal excitations:** Modal excitations describes the case where the liquid height in the column (H_0) is larger than the standing acoustic wavelength (λ), $H_0 > \lambda$. Increasing the vibration frequency exhibits modal behavior in void fraction and mass transfer trends due to bubble aggregation at the antinodes.

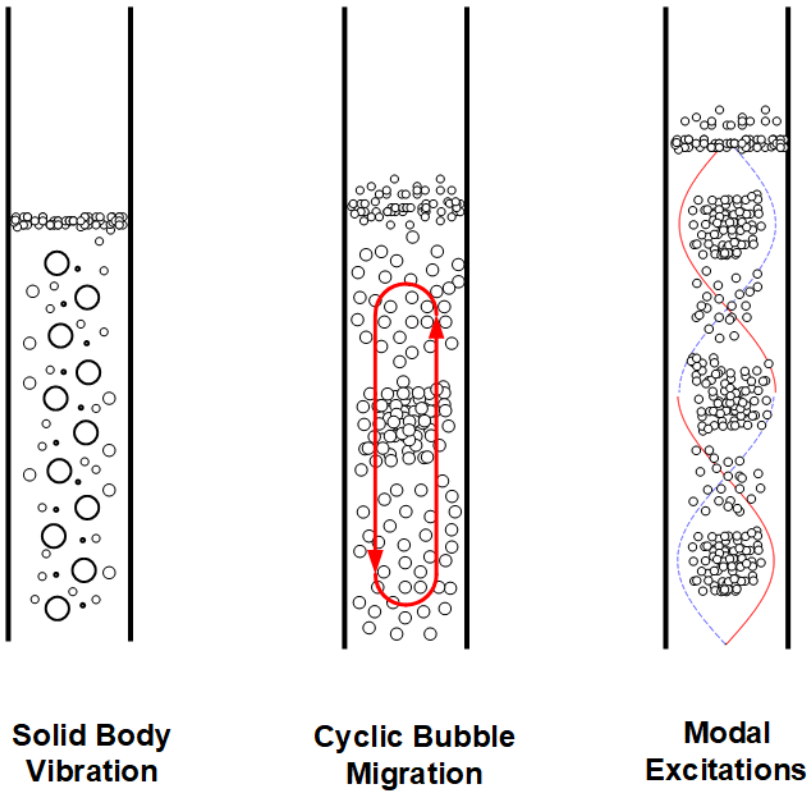

Figure 1-2. Proposed flow patterns in vibrating bubble columns.

1.3 Gas-Liquid Annular Pipe Flow

1.3.1 Problem overview

In gas-liquid pipe flow research the void fraction, pressure drop, and heat transfer measurements can be used to understand the physical behavior of the multiphase system. The frictional pressure drop can only be accurately predicted when the physical structure of gas-liquid flow field is properly characterized. The lack of experimental initiatives and robust models, motivates the current experimental work on annular flow with the aim of expanding the available data on characteristics of the flow field. This will pave the way for producing

future models with improved accuracy. Due to the abundance of flow regimes with significantly different fluid dynamic behaviors, the current study is confined to a specific flow regime.

1.3.2 *Pipe flow regimes*

Based on the physical structures of the flow field gas-liquid pipe flows can be categorized into classes, commonly called flow pattern or flow regimes. The physical structures of the gas-liquid pipe flow are produced by the alignment of gas and liquid phases across the pipe cross section. This alignment is sensitive to pipe orientation due to significant difference between the gas and liquid density. Thus, the effect of gravity (i.e. pipe orientation) is an independent variable in the study of flow regimes in gas-liquid pipe flow. Hence an overview of the flow patterns associated with the gas-liquid pipe flows in both the vertical and horizontal orientations are provided below.

1.3.2.1 Flow patterns in vertical gas-liquid pipes

Figure 1-3 illustrates the various flow patterns in a gas-liquid pipe flow in the vertical orientation, which has been adapted from Brennen (2005). Flow patterns in gas-liquid vertical pipes at low gas volume fractions share similarities to those of bubble columns. This is expected given that the bubble column represents this orientation when the liquid phase velocity goes to zero. However, at high gas volume fractions new flow patterns are observed, specifically annular and dispersed flows. Hence, only annular and dispersed flow regimes are discussed here.

- **Annular:** Annular flow occurs when the liquid flow in contact with the pipe wall forms a thin film. This film surrounds a fast moving gas core, which entrains drops of liquid from the thin film. It is only in vertical pipes that circumferential film thickness distribution is uniform.
- **Dispersed:** Dispersed flow (also known as annular-misty) is innately an annular flow when liquid film decays significantly due to the liquid entrainment; here a spray of liquid drops moves along within a continuous gas flow.

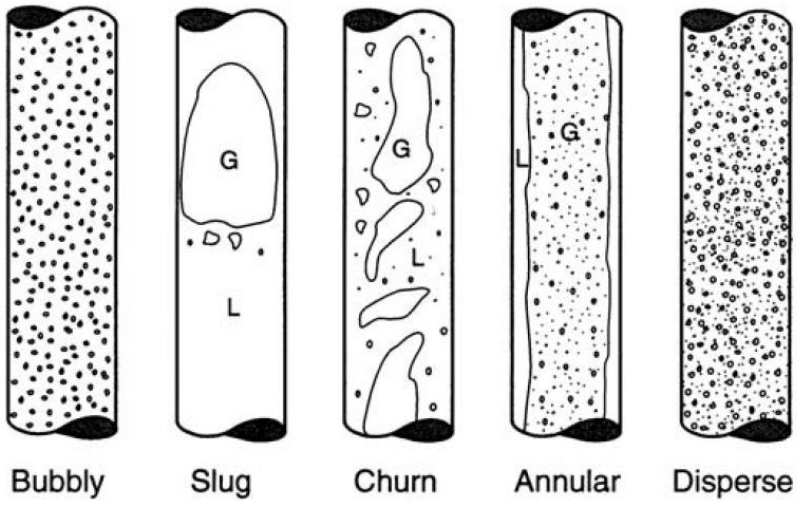

Figure 1-3. Flow patterns in a vertical gas-liquid pipe flow (adapted from Brennen, 2005).

1.3.2.2 Flow patterns in horizontal gas-liquid pipes

The flow patterns observed in horizontal gas-liquid pipe flow are illustrated in Figure 1-4, which was also adapted from Brennen (2005). The general descriptions of the flow patterns are:

- **Bubbly:** Bubbly flow is characterized by dispersed bubbles within a continuous liquid phase; however, in horizontal pipes due to buoyancy the bubbles are in contact with top section of the pipe.
- **Plug:** Plug flow is characterized by long batches of gas at the top section of pipe.
- **Stratified:** At low liquid and gas mass flow rates, the gas phase flows at the top section of the pipe parallel to the liquid phase.
- **Wavy:** Wavy flow occurs the gas volume fraction is increased in the stratified flow regime; producing instabilities at the gas-liquid interface.
- **Slug:** This flow pattern is characterized by alternating flow of elongated gas bubbles and liquid plugs.
- **Annular:** Similar to vertical pipes, annular flow in horizontal pipes is characterized by a thin film of liquid at the wall that surrounds a fast moving gas core. Due to gravity effects in horizontal pipes, the circumferential distribution of film thickness is not uniform.
- **Dispersed:** The spray of liquid drops moving along the continuous gas flow characterizes dispersed flow.

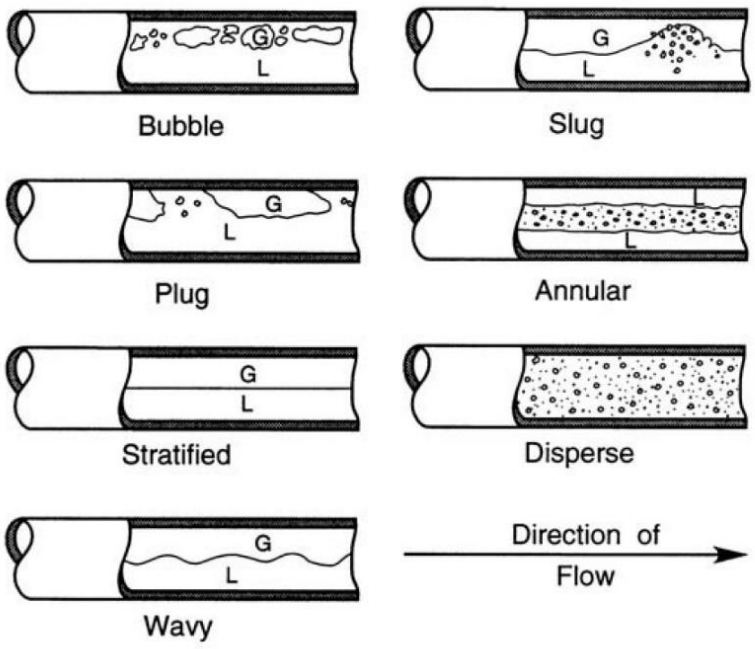

Figure 1-4. Flow patterns in a horizontal gas-liquid pipe flow (adapted from Brennen, 2005).

1.4 Research Objectives

Based on the above discussion, the current research is divided into four objectives. The first objective is to investigate the effect of operation regime on multiphase parameters. Bubble column experiments were designed to investigate the bubble size and void fraction in homogenous and heterogeneous regimes. The second objective of this research is to explore and understand the effect of vibration on multiphase parameters as well as the physical structure of flow patterns in a bubble column. Systematic measurements of bubble size distributions were the main focus toward accomplishing this research objective. The third objective of the current work is to explore the hydrodynamics of vibrating bubble column. The

primary measurement for this objective is mixing time of a passive scalar under bubble induced diffusion in static and vibrating scenarios. The final objective of the current study is to investigate the effect of gravity on annular film thickness. A variable inclination multiphase pipe flow setup was used to study the annular film at inclined pipe configurations. Based on the literature review and initial testing the following hypothesis driven research plans were identified:

Objective 1: Characterization of bubble size and void fraction in a sparged bubble column operating in the homogenous or heterogeneous regime.

Research Question: In a sparged vibrating bubble column, how does the operation regime effects the bubble size and void fraction scaling?

Hypothesis: In the homogeneous regime, both bubble size and void fraction will heavily depend on the injection condition due to the lack of breakage and coalescence. In the heterogeneous regime (churn-turbulent), the non-dimensional bubble size should scale with the non-dimensional specific input power. In addition, the void fraction is expected to be a function of bubble size and gas superficial velocity.

Approach:

a) Bubble size and void fraction was measured over a parametric study to test the effect of liquid properties (i.e. ρ_L, μ_L, and σ) and characterize the bubble size statistics at associated regimes.

b) Using dimensional analysis correlations were produced to predict the bubble size, these correlations were validated against experimental data from the current work and literature.

Objective 2: Bubble size scaling and void fraction modeling in a vibrating bubble column

Research Question: In a vibrating batch bubble column, operating within the poly-dispersed bubbly flow regime via use of a single point gas injection: why is there an inverse trend between the mechanical power and bubble size?

Hypothesis: Vibration reduces the bubble size via breakage and increases the void fraction via retardation, the given specific vibration power is the main cause for bubble retardation and breakage.

Approach: The aim of this work is (i) to provide a comprehensive understanding of the bubble size in a vibrating bubble column reactor, and (ii) produce a physics-based correlation between bubble size and specific input power.

Objective 3: Characterization of the mixing of a passive scalar in a vibrating bubble column.

Research Question: In a sparged vibrating bubble column, how does the vibration effect the mixing performance of the bubble column?

Hypothesis: In a homogeneous swarm of bubbles the mixing time is a function of the mechanical input power; therefore, increasing the vibration power enhances (accelerates) the mixing.

Approach: Mixing of a passive scalar was investigated to characterize the effect of vibration on hydrodynamics of the bubble column.

Objective 4: Effect of inclination angle (gravity force) on film thickness in annular flow.

Research Question: How does the thickness of the annular film at the bottom of the pipe respond to changes in the gas and liquid phase flow rates at various pipe inclination angles?

Hypothesis: Given the literature review and preliminary results from Bhagwat (2015) acquired in the Multiphase Heat Transfer Laboratory (Dr. Ghajar's lab), the following hypothesis was identified. In multiphase pipe flow, the interaction of gravitational, inertial, and surface tension forces effects the annular liquid film thickness. The film thickness is expected to be insensitive to flow rates; however, it is expected that there would be a significant impact observed from pipe orientation.

Approach: Using the inclined multiphase pipe flow setup (Prof. Ghajar's lab), the effect of gravity on film thickness on the bottom wall (δ) was quantified. This was achieved using Planar Laser Induced Fluorescent (PLIF) to measure the liquid film thickness within the annular flow regime, and simultaneously measure the pressure drop to calculate the multiphase friction multiplier and liquid entrainment fraction.

1.5 Summary of the Current Study

This research is presented in eight chapters (including this introduction), and provides details of the background knowledge, experimental advances and technical contributions. A comprehensive review of previous work is presented in Chapter 2. Chapter 3 provides details

of the experimental setup, instrumentation and data collection procedures. Chapter 4 provides characterization and scaling of the bubble size and void fraction in a static column with regime considerations. Chapter 5 presents experimental results regarding the effect of vibration on bubble size distribution in a bubble column with a single point gas injector. Chapter 5 also provides a physics-based model for void fraction prediction. Chapter 6 presents a study on the effect of vibration on the mixing rate of a passive scalar under bubble induced diffusion. Chapter 7 provides a study on annular flow at inclination angles with experimental measurements of film thickness on the bottom wall. Finally, in Chapter 8 the final remarks and conclusions of this work are provided in addition to recommendations for future work.

CHAPTER II

LITERATURE REVIEW

Early studies of gas-liquid two-phase flow with the scope of characterization of multiphase parameters dates back to 1960's. So far, the number of contributions is considerable including many interesting findings. In this chapter, a review of past studies is provided to identify current gaps within the scope of bubbly and annular flow research. Section 2.1 gives a detailed review of previous studies on vibrating bubble columns. Section 2.2 summarizes past studies on bubble induced mixing in bubbly flows. In addition, section 2.3 reviews experimental studies on film thickness in annular flows.

2.1 Vibrating Bubble Column Literature Review

Bubble columns are used in many applications, including aeration of organic organisms in bioreactors, indirect liquefaction of coal-slurries to produce synthetic fuels via Fischer-Tropsch process, and gasification of solvent for chemical reactions. Vibrating bubble columns was initially an active area of research starting in the early 1960's with the very first works carried out for the purpose of mass transfer enhancement (e.g., Harbaum & Houghton, 1960; Harbaum & Houghton, 1962; Houghton, 1963; Bretsznajder, 1963; Baird & Garstang, 1972). The vibrating bubble column literature can be broadly divided into three categories:

i. Mass transfer and void fraction studies
ii. Modeling the bubble dynamics

iii. Modeling the multiphase parameters (e.g. bubble size and void fraction)

The comprehensive vibrating bubble column literature review is divided using these categories.

2.1.1 Mass transfer and void fraction studies

Mass transfer (k_La) and void fraction (ε) intensification in vibrating bubble column has been the topic of several studies in the literature. Harbaum & Houghton (1962) studied the effect of vibration frequency (f) and amplitude (A) on absorption rate of carbon dioxide (CO_2) in water. This study showed a stronger linkage between vibration frequency (f) and mass transfer (k_La) improvement in comparison with vibration amplitude. Harbaum & Houghton (1962) also shows that mass transfer enhancement is primarily due to an increase in phase interfacial area (a) rather than mass transfer coefficient (k_L). While this study presents the phase interfacial area (a), no quantitative data on bubble size and shape characteristics were provided.

Baird & Davidson (1962) studied the absorption rate of a single carbon dioxide bubble injected into a column of water, *n*-butanol, or *n*-hexanol with the aim of finding insights into the mass transfer mechanism and governing physics. This study concluded that for a dissolving bubble the mass transfer coefficient (k_L) is not time dependent. Furthermore, the absorption rate of a bubble is influenced by phase slip velocity, surface tension, and bubble wake characteristics. This study also contributes to vibrating bubble column research by explaining that vibration can detach the high concentration layer of dissolved gas from the bubble causing the mass transfer to increase (k_La).

In the beginning of the 21st century the vibrating bubble column research was reinvigorated, this time modern measurement techniques and instrumentation helped better explore the problem. Krishna et al. (2000) provided an experimental study of bubble breakup under high frequency vibration (100 Hz < f < 200 Hz). Following that a series of studies were carried out by the same research group (Krishna & Ellenberger, 2002; Ellenberger & Krishna, 2003; Ellenberger et al., 2005) to explore the effect of vibration on void fraction and mass transfer. It is worth mentioning that all these additional studies were carried out at low amplitudes ($A \leq 1.2$ mm) and higher frequencies (f > 120 Hz). Krishna & Ellenberger (2002) find an optimum vibration condition, which produces a two-fold increase in void fraction. Furthermore, this study showed that the mass transfer ($k_L a$) increases up to twice as rapidly as void fraction as the vibration frequency increases (see Figure 2-1). Krishna & Ellenberger (2002) also propose that the increase in mass transfer rate ($k_L a$) is not only due to an increase in phase interfacial area (a), but the mass transfer coefficient (k_L) could experience increases due to additional velocity fluctuations.

Ellenberger & Krishna (2003) attempts to distinguish between the effect of frequency and amplitude on two-phase parameters in a vibrating bubble column. While increasing both frequency and amplitude increases the void fraction, increasing the amplitude exhibits a more dramatic increase in void fraction (see Figure 2-2). Under vibration, a modal behavior in the general increasing trend of void fraction was observed. Figure 2-3 demonstrates the local maxima's at specific frequencies in the increasing trend of void fraction as vibration frequency increases (Ellenberger et al., 2005). It is worth mentioning, Budzyński et al. (2017) observed similar results in void fraction behavior under vibration.

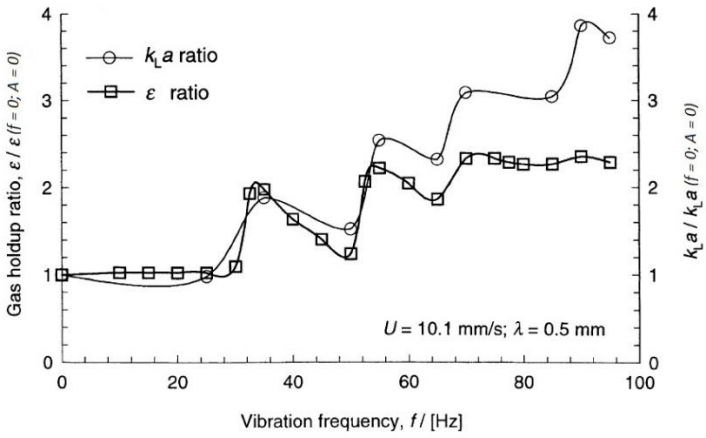

Figure 2-1. Void fraction and mass transfer enhancement with respect to a stationary case; U_{SG} = 10.1mm/s and A = 0.5mm (adapted from Krishna & Ellenberger, 2002).

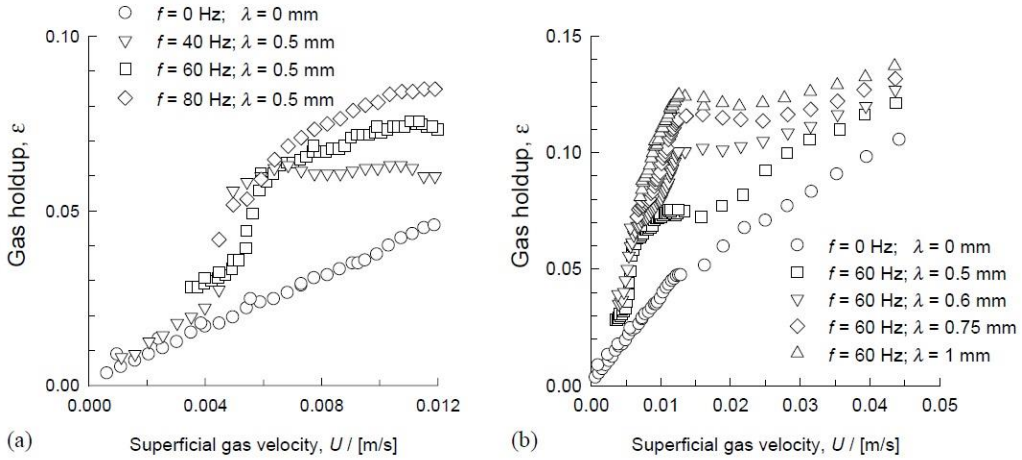

Figure 2-2. Void fraction under vibration showing the (a) effect of frequency and (b) the effect of amplitude (adapted from Krishna & Ellenberger, 2003).

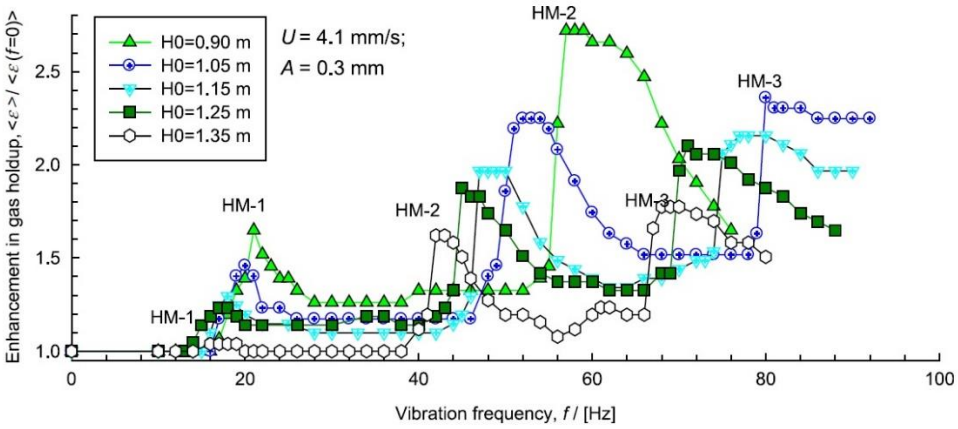

Figure 2-3. Void fraction intensification with vibration frequency; U_{SG} = 41mm/s, A = 0.3mm, H_0 = 0.85-1.35m (adapted from Ellenberger et al., 2005).

In summary, mass transfer intensification in vibrating bubble columns has been well studied up to this point and a considerable number of contributions are available. The interested reader is referred to Elbing et al. (2015) for a review of previous work on mass transfer in vibrating bubble columns. In spite of the previous studies, a fundamental question remains unanswered; how does vibration influence the mass transfer coefficient (k_L)?

2.1.2 Modeling the bubble dynamics

Bubble dynamics under vibration has been the topic of several studies from the beginning of the vibrating bubble column research in the 1960's. Buchanan et al. (1962) studied the effect of vibration on bubble migration in a vibrating bubble column. This study was the first study reporting a counter-buoyancy bubble migration at specific vibration frequencies. Buchanan et al. (1962) derives the stabilization (i.e. levitation) frequency (ω_s) using electromagnetic-hydrodynamics analogies (see Equation 2-1).

$$\omega_S^2 A = -g \pm \sqrt{3g^2 + \frac{2gP_e}{\rho_L h}}$$ Equation 2-1

Here g is the gravitational acceleration, ρ_L is the liquid density, h is the height of water above the bubble, and P_e is ambient pressure. It is noteworthy that the effect of surface tension, radial velocity, and viscosity were neglected when deriving Equation 2-1. Buchanan et al. (1962) compared the stabilizing frequency (ω_s) with the cut-out frequency (ω_c) (i.e. frequency at the onset of counter-buoyancy migration determined experimentally) to check the validity of Equation 2-1. Figure 2-4 demonstrates an excellent agreement between the predicted stabilization frequency and that experimentally determined (ω_c).

Houghton (1963) studied the dynamics of particle suspension in an oscillating velocity field, ultimately this study provides careful selection of frequency (f) and amplitude (A) combinations that results in motionless bubbles. This study also concludes that the drag coefficient at the particle terminal velocity should be used to study the dynamics of a particle in an oscillating flow.

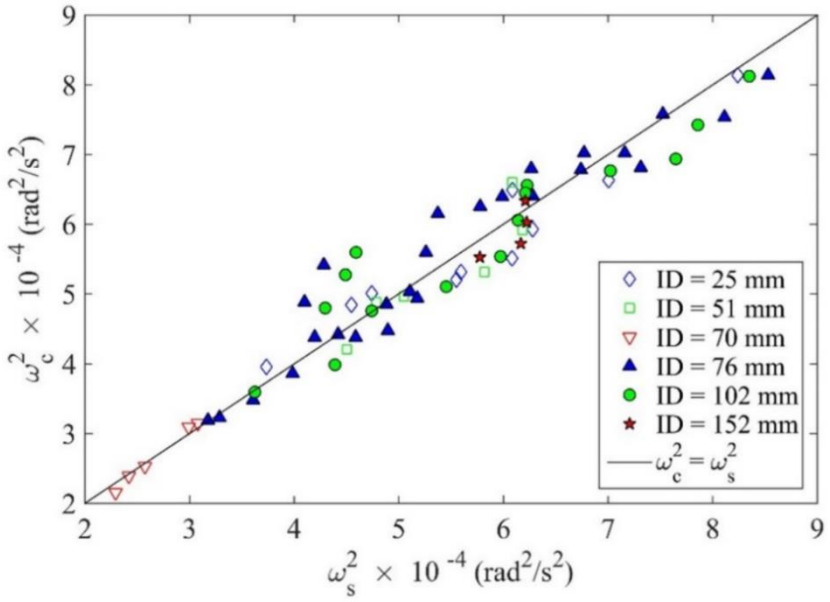

Figure 2-4. Comparison between the predicted stabilization frequency (ω_s) from Equation 2-1 and that of cut-out frequency (ω_c), (adapted from Elbing et al., 2015).

Jameson & Davidson (1966) performed analysis to predict the levitation of a single bubble based on the vibration condition, liquid density, and absolute pressure at the bubble location. It is noteworthy that Jameson & Davidson (1966) used a velocity potential function for the liquid phase and employed the assumptions of Buchanan et al. (1962) to derive the levitation condition. Jameson & Davidson (1966) claimed that the levitation condition occurred when the Bjerknes number ($Bj = \frac{A^2\omega^4\rho_L h}{2gP_0}$) equals unity. However, experimental results did not support this proposed analysis. Later Rubin (1968) used the Rayleigh-Plesset equation for bubble expansion and contraction under vibration to argue that the levitation happens when *Bj* = 1.4. It is interesting to note that in both Jameson & Davidson (1966) and Rubin (1968) finds *Bj* at the levitation condition is equal to the polytropic index, former corresponds to an isothermal process (i.e. expansion and contraction) and the later corresponds to an adiabatic process. In another study, Jameson (1966) carried out more experimental

measurement of *Bj* at the levitation condition. Jameson (1966) clearly shows that *Bj* at levitation is a function of the bubble unsteady Reynolds number ($Re = A\omega R_0/\nu$) when $Re >$ 2 (see Figure 2-5).

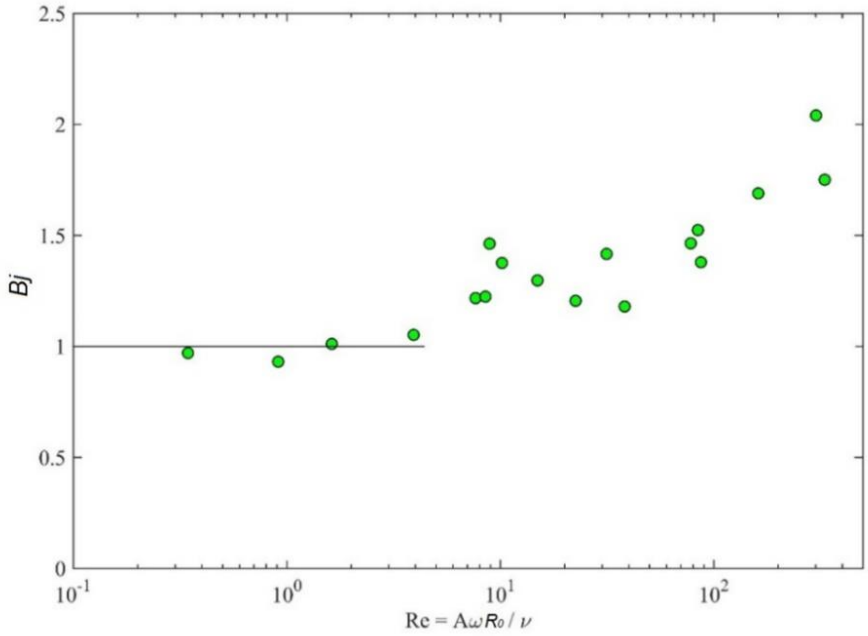

Figure 2-5. *Bj* versus bubble Reynolds number at levitation condition (adapted from Elbing et al., 2015).

In two relatively new contributions (Ellenberger & Krishna, 2007a; Ellenberger & Krishna, 2007b) levitation of single bubbles and slugs were experimentally studied. These works proposed a mathematical model for prediction of the levitation depth (distance vertically downward from the free surface) based on balancing the transient buoyancy force with the drag force acting on the bubble at a terminal velocity. It is noteworthy that in following studies the transient buoyancy force was obtained based the bubble size from time averaging the Rayleigh-Plesset equation over a vibration cycle. Ellenberger & Krishna (2007a,b) also investigated the effect of column aspect ratio, liquid properties (i.e. density and viscosity), vibration condition,

and operation pressure on the levitation condition. Experimental observation of levitation (Ellenberger & Krishna, 2007a,b) of a single bubble and slugs are in good agreement with the proposed mathematical model.

In summary, contributions to bubble dynamics under vertical vibration has been limited so far and the currently available literature primarily focuses on predicting the levitation condition with marginal success. The current predictions of the levitation condition are subject to over simplification of the governing equations. Hence, a comprehensive analysis for deriving the levitation criterion is needed, here any simplification should be supported with physical evidence.

2.1.3 Modeling bubble size and void fraction

Recently there has been growing interest in modeling the multiphase parameters (e.g. bubble size and void fraction) in vibrating bubble columns. Studies with this scope has been mainly carried out with the purpose of contributing to scaling the vibrating bubble column from small laboratory scale to large industrial scale. In this section, contributions on modeling the void fraction and bubble size are reviewed.

Waghmare et al. (2007) studied the effect of the liquid viscosity (μ_L) on mass transfer and provided experimental data as well as a theoretical relationship that predicts the dependence of the mass transfer on the liquid viscosity. Waghmare et al. (2007) also scales the Sauter mean diameter (d_{32}) with the specific power input (P_m) using the Hinze (1955) correlation for bubble breakage under shear. Waghmare et al. (2008) proposed a unified model to predict the void fraction that was successfully tested against experimental results. Equation 2-2 shows this model for the void fraction (Waghmare et al., 2008); the interesting outcome of

this work is that the fluid properties (i.e. surface tension, density, and viscosity) contributes to the prediction of void fraction. It is noteworthy that the void fraction model in Waghmare et al. (2008) was based on the analysis from Buchanan et al. (1962). The corner stone of void fraction model in Waghmare et al. (2008) is the assumption that the ambient pressure is significantly larger than both hydrostatic and vibration pressure. This assumption is only valid for a small fraction of experimental studies in the literature.

$$\langle \varepsilon \rangle = 6.75 \left[\frac{U_{SG}(gU_{SG} + 0.5A^2\omega^3)^{0.4}}{(\frac{\sigma}{\rho_L})^{0.6}(\frac{g}{\sqrt{\nu_L}})^{2/3}} \right] \left[\frac{1-(1-Bj)^{1/3}}{Bj} \right] \quad \text{Equation 2-2}$$

Waghmare et al. (2009) presented a model to predict the bubble size based on population modeling. This model was tested against experimental bubble size to verify the sensitivity of the model to measurement location and vibration condition. Results showed that the model was partially successful in predicting the bubble size distribution under vibration. In summary, the overall contributions to modeling void fraction under vertical vibration has been limited, and the available models in the literature are derived based on assumptions that significantly limit their applicable range.

Literature on bubble size under vibration is utterly scarce and offer no fundamental understanding of the breakage mechanism. This necessitates the need for improving physics based model for the prediction of void fraction and bubble size and a broad body of experimental data to test the validity of the current and new models. From this review, the necessity for further experimental examination of vibrating bubble columns is apparent, in addition to needs for contributions to the fundamental understanding of the gas-liquid two-

phase flows under mechanical vibration. Furthermore, due to potential applications in large-scale synthetic fuel production; it is desired to have physics based models that predicts bubble size and void fraction over a large operation range.

2.2 Review of Bubble Induced Mixing

In many industrial applications, bubbly flows are employed for the purpose of enhancement of a chemical reaction. Bubble columns offer robust and cost effective mixing. In a homogeneous bubble swam the slip velocity at the gas-liquid interface of bubbles generates liquid agitations (induced velocity fluctuations) that promote the mixing of the species in the absence of a mean flow. Correct prediction of the mixing time scale is of great importance when working with chemical reactions or shear-sensitive products. Therefore, quantify the mixing time is a critical step in characterizing and/or prediction of a bubble column performance. In spite of the ever growing demand for scaling the mixing time, little is known about the dispersion mechanism even in the simple case of a passive scalar (i.e. non-reactive dye or ink) without complexity of a simultaneous chemical reaction.

Besnaci et al. (2010) argues that the dispersion of a passive scalar within a bubbly flow is the result of two synergic mechanisms. First, dispersion from the direct interaction between the passive scalar and bubbles. In particular, the passive scalar can be caught in the wake of a bubble and migrate at the bubble velocity. The second mechanism is dispersion due to liquid velocity fluctuations (bubble-induced turbulence) due to bubble wake interactions.

Characterization of the properties of bubble induced turbulence has been the focus of several studies (Lance and Bataille, 1991; Martinez-Mercado et al., 2007; Riboux et al., 2010; Martinez-Mercado et al., 2010; Mendez-Diaz et al., 2013; Alméras et al., 2015). These studies

show that the bubble-induced turbulence is substantially different from shear-induced turbulence. The bubble generated agitations and bubble wake interactions are the main reasons for the aforementioned difference. The most distinct and intricate feature of bubble induced turbulence is the slope of the energy spectra in the inertia subrange. Figure 2-6 shows the –5/3 slope for smaller length scales corresponding to Kolmogorov law for isotropic turbulence; however, within certain wavelengths corresponding to bubble size scale and integral length scale the slope of spectra changes to –3.

The multiscale nature of flow field structures in a bubble swarm, makes the bubble induced mixing a multiscale process as well (Besagni et al., 2018). In bubble columns, mixing is characterized by concentration measurements at the global system (i.e. macroscale), bubble scale (i.e. mesoscale), or turbulent eddy scale (i.e. microscale). Advection and the mean velocity of liquid in the bubble column generates the large scale mixing. Mixing at the bubble scale is a diffusion process and has been modeled using two diffusion-coefficients in vertical and horizontal directions (Maregue and Lance, 1995; Abbas et al., 2009; Alméras et al., 2016a; Alméras et al., 2016b; Loisy, 2016; Alméras et al., 2018). Alméras et al. (2015) shows that the diffusion coefficient the in the vertical direction (buoyancy driven) is larger than in the horizontal direction. Moreover, both diffusion coefficients exhibit direct relationship with void fraction; however, at large void fractions the diffusion coefficients are constant. Mixing by shear induced velocity agitations (microscale) can be modeled setting the turbulent Schmidt number (Sc_t) to unity and calculating the diffusion coefficient from turbulent eddy viscosity (ν_t).

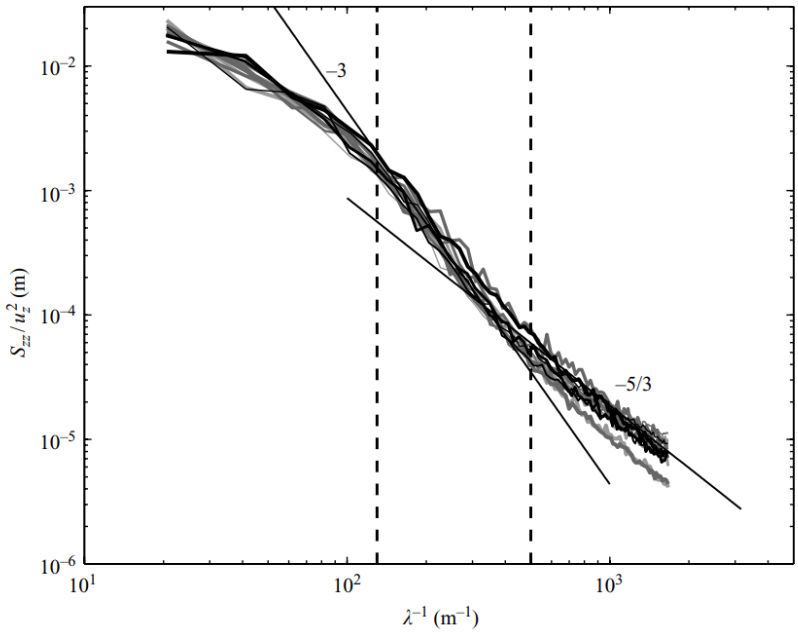

Figure 2-6. The power spectra of normalized liquid velocity agitations with wavelength in the buoyancy direction (adapted from Riboux et al., 2010).

Wiemann and Mewes (2005) used numerical simulations to study the mass transfer and mixing in a bubble column. This study employs a one dimensional dispersion model in the longitudinal direction of the bubble column and calculates the dispersion coefficient. The resulting diffusion coefficients were in a good agreement with experimental data (see Figure 2-7). Radl et al. (2010) studies mixing in the presence of mass transfer and chemical reaction using a numerical simulation of a diluted bubble swarm in a thin rectangular bubble column. This study provides insights in to the physics of bubble mixing by introducing a quantitative measurement of the mixing driving force Φ (i.e., scale of segregation). Furthermore, these result show a direct relationship between the mixing time scale (t_∞) and the phase interfacial area (a). It is worth mentioning that both Wiemann & Mewes (2005) and Radl et al. (2010) provide very good information on time evaluation of concentration in the entire flow field. Comparison of the finding with experimental point measurements of concentration shows that

having the time evaluation of the concentration across the entire flow field is an advantage. However, in Radl et al. (2010) the effect of bubble induced turbulence was not included in the computational model.

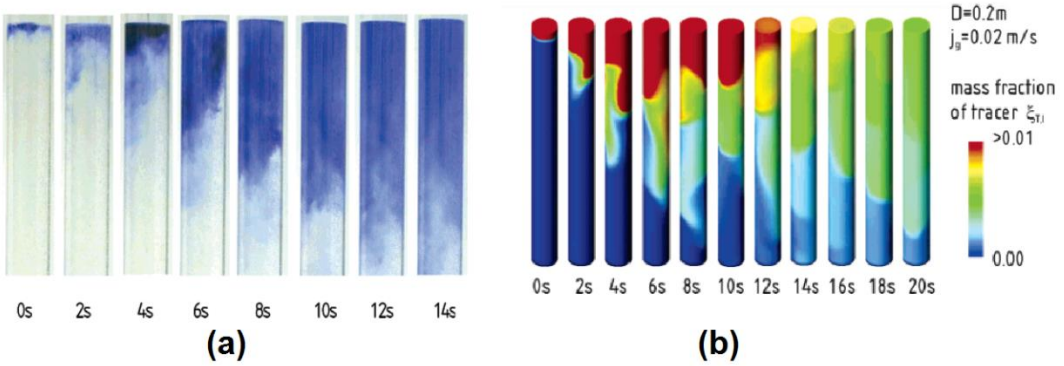

Figure 2-7. Time trace of the concentration distribution of a passive scalar in a bubble column (air and water, D = 0.2m, U_{SG} = 20mm/s); (a) experimental and (b) numerical simulation results (adapted from Weimann & Mewes, 2005).

Bouche et al. (2013) and Alméras et al. (2016a) studied the bubble induced mixing in (two-dimensional) rectangular bubble column. These studies used planar laser induced fluorescent (PLIF) to measure the time evolution of the concentration field of a passive scalar. Bouche et al. (2013) observed the capture of the fluorescent dye inside the wake of bubbles (see Figure 2-8). Bouche et al. (2013) also argues that each bubble can only maintain a finite amount of dye over a finite distance. This study also shows the concentration of fluorescent dye within a given window exhibits and exponential decay with time and increasing the void fraction accelerates the mixing process. Alméras et al. (2016a) uses a novel technique in order to provide high temporal single-point measurements of the concentration of fluorescent dye under bubble mixing. Time evolution of the concertation in Alméras et al. (2016a) exhibits the exponential decay with time scales similar to Bouche et al. (2013). Alméras et al. (2016a) argues that dye transport in bubble mixing is not a pure diffusion process since the upward and

downward transport is not identical. “The spectrum of the fluctuations shows an evolution in power −3 of the frequency in the same range as the spectrum of the velocity fluctuations previously measured by Bouche et al. (2014). As for the liquid velocity fluctuations (Risso, 2011), the concentration can thus be interpreted as a collection of random patches of dyes of various sizes” (Alméras et al. 2016a; see Figure 2-9).

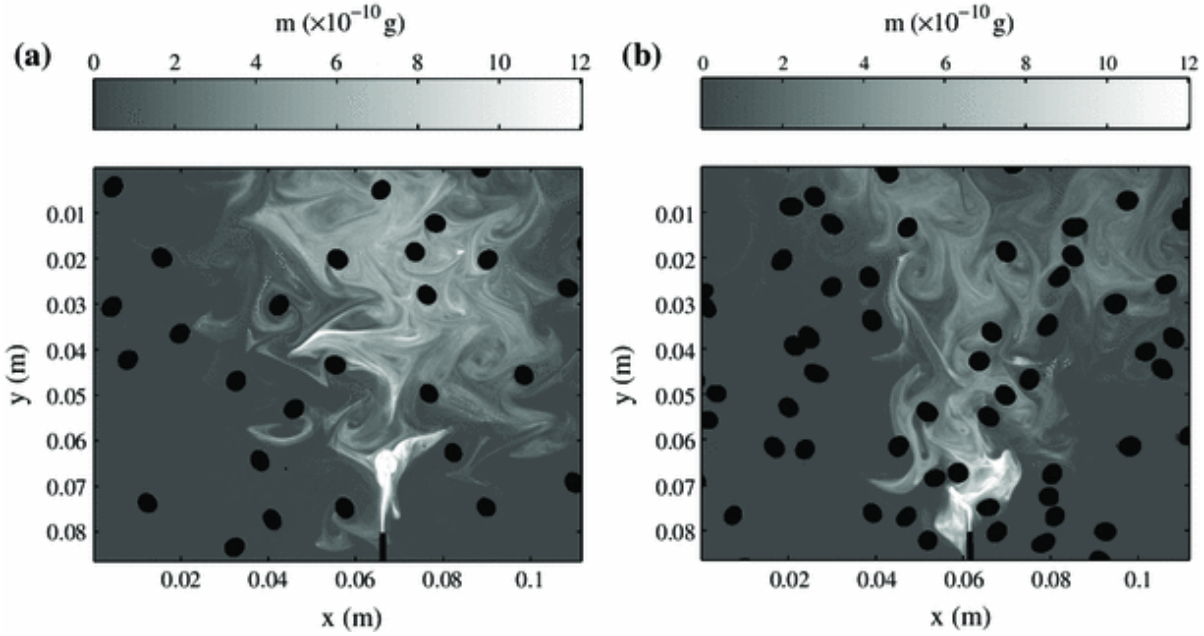

Figure 2-8. Instantaneous concentration field of the passive scalar (fluorescent dye) at (a) ε = 3.2% and (b) ε = 7.5% (adapted from Bouche et al., 2013).

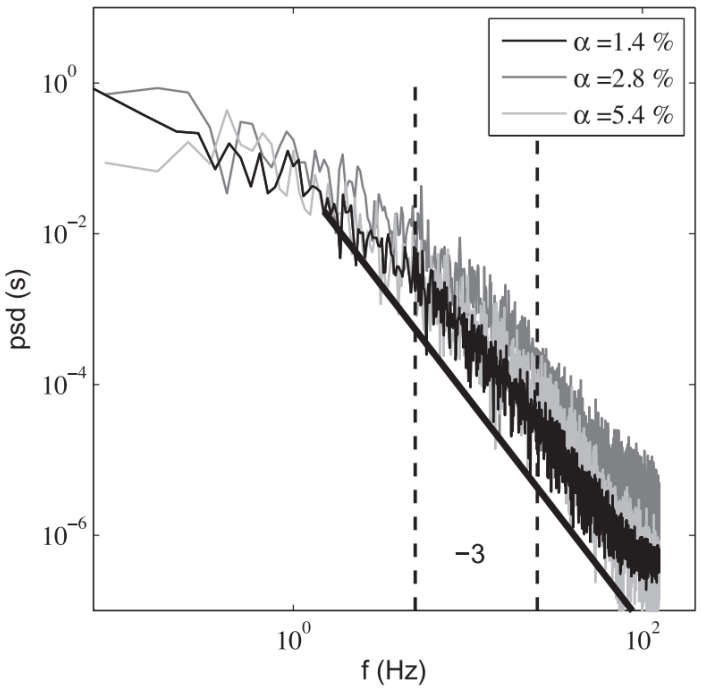

Figure 2-9. Spectrum of the normalized concentration fluctuations, slope of −3 is located within 5 to 25 Hz (adapted from Alméras et al., 2016a).

In summary, studies of the mixing performance of bubble columns is an active area of research. However, little is known about the physics of bubble mixing. Although literature has taken critical steps to dissect the bubble mixing mechanism, there is still no correlation available for prediction of mixing time of passive scalar in a bubble swarm. The computational simulations of the bubble mixing lack a proper modeling of the bubble wake interactions and the resulting velocity fluctuations (Weimann & Mewes, 2005; Radl et al., 2010). The experimental investigations of bubble mixing are focused on bubble-size length-scales (Bouche et al., 2013; Alméras et al., 2015; Alméras et al., 2016a) without taking into account the input power from bubble injection. From the above, there is a gap in the literature for scaling the mixing time of a passive scalar in a bubble swarm. Precise energy considerations, system properties (e.g. surface tension and viscosity) as well as multiphase parameters (e.g.

void fraction, and bubble size) can be used to produce a correlation for mixing time using dimensional analysis.

2.3 Annular Flow Film Thickness Literature Review

This section reviews the past studies on annular film thickness and summarizes the current state of research as well as identifying the gaps in the literature. The annular flow research was categorized based on pipe orientation into three different groups, namely horizontal (Section 2.3.1), vertical (Section 2.3.2), and inclined (Section 2.3.3) pipes. The basic definitions and concepts in the annular flow research are explored in the following paragraphs.

Annular flow is a flow pattern in gas-liquid two-phase pipe flows, where the liquid phase primarily flows as a thin film on the pipe wall that surrounds a fast moving gas core. At the gas-liquid interface, drops of liquid detach from the film and get carried by the gas core flow, these entrained drops then join the film and this phenomenon repeats itself. Droplet entrainment occurs when wave crests at the liquid surface break due to the velocity difference at the interface. The main parameters that govern the physical processes within annular flow are the liquid entrainment, (liquid) surface-wave characteristics and circumferential distribution of the film thickness. Unlike other flow patterns in gas-liquid pipe flows, the literature on direct measurements of the film thickness in annular flow is rather scarce. This is mostly due to the fact the film thickness is typically approximately few tenths of a millimeter, which makes film thickness measurements (especially the circumferential distribution) extremely cumbersome.

Figure 2-10 shows a schematic of the liquid film in annular flow, entrained drops, surface waves and a base film are the main features of the liquid flow in the annular flow

regime. The surface waves are categorized into two classes, ripple (waves) and disturbance waves. Ripple waves are momentary and significantly smaller in amplitude compared to the film thickness. The wavelength of a ripple wave is also significantly smaller than the pipe perimeter (Hewitt & Govan, 1990; Schubring & Shedd, 2008; Alekseenko et al., 2008, 2009). Disturbance waves have large amplitudes relative to the film thickness and long lifespans. These disturbance waves are able to carry mass in the stream-wise direction (Hanratty & Hershman, 1961; Asali & Hanratty, 1993; Schubring & Shedd, 2008; Alekseenko et al. 2008, 2009). The ripple waves only dominate the liquid surface at very low liquid flow rates (Berna et al., 2014). A critical liquid flow rate is necessary for the formation of disturbance waves (Andreussi et al., 1985; Schadel, 1988). At low gas velocity, the surface of the liquid film is smooth; however, Levich (1962) and Lamb (1975) argue that Kelvin-Helmholtz instabilities will produces a wavy interface when increasing the gas flow rate. It is noteworthy that in the horizontal and inclined pipe orientations, the gravitational and surface tension forces work together to suppress the instabilities (from pressure variation) over the wave surface.

In annular flow, the average distance between the pipe wall to the liquid surface profile is called the liquid film thickness (see Figure 2-10). Observations by Levy (1999) indicates that the liquid film can be divided into a continuous bottom layer (base layer) and a disturbed wavy interface (wave layer). The circumferential liquid film thickness distribution in vertical pipes is uniform when the pipe diameter is smaller than 60mm (Asali et al., 1985) and cause the disturbance wave to be radially coherent (Tylor and Hewitt, 1963; Hewitt & Lovegrove, 1969; Asali & Hanratty. 1993). Sekoguchi et al. (1985) present flow visualization of disturbance waves in a 25.8mm diameter pipe in a vertical orientation. It is clear that in vertical annular flow, the properties are innately uniform. In horizontal annular flow, the radial

distribution of the film thickness is asymmetric due to gravity effects. However, Paras & Karabelas (1991) showed that increasing the gas flow rate improves the uniformity of the properties, suppressing the influence of gravity. The number of contributions on liquid film in annular flow is significant. Based on pipe orientation (i.e. horizontal or vertical) these important studies on film thickness measurement and modeling (correlations) are reviewed in the following.

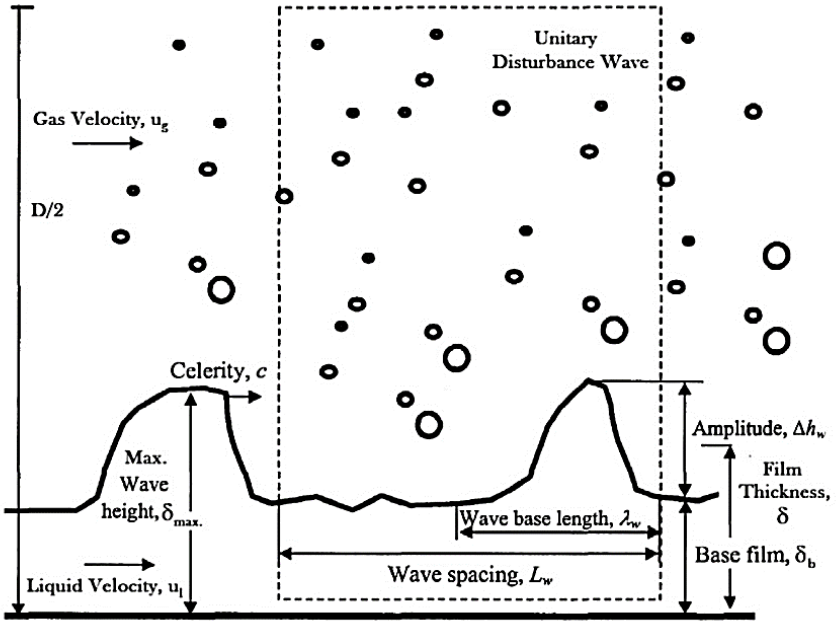

Figure 2-10. Schematic of liquid film in annular flow (adapted from Berna et al., 2014).

2.3.1 Horizontal pipe

Tatterson et al. (1977) used electrical probes to measure the film thickness in a horizontal channel with a cross section of 25mm x 305mm (width x height). Paras & Karabelas (1991) used parallel-wire conductance probes to measure the annular liquid film thickness along a pipe with an internal diameter of 51mm. Rodriguez (2004) showed that the conductivity probes are not able to detect bubbles within the film; therefore, conductivity

probes under predict the film thickness, especially if it is wavy on the surface. Visual imaging of the film thickness was first employed by Jacowitz et al. (1964) and Hewitt et al. (1990); these studies used backlit visualization and refractive index matching with fluorinate ethylene propylene (FEP). Shedd & Newell (2004) used novel optical probes (Shedd & Newell, 1998) to measure the circumferential film thickness distribution in horizontal pipes with round (12.7mm and 25.4mm internal diameter), square (15.2mm and 22.7mm sidewall), and equilateral triangle (40mm sidewall) cross-sections. Figure 2-11 shows the results of circumferential film thickness distribution measurements in a horizontal annular flow. This work used the normalized coordinates from wall bounded turbulent shear flow for presenting the experimental measurement of liquid film thickness. Results of this work shows that the majority of film thicknesses fell between $5 < \delta^+ < 35$ ($\delta^+ = \delta[\tau_i/\rho_L]^{0.5}/\nu_L$) corresponding to the buffer layer (transition region) in turbulent boundary layer and liquid film dries out for $\delta^+ < 5$.

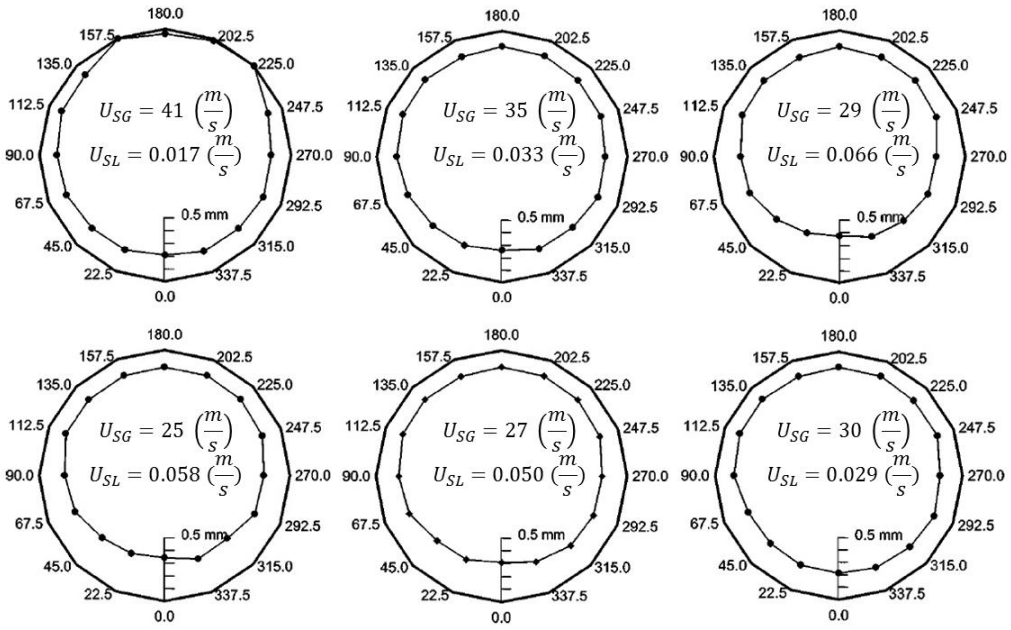

Figure 2-11. Circumferential film thickness measurements in a 12.7mm pipe (adapted from Shedd & Newell, 2004).

Schubring (2009) used a non-intrusive technique based on patterns of reflected light from the liquid film surface to measure the liquid film thickness in horizontal annular flow. Figure 2-12 shows that increasing the liquid superficial velocity increases the film thickness; however, this trend becomes weak with increasing the gas superficial velocity. Figure 2-12 also shows that for U_{SG} < 60 m/s, increasing the gas superficial velocity increases the film thickness.

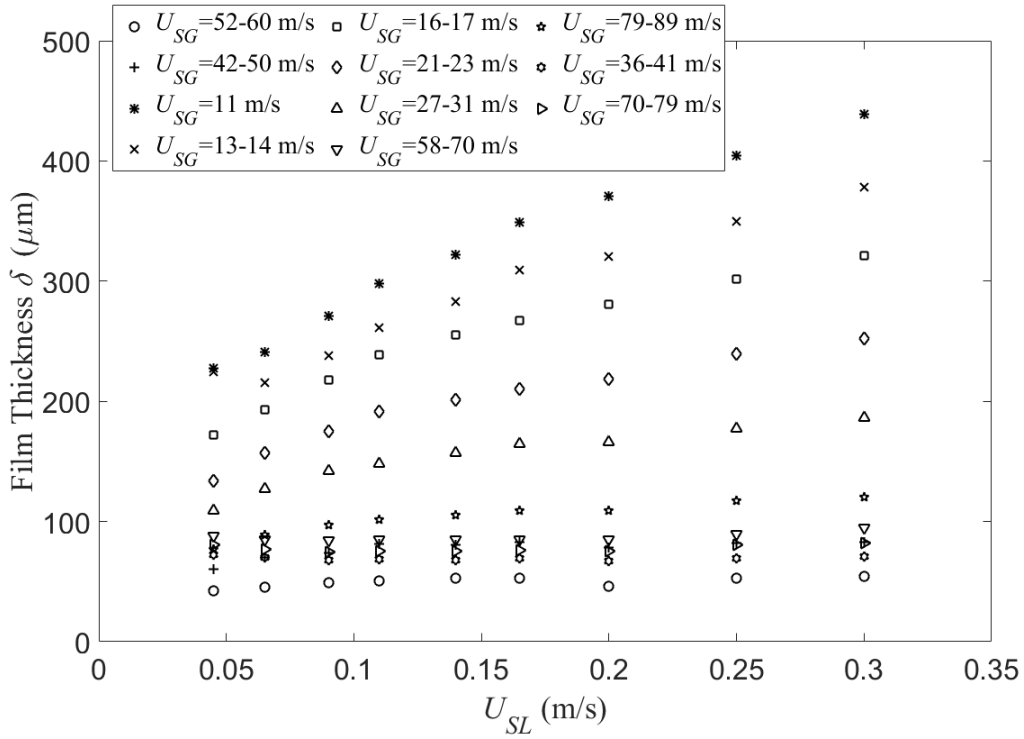

Figure 2-12. Experimental measurement of liquid film thickness (δ) in a horizontal pipe versus liquid superficial velocity (U_{SL}) at different gas superficial velocities (U_{SG}). Pipe diameter D=8.8mm, air-water at ambient pressure and temperature (adapted and reproduced from Schubring, 2008).

In the annular flow regime, the pressure gradient $(dP/dL)_f$, liquid film thickness (δ), and liquid mass flow rate ($\dot{m}_{LF}$) are the dependent system parameters. Measurement of the liquid entrainment fraction (E) and interfacial friction factor (f_i) are challenging due to the

nature of the multiphase flow. The "Triangular Relationship" in annular flow is a relationship between the aforementioned system parameters (connected to each other with solid lines in Figure 2-13) that helps calculating either E or f_i given two of the system parameters. See section 2.3.4 for a more detailed discussion of this relationship.

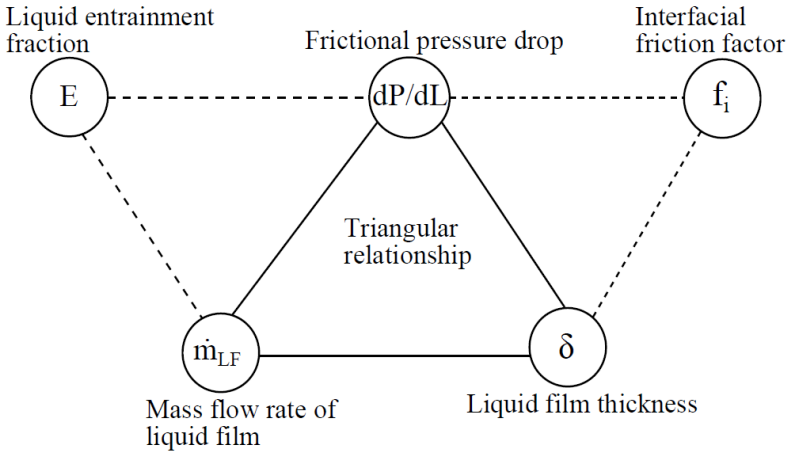

Figure 2-13. Triangular relationship in annular flow (adapted from Bhagwat, 2015).

Experimental measurements of film thickness in annular flow are difficult and require accurate instrumentation. Therefore, physics based models able to predict the film thickness based on phase properties and operation settings (test conditions) are of great interest for annular flows. Table 2-1 summarizes the available correlations for liquid film thickness predictions in horizontal annular flow. Figure 2-14 and Figure 2-15 compare the experimental measurements of film thickness in annular flow from Tatterson et al. (1977) and Schubring (2009), respectively, with the film thickness prediction from the available models to survey the accuracy of available models in the literature. Figure 2-14 shows the effect of liquid superficial velocity on film thickness at a constant gas superficial velocity (U_{SG} = 35m/s), here Ishii & Grolmes (1975) provide the most accurate prediction in comparison with other models

in this range. Figure 2-15 shows the effect of gas superficial velocity on film thickness at a constant liquid superficial velocity (U_{SL} = 0.192m/s). Berna et al. (2014) provide the most accurate prediction in comparison with other models in this range. From Figure 2-14 and Figure 2-15 it is apparent that there is a need for more accurate models to predict the film thickness, as well as a broad body of experimental data for providing a verification of any model within a given range.

From the review of the past literature on measurements and modeling of the liquid film thickness in annular flow at horizontal orientation, it is clear that the available models are not able to provide accurate prediction of film thickness. In addition, the available models have been tested only against gas and liquid flow rates while, studies on the effect of phase properties and pipe geometry (e.g. pipe diameter) are scarce. Furthermore, there is a lack of experimental data for verification of the current models and any future models. It is noteworthy that majority of the available film thickness data in the literature has been collected using intrusive techniques which inherently reduces the accuracy of the measurement. Therefore, film thickness measurements in horizontal annular flow using a non-intrusive technique provides a significant contribution to current state of film thickness research. Both for validation of the experimental measurements and the available models.

Table 2-1. Summary of correlations for the liquid film thickness in horizontal annular flow.

Reference	Correlation	
Henstock & Hanratty (1976)	$\frac{\delta}{D} = \frac{6.59F}{(1+850F)^{0.5}}$ $F = \frac{Re_{SL}^{0.5}\mu_L\rho_G^{0.5}}{\sqrt{2}Re_{SG}^{0.9}\mu_G\rho_L^{0.5}}$	Equation 2-3
Tatterson et al. (1977)	$\frac{\delta}{D} = \frac{6.59F}{(1+850F)^{0.5}}$ $F = \frac{\gamma(Re_{SL})\mu_L\rho_G^{0.5}}{\sqrt{2}Re_{SG}^{0.9}\mu_G\rho_L^{0.5}}$ $\gamma(Re_{SL}) = [(0.707Re_{LF}^{0.5})^{2.5} + (0.0379Re_{LF}^{0.9})^{2.5}]^{0.4}$	Equation 2-4
Ishi & Grolmes (1975)	$\delta = 0.347Re_{LF}^{2/3}\sqrt{\frac{\rho_L}{\tau_i}}\frac{\mu_L}{\rho_L}$	Equation 2-5
Okawa et al. (2002)	$\frac{\delta}{D} = 0.25\sqrt{\frac{f_w\rho_L}{f_{Gi}\rho_G}}\frac{U_{LF}}{U_{SG}}$	Equation 2-6
Berna et al. (2014)	$\frac{\delta}{D} = 7.165Re_{SG}^{-1.07}Re_{SL}^{0.48}\left(\frac{Fr_{SG}}{Fr_{SL}}\right)^{0.24}$	Equation 2-7
Owen (1987)	$\dot{m}_{LF}^{+} = \begin{cases} 0.5\delta^{+2}, & \delta^+ < 5 \\ -64 + 3\delta^+ + 2.5\delta^+\ln(\delta^+), & 5 < \delta^+ < 30 \\ 12.05 - 8.05\delta^+ + 5\delta^+\ln(\delta^+), & 30 < \delta^+ \end{cases}$	Equation 2-8
Hurlburt et al. (2006)	$\frac{U_G(y_G^+)}{u^*} = 2.44ln(y_G^+) + 5 - \Delta B$ $\Delta B = 2.44\ln(1 + c_B\frac{\epsilon u^*}{\nu_G})$	Equation 2-9

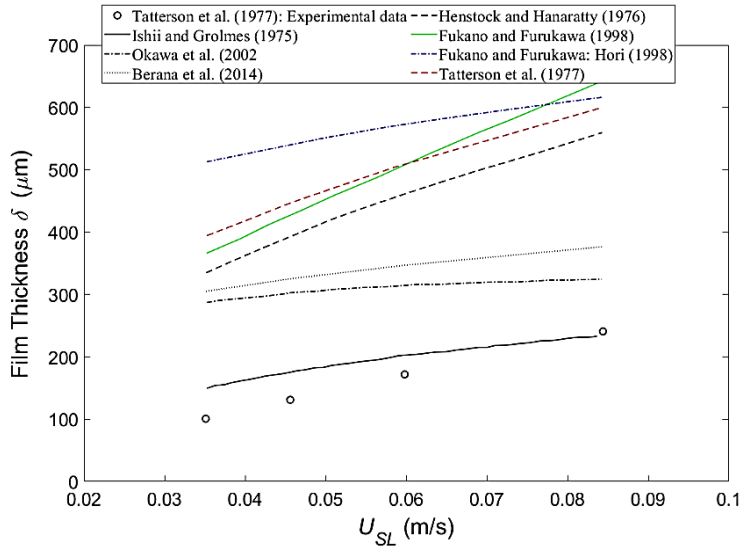

Figure 2-14. Film thickness (δ) versus superficial liquid velocity (U_{SL}), comparison between experimental data (horizontal channel flow, 0.305m x 0.025m, U_{SG} = 35m/s) from Tatterson et al. (1977) and available models (adapted and reproduced from Berna et al., 2014).

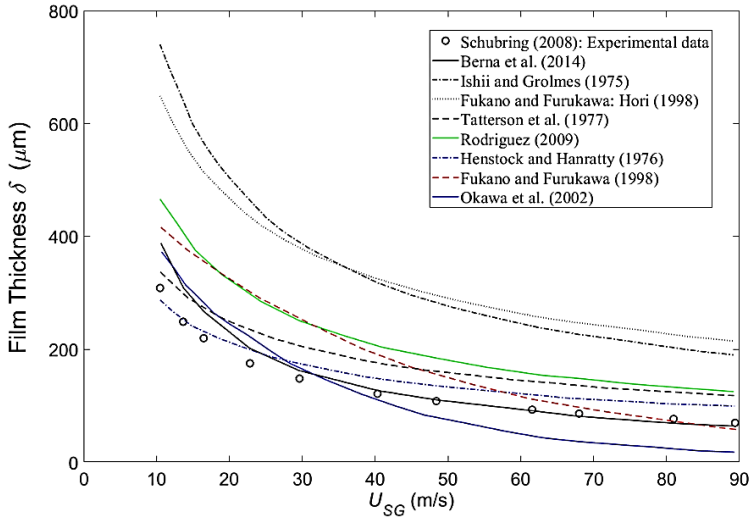

Figure 2-15. Film thickness (δ) versus superficial liquid velocity (U_{SG}), comparison between experimental data (horizontal channel flow, D = 8.8 mm, U_{SL} = 0.192m/s) from Schubring (2009) and available models (adapted and reproduced from Berna et al., 2014).

2.3.2 Vertical pipe

Annular flow in vertical pipes has a symmetric circumferential film thickness distribution. Alamu (2010) used electrical conductance probes for film thickness measurements in a vertical annular flow, in this study the internal pipe diameter was 19mm. Figure 2-16 shows that increasing the gas superficial velocity reduces the film thickness; however, a consistent trend in data shows that increasing the liquid flow rate thickens the liquid film. It is worth mentioning that in Alamu (2010), water-glycerin (μ_L= 3.6 mPa·s and ρ_L = 1097 kg/m^3) and air were used as working fluids.

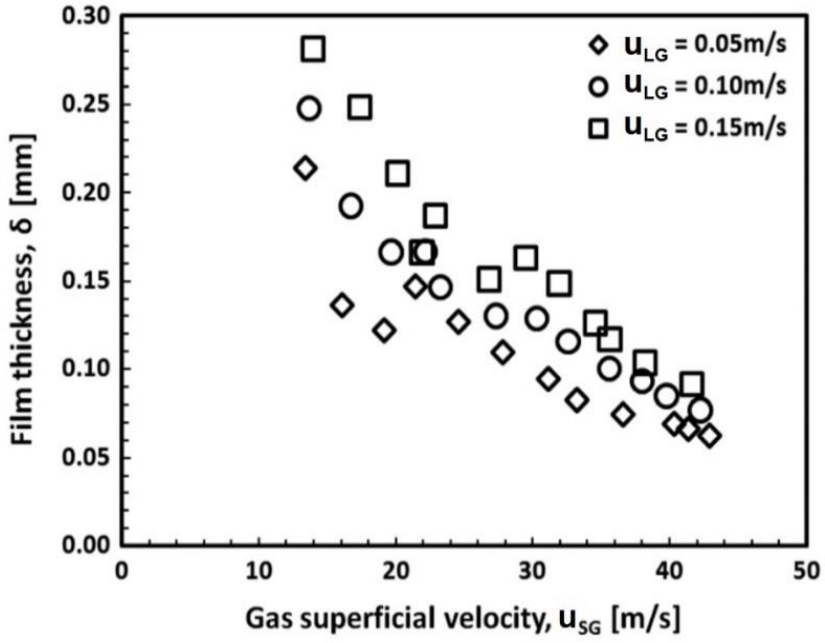

Figure 2-16. Effect of gas superficial velocity as well as liquid superficial velocity on film thickness in vertical annular flow (adapted from Alamu, 2010).

More recently, Schubring (2009) used planar laser induced fluorescent (PLIF) for non-intrusive measurement of liquid film thickness in vertical pipe flow with an internal diameter of 23.4mm. Figure 2-17 shows a PLIF image of the liquid film from Schubring & Shedd

(2008). Figure 2-18 shows the results of PLIF measurements of the liquid film thickness in vertical annular flow. It can be seen that increasing the gas superficial velocity reduces the liquid film thickness and vice versa. In addition, a direct correlation between liquid film thickness and liquid superficial velocity can be seen in Figure 2-18. However, at higher gas superficial velocities, the liquid film thickness appears to be insensitive to changes in liquid superficial velocity. Similar to the liquid film thickness response to gas superficial velocity and liquid superficial velocity in horizontal annular flow (see Figure 2-12), in vertical annular flow at higher gas superficial velocity an increase in liquid film thickness can be seen in the data from Schubring (2009).

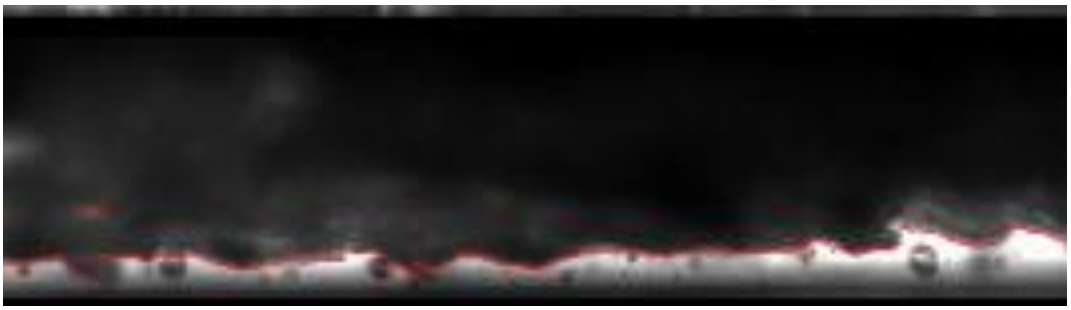

Figure 2-17. Processed PLIF image of vertical annular flow; U_{SG} = 55.3m/s, U_{SL} = 0.127m/s, D = 23.4mm (adapted from Schubring & Shedd, 2008).

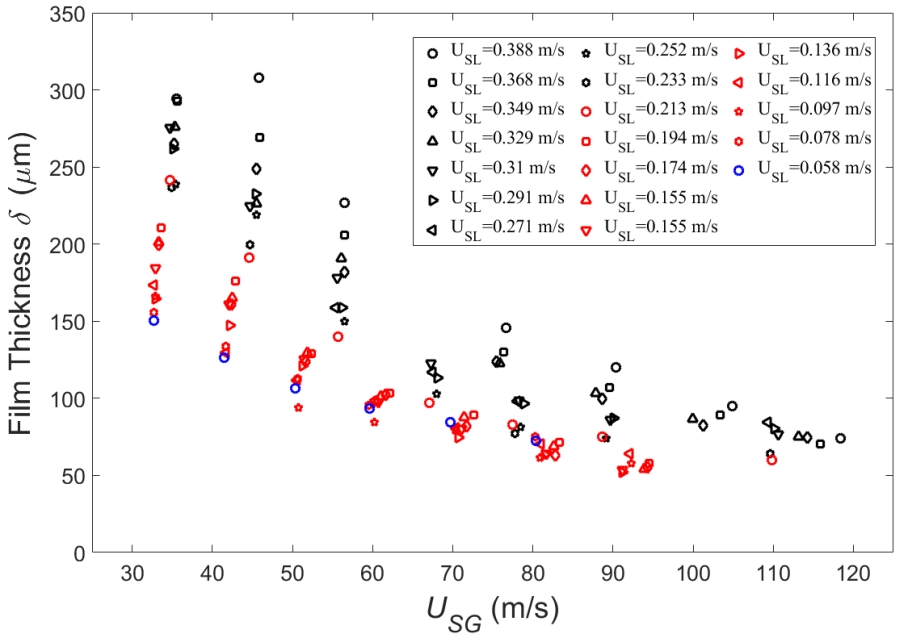

Figure 2-18. Experimental measurements of the liquid film thickness (δ) in a vertical pipe versus gas superficial velocity (U_{SL}) at different liquid superficial velocities (U_{SG}). Pipe diameter D=23.4mm, air-water at ambient pressure and temperature (adapted and reproduced from Schubring, 2009).

Table 2-2 summarizes the available correlations for liquid film thickness prediction in horizontal annular flow. Figure 2-19 and Figure 2-20 compare the experimental measurement of liquid film thickness in vertical annular flow from Alamu (2010) and Schubring (2009) with the film thickness prediction from the available models to survey the accuracy of the available models in the literature. From Figure 2-19 it can be seen that the most recent correlation from Berna et al. (2014) is able to predict the liquid film thickness in annular flow. However, Berna's model (Equation 2-17) shows a bias error in predicting film thicknesses from Schubring (2009), which raises the question of how pipe diameter effects the annular flow even in the vertical orientation with symmetric distribution of properties.

From the review of the past literature on measurements and modeling of the liquid film thickness in annular flow at vertical orientation, one can see that the accuracy of available models is sensitive to pipe geometry. Furthermore, there is a lack of experimental data for better verification of the current models and any future models. Therefore, film thickness measurements in a vertical annular flow using a non-intrusive technique would provide a significant contribution to the current state of film thickness modeling. In addition, investigating the effect of pipe geometry (i.e. diameter) contributes to better understanding the physics of annular flow.

Table 2-2. Summary of correlations for the liquid film thickness in horizontal annular flow.

Reference	Correlation	
Rodriguez (2009)	$\delta^+ = \begin{bmatrix} 0.34Re_{LF}^{0.6} & Re_{LF} \le 1000 \\ 0.34Re_{LF}^{0.875} & Re_{LF} > 1000 \end{bmatrix}$ $\delta^+ = \frac{\rho_L \delta u_L^*}{\mu_L}, u_L^* = \sqrt{\frac{\tau_i}{\rho_L}}, \tau_i = 0.5 f_{gi} \rho_g (u_G - u_{LF})$ $f_{gi} = f_g\left(1 + 300\frac{\delta}{D}\right), f_g = \frac{0.079}{Re_G^{0.25}}$	Equation 2-10
Fukano & Furukawa (1989)	$\frac{\delta}{D} = 0.0594 \exp\left(-0.34 Fr_{SG}^{0.25} Re_{SL}^{0.19} \chi^{*0.6}\right)$ $\chi^* = \frac{\rho_G U_{SG}}{\rho_G U_{SG} + \rho_L U_{SL}}$	Equation 2-11
Hori et al. (1978)	$\frac{\delta}{D} = 0.905 Re_{SG}^{-1.45} Re_{SL}^{0.9} Fr_{SG}^{0.93} Fr_{SL}^{-0.68} \left(\frac{\mu_L}{\mu_{L,ref}}\right)$	Equation 2-12
Henstock & Hanratty (1976)	$\frac{\delta}{D} = \frac{6.59F}{(1 + 1400F)^{0.5}}$ $F = \frac{Re_{SL}^{0.5} \mu_L \rho_G^{0.5}}{\sqrt{2} Re_{SG}^{0.9} \mu_G \rho_L^{0.5}}$	Equation 2-13
Tatterson et al. (1977)	$\frac{\delta}{D} = \frac{6.59F}{(1 + 1400F)^{0.5}}$ $F = \frac{\gamma(Re_{SL}) \mu_L \rho_G^{0.5}}{\sqrt{2} Re_{SG}^{0.9} \mu_G \rho_L^{0.5}}$ $\gamma(Re_{SL}) = [(0.707 Re_{LF}^{0.5})^{2.5} + (0.0379 Re_{LF}^{0.9})^{2.5}]^{0.4}$	Equation 2-14
Ishi & Grolmes (1975)	$\delta = 0.347 Re_{LF}^{2/3} \sqrt{\frac{\rho_L}{\tau_i} \frac{\mu_L}{\rho_L}}$	Equation 2-15
Okawa et al. (2002)	$\frac{\delta}{D} = 0.25 \sqrt{\frac{f_w \rho_L}{f_{Gi} \rho_G}} \frac{U_{LF}}{U_{SG}}$	Equation 2-16
Berna et al. (2014)	$\frac{\delta}{D} = 7.165 Re_{SG}^{-1.07} Re_{SL}^{0.48} \left(\frac{Fr_{SG}}{Fr_{SL}}\right)^{0.24}$	Equation 2-17

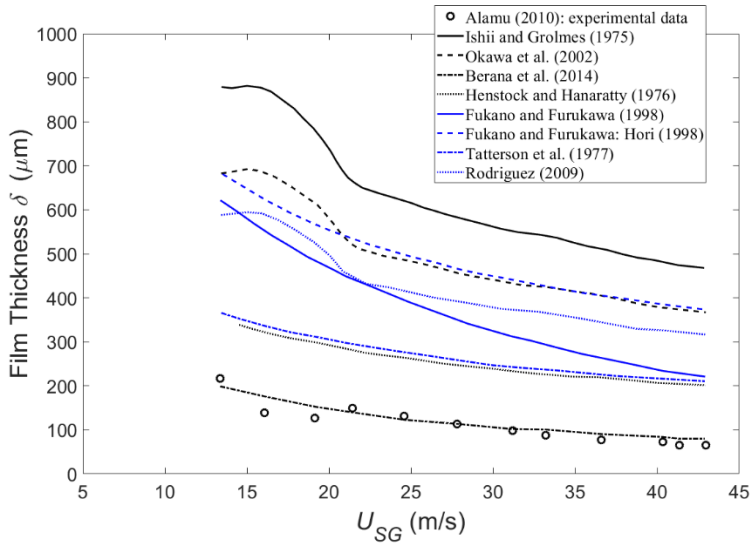

Figure 2-19. Film thickness (δ) versus superficial liquid velocity (U_{SL}), comparison between experimental data (vertical pipe, D = 19mm, U_{SL} = 0.05m/s) from Alamu (2010) and available models (adapted and reproduced from Berna et al, 2014).

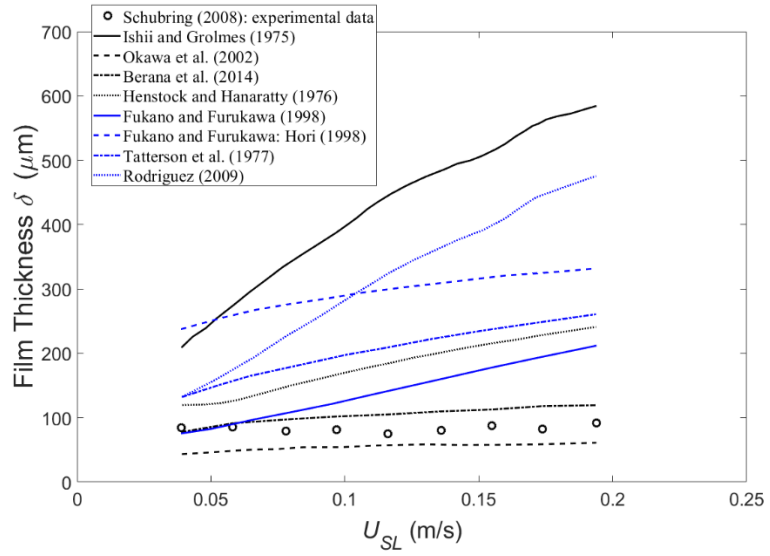

Figure 2-20. Film thickness (δ) versus superficial liquid velocity (U_{SG}), comparison between experimental data (horizontal channel flow, D = 23.4 mm, U_{SG} = 71m/s) from Schubring (2009) and available models (adapted and reproduced from Berna et al, 2014).

2.3.3 Inclined pipe

In comparison to annular flow at vertical and horizontal pipe orientations, there are only two research articles (from the same research group) to the author's knowledge on annular flow in inclined pipe orientations. In this section, the aforementioned studies are reviewed. Geraci et al. (2007) presented measurements of the circumferential liquid film thickness distribution in an inclined annular pipe flow with an internal diameter of 38mm. The experimental setup in this work allows for the inclination to be fixed at 0°, 30°, 45°, 60°, and 85°. Film thickness measurements were carried out using electrical probes (intrusively). Figure 2-21 shows the film thickness distribution from Geraci et al. (2007), result of this work clearly shows the asymmetric film distribution due to gravity effects. This work also argues that the lower part of pipe with higher film thickness is dominated by the presence of disturbance waves, however increasing the inclination angle toward the vertical orientation improves the symmetry of the film thickness distribution and suppresses the disturbance waves by spreading the waves up the sides of the pipe. In addition, power spectra analysis of the disturbance waves showed that the majority of the wave energy at the bottom portion of the pipe was carried by wave frequencies below 12Hz. It is worth mentioning that theses measured film thicknesses showed significant variation from two different models, Taitel & Dukler (1976) and Fulkano & Furukawa (1989).

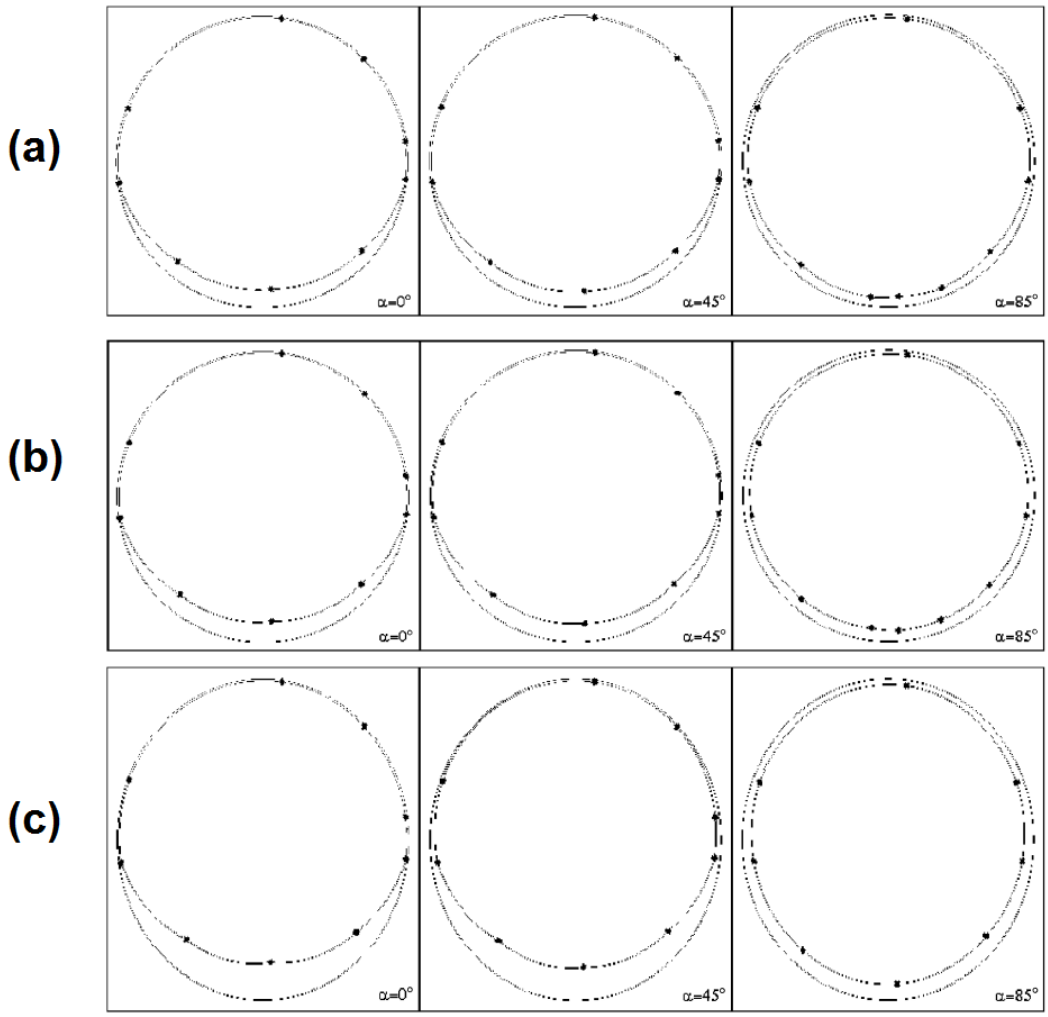

Figure 2-21. Circumferential liquid film thickness distribution at (from left to right) 0°, 45°, and 85°; (a) U_{SG} = 21.5m/s, U_{SL} = 0.007 m/s; (b) U_{SG} = 21.5m/s, U_{SL} = 0.011 m/s; and (c) U_{SG} = 21.5m/s, U_{SL} = 0.028 m/s (adapted from Geraci et al., 2007).

The other study (Al-Sarkhi et al., 2012) focused on the effect of pipe inclination on wave characteristics in annular flow in a 76.2mm internal diameter pipe. The experimental setup in this work allows the inclination angle to be fixed at 0°, 20°, 45°, 60°, 75°, and 90°. Liquid film thickness was measured at the bottom of the pipe using a series of conductivity probes placed radially around the pipe. Similar to Geraci et al. (2007), here increasing the inclination angle increased the liquid film thickness at the bottom of the pipe. Detailed work

of Al-Sarkhi et al. (2012) shows a direct relationship between the liquid film thickness and wave amplitude at the bottom of the pipe. This study also argues that the inclination angle does not effect the symmetry of the film distribution once the gas superficial velocity is high enough.

In summary both of the past studies on liquid film thickness measurements in inclined annular flow have been carried out using intrusive instruments. Furthermore, both studies used relatively large pipe diameters that effects the characteristics of annular flow, especially in horizontal and near horizontal orientations. It is also worth mentioning that none of these studies investigated the onset of asymmetric film distribution due to the change of the pipe orientation from vertical.

The absence of a sound understanding of the effect of pipe inclination on the physical structure of the annular flow is an opportunity for experimental initiatives to fill the gap in annular flow research. Thus, further experimental investigation of two-phase flow parameters in annular flow at inclined pipe orientations will contribute to the fundamental understanding of the gas liquid two-phase flow mechanism. In addition, with the wide industrial application of annular flow, especially in boiling and condensation (Crowe, 2005) in power production or HVAC, there is a strong benefit to improving our understanding of the interrelation of multiphase parameters under the effect of inclination.

2.3.4 Triangular Relationship

In annular flow regime the pressure drop $(dP/dL)_f$, film thickness (δ), and the liquid flow rate inside of the film ($\dot{m}_{LF}$) are the dependent system parameters. The concept of triangular relationship has been discussed in Hewitt & Hall-Tylor (1970) and Collier & Thome (1994). The interrelation between two of the aforementioned parameters can be used to

calculate the third one. It is noteworthy that these dependent parameters cannot be calculated from the system independent parameters (e.g. mass flow rates, phase properties, and pipe geometry). As illustrated in Figure 2-13 the triangular relationship consists of two sets of closure equations to calculate the liquid entrainment fraction (E) and interfacial friction factor (f_i). The two-phase pressure drop and two-phase frictional multiplier can be modified into the aforementioned closures. The following assumptions and simplifications are required for forming the triangular relationship:

i. The liquid film thickness is smaller than the pipe diameter and the circumferential distribution of the film thickness is uniform.
ii. The shear stress from the wall to the gas liquid interface is constant $\tau_w \approx \tau_i$.
iii. The frictional component of pressure drop is larger than gravitational and accelerational components.
iv. The gradient of liquid entrainment fraction is negligible.

It is worth mentioning that using these assumptions, the triangular relationship is only valid for high void fractions in the excess of 0.8.

The two-phase frictional pressure drop can be expressed in terms of the velocity of the liquid inside of the film (Equation 2-18) assuming a negligible entrainment fraction. Equation 2-19 gives the definition of the two-phase frictional multiplier that correlates the frictional pressure drop to the liquid pressure drop. Hewitt & Hall-Tylor (1970) discussed that the Reynolds number of the liquid film in annular flow is equal to the Reynolds number of liquid flowing alone (Equation 2-20) in a pipe under no liquid entrainment and equal pressure drop; thus, the friction factor for these flows are also identical (i.e. $f_{TP} = f_L$). It is also worth

mentioning that the neglecting of the liquid entrainment fraction is a drawback of this approach.

$$\left(\frac{dP}{dL}\right)_f = \frac{4\tau_w}{D} = \frac{2f_{TP}\rho_L U_L^2}{D}$$ Equation 2-18

$$\Phi_L^2 = \frac{\left(\frac{dP}{dL}\right)_f}{\left(\frac{dP}{dL}\right)_L} = \frac{1}{(1-\alpha)^2}\left(\frac{f_{TP}}{f_L}\right)$$ Equation 2-19

$$\frac{\rho_L U_L 4\delta}{\mu_L} = \frac{\rho_L U_{SL} D}{\mu_L}$$ Equation 2-20

Turner & Wallis (1965) proposed an improvement to the Hewitt & Hall-Tylor (1970) approach by using the actual liquid flow rate inside of the film from direct measurements. In this case Equation 2-19 can be modified to Equation 2-21, and the liquid film frictional pressure drop can be calculated from Equation 2-22. Since Equation 2-22 lacks information on interfacial roughness (shear) even at a known void fraction and entrainment fraction, Equation 2-22 may not predict the two-phase frictional pressure drop. Equation 2-23 uses the two-phase frictional multiplier and momentum balance on the gas core to express the frictional pressure drop across the pipe.

$$\Phi_L^2 = \frac{\left(\frac{dP}{dL}\right)_f}{\left(\frac{dP}{dL}\right)_L} = \frac{1}{(1-\alpha)_{LF}^2}$$ Equation 2-21

$$\left(\frac{dP}{dL}\right)_{LF} = \frac{2f_{TP}\rho_L(U_{SL}(1-E)^2}{D} = \frac{2f_{TP}\rho_L(G(1-x)(1-E)^2}{D}$$ Equation 2-22

$$\Phi_G^2 = \frac{\left(\frac{dP}{dL}\right)_f}{\left(\frac{dP}{dL}\right)_G} = \frac{{}^{4\tau_i}/_{(D-2\delta)}}{{}^{4\tau_G}/_{D}}$$ Equation 2-23

$$We_c = \frac{\rho_G U_{SG}^2 D}{\sigma}$$ Equation 2-24

$$E_P = (1 + 280 \times (We_c)^{-0.8395})^{-2.209}$$ Equation 2-25

$$\rho_c = \frac{x + E_P(1-x)}{{}^{x}/_{\rho_G} + E_P {}^{(1-x)}/_{\rho_L}}$$ Equation 2-26

$$We_c = \frac{\rho_c U_{SG}^2 D}{\sigma}$$ Equation 2-27

$$E = (1 + 280 \times (We_c)^{-0.8395})^{-2.209}$$ Equation 2-28

Cioncolini & Thome (2012) presented a correlation for calculating the liquid entrainment fraction to be used in the triangular relationship; this correlation is given by Equation 2-24 to Equation 2-28. Cioncolini & Thome (2012) is a two-step method, the predictive step (Equation 2-24 and Equation 2-25) estimates the liquid entrainment fraction (E_p) as a function of Weber number in the gas core calculated from gas density. The corrector step (Equation 5-16 and Equation 5-17) uses the Weber number in the gas core based on core density to calculate the entrainment fraction. The core density is calculated from the predicted entrainment fraction (E_p) by Equation 2-26.

CHAPTER III

EXPERIMENTAL METHODS

3.1 Vibrating Bubble Column Testing

3.1.1 Test facility

The vibrating bubble column experimental setup is comprised of two primary components, namely the shaker table and the bubble column. These components allow the user to produce different test conditions to investigate the effect of operation parameters on the fluid dynamics of bubbles in the column using quantitative flow visualization instruments. The vibrating bubble column test facility was initially designed and built by Mr. Adam L. Still (Still, 2012) and funded by Sandia National Laboratories (DE-AC04-94AL85000, Dr. O'Hern). In the spring of 2015 the test facility was transferred from the OSU Multiphase Lab (Prof. Afshin J. Ghajar) to the Experimental Flow Physics Lab (Dr. Elbing). The components of the vibrating bubble column setup as well as the test procedure and uncertainties associated with data collection are presented in the following sections.

The shaker table was custom made for use in the current vibrating bubble column setup (Still, 2012). Essentially the shaker uses an eccentric drive mechanism (EDM) to convert the rotational motion of an AC motor to a reciprocating motion to oscillate the shaker base plate (see Figure 3-1). The EDM is capable of changing the vibration amplitude in the range of 0.5-

11 mm. A single-phase variable frequency drive (10A, 230V) was employed to control the vibration frequency in the range of 7-30 Hz. Based on power requirements a 3 Phase, 3 BHP, 208-230V AC WEG motor powers the shaker. A flywheel from a 12 BHP internal combustion engine along with a gear box from the same engine were used for inertia profile considerations. The gearbox ratio was set to 1:1 and therefore, each revolution of the shaft produced one oscillation at the shaker. A custom made carriage houses the motor and gearbox assembly. A Lovejoy coupling was used to couple the motor shaft to the gearbox and the gearbox-flywheel to the shaker shaft. Figure 3-2 shows a picture of the shaker table components (AC motor, gearbox-flywheel and EDM/shaker).

Measurement of the input vibration characteristics is crucial in order to provide controlled and repeatable tested conditions. An LED display on the VFD sets the frequency with a 0.1Hz resolution. The vibration acceleration profile was collected using two different accelerometers, each mounted on the center of the base plate for individual testing. First, a three axis accelerometer (Vernier 3D-BTA; ±5g's) was employed for comparing the vertical acceleration (a_z) with ones in planar directions (a_y and a_x). The data acquisition system was comprised of a DAQ card (Vernier, SensorDAQ) and a desktop computer. Data was recorded using a Logger Lite 1.9.2 at 1000Hz for a period of ten seconds. The second accelerometer (OMEGA ACC786, ±80g's) was employed to collect the acceleration profile at 1000Hz in those experiments where vertical acceleration exceeds the range of the three axis accelerometer.

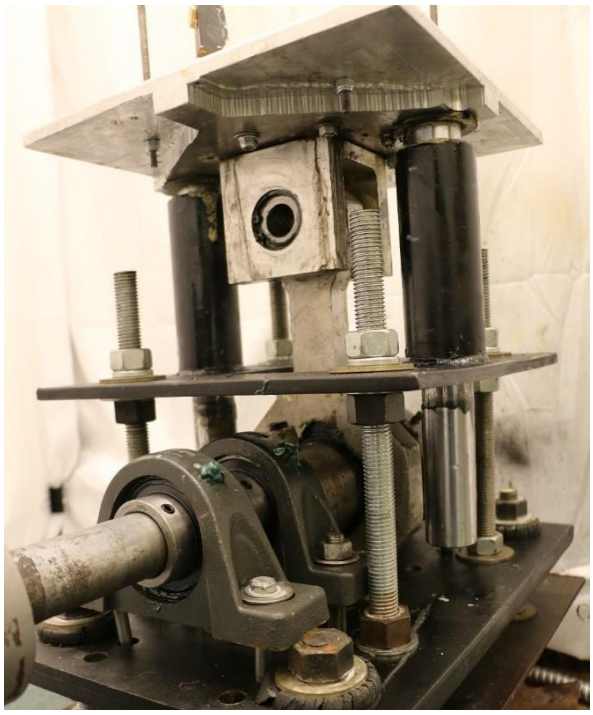

Figure 3-1. Shaker table; eccentric drive mechanism and base plate.

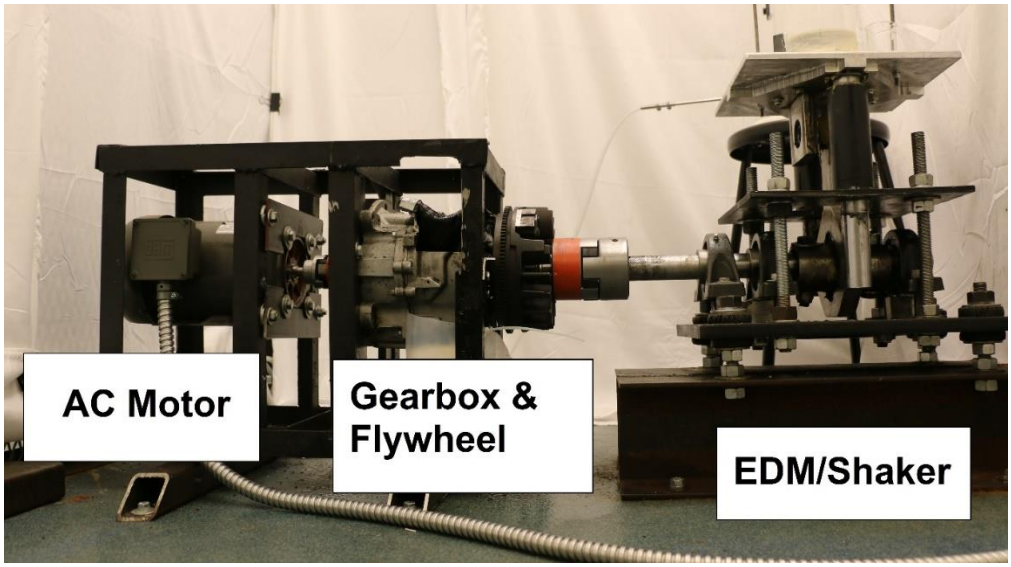

Figure 3-2. From left to right, AC motor and gearbox (inside the carriage), and EDM (shaker).

The same DAQ that was used for collecting the differential pressure was used to record the acceleration profile from the second accelerometer. Figure 3-3 shows the ratio of expected

vertical vibration to measured vertical vibration versus the ratio of measured planar vibration to measured vertical vibration. Stokes number S_k was calculated based on the vibration input to investigate the effect of planar vibration on bubble behavior. Defined as the ratio of particle response times scale (τ, Equation 3-1) to that of the flow field (τ_f, Equation 3-2), the Stokes number quantifies the ability of trace particles to accurately follow the flow, which is critical for particle based flow measurements. It is known that when $S_k < 0.1$ the particles return an acceptable tracing accuracy within ±1%. However, in the present case $S_k \sim 4$, meaning the unwanted planar vibration will not influence the motion of the bubbles.

$$\tau = \frac{1}{18} d_b^2 \frac{\rho_L - \rho_G}{\mu_L}$$ Equation 3-1

$$\tau_f = \frac{1}{f}$$ Equation 3-2

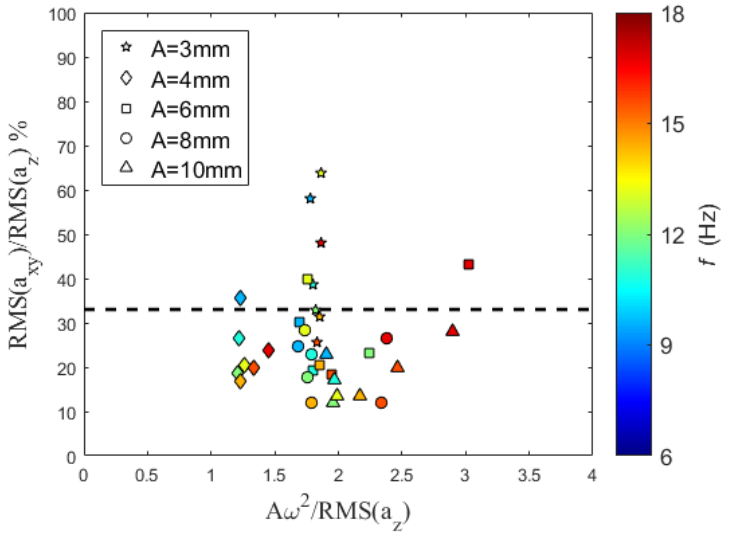

Figure 3-3. Comparison of shaker vibration acceleration in longitudinal and planar direction, the dashed line represents RMS (a_{xy}) / RMS (a_z) = 33%.

The bubble columns were made from cast acrylic to achieve higher strength and increased optical clarity compared to extruded acrylic. Strength is an important factor due to the large unsteady forces from vibration and increased optical clarity improves the quantitative optical measurements. Three round columns were available for this work with diameters of 25, 63, and 102mm; all columns had a 4mm thick wall. Except for the 102mm diameter column, which was 1.2m tall, the other two columns had a length of 0.6m. Columns were filled with tap water that was passed through a cartridge filter (W10-BC, American Plumber, Pentair Residential Filtration, LCC) with 5μm nominal filtration. Surface tension of the filtered water supply was measured with a force tesiometer (K6, Krüss GmbH) and platinum ring (RI0111-282438, Krüss GmbH). Over several days the surface tension of the supply water was measured to be 72.6 ±0.4 mN/m, which is comparable to the nominal surface tension of the pure water (~72.8 mN/m). Water temperature was measured using a thermocouple (HSTC-TT-K-20S-120-SMPW-CC, Omega Engineering). In order to provide a mounting base all columns

were capped from both ends with flanges that provided a base for mounting (in the bottom) and a pressure cap seal at the top. Figure 3-4 shows the column under operation, a top seal made of aluminum secures the column using four threaded rods connected to the base plate.

Figure 3-4. Bubble column mounted on the shaker table via vertical beams (threaded rods).

The compressed air injection manifold is shown schematically in Figure 3-5. Air flow passes through a cartridge filter (SGY-AIR9JH, Kobalt, Lowe's Companies, Inc.) with 5μm nominal filtration. The mass flow of air was controlled and monitored with a combination of a pressure regulator (Spectra Gases, Inc.), rotameter (EW-32461-50, Cole-Palmer), and a thermocouple (5SC-TT-K-40-39, Omega Engineering). The aforementioned components are pictured in Figure 3-6. The rotameter measured the volumetric flow of air with an accuracy of 2% of the full scale (FS). The thermocouple measures the air temperature immediately upstream of the rotameter with accuracy of ±0.1°C. All tests were conducted with the air

temperature between 20 ℃ and 22 ℃, and temperature difference between the air and water was less than ±2 ℃.

The air injection method is known to impact the fluid dynamics of a bubble column (Besagni et al, 2018). The current study used two different injection methods, namely single point injection (i.e. injector tube) and sparger injection. In the single point injection method, compressed air was s\delivered to the column via a single gas injector tube mounted near the column base as shown in Figure 3-7. After the stainless steel tube passed through the column wall, it was smoothly curved to produce either a 45° or 90° bend. The tube outlet was centered in the cylinder and pointed vertically upward. The injector tube had an inner diameter of 0.8 or 1.6 mm, which, for reference, should produce initial bubble sizes of 3.4 and 4.3 mm, respectively, when surface tension dominates detachment (Gaddis & Vogelpohl, 1986). It is also worth mentioning that the height of water in the bubble column was kept constant at 9*D* based on the recommendation of Besagni et al. (2017a).

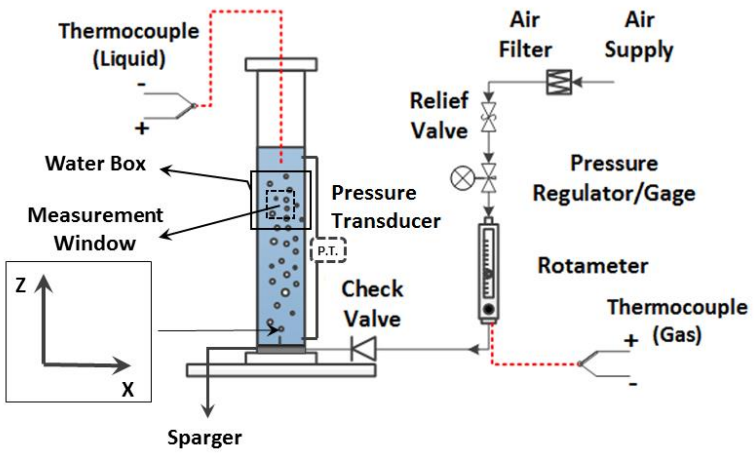

Figure 3-5. Schematic of the bubble column assembly and the compressed air injection system.

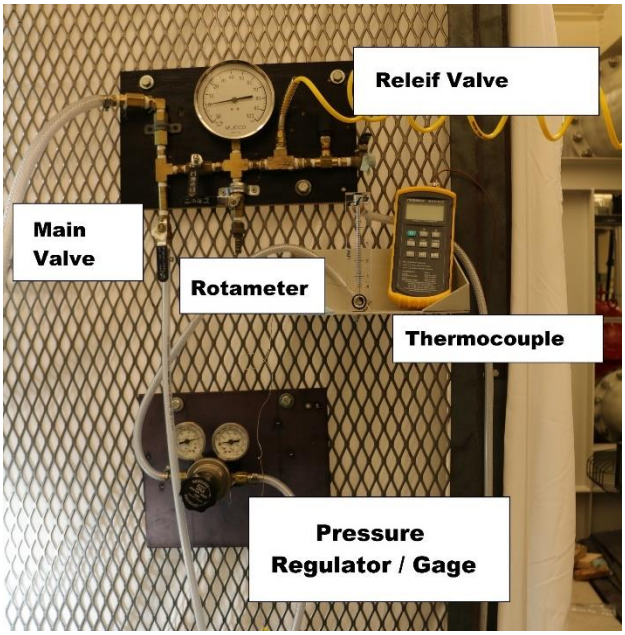

Figure 3-6. Compressed air injection manifold and control/monitoring system.

Figure 3-7. Single point injection of air inside of the column (D = 102mm, d_{inj} = 1.6mm at 90°, and U_{SG} = 6.9mm/s at P_m = 600 kPa).

In sparge injection, the same air manifold (Figure 3-6) was used to control and measure the air flow rate. However, instead of bubbling via a single tube injector at the center of column cross section a porous disk covering ~85% of the cross section of the column was employed as a bubble diffuser. The bubble sparger consists of a pressure plenum and a porous bubble diffuser, see Figure 3-8a. The plenum has a cylindrical geometry; it is capped from the bottom and the porous sparger is mounted on top of it. The plenum was machined from an aluminum cylinder and two layers of spray paint and enamel protected the aluminum surface from corrosion when in contact with water. Inside of the plenum were 350ml of additional porous material identical to the pore disk, that supplied additional pressure drop for cross-sectional uniformity of bubble distribution. The sparger was designed to be pressurized up to 7 bar. A pressure gage at the sparger indicated the pressure drop along the line up to the plenum. Figure 3-8b shows the sparger in use.

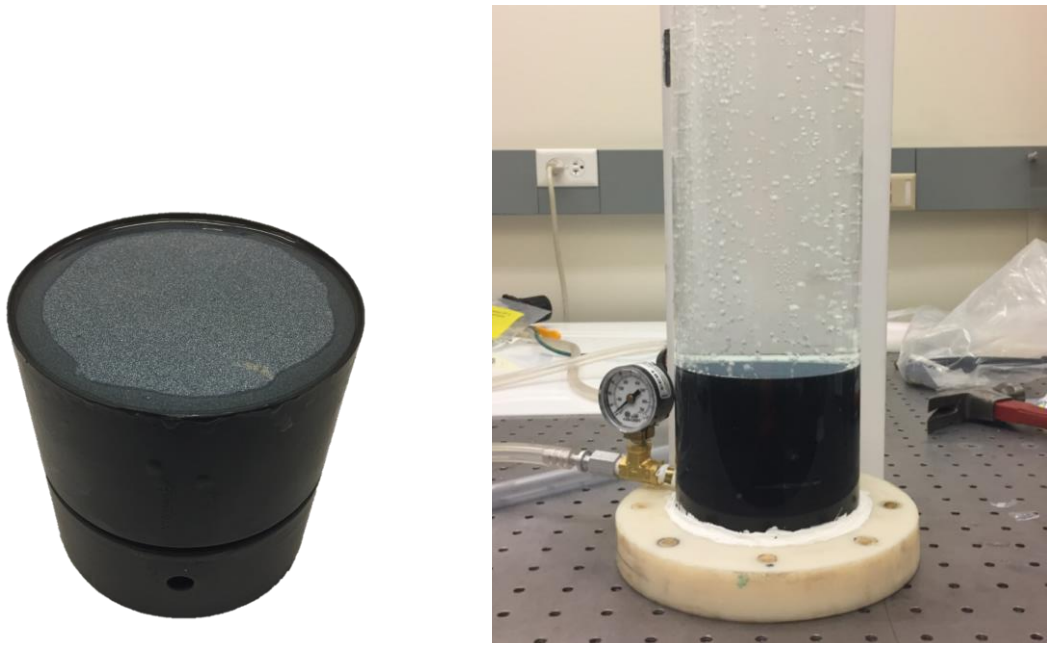

(a) (b)

Figure 3-8. Porous bubble sparger used in diffusion experiments. (a) Plenum and pore bubble diffuser and (b) bubble sparger in operation at U_{SG} = 0.5mm/s.

The bubble column was made from cast acrylic to achieve optical clarity to improve the quantitative optical measurements. Changes in light refraction index as well as the round geometry of the acrylic column introduced a significant image distortion for optical measurements. A refractive index matching box (water-box) around the column can compensate for the curvature. It is worth mentioning that the waterbox should be filled with a liquid with the same (or very close) refractive index to eliminate the image distortion error from optical measurements. The optical box used in the current study (0.2 x 0.15 x 0.15m) was made from casted acrylic (n=1.49) and filled with water (n=1.33). The difference in water and acrylic refractive indices will introduce a minor error in the optical measurements that should

be quantified; this will be discussed subsequently. Spatial calibration was carried out using a costume made calibration plate, to quantify the impact of distortions on bubble size measurements. Figure 3-9a illustrates the use of the calibration plate to identify the distortions, and Figure 3-9b shows the spatial variation of the calibration coefficient for each radial column location. From Figure 3-9, it is apparent that the waterbox mitigates the optical distortions; therefore an average spatial calibration coefficient throughout the column was used for bubble size measurement. It is worth mentioning that the waterbox was used only with the sparged injection experiments.

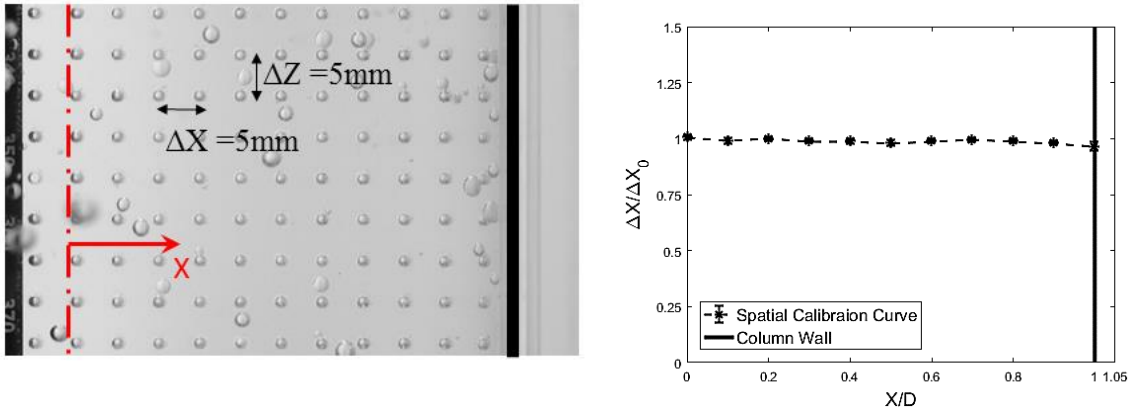

(a) (b)

Figure 3-9. Spatial calibration using a waterbox to correct for distortions from edge effects, (a) ΔX = 5mm, *D* = 102mm. (b) Spatial variation of the calibration coefficient across the column mid-plane.

3.1.2 Bubble size measurement

The bubble size distribution was determined from 2D optical imaging with a high-speed complementary metal–oxide–semiconductor (CMOS) camera (Phantom Miro 110, Vision Research, Wayne, NJ, USA), which has a resolution of 1280 × 800 pixels. The camera pixel size was 20 μm × 20 μm with a 12-bit depth. For the current work, the sample rate was 400 Hz with a reduced resolution of 1280 × 400 pixels, which the onboard memory (12 GB)

allows ~38 s of recording with these settings. A 60 mm diameter, f/2.8D lens (AFMicro-NIKKOR, Nikon Corporation, Tokyo, Japan) was used with the camera, which produced a field-of-view of 470 mm × 150 mm. The exposure time was 600μs to provide maximum illumination without bubble blurring. The column was backlit with four 500 W halogen lights and twelve 45 W fluorescent lights. The light was uniformly diffused using several 2.3 m × 2.6 m solid white microfiber fabric sheets. Consistent and uniform backlighting simplifies image-processing and decreases uncertainty. The final lighting configuration (shown in Figure 3-10) produced a homogenous light intensity distribution.

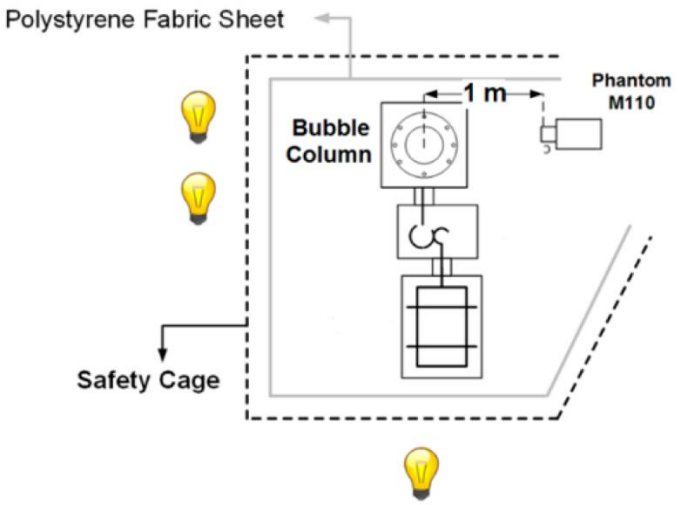

Figure 3-10. Top view of the bubble column test facility showing the camera and lighting configuration for bubble imaging.

Imaging through a round cylindrical column produces optical distortions, especially near the column edges. For measurements without a waterbox, a spatial calibration was performed with a high precision particle image velocimetry (PIV) calibration target (Type 58-5, LaVision, Göttingen, Germany), which also quantified the impact of these distortions. Figure 3-11a illustrates use of the target to identify the distortions, and Figure 3-11b shows the

spatial variation of the calibration coefficient for each column without a waterbox. Cropping the images at the lines shown (11 mm and 14 mm from the wall for the 63 and 102 mm columns, respectively) results in a maximum size variation of ±0.4 mm due to the calibration variation, which is below the minimum bubble size (1.6 mm) for these tests. Since this variation is comparable to the variation associated with out-of-plane motion, an average mid-plane spatial calibration was used for the entire image.

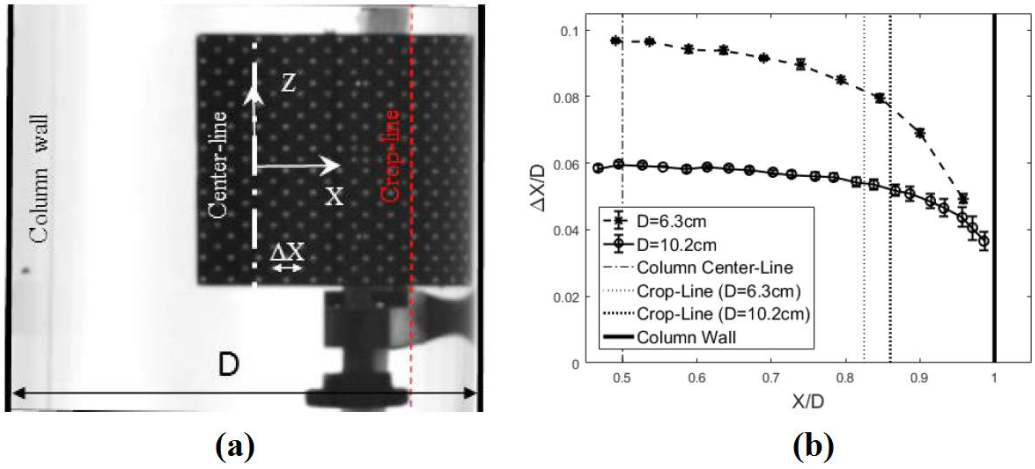

Figure 3-11. Effect of column curvature on spatial calibration, ΔX = 5mm, *D* = 102mm. (a) Raw image of the calibration plate, and (b) spatial variation of the calibration coefficient across the column mid-plane.

Bubble images were acquired with commercial data acquisition software (2.5.744.0v, Phantom Camera Control, Vision Research, Wayne, NJ, USA) and then post-processed using ImageJ (1.49v, National Institutes of Health (NIH), Bethesda, MD, USA) (Abràmoff et al., 2004; Peters, 2012; Schneider et al., 2012; Rasband, 2013), a common open access image-processing program. Within ImageJ, an edge detection algorithm was used to sharpen the bubble edges, subtract the background, and apply a grayscale threshold to convert the 12-bit images to binary images. A subset of images from each condition were manually processed

and then used to determine the appropriate grayscale threshold. Note that a range of acceptable threshold values were explored and had a 2% variation on measured bubble size. Figure 3-12 provides an example of a raw image with the identified bubbles using the appropriate threshold outlined.

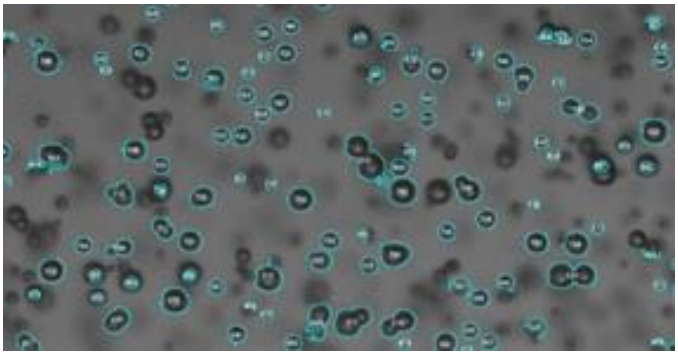

Figure 3-12. Example image of bubble identification (identified bubbles are outlined). Note that out-of-focused bubbles are not identified due to blurred edges.

This illustrates that the processing algorithm can identify in-focus bubbles and exclude out-of-focus bubbles, which minimizes the impact of out-of-plane bubble locations on the spatial calibration. Note that for the current study in-focus bubbles were limited to ±12 mm of the focal plane. Figure 3-12 was also selected to show that, even with a proper threshold, overlapping and defective bubbles (e.g., defected bubble outlined at bottom left of Figure 3-12) can contaminate the size distributions. Consequently, each image was manually inspected for the aforementioned problems and impacted bubbles were removed from the population sample. These manual inspections were also used to confirm that the grayscale threshold was not impacted by changes in void fraction between conditions.

The cross-sectional area, bubble centroid location and the aspect ratio were then calculated for identified bubbles. Note that any deviation in orientation perpendicular to the

visualization plane when the aspect ratio is greater than 1 (i.e., bubbles larger than ~2 mm) results in an overestimate of the bubble projected area. A high-pass filter with a cutoff area of $A_{proj} = 2\text{mm}^2$ was used to remove noise contamination from bubble size distribution (BSD) and consequently the probability density functions (PDF). Given the cross-sectional area and aspect ratio (b), and assuming that the bubbles are well approximated by ellipsoids (or more specifically an oblate spheroid) an equivalent bubble chord length was determined, using Equation 3-3.

$$d_{eq} = \sqrt{\frac{4bA_{proj}}{\pi}}$$

Equation 3-3

Note that not every image was processed because the sample rate (400 Hz) did not produce a sufficient duration for a new bubble population in each image. Consequently, the period between processed images was increased such that each processed image contained a new bubble population to ensure statistically independent bubble samples. Given by Equation 3-3, Sauter mean diameter (d_{32}) is the ratio of the representative bubble volume to the bubble surface area, which is a weighted average, and this is a common measure of bubble size for mass transport considerations.

$$d_{32} = \frac{\sum_{j=1}^{n} n_j d_j^3}{\sum_{j=1}^{n} n_j d_j^2}$$

Equation 3-4

3.1.3 Void fraction measurement

Void fraction measurements were carried out using two separate approaches namely, surface tracking and differential pressure measurement. In surface tracking the liquid free surface displacement (see, Figure 3-13) due to the injected volume of air was measured and related to void fraction (ε) using Equation 3-5.

$$\varepsilon = 1 - \frac{H_0}{H_D} \qquad \text{Equation 3-5}$$

Here H_0 is the height of water in column before air injection and H_D is the dynamic-height of liquid surface during column aeration. In order to track the surface rise, a Styrofoam disk was placed on the liquid surface and a physical point (black dot) was tracked during the experiments using a video digitization tool (Hedrick, 2008). Having the styrofoam motion profile one can calculate the height of the liquid dynamic surface (H_D). The reliability of this approach is heavily limited by imaging temporal and spatial resolution. It was only used in static column experiments since sloshing with vibration produced large uncertainties.

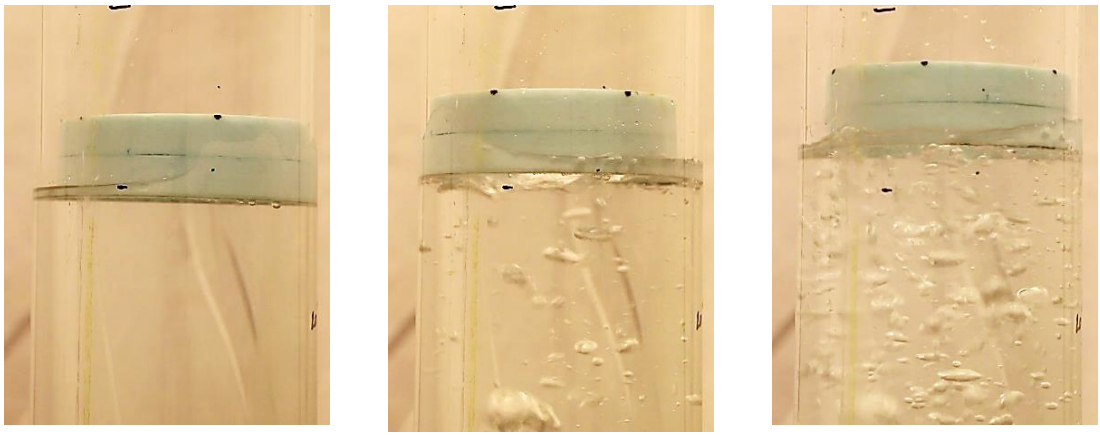

Figure 3-13. Void fraction measurement using surface displacement from tracking the Styrofoam at U_{SG} of (a) 0, (b) 4mm/s, and (c) 10mm/s

In the second approach, the void fraction was calculated from differential pressure (ΔP) along the column height during operation. Two pressure taps were located at Z = 0.08m and Z = 1.0m (see Figure 3-5) to measure the oscillating fluid pressure during vibration via a differential pressure transducer (PX2300-DI, OMEGA). A data acquisition card (National Instruments, USB-6218 BNC) was used to acquire the output signal from the pressure transducer and the signal was recorded on a desktop computer (via LabVIEW 15.0.1). Void fraction was calculated using Equation 3-6. Here ΔH is the vertical distance between the pressure taps. The second approach in void fraction measurement was only used with sparge injection.

$$\varepsilon = \frac{\Delta P}{(\rho_L - \rho_G) g \Delta H} \qquad \text{Equation 3-6}$$

3.1.4 Liquid diffusion measurement

The mixing experiments consisted of the measurements of the evolution of a passive scalar (i.e. dye) within the bubble column. The passive scalar was food color (chef-o-van), which had a density of 1.025kg/m^3 and surface tension of 65.9 ± 0.1 mN/m. The dye was

injected through the bubble column using a vertical tube of 0.6mm inner diameter and 1.6mm outer diameter. The tube was mounted on the column wall and placed in a vertically downward orientation to inject the dye at the center of the column. The injection point was located 0.45m above the sparger. For each experiment, 0.6ml of dye was injected during ninety seconds at a constant rate of 0.4ml/min using a volumetric syringe pump (NE-300, New Era). This creates a laminar filament of dye with Reynolds number, $Re << 1$ at the injection point. Ninety seconds after the injection the initial condition has been forgotten and bubble injection began. The start of injection sets the origin of time in each test and quantitative measurements continued until one minute after the injection began.

A Canon EOS 70D DSLR camera was used to capture monochrome still images of the bubble mixing. This camera had an APS-C CMOS image sensor (22.5mm × 15mm) with a maximum resolution of 5472 × 3648 pixels. The camera pixel size was 4.1 μm × 4.1μm with a 14-bit depth. A Canon 60 mm 1:2.8 camera lens was employed for image acquisition. Recordings of bubble mixing were carried out with a reduced resolution of 1280 × 720 pixels which produced a field-of-view of 120mm x 67mm. For the current work we made recordings of the entire test from before dye injection until after the dye was fully mixed. Recordings of bubble mixing at 60Hz were acquired to obtain the temporal evolution of the dye concentration. During the experiments, the camera exposure time was set to 312μs. The column was backlit with a LED panel (Daylight 1200, Fovigtec StudioPRO). The LED panel delivered up to 13,900 illumination flux (5600K color temperature) at 1 meter. Light was uniformly diffused using a 3mm thick white acrylic sheet.

Temporal evolution of the dye concentration was quantified from the change in the grayscale value of the monochromic images within the measurement section. First an *in situ* calibration were carried out to correlate the grayscale value of the images with the injected mass of dye. Figure 3-14 shows the calibration curve, which based on Elbing et al. (2010), measurement of light intensity for concentration evaluation should be carried out in a range that offers a linear correlation between concentration and light intensity. Therefore, in the current work a maximum of 0.6g of the dye was used for mixing time measurements.

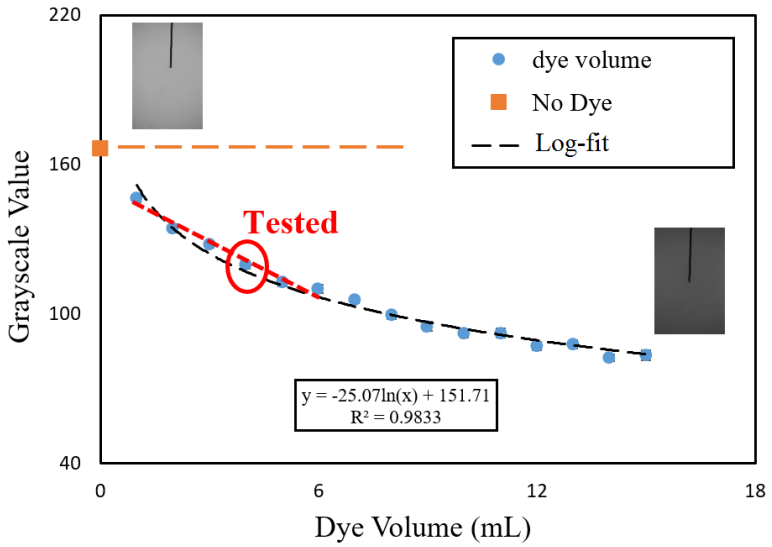

Figure 3-14. Change of grayscale value with the injected solution of 10% dye and 90% water.

All the measurements were carried out 25mm below the injection needle. Here ImageJ was used again to obtain the grayscale value across the column diameter. Figure 3-15 shows a sample measurement of the grayscale value across the column diameter. It can be seen that both dye and bubbles produce similar signatures in the grayscale profile. A post processing MATLAB code was developed to detect the bubbles based on the minimum grayscale value and filter it from the measurement. Figure 3-16 shows the results of grayscale distribution

along the column diameter from a preliminary experiment. It can be seen that the post processed data is not continuous; however, there are enough data points to demonstrate the distribution of the dye in the radial direction. In addition, this technique successfully captures the temporal evolution of the dye concentration in bubble mixing.

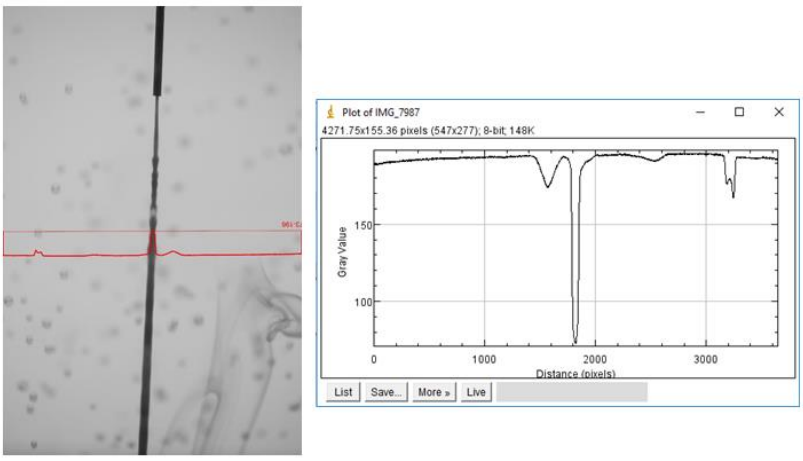

Figure 3-15. Grayscale value measurements from the bubble images, (a) raw image and the resulting (b) grayscale profile along the column diameter.

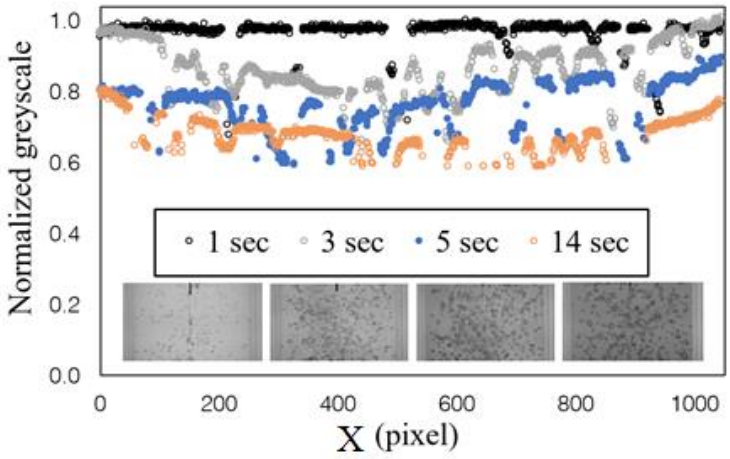

Figure 3-16. Grayscale measurement for evaluation of the temporal evolution of the dye concentration in bubble mixing.

3.2 Inclined Gas-Liquid Pipe Setup

3.2.1 Test facility overview

The variable inclination gas-liquid pipe flow setup was located in the OSU Multiphase Lab (Prof. Ghajar). Cook (2008) was the first published document on the variable inclination gas-liquid pipe flow setup. Since Cook (2008), a number of studies on hydrodynamics of the gas-liquid pipe flow have been conducted (Bhagwat et al., 2012a,b; Bhagwat & Ghajar, 2012a,b, 2014, 2015a,b, 2016a,b, 2017; Ghajar & Bhagwat, 2013; 2014a,b; Oyewole, 2013; Lares 2014). In the current study the variable inclination gas-liquid pipe flow setup was used to study the film thickness at inclined annular flow using planar laser induced fluorescent (PLIF).

The experimental setup was comprised of two major components, a variable inclination frame (VIF) and the instrumented multiphase pipe flow setup (IMPFS). The VIF is schematically shown in Figure 3-17. The IMPFS was mounted on the VIF with pulleys and bolts, making it able to rotate from +90° (upward) to -90° (downward). The IMPFS was made of two parallel pipes, a 12.7mm inner diameter polycarbonate transparent pipe for measurements of flow visualization (using polycarbonate transparent pipe), void fraction, and phase pressure drop. In addition, a 12.5mm internal diameter stainless steel (40 IPS alloy 304) pipe with a surface roughness of 0.02mm was available for heat transfer and pressure drop measurements.

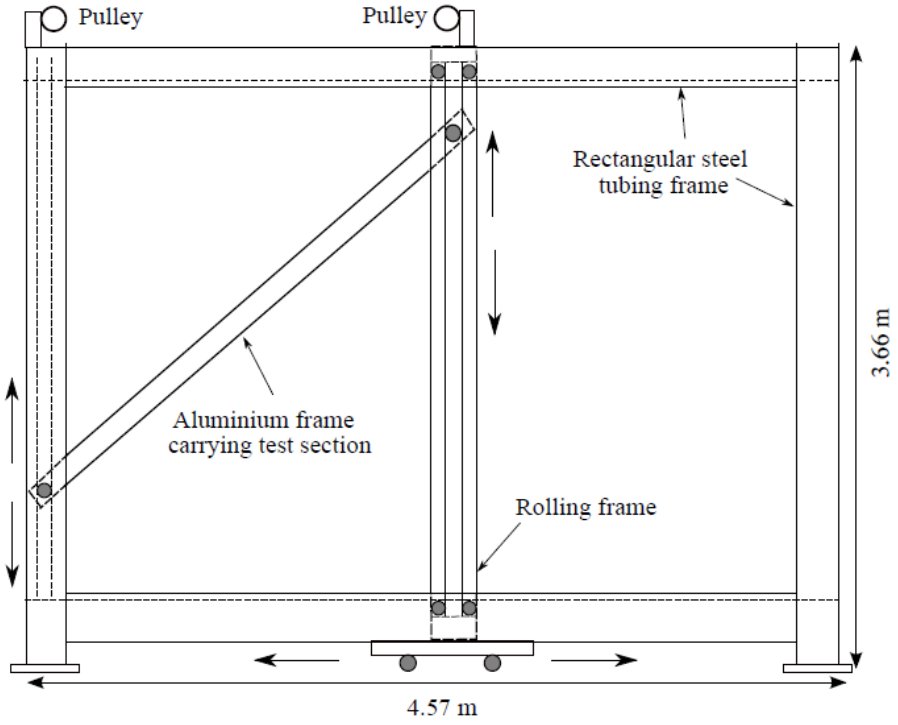

Figure 3-17. Schematic of the variable inclination frame mechanism and relative position of the test section adopted from Bhagwat (2015).

Figure 3-18 depicts a schematic of the flow visualization and void fraction measurement section of the IMPSF. A thermocouple (TMQSS-062U-6, Omega) immediately after the static mixer measures the two-phase mixture temperature within ±0.1 °C accuracy. Flow visualization tests were carried out in the 1.6m long polycarbonate section of the setup. This section also was used for pressure drop measurements using two pressure taps 890mm apart. In order to make sure that the pressure drop measurements were not influenced by the inlet condition, the first pressure tap was located 100D downstream of the static mixer. The distance between the static mixer and the first pressure tap (development length) was one of the most significant design considerations in order to provide a fully developed flow at the

measurement location. In the context of gas-liquid flow, a fully developed flow is defined as the situation where alignment of the phases does not change with the location of observation window. Unlike single phase pipe flow, there is no consensus in the gas-liquid pipe flow literature on the exact calming length. However, previous studies using the same experimental setup (Bhagwat, 2015; Lares 2014; Oyewole, 2013) reported a fully developed gas-liquid flow at 100D from the inlet.

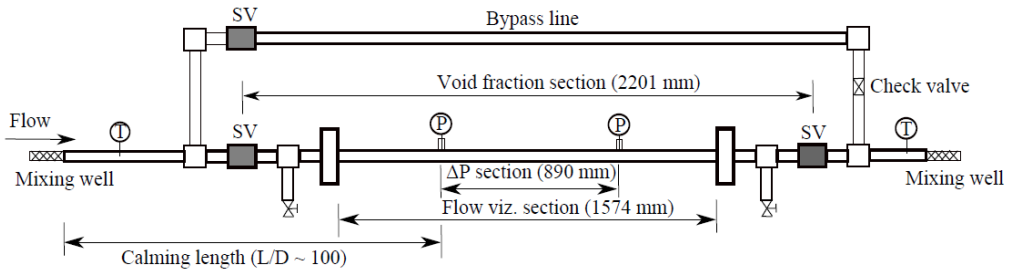

Figure 3-18. Schematic of the IMPSF flow visualization and void fraction test section, which was adopted from Bhagwat (2015).

3.2.2 Flow loop control and monitoring

The IMPFS components are shown in Figure 3-19. The liquid phase used in this study was tap water stored in a 55 gallon (208 liter) polyethylene tank. A Bell and Gosset centrifugal pump (series 1535, model number 3445 D10) circulates the water inside of the test setup. Water passes through a filter (AP12-T Aqua pure), heat exchanger (BCF 4063, ITT one shell and two tube pass) and a Coriolis mass flow meter (CFM 100, Micro Motion Elite Series) before entering the test section. The heat-exchanger was necessary to remove the friction heat and maintain a constant water temperature. A gate valve upstream of the liquid mass flow meter

allows regulating the mass flow of water in the range of 0.25kg/min to 40kg/min. Water returns to the storage tank after it passes through the test section.

An air compressor (2545 T-30, Ingersoll-Rand) supplies the compressed air with the maximum pressure of 125psi (850kPa) in the current work. The compressed air passes through a regulator (4ZM22, Speedaire), a custom submerged copper coil heat exchanger, and a filter/drier (4ZL49, Speedaire). The heat exchanger maintains the air at room temperature to ensure that both air and liquid enter the test section at the same temperature. The filter/drier unit removes any contamination and prevents unwanted condensation. Compressed air then passed through a mass flow meter, (LMF 3M and CMF 025, Micro Motion Elite Series). The LMF 3M operates in low mass flow rate ranges (0.001 kg/min to 0.007 kg/min) and the CMF 025 handles higher mass flow rates (0.01 kg/min to 0.25 kg/min). The air mass flow rate can be controlled using a Parker needle valve (24NS 82(A)-8LN-SS) located upstream of the mass flow meter. Finally, a static spiral mixer (3/8-40C-4-3V-23/8, Koflo) located at the entrance to the IMPFS mixes the gas and liquid phases thoroughly.

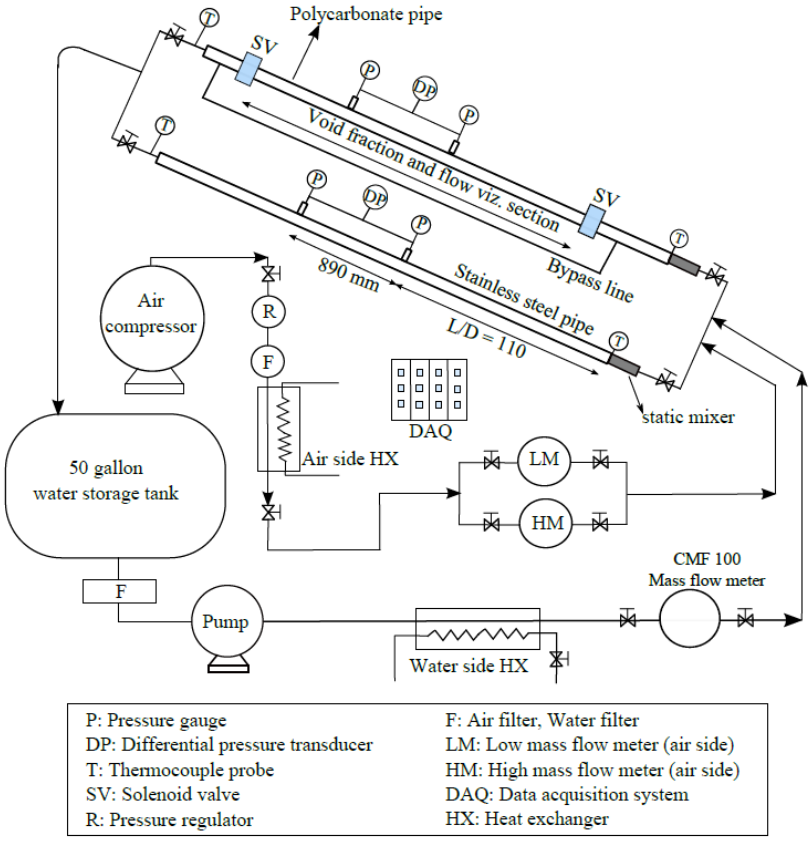

Figure 3-19. Schematic of the instrumented multiphase pipe flow setup, adopted from Bhagwat (2015).

3.2.3 Planar laser induced fluorescent

Film thickness measurements in the annular flow system was the main objective using the variable inclination gas-liquid pipe flow setup. Planar laser induced fluorescent (PLIF) was chosen for the liquid film thickness measurements because of its non-invasive advantage. PLIF measurement require a fluorescent agent in the liquid phase, a monochromic laser light, and a camera for optical recording of the Stokes shifted light. Low concentrations (3wppm) of Rhodamin-6G dye (Sigam-Aldrich) were introduced into the water following the

recommendation from Elbing et al. (2010); this fluorescent agent tints the water in red-orange. Rhodamin 6G fluoresces maximally at 590nm and absorbs maximally at 530nm. The image plane was illuminated with a 532nm Nd:YAG laser (Gemini-200, New Wave) beam formed into a sheet. Figure 3-20 shows a schematic of the laser position for the PLIF measurements of liquid film thickness and associated measurements uncertainty (Ξ_b) due to pipe curvature. The laser sheet thickness was calculated to be 0.7mm in order to reduce the film thickness measurement uncertainty to around 1%. It is noteworthy that the film thickness was on the order of magnitude of a few tenths of a millimeter. For optical imaging, a sCMOS camera with a resolution of 2560 x 2160 pixels (Imager, LaVision) was used. The field-of-view was nominally 14mm x 11.8mm.

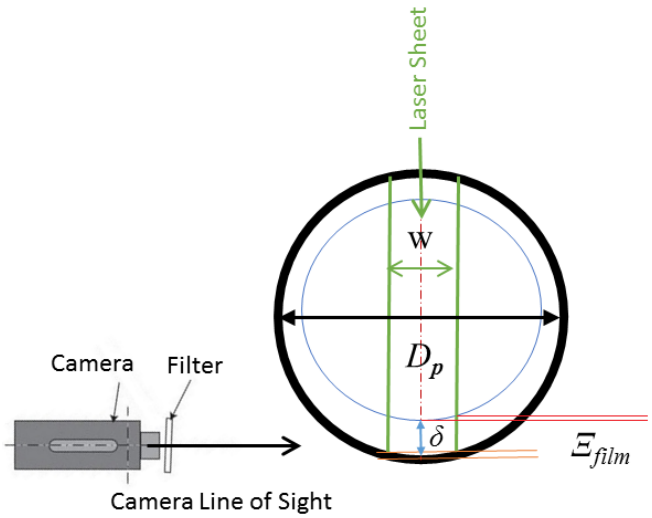

Figure 3-20. Schematic of laser position in PLIF measurement of liquid film thickness and associated measurement uncertainty (Ξ_{film}) due to pipe curvature.

A waterbox was made of casted acrylic sheets to eliminate the optical distortions at the edges of the pipe. Using a custom calibration target the spatial calibration of the field-of-view was carried out using a third order polynomial fit (DaVis8, LaVision), see Figure 3-21. A

sample PLIF image taken in annular flow in a horizontal orientation is shown in Figure 3-22. The film thickness was measured from the PLIF images using ImageJ.

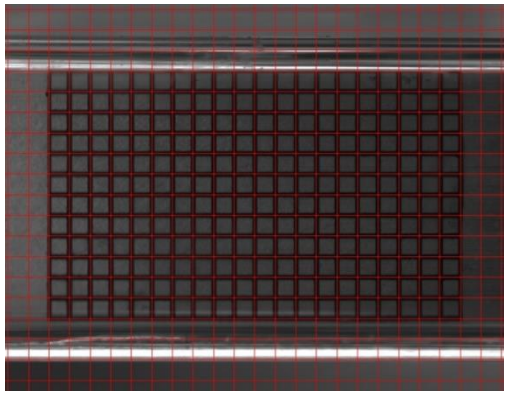

Figure 3-21. Optical calibration of the field-of-view using Davis8 (Lavision).

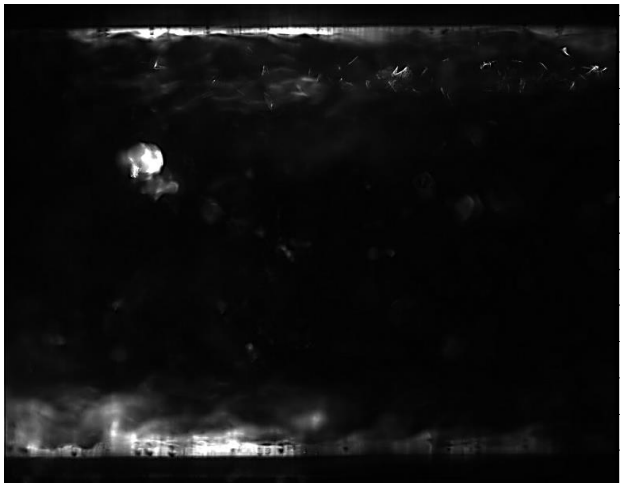

Figure 3-22. Flow visualization of horizontal annular flow using PLIF with $\dot{m}_G$ = 0.5kg/min and $\dot{m}_L$ = 1.6kg/min.

CHAPTER IV

CHARACTERIZATION OF STATIC BUBBLE COLUMN REGIMES

4.1 Introduction

Bubble columns are multiphase contact reactors with a broad application in chemical and bio-chemical industries. Due to their simplicity and low operation costs, bubble columns are heavily used in laboratory and industrial-operation scales. Bubble columns are mainly used for mass transport applications; therefore, the most important bubble column design parameter is the phase interfacial area, which is governed by bubble size distribution and void fraction. Depending on the operation regime the spatial distribution of the phases and consequently bubble size distribution and void fraction exhibits different behaviors. It is the main objective of the present chapter to provide a fundamental understanding of bubble size distribution and void fraction characteristics in a bubble column with respect to operation regime (i.e. homogeneous and heterogeneous). Design and scale-up of a bubble column has been subjected to significant uncertainty for two reason. One is the complexity associated with multiphase flow; especially, due to the slip boundary condition at gas-liquid interface. Second is that the majority of the attempts are based on producing empirical models for design and scale-up of bubble columns, these models are only valid for a narrow range of experimental conditions. This chapter presents a systematic approach for scaling the bubble size and void fraction in a bubble column reactor using dimensional analysis. Different models were produced based on the operation regime; these models were validated against experimental data. The following

sections of this chapter presents a parametric characterization of bubble size and void fraction. In the following, the experimental measurements were analyzed to put together a parameter space for scaling the multiphase parameters (i.e. bubble size and void fraction) using dimensional analysis. In the last subsection of this chapter, a summary of these results and conclusions are presented.

4.2 Characterization of Bubble Size Distribution

This section aims to provide a systematic approach for regime demarcation based on visual inspections, bubble size distribution, and void fraction levels. A parametric study was carried out to investigate the dependency of the operation regime to the gas superficial velocity as well as liquid properties, specifically surface tension (σ), viscosity (ρ_L), and density (μ_L). In this investigation the operation regime was marked by visual inspection, then the measurements were classified based on operation regime to provide a description on how bubble size and void fraction changed from the homogenous to the heterogeneous regime. Details of the experimental setup, instrumentation, and measurement methods are provided in Chapter 3.

The current experimental setup employs a porous sparger disk for introducing the compressed air into the column. In general pore spargers are able to produce a uniform bubble swarm when the pore medium is gassed uniformly. In the case of a porous sparger with a wide range of pore sizes, the bubble swarm is likely to be non-uniform since activating the smaller pore requires a higher back pressure in the manifold. Manual inspection was carried out to confirm the uniformity of bubble generation from the porous disk prior to mounting the manifold into the column (see Figure 4-1). The average pore size on the sparger disk was calculated using

Equation 4-1. Assuming that when the manifold pressure reaches the hydrostatic pressure at the sparger surface the bubble formation begins. Here the bubble pressure is equal to the capillary pressure (ΔP_{Cap}) inside the pore of radius R_{sp}. Houghton et al. (1957) showed that Equation 4-1 can be used to calculate the average pore size (r_p), within ±15% of the reported pore size by scanning electron microscopy (SEM). In the present work, a total of 20 tests were carried out to calculate the pore size using Equation 4-1; and the average pore size was calculated to be 85µm ± 10µm. It is worth mentioning that Houghton et al. (1957) explains that the capillary pressure (ΔP_{Cap}) is the manifold pressure at the onset of the bubble formation at the sparger disk.

$$\Delta P_{Cap} = {}^{2\sigma_L}\Big/_{R_{sp}} \qquad \text{Equation 4-1}$$

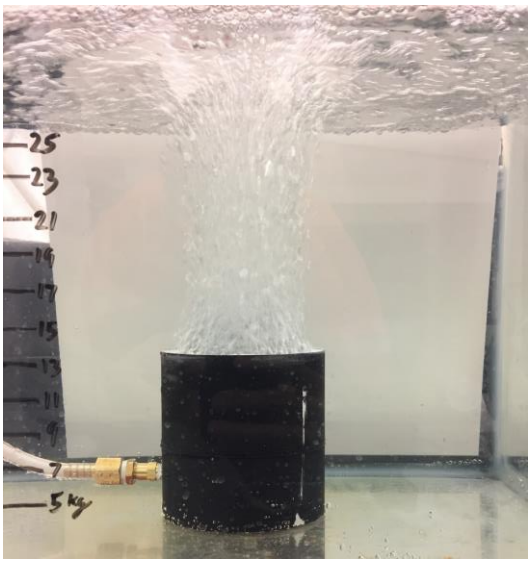

Figure 4-1. Sparger submerged in a fish tank for preliminary testing, a uniform bubble generation from the pore disk was observed.

A range of gas superficial velocities was tested in the current work, Chapter 3 provides details on the control and measurement of the gas superficial velocity. For more information

on the uncertainty associated with the reported gas superficial velocity the interested reader is referred to Appendix B. To explore the effect of liquid properties on bubble size and void fraction, aqueous solutions of glycerin with different concentrations were tested. Table 4-1 provides the test matrix for testing the effect of liquid properties on multiphase parameters in the current work. It is noteworthy that in the current work, the range of the liquid viscosity tested was in excess of two orders of magnitude. However, surface tension and liquid density were changed by about 10% and 20%, respectively, relative to water.

Table 4-1. Test matrix for characterization of multiphase parameters in the sparged bubble column

#	%H_2O	%Glycerin	μ_L (Pa.s)	ρ_L (kg/m^3)	σ (mN/m)	U_{SG} (mm/s)
1	15	85	0.1612	1224	64.7	6, 11, 14, 21, 28, 35, 41, 48, 55, 62, 69
2	21	79	0.083	1208	65.4	
3	40	60	0.016	1157	67.4	
4	100	0	0.001	998	71.8	

It is appropriate to start by examining the bubble size in a sparged bubble column via comparison of the Sauter mean diameter (see Equation 3-4) in the sparger to that of a single point injector. Details of bubble size distribution in a single point injection method are fully presented in the following chapter; however, it is intended here to demonstrate the effect of injection method on the average bubble size. Figure 4-2 compares the Sauter mean diameter of air bubbles in water produced from single point injector (Chapter 5) with that of the sparger porous disk. Results clearly shows that Sauter mean diameter is significantly larger when a single point injection method was employed. In addition, superficial gas velocity has an inverse effect on the bubble size; in a single point injection (SPI) the bubble size decreases with increasing the gas superficial velocity due to elevated shear in the heterogeneous regime.

However, in a sparged bubble column increasing the gas superficial velocity produces larger bubbles due to an entirely different bubble formation mechanism and the absence of breakup and coalescence. Another interesting bubble characteristic in the sparged bubble column is the bubble size distribution. Akita & Yoshida (1974) showed that single point injection produces a log-normal distribution of the bubble size, Figure 4-3 shows that sparged injection produces a near Gaussian bubble size distribution, this is also in agreement with Kazakis et al. (2008). Table 4-2 presents the higher order statistics (i.e. skewness and kurtosis) calculated from a large sample population (> 5000 bubbles), results confirms that bubble size distribution exhibits near Gaussian behavior (S~0, κ~3).

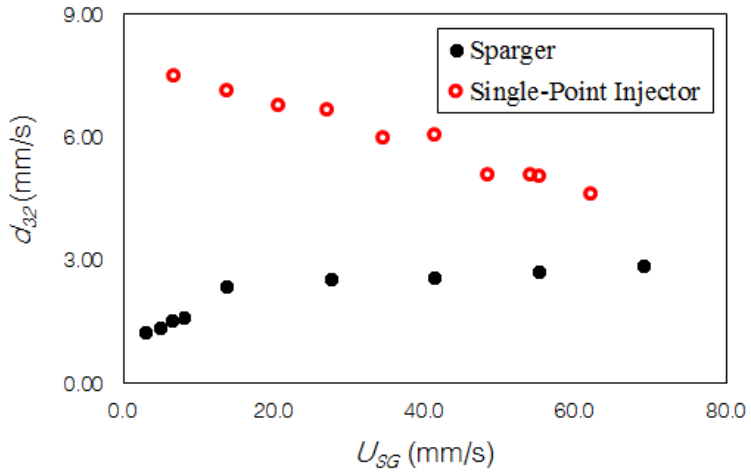

Figure 4-2. Comparison of the Sauter mean diameter from a sparger and single point injector (d_{inj}=1.6mm) using air and water.

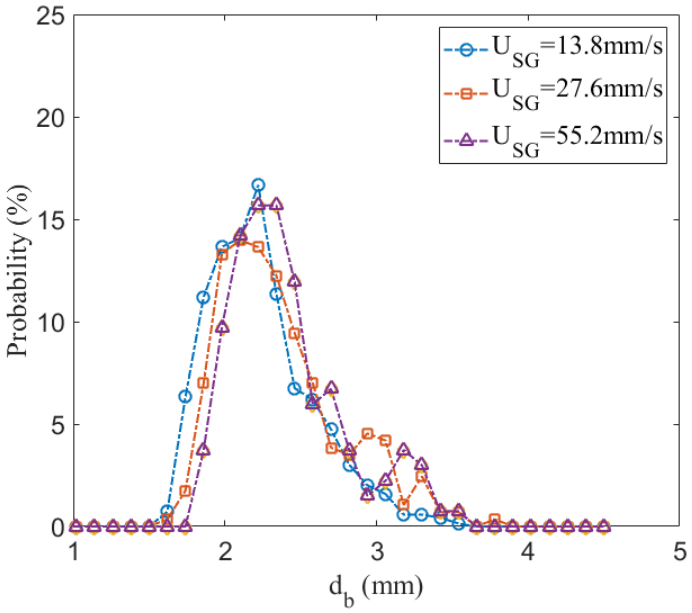

Figure 4-3. Bubble size distribution in the sparged bubble column at 3 different gas superficial velocities.

Table 4-2. Skewness and kurtosis from bubble size distribution in the sparged bubble column.

U_{SG} (mm/s)	Skewness, S (--)	Kurtosis, κ (--)	Mean, d_{10} (mm)	Standard Deviation, σ (mm)
13.8	0.85	3.60	2.23	0.19
27.6	0.90	3.32	2.37	0.20
41.4	1.14	4.06	2.42	0.20
55.2	0.56	2.64	2.54	0.22
69.0	0.65	2.71	2.69	0.23

To further understand the physics of the multiphase system in the current study the effect of liquid properties on the characteristics of the bubble size distribution was investigated. Three aqueous solutions of glycerin (see Table 4-1) were tested for a qualitative inspection of the physical behavior of the multiphase system; in each case the bubble size distribution and Sauter mean diameter was measured. Interestingly, it was observed that increasing the

viscosity enhances the regime transition from homogenous (bubbly) to heterogeneous (churn-turbulent). Figure 4-4 presents the Sauter mean diameter measured from a single point injection (in water) compared with that of the sparger using water and aqueous glycerin solutions. Results show that in the sparger tests, increasing the viscosity changes the trend between U_{SG} and d_{32}. Sauter mean diameter in aqueous solutions of glycerin exhibit a decreasing trend with increasing the gas superficial velocity, similar to that of the single point injector (though not as significant). This behavior is known to be a characteristic of the churn-turbulent (heterogeneous) regime. Liquid properties effect the bubble size and, consequently, the void fraction by promoting the coalescence and breakage of the primary bubbles formed at the sparger. Viscosity increases the bubble size by inhibiting the coalescence process; however, excess shear due to higher viscosity causes bubble breakage and shifts the distribution, this can also be seen in Figure 4-4. Figure 4-5 shows the bubble size distribution from aqueous solutions of glycerin (85% and 60%), one can see that in both cases the distribution changes from a bell shape (near Gaussian) into a spike shape (log-normal) as the gas superficial velocity exceeds 27.6mm/s. This regime change can also be inspected from the higher order statistics of the bubble size distribution. Table 4-3 shows a significant deviation from Gaussian characteristics (S~0, κ~3) after U_{SG} = 34mm/s, where both skewness and kurtosis increase from Gaussian characteristics.

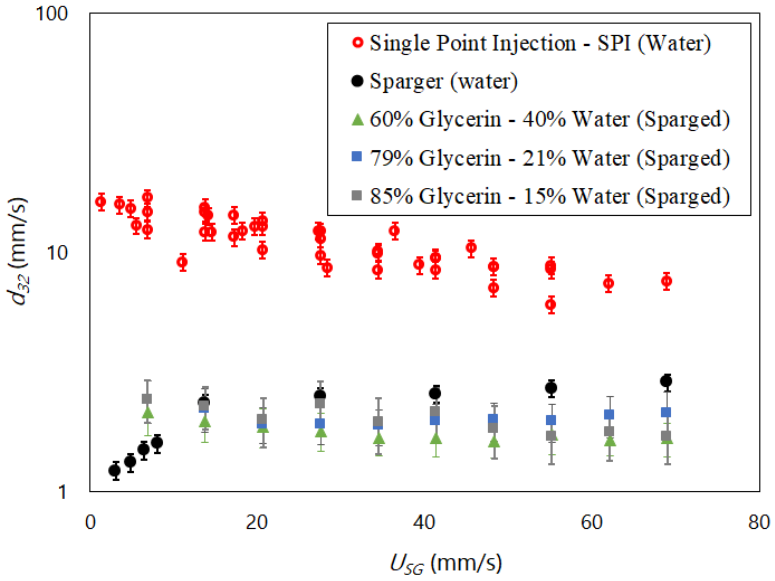

Figure 4-4. Sauter mean diameter (d_{32}) measured using a single point injector (water) and a sparger disk (water and aqueous solution of 85% glycerin).

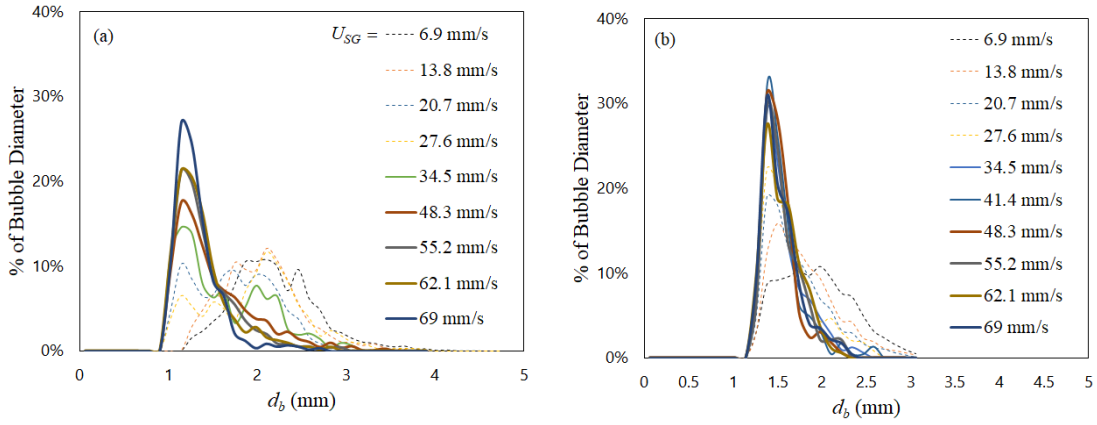

Figure 4-5. Bubble size distribution in aqueous solution; (a) 85% glycerin and (b) 60% glycerin. Measurements were carried out at ten different gas superficial velocities.

Table 4-3. Bubble size and higher order statistics, bubbles were produced using a sparger disk in water and aqueous solution of 85% glycerin.

U_{SG} (mm/s)	d_{32} (mm)	d_{10} (mm)	$\sigma(d_b)$ (mm)	$S(d_b)$ (--)	$\kappa(d_b)$ (--)
6.9	2.42	2.20	0.49	0.79	4.30
20.7	2.00	1.75	0.47	0.49	3.43
27.6	2.32	1.99	0.57	0.51	3.96
34.5	1.95	1.62	0.51	0.80	2.99
41.4	2.15	1.75	0.56	1.37	6.40
48.3	1.83	1.52	0.46	1.43	5.11
55.2	1.69	1.42	0.39	2.34	12.2
62.1	1.76	1.41	0.43	3.32	20.0
69.0	1.69	1.35	0.39	4.23	28.4

Figure 4-6 presents the PDF of the Bubble size distribution depicting the effect of increasing the viscosity of the shape of the distribution, it can be seen that once the gas superficial velocity is high enough (in this case U_{SG}~28mm/s) then viscosity modifies the Gaussian like distribution (in water) to bimodal and spike shape distributions. Visual observations the aforementioned shift in the distribution shape is a representative of a regime change from homogenous to heterogeneous. High speed recordings showed that, increasing the viscosity reduces the bubble terminal velocity due to friction drag; moreover, increasing the viscosity effects the bubble motion by creating planar oscillation in the bubbles trajectory. Visual observation also showed that increasing the viscosity enhances bubble coalescence, this results in the formation of larger bubbles that are susceptible to shear breakage. Larger bubbles rise faster and exhibit churn-turbulent flow patterns; at this point, the physical behavior of the bubble column shifts towards heterogeneous characteristics.

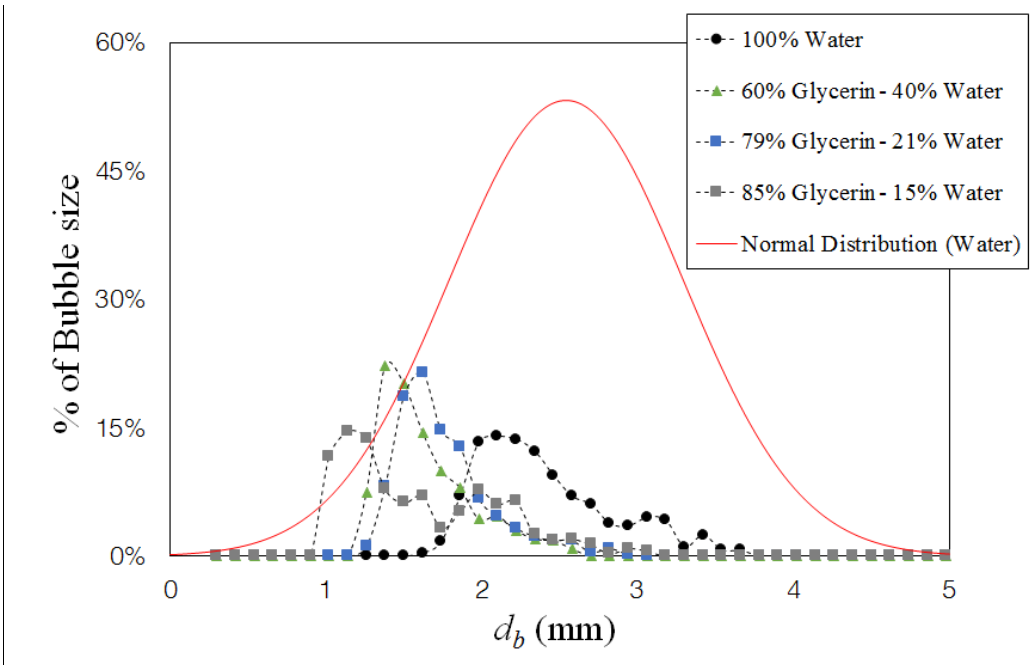

Figure 4-6. Probability density function of bubble size distribution, effect of liquid viscosity on the distribution shape and operation regime (U_{SG}=27.6mm/s).

Here a statistically stationary population sample of bubble size had been collected for analysis. It was hypothesized that in the heterogeneous regime the interfacial momentum transfer would set the bubble size. Therefore, it is expected that the interfacial momentum transfer was fed from input power given to the liquid phase from the gas phase. Sauter mean diameter was measured according to the test matrix in Table 4-1 to test the relationship between bubble size and specific input power per unit mass ($P_m = gU_{SG}$). It is worth mentioning that Hinze (1955) recommends using the Sauter mean diameter as a stable bubble size under shear breakage. Figure 4-7 shows the measured d_{32} at various P_m's illustrating a downward trend. Using dimensional analysis it was attempted to find a scaling law that correlates the bubble size (d_{32}) with the input power ($P_m = gU_{SG}$) and liquid properties (i.e. surface tension, viscosity, and density of water). Equation 4-2 shows the outcome correlation for scaling the bubble size where *f()* is an unknown function. Equation 4-3 was produced based on the recommendations

from Hinze (1955) and Lewis & Davidson (1982) suggesting that *f()* is a linear function that correlates the bubble size and specific input power in Equation 4-2 with a proportionality coefficient (*k*). Figure 4-7 shows the predicted bubble size from Equation 4-3 (power law curve fits) against the measured bubble size (Sauter mean diameter) from both single point injection and the sparged tests. Two interesting results are shown in Figure 4-7. First, the proportionality coefficient in Equation 4-3 is different based on the injection method. The single point injection has the d_{32} data collapse with $k = 1.7$, which is consistent with the recommendation of Lewis & Davidson (1982) for bubble size under shear breakage. In the sparged injection tests, the proportionality coefficient is lower ($k = 0.45$), which is consistent with the fact that the current sparger disk produces smaller bubbles than the single point injection. The second interesting result from Figure 4-7 is that with both injection methods, the data points with lower specific input power do not collapse on the curve predicted by Equation 4-3. Detailed inspections show that at lower specific input powers the bubble column is still operating in the homogenous regime; consequently, in the absence of shear breakage bubble size cannot be predicted from Equation 4-3.

$$\frac{\rho_L d_{32} \sigma}{\mu^2} = f\left(\frac{P_m \mu^5}{\rho_L \sigma^4}\right) \qquad \text{Equation 4-2}$$

$$d_{32} = k \frac{\left(\frac{\sigma}{\rho}\right)^{3/5}}{{P_m}^{2/5}} \qquad \text{Equation 4-3}$$

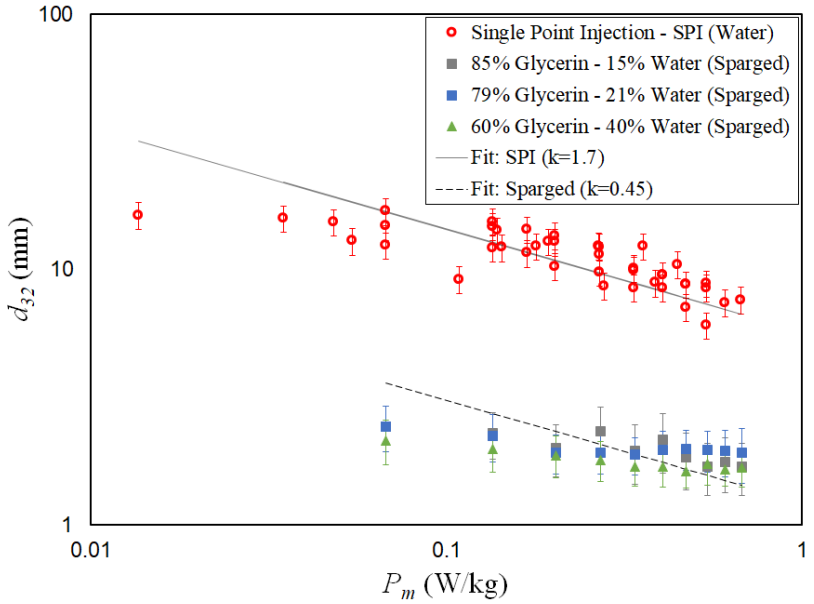

Figure 4-7. The bubble Sauter mean diameter (d_{32}) plotted versus the specific input power (Equation 4-3) for both single point injector (water) and a sparger disk (water and aqueous solutions of glycerin). These results are compared against Hinze based correlations for the maximum stable bubble size.

4.3 Bubble Size Scaling

Here it is attempted to find the unknown function *f()* in Equation 4-2, which would establish a correlation between the scaled bubble size and the scaled specific input power. Figure 4-8 uses the non-dimensional coordinates from Equation 4-2 to plot the measured bubble size at the corresponding specific input power; it is shown that the bubble size data collapsed as a power-law correlation given in Equation 4-4.

$$\frac{\rho_L d_{32} \sigma}{\mu^2} = 300 \times \left(\frac{P_m \mu^5}{\rho_L \sigma^4}\right)^{-0.184} \qquad \text{Equation 4-4}$$

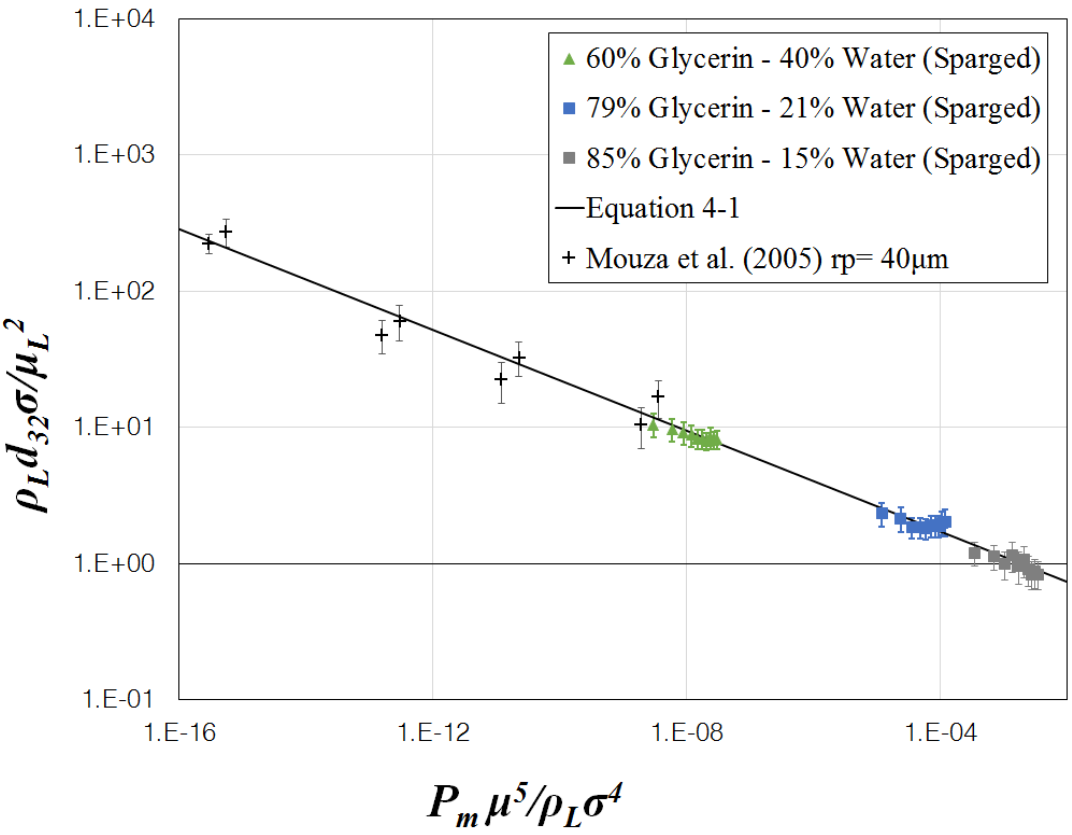

Figure 4-8. Effect of liquid phase properties and specific input power on Sauter mean diameter in Churn-turbulent regime. A new dimensionless term S_i (*Mo.Ca*) plotted versus the Ohnesorge number (based on Sauter mean diameter).

The coordinates in Figure 4-8 are established non-dimensional terms. The scaled bubble size is the Ohnesorge number ($Oh = {\rho_L \sigma d_{23}}/{\mu_L^2} = {We}/{Re^2}$), which is the ratio of the product of the inertia and surface tension forces to viscous forces. The scaled specific input power, which is related to the shear breakage term ($S_i = g\mu_L^5 U_{SG}/\rho\sigma^4$), is the product of the Morton number ($Mo = g\mu_L^4/\rho_L\sigma^3$) and the Capillary number ($Ca = \mu_L U_{SG}/\sigma$). This scaled P_m term is a combination of viscous, inertia, surface tension, and gravitational forces. To the author's knowledge, S_i has not been reported in the bubble size literature; therefore, in the current work the S_i is referred to as *Breakage Budget*. Attempts were made to validate Equation

4-4 using experimental data from the literature. Mouza et al. (2005) studied the effect of liquid properties on characteristics of bubble size distribution. The Sauter mean diameter data from this study were used to further evaluate the bubble size scaling law in the present work. Figure 4-8 shows that the data from Mouza et al. (2005) is in excellent agreement with Equation 4-4, supporting the initial hypothesis that the unsteady mechanical power to a batch bubble column operating in heterogeneous regime scales the Sauter mean diameter.

Since Equation 4-4 was not able to predict the bubble size in the homogenous regime, a new parameter space was considered for analysis. To scale the bubble size in the homogenous regime, the proposed parameter space was comprised of the sparger pore size (r_{sp}), liquid properties (i.e. surface tension-σ, viscosity-μ_L, and liquid density-ρ_L), gas superficial velocity, and external field force (g). Homogeneous bubbly flow is characterized by the absence of breakage and coalescence and a Gaussian BSD; therefore, any attempt to scale the bubble size should include the effect of pore size since it sets the initial bubble size.

Table 4-4 gives the non-dimensional terms as well as the proposed correlation for scaling the Sauter mean diameter.

Table 4-4. Dimensionless terms and the correlation for bubble size scaling in homogeneous bubbly flow.

Froude Number	$Fr = \sqrt{U_{SG}/gd_{32}}$	Equation 4-5
Weber Number	$We = d_{32}U_{SG}^2 g/\sigma$	Equation 4-6
Reynolds Number	$Re = \rho_L U_{SG} d_{32}/\mu$	Equation 4-7
	$d_{32}/2r_p = 7.81 \times 10^5 (Fr^{1.8} We^{-1.7} Re^{0.7})^{-7.362}$	Equation 4-8

Figure 4-9 validates the correlation for predicting bubble size (d_{32}) in homogeneous regime (see

$d322rp=7.81\times105Fr1.8We-1.7Re0.7-7.362$	Equation 4-8

) against experimental bubble size data. Results show that the proposed correlation is able to predict the bubble size in water; however, there is a slight deviation in the data from aqueous solutions of glycerin. This deviation is due to early transition of the operation regime from homogenous bubbly flow to churn turbulent. Increasing the viscosity accelerates the regime transition; therefore, in Figure 4-9 the aqueous solutions of glycerin exhibit some deviations from the water data. It is noteworthy that in

$d322rp=7.81\times105Fr1.8We-1.7Re0.7-7.362$	Equation 4-8

the power exponents where found following the recommendation from Kazakis et al. (2008). Kazakis et al. (2008) also argues that the sparger material effects correlations of this type due to the sensitivity of bubble size to pore dimensions in homogeneous bubbly flow. This is interesting to see that Figure 4-9 scales the bubble size data in water and there are inconsistencies with data from glycerin solutions. It is worth mentioning that for water within the range tested, Sauter mean diameter and bubble size distribution exhibit the homogenous characteristics (i.e. Sauter mean diameter decreases with increasing the gas superficial velocity and BSD is nearly Gaussian) while with the glycerin data only the bubble size distribution has homogenous characteristics. From this it can be concluded that any attempt for regime demarcation requires three different inspections namely; visual inspection, Sauter mean diameter trend with gas superficial velocity, and shape of bubble size distribution.

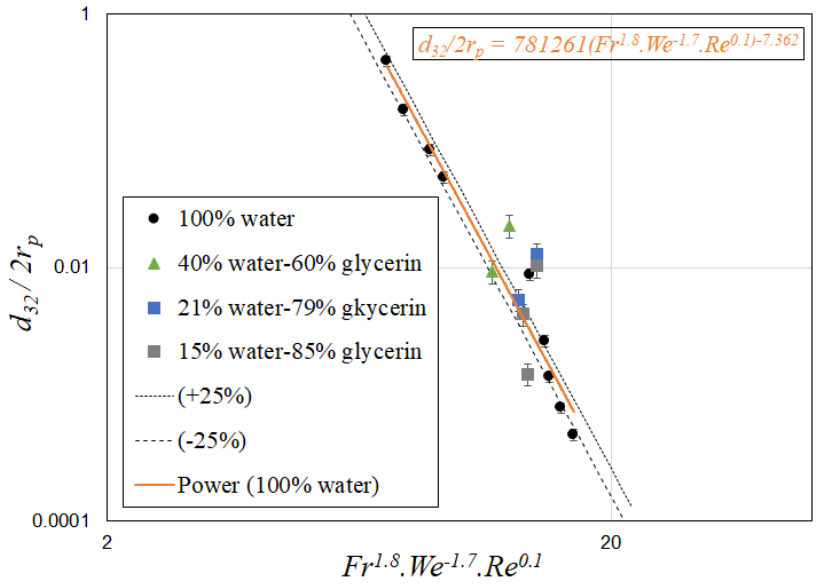

Figure 4-9. An emperical correlation for bubble size scaling in the homogenous regime using dimensional analysis.

4.4 Void Fraction Scaling

This section presents the results of void fraction characterization the current bubble column setup. Same test conditions from Table 4-1 were repeated to characterize the void fraction in the current work. Figure 4-10 presents the void fraction measurement, which the uncertainty associated with the void fraction measurement was less than 2% of the measured values. This uncertainty was calculated from the standard deviation of the output voltage from the pressure transducer, for more details on the void fraction measurement the interested reader is referred to Chapter 3. It was argued in the previous section that from results of bubble size measurement in aqueous solutions of glycerin regime transition from homogeneous to heterogeneous can be inspected from higher order statistics and probability density function. Here, regime transition at similar gas superficial velocity (U_{SG} = 28mm/s) can be observed in void fraction data. Figure 4-10 shows that above U_{SG} = 28mm/s void fraction (ε) deviates from

the linear trend with gas superficial velocity, which indicates that the homogeneous regime was no longer present.

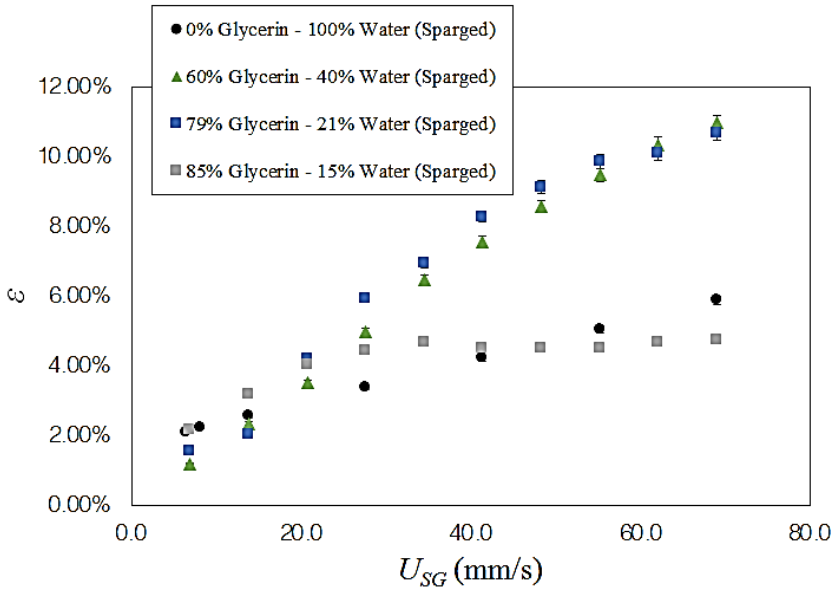

Figure 4-10. Effect of gas superficial velocity and liquid phase properties on void fraction in a static-sparged bubble column.

It is interesting to see that the most viscous solution (85% glycerin, 15% water) shows a very different trend with gas superficial velocity. Raw images at the waterbox (test section, six column diameters-6D downstream of the sparger) show that with increasing the gas superficial velocity above U_{SG} = ~28 mm/s, this most viscous condition has frequent coalescence events in the bubble column cause the physical behavior of the bubble column to change from a bubble flow to slug flow. Large slugs travel significantly faster than the small bubbles and reduces the average residence time of the gas phase within the liquid; therefore, the void fraction levels flatten out above U_{SG} = 28mm/s.

A parameter space was identified via careful inspection of the experimental setup in an attempt to formulate a correlation to predict the void fraction using dimensional analysis,

which would help identify the governing physics. It was concluded that the parameter space should be comprise of liquid properties (i.e. surface tension, viscosity, and density), external body force (i.e. gravity), bubble size (d_{32}) and the gas flow rate (i.e. gas superficial velocity). Table 4-5 gives the non-dimensional terms as well as the correlation for scaling the void fraction. The effect of gas superficial velocity and gravity were scaled using the Froude number (*Fr*), Archimedes number (*Ar*), and Evotos number (*Eo*). Mouza et al. (2005), Kazakis et al. (2007), and Anastasiou et al. (2010) suggest a power-law functional from for a non-dimensional correlation that scales the void fraction given by Equation 4-9. In the current work, it was assumed that the bubbles are traveling with a terminal velocity (see Figure 4-11); therefore, the drag force ($F_{drag} \sim \rho_L d_{32}^2 U_b^2$) was balanced with buoyancy force ($F_{buoyancy} \sim \rho_L g d_{32}^3$). This assumption assists in forming a relationship between bubble size and bubble velocity ($U_b^2 \sim g d_{32}$). It is known that the void fraction is the ratio of gas superficial velocity to the bubble velocity ($\varepsilon = U_{SG}/U_b$); therefore, the void fraction is proportional to $U_{SG}/(g d_{32})^{0.5}$ and the exponents in Equation 4-9 (i.e. X, Ψ, and Ω) can be found analytically from Equation 4-10. Note that the Sauter mean diameter in Equation 4-10 comes from the bubble size scaling correlation in Equation 4-4.

$$\varepsilon \cong Fr^{X} Ar^{\Psi} Eo^{\Omega} \qquad \text{Equation 4-9}$$

$$\frac{U_{SG}}{\sqrt{g d_{32}}} \cong Fr^{X} Ar^{\Psi} Eo^{\Omega} \qquad \text{Equation 4-10}$$

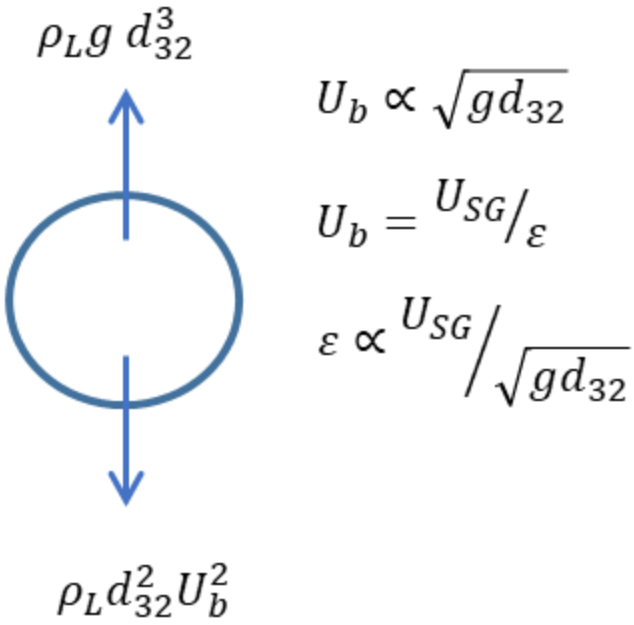

Figure 4-11. Schematic of the primary acting forces on a single bubble at terminal velocity.

Figure 4-12 shows the results of this proposed void fraction scaling using the aforementioned dimensionless terms. Figure 4-12 shows that the proposed correlation (see Equation 4-14) was able to successfully scale the void fraction within the homogenous regime (water). From Figure 4-12 one could see that Equation 4-14 was only able to predict the void fraction in pure water, it was argued in the previous section that data from water tests are in the homogenous regime. Therefore, Equation 4-14 cannot be used for the rest of test conditions in the current study because those conditions are in the heterogeneous regime. Equation 4-15 gives a functional form between the non-dimensional terms (Froude number, Archimedes number, and Evotos numebr) that scales the void fraction in the heterogeneous regime. Figure 4-13 shows the void fraction measurements in the heterogeneous regime from the current work against the proposed correlation (Equation 4-15). These results show that Equation 4-15 is able to provide a very good estimate of the void fraction within the heterogeneous regime.

Table 4-5. Dimensionless terms and the correlation for void fraction scaling.

Froude Number	$Fr = \frac{U_{SG}}{\sqrt{g d_{32}}}$	Equation 4-11
Archimedes Number	$Ar = \frac{{d_{32}}^3 \rho_L^2 g}{\mu_L^2}$	Equation 4-12
Evotos Number	$Eo = \frac{{d_{32}}^2 \rho_L g}{\sigma}$	Equation 4-13
$\varepsilon = 0.0278(Fr^{1.117} Ar^{0.1} Eo^{-0.032})^{0.46}$		Equation 4-14
$\varepsilon = 0.035(Fr^{1.117} Ar^{0.1} Eo^{-0.032})^{0.75}$		Equation 4-15

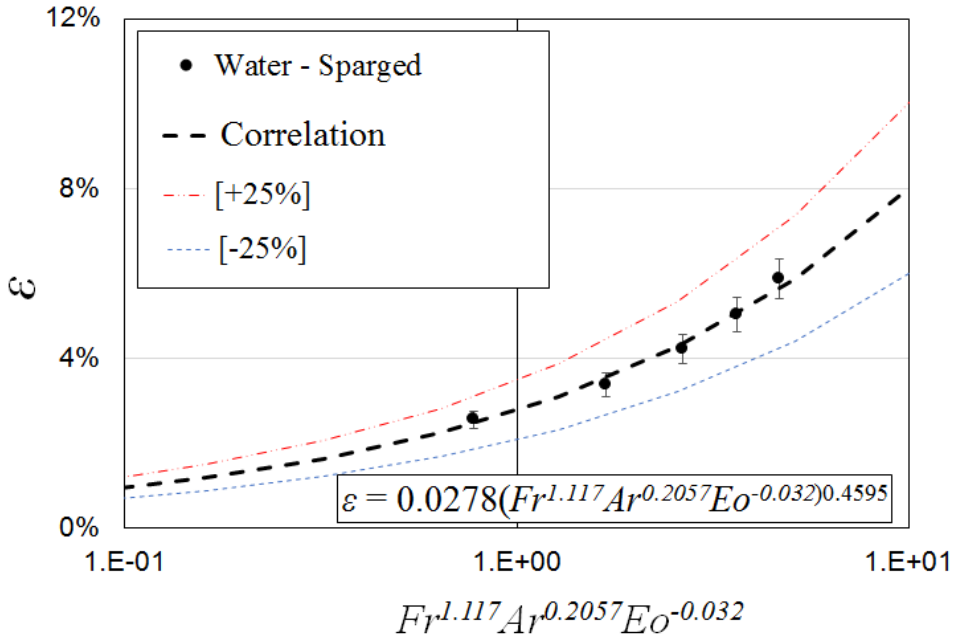

Figure 4-12. A correlation for scaling the void fraction in the homogenous regime.

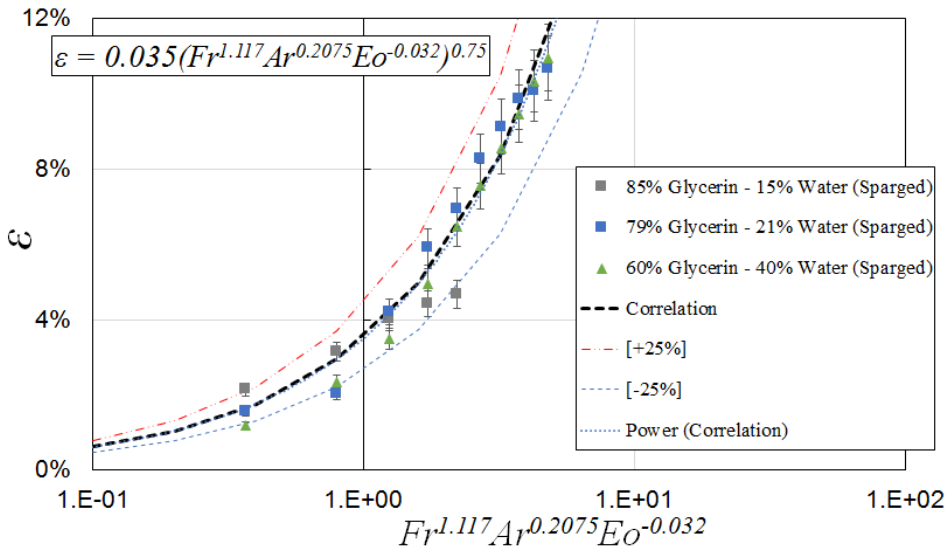

Figure 4-13. A correlation for scaling the void fraction in heterogeneous regime.

4.5 Conclusions

This chapter presents a systematic study of bubble size and void fraction in a batch bubble column with a pore sparger. The measurements were carried out in the homogenous and the heterogeneous operation regimes. The physical behavior of the bubble column changes from homogenous to heterogeneous regime; therefore, it is appropriate to present any measurements with consideration of the operation regime. Current work shows that the probability density function of the bubble size distribution exhibits near Gaussian characteristics in the homogenous regime. In the heterogeneous regime the shear breakage sets the bubble size; therefore, the distribution becomes mono-dispersed and the probability density function has a "spike" shape (log-normal distribution). Aqueous solutions of glycerin with different concentrations were used to test the effect of liquid properties on operation regime. Results showed that increasing the viscosity enhances the regime transition from homogenous

to heterogeneous by allowing the formation of larger bubble as well as bubble interaction (i.e. breakage and coalescence). Bubble size measurements were carried out in both operation regimes. In the homogenous regime the characteristic bubble size (i.e. Sauter mean diameter) shows strong dependency on the sparger characteristics and injection condition due to the absence of breakage and coalescence. In the heterogeneous regime experimental data exhibits a strong correlation between the Sauter mean diameter and specific input power (per unit mass). Dimensional analysis was used to propose a correlation between the scaled bubble size and the scaled specific input power. This correlation was validated by changing the liquid properties as well as comparing with experimental data from the literature. Void fraction was also measured in both the homogenous and heterogeneous regimes. As expected the trend between void fraction and gas superficial velocity was dependent on the operation regime. In the homogeneous regime there was a linear relationship between the void fraction and gas superficial velocity, which became non-linear after transition to the heterogeneous regime. Using correlations from literature that were modified using physical reasoning given the scaled bubble sizes, the void fraction was successfully scaled for the measurement conditions tested in the current study (see Table 4-1).

CHAPTER V

EFFECT OF VERTICAL VIBRATION ON BUBBLE SIZE AND VOID FRACITON

5.1 Introduction

Bubble columns are frequently used as contact reactors in chemical processing, bio-chemical applications and metallurgical applications due to their simplicity (e.g., no moving parts), low operation cost and high efficiency at heat and mass transfer. Design and scale up of a bubble column relies on characterization of transport coefficients, which are sensitive to the bubble size and spatial distribution (local void fraction). Relative velocity between phases coupled with nonhomogeneous distributions has significantly limited the ability to apply laboratory insights to industrial applications. This is due in part to the fact that bubble size is frequently characterized with a single length scale (commonly the Sauter mean diameter, d_{32}), which fails to capture details of the size distribution. Thus, the current work aims to characterize the bubble size distribution (BSD) and its dependence on bubble column conditions via examination of the probability density function (PDF) and higher order statistics.

The physical behavior of a gas-liquid system has been described by operation regime, and conveys the governing forces that control the characteristics of the system. BSDs are heavily dependent on the operating regime (Kantarci et al., 2005). The current work does not aim to provide an analysis of characteristic length scales over a range of flow regimes, but

rather focuses on relatively low volumetric injection fluxes to assess the sensitivity of the distribution to a range of parameters. In the current study, it is hypothesized that the size distribution characteristics can provide a robust means of identifying regime transitions.

Use of a single length scale would be appropriate for characterizing the bubble size if the bubble size/shape was readily represented with a single length (e.g., spherical bubbles) and the shape of the size distribution was constant. Many researchers implicitly make this assumption without examining the higher order statistics, primarily due to the challenge of generating a sufficiently large sample size to accurately estimate the higher order statistics. Sauter mean diameter (d_{32}) is the most widely used characteristic length in bubble column studies (e.g., Krishna & Ellenberger, 2000; Oliviera & Ni, 2001; Waghmare et al., 2008; Hur et al., 2013). Sauter mean diameter (see, Equation 3-4), is the ratio of the representative bubble volume to the bubble surface area, which is a weighted average. A common alternative to d_{32} is a probabilistic approach, which uses the mean of the PDF of the bubble chord length (Clark and Turton, 1988; Wu et al., 2008; Xue et al., 2008). This method is most common when the measurements are acquired with electrical impedance/resistivity (Van Der Welle, 1985; George et al., 2000; Makiharju et al., 2013), wire mesh (Manera et al., 2006; Omebere-Iyari et al., 2008) or optical point probes (Youssef et al., 2009), which can only provide a single length scale but a relatively large sample size. These measurements are sensitive to the bubble size, velocity, shape and orientation as well as the sensor design (e.g., response from optical/impedance probes are unique to the sensor design and fluid properties). Consequently, these measurements are unable to provide details about the shape due to the required ad hoc assumptions to relate the signals to a bubble size.

The current work uses bubble imaging of a large bubble population to produce PDFs that are not dependent on the assumption that the bubbles are spherical. These PDFs are then analyzed to identify an alternative length scale based on the peak in the PDF, which is then used along with the Sauter mean diameter to test sensitivity of the scales to operation conditions. In addition, higher order statistics from the PDFs are reported.

5.2 Static Bubble Column

5.2.1 Bubble size measurement and scaling

A subset of conditions were tested to evaluate the repeatability of the experiment, which also provided insight into the target measurement location. Three air volumetric flowrates (Q_m) were selected that produced superficial gas velocities (volume averaged phase velocity; $U_{SG} = Q_c/A_{cs}$) of 6.9 mm/s, 27.6 mm/s and 55.1 mm/s. Under these conditions, the bubble column was operating within the poly-dispersed bubbly regime, which is true throughout the current chapter. Each condition was repeated at least ten times with a minimum of 3000 bubbles sampled per condition. Results from these tests are shown in Figure 5-1 with the Sauter mean diameter (d_{32}) plotted versus the vertical distance above the injection location (Z) scaled with the column diameter (D). Error bars represent the standard deviation of the mean for each condition. Similar to Akita & Yoshida (1974), these results exhibit a decrease in d_{32} with increasing gas flux for locations sufficiently far from the injection location. Note that increasing superficial velocity is known to increase or decrease (Fukuma et al., 1987; Saxena et al., 1990) bubble size due to its complex role in manipulating the bubble formation process and liquid velocity field. Figure 5-1 also indicates that beyond $Z \sim 4D$ the bubble size remains constant within the measurement uncertainty. Consequently, the current work focuses

on bubble measurements in the range of $4 < Z/D < 6$ to minimize the influence of the injection method. It is noteworthy that the minimum height above the injector will be sensitive to the injection condition, which will be discussed subsequently. Furthermore, inspection of the images within the target height range showed minimal influence of bubble breakup and/or coalescence.

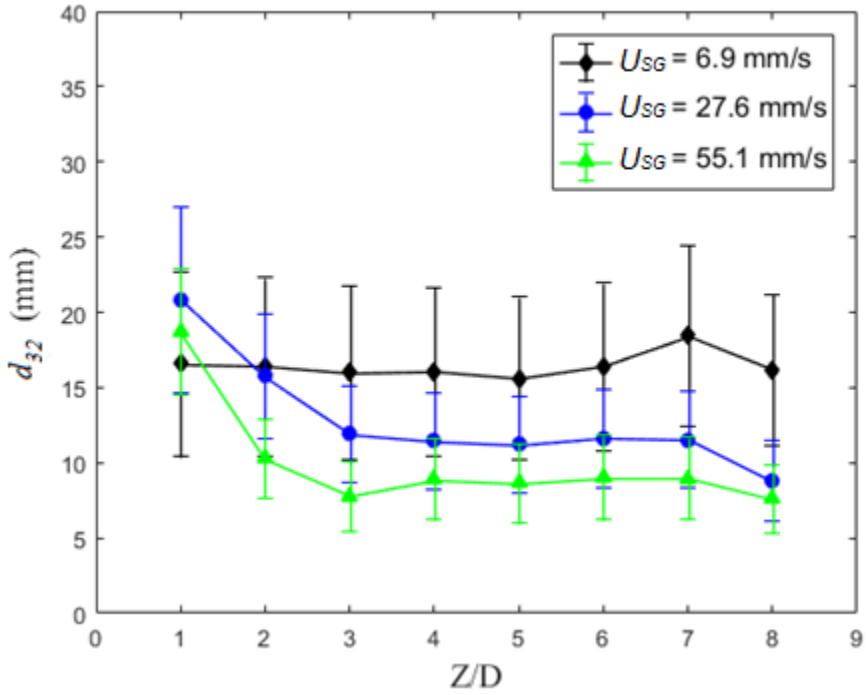

Figure 5-1. Sauter mean diameter (d_{32}) plotted versus the scaled vertical distance above the injection location. Each data point is the average of 10 repetitions, and the error bars are the standard deviation of the mean (P_{me} = 600 kPa, T_c = 21 ± 1 °C, D = 102 mm, d_{inj} = 1.6 mm).

While Sauter mean diameter (d_{32}) is widely used as the characteristic bubble length scale, bubble size distributions are often poly-dispersed in a single point gas injection scenario, which makes a single length scale insufficient to characterize the distribution. Consequently, in the current work the PDF was examined to identify a length scale(s) that represents the size

distribution. The PDFs generated from counting at least 10,000 bubbles per condition is provided in Figure 5-2 (PDF of conditions shown in Figure 5-1, though limited to $4 < Z/D < 6$). Here there is a noticeable shift between the PDF peaks and d_{32}. Consequently, the most frequent bubble size (d_{mf}) was defined as the size corresponding to the peak in the PDF (mode). These representative conditions illustrate the different behavior between d_{32} and d_{mf}, with d_{mf} being significantly smaller than d_{32} over the range tested. In addition, while there is a noticeable dependence between d_{32} and the volumetric gas flux, d_{mf} appears to have negligible variation. It is worth mentioning that the high-pass filter forces the left leg of PDFs to be zero when $A_{proj} < 2$ mm^2, this minimum area translates into a minimum bubble size of $d_b < 1.6$ mm.

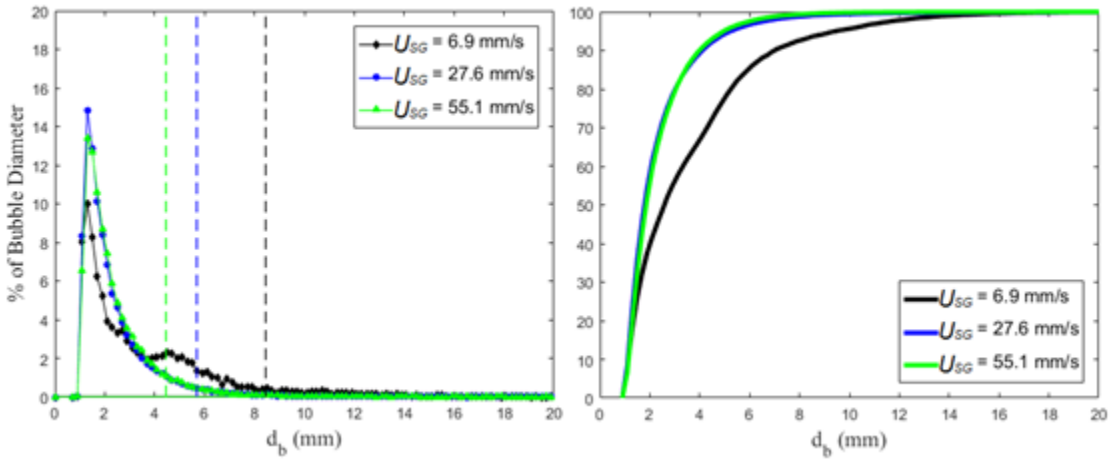

Figure 5-2. (**a**) Probability density functions (PDF) and (b) cumulative density function (CDF) of bubble size (d_b) for the same conditions shown in Figure 5-1. The PDF/CDF for each U_{SG} was determined from counting at least 10,000 bubbles. Dashed lines in (**a**) correspond to the d_{32} values for each condition (P_{me} = 600 kPa, T_c = 21 ± 1 °C, D = 102 mm, d_{inj} = 1.6 mm).

The obvious question is what accounts for the difference between d_{32} and d_{mf}. As seen in Equation 3-4, d_{32} is a weighted average; thus, it is biased towards the largest bubbles

generated due to the diameters being raised to powers before summing. Consequently, the influence of a large quantity of small bubbles has a weaker impact on d_{32} than a few large bubbles. This can be seen in the cumulative density function (CDF) for these conditions provided in Figure 5-2b. The lowest flow rate exhibits significantly larger bubbles (e.g., 23% of bubbles are larger than 10 mm) than the highest injection flux (<5% of bubbles are larger than 10 mm), thus illustrating how these three conditions with nearly identical d_{mf} values generate measurable deviations in d_{32}.

A comprehensive examination of the variation between d_{32} and d_{mf} is provided in Figure 5-3 with the most frequent bubble size plotted versus Sauter mean diameter for all test conditions. For reference, a dashed line corresponding to $d_{mf} = d_{32}$ has been included, which shows that for all conditions d_{mf} is smaller than d_{32}. The majority of the data points collapse on a curve that appears to asymptote to $d_{mf} \approx 2$ mm. The uniformity of these bubbles and insensitivity to the injection condition suggests that they are being generated by the flow-field, which the most likely mechanism would be the turbulent motions generated by the bubble wakes. This would suggest that d_{mf} is a length scale associated with the velocity fluctuations within the flow-field. This conjecture is supported by the known Reynolds number dependence of bubble wakes. Bubble diameter (d_{mf}) based Reynolds numbers ($Re = V_b \cdot d_{mf}/\nu$, where V_b is the mean bubble rise velocity that is nominally U_{SG}/α, α is the void fraction and ν is the kinematic viscosity) tested ranged between 590 and 11,000. It is known (Brennen, 2005) that starting at a Reynolds number of ~500, vortices begin to be shed from bubbles and the flow-field becomes quite unsteady until ~1000. Starting at $Re \sim 1000$, a boundary layer forms on the bubble with a laminar near-wake region. However, the shear layer spreads resulting in a

turbulent far-wake region. This behavior exists until $Re \sim 3\times10^5$, which is beyond the range of bubbles observed in the current study.

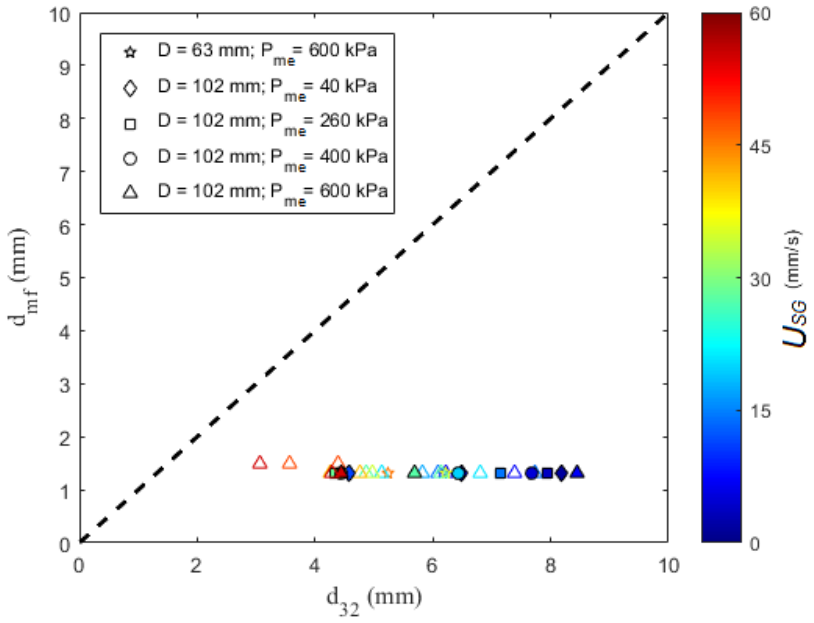

Figure 5-3. Comparison between the most frequent bubble size (d_{mf}) and the Sauter mean diameter (d_{32}). The dashed line corresponds to $d_{mf} = d_{32}$. Open and closed symbols correspond d_{inj} = 0.8 and 1.6 mm, respectively.

Similar to the Chapter 4 it is hypothesized that the turbulent motion is fed from input power given to the liquid phase from the gas injection. Sauter mean diameter was measured over a range of gas superficial velocities (U_{SG}=1.4m/s to 55m/s) to test the relationship between bubble size and specific input power ($P_m = gU_{SG}$). Figure 5-4 shows the Suater mean diameter versus the specific input power. Hinze (1955) and Lewis & Davidson (1982) suggest a linear correlation between bubble size and specific input power. Figure 5-4 also shows the predicted bubble size from Equation 4-3 (solid line) against the measured bubble size. There is an excellent agreement between the measurements and the proposed scaling law for $P_m >$ 0.06W/kg. It is noteworthy that Equation 4-3 was linear function between scaled bubble size

and scaled specific input power produced by dimensional analysis. The proportionality coefficient (k = 1.7) in Equation 4-3 was selected based on the recommendation of Lewis & Davidson (1982) for bubble size under shear breakage. It was also attempted to find the unknown function in Equation 4-2 to establish a correlation between scaled bubble size and scaled specific input power. Figure 5-5 uses the non-dimensional coordinates from Equation 4-2, and results show that the bubble size data collapsed well with a power-law correlation given in Equation 5-1.

$$\frac{\rho_L d_{32}\sigma}{\mu^2} = 400 \times \left(\frac{P_m \mu^5}{\rho_L \sigma^4}\right)^{-0.234} \qquad \text{Equation 5-1}$$

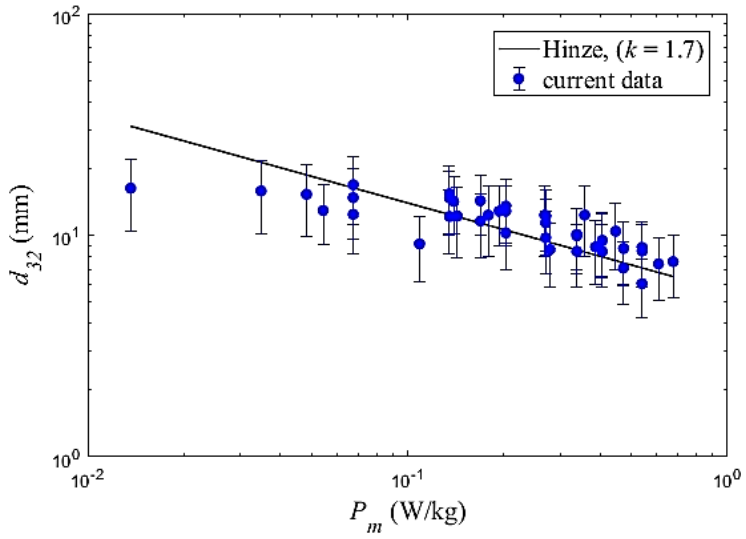

Figure 5-4. The bubble Sauter mean diameter (d_{32}) in static test conditions plotted versus the input power (Equation 4-3). These results are compared against Hinze (1955) suggestion for scaling the maximum stable bubble size.

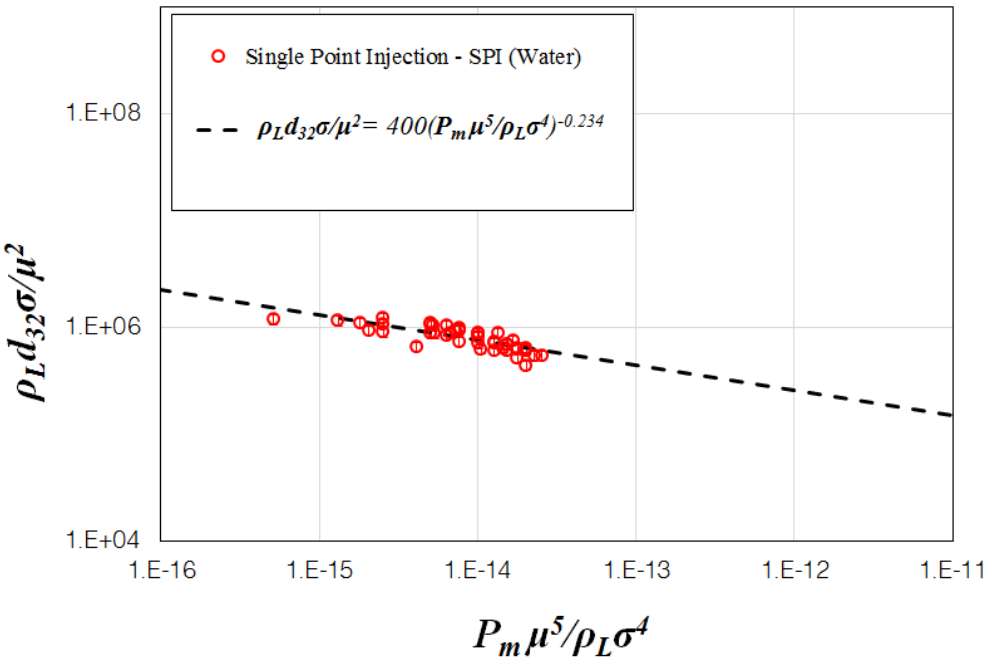

Figure 5-5. A power-law correlation between the scaled bubble size and the scaled specific input power (Equation 5-1) in static test conditions.

There are four data points in Figure 5-4 (P_m > 0.06W/kg) that are at lower Reynolds number in comparison to the rest of the measurements (590 < *Re* < 2300). Of note, a bimodal distribution is observed for these outlier cases, which are shown in Figure 5-6. This is a curious observation given that in this range the bubble wakes are unsteady with periodic shedding of vortex rings. The Strouhal number for *Re* ~ 1000 is ~0.3 (Brennen, 2005), which the shedding from a 1.6 mm diameter bubble (nominal d_{mf} for conditions in Figure 5-6) would produce an 5.2 mm long wavelength. This is comparable to the size of the second peak in the distribution.

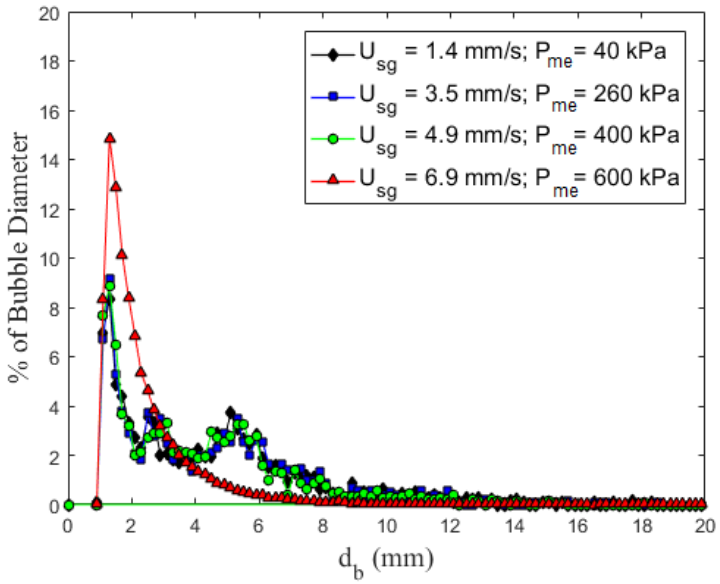

Figure 5-6. PDFs from bimodal conditions (U_{SG} = 1.4, 3.5, 4.9 and 6.9 mm/s). While the d_{mf} is still determined from the smaller bubbles, there is a second weaker peak near 5 mm (D = 102 mm; d_{inj} = 1.6 mm).

Assuming that the PDF shape changes are related to regime transitions, higher order statistics (i.e., standard deviation, skewness and kurtosis) for a subset of conditions are presented in the conclusions of the parametric study. The use of both d_{mf} and d_{32} are explored in more detail in the following section with a parametric study to assess the sensitivity to individual control parameters. Of note, over the conditions explored d_{mf} (mode of PDF) is similar to d_{10}. Given that the PDFs are skewed to larger bubbles, d_{10} is generally larger than d_{mf} and smaller than d_{32}. While the behaviors are similar, they carry distinctly different physical information. While not explored in the current study, if the Reynolds number based on bubble diameter decreased below ~500, it is expected that $d_{mf} > d_{10}$. This is contrary to the current work where $d_{mf} < d_{10}$ for all conditions.

5.2.2 Effect of gas injection rate

The volumetric flowrate of gas within the column (Q_c) is determined from the mass flowrate into the column ($\dot{m}$), column pressure (P_c) and column temperature (T_c). In the current experiment, the column temperature and pressure were held nearly constant at $T_c = 21 \pm 1$ °C and atmospheric pressure (plus hydrostatic pressure), respectively. Consequently, the mass flow rate was the only parameter varied, which was controlled with a combination of meter pressure (P_{me}) and metered volumetric flow rate (Q_m). Figure 5-7 compares d_{32} and d_{mf} dependence on the superficial velocity (U_{SG}). Four different meter gauge pressures (P_{me} = 40, 260, 400 and 600 kPa) were used to achieve $1.4 \leq U_{SG} \leq 55$ mm/s. Sauter mean diameter shows good collapse over most of the test conditions, but there is some deviation observed with the P_{me} = 40 kPa condition. Conversely, d_{mf} collapses at all superficial velocities and show some deviation at lower fluxes.

The only significant outlier condition from Figure 5-7a is the P_{me} = 40 kPa with U_{SG} = 11.1 mm/s condition. Images at the injection location compare this condition with other low mass flux conditions in Figure 5-8. Here it is apparent that the initial bubble size distribution is significantly different compared to the other low mass flux conditions. The Reynolds number based on the injector tube diameter for the outlier condition was 4800, which is at the transition between laminar and turbulent flow in a pipe. This makes the airflow at this superficial gas velocity transitional, which transitional flows are extremely sensitive to the operating condition. The data suggests that the lower metering pressure makes the initial bubble formation more sensitive to the inlet airflow condition. The metering pressure could impact bubble detachment from the injection tube since the upstream pressure could modify the bubble

shape during expansion (especially with transitional flow). In addition, the initial bubble size distribution as well as breakup and coalescence behaviors are sensitive to the density of the gas (Hecht et al., 2015).

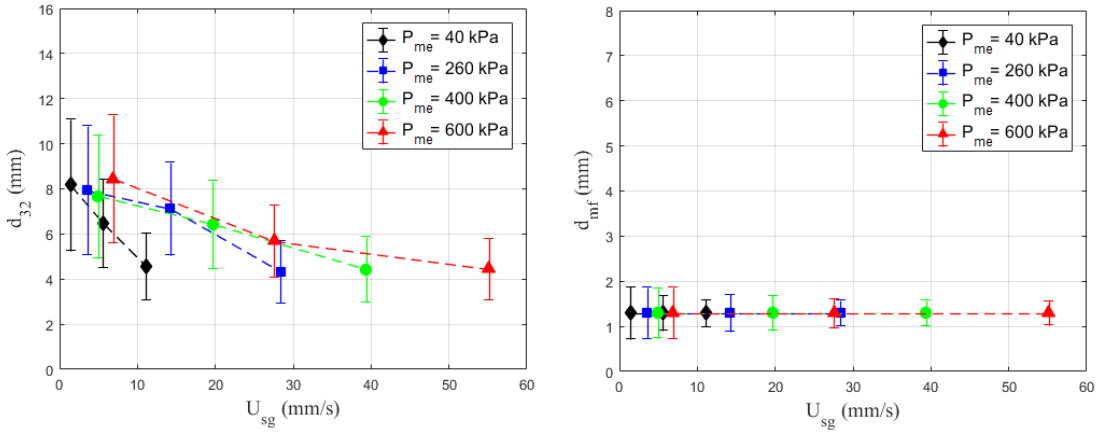

Figure 5-7. (**a**) Sauter mean diameter and (**b**) most frequent bubble size plotted versus the superficial gas velocity. Error bars represent the standard deviation for the given condition (D = 102 mm; d_{inj} = 1.6 mm; T_c = 21 ± 1 °C).

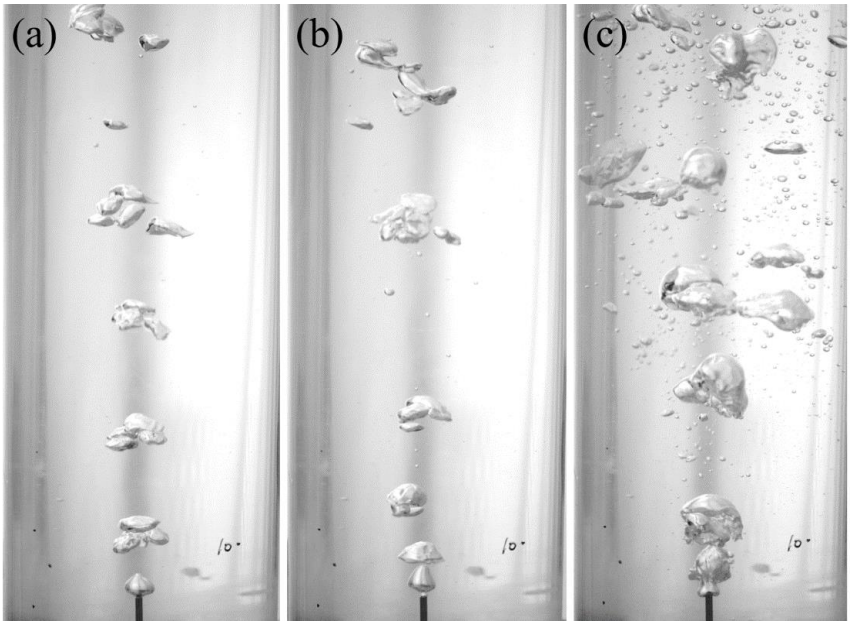

Figure 5-8. Still frames in the D = 102 mm column with d_{inj} = 1.6 mm with an injection condition of (**a**) P_{me} = 260 kPa, U_{SG} = 3.5 mm/s; (**b**) P_{me} = 600 kPa, U_{SG} = 6.9 mm/s and (**c**) P_{me} = 40 kPa, U_{SG} = 11.1 mm/s.

5.2.3 Effect of injector tube angle

The experimental setup had the injector tube positioned such that it was pointed upward and aligned with gravity. However, the setup made fine adjustments to the injector tube orientation difficult once installed. Thus, testing was performed to assess the sensitivity of the BSD to injector orientation. Here, two different injector orientations were tested, 45° and 90° (vertical, design condition) measured from horizontal with D = 102 mm and d_{inj} = 0.8 mm. Results for both d_{mf} and d_{32} are provided in Figure 5-9 at each injector tube angle. These results show that d_{mf} has negligible variation even with the significant misalignment. Conversely, d_{32} has a measurable decrease at 45° relative to the 90° condition. There are two potential mechanisms responsible for this deviation; (i) the misalignment between gravity (buoyancy force) and the bubble wake where the turbulent production is located and/or (ii) increased influence of wall effects as the initial bubbles were directed into the column wall where the

stress distribution will deviate from the core of the column. The wall effects are mostly likely for the current work since the decrease in bubble size suggests a higher shear stress.

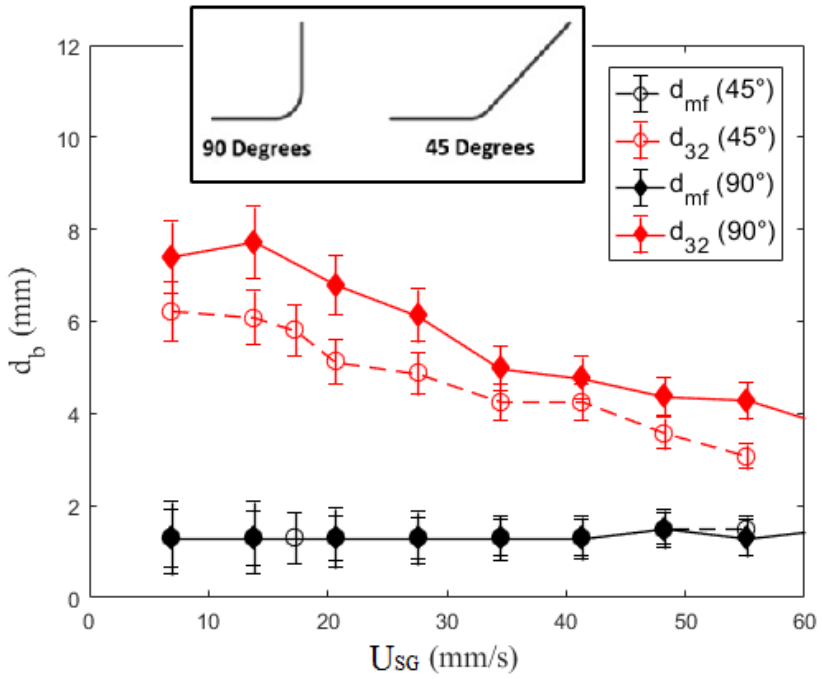

Figure 5-9. Bubble sizes (d_{mf} and d_{32}) plotted versus the superficial gas velocity with the injector tube angled at either 45° or 90° from horizontal (see insert sketch) (D = 102 mm; d_{inj} = 0.8 mm; P_{me} = 600 kPa).

5.2.4 Effect of injector tube diameter

The injection tube diameter is one of the key parameters that modifies the BSD, especially in the homogenous regime by effecting the bubble formation process. It is commonly accepted that bubble chord (vertical length from tube to top of bubble) at detachment is on the same order of magnitude as the injector tube diameter (Kulkarani & Joshi, 2005), which is supported with observations that decreasing orifice diameter decreases the bubble size (Basha et al., 2015). This is because at the time of detachment the surface tension forces are balanced with hydrostatic pressure and buoyancy forces, where the outer diameter

of the injector sets the contact angle (Liow, 2000). Thus, the injector size has a significant impact on the initial bubble size, which is known to affect the flow pattern (Cheng et al., 2002) and consequently the flow regime as discussed above.

Given the above observations, the current study examined the effect of the injector diameter on the BSD with two injector sizes (d_{inj} = 0.8 and 1.6 mm). Based on past observations (Wilkinson et al., 1992), it is expected that increasing the injector tube diameter will increase the bubble size. Results for both d_{mf} and d_{32} are provided in Figure 5-10. The most frequent bubble size shows negligible variation between the injector tube diameters. This is consistent with the turbulent scales within the wakes setting d_{mf}. The Sauter mean diameter trend is nearly identical between tube diameters, but the curve for the smaller tube is shifted downward slightly. This supports previous observations since it exhibits a dependence on the tube diameter, but the tube diameter was not varied by an order of magnitude resulting in the bubble size having a relatively small variation.

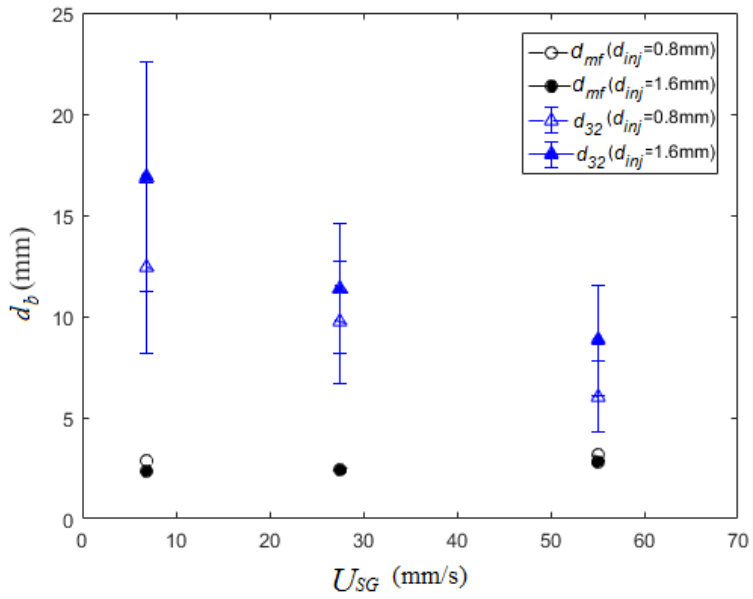

Figure 5-10. Bubble sizes (d_{mf} and d_{32}) plotted versus the superficial gas velocity varying the injector tube diameter (D = 102 mm; P_{me} = 600 kPa).

It is instructive to examine the PDFs from these conditions to determine how the tube diameter is modifying the BSD. Figure 5-11 provides the PDF for two of the volumetric flow rates tested with each of the injector tube diameters. These two representative conditions (U_{SG} = 6.9 mm/s produced PDFs with and without an apparent second peak) demonstrate that the PDFs are nearly identical between the two injectors. This explains why d_{mf} is nearly identical between the two injector diameters, but not the shift in d_{32}. The difference between the PDFs is that the larger injector tube diameters produced larger maximum sized bubbles (i.e., larger tube diameter produces a longer tail in the PDFs). Maximum measured bubble sizes (d_{max}) for U_{SG} = 6.9, 27.6 and 55.1 mm/s are provided in Table 5-1. This shows that the smaller bubble tube diameter produces significantly smaller d_{max} (up to 40% smaller than the large tube). This supports the comments that both length scales are important since while d_{mf} is insensitive to these changes, d_{32} is modified because of these larger bubbles. While d_{32} is sensitive to these

variations, higher order statistics (particularly skewness, a measure the asymmetry of a distribution) should be more sensitive to these variations.

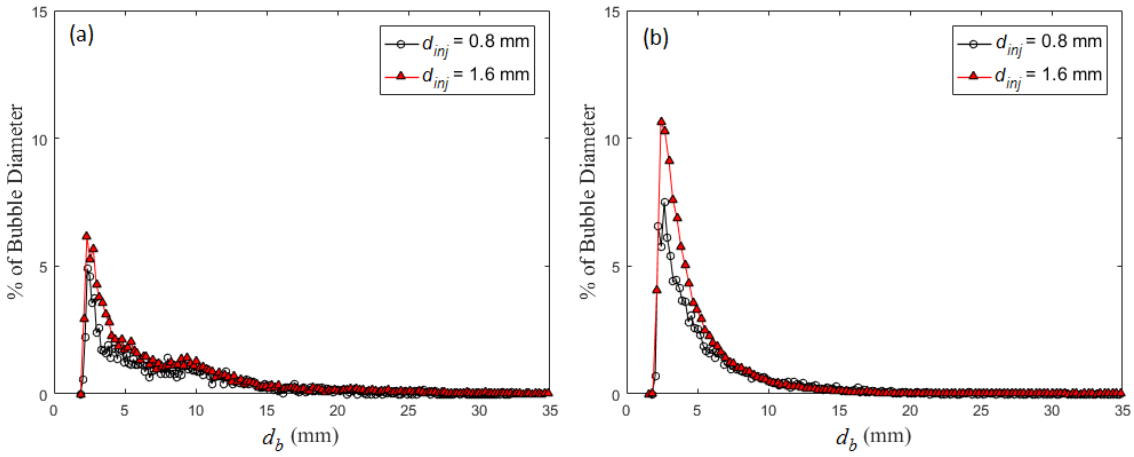

Figure 5-11. Bubble size PDF for the two injector tube diameters (d_{inj} = 0.8 or 1.6 mm) tested at (**a**) U_{SG} = 6.9 mm/s and (**b**) U_{SG} = 27.6 mm/s (D = 102 mm; P_{me} = 600 kPa; T_c = 21 ± 1 °C).

Table 5-1. The maximum measured bubbles size (d_{max}) spanning the flow rates tested with both injector tube diameters

U_{SG} (mm/s)	Maximum Measured Bubble Size (mm)	
	d_{inj} = 0.8 mm	d_{inj} = 1.6 mm
6.9	10.2	11.7
27.6	9.9	16.7
55.1	9.4	15.8

5.2.5 Effect of column diameter

Wall effects play a significant role when the column diameter is below 0.15 m (Wilkinson et al., 1992). This explains the contradictory trends between bubble size and column diameter in the literature (Daly et al., 1992; Koide et al., 1979; Sasaki et al., 2017). These contradictory observations are the product of operation within different flow regimes or transitioning between regimes. In particular, there are a number of studies (Zahradnik et al.,

1997; Sarrafi et al. 1999; Ruzicka et al., 2001) that indicate column diameter has an impact on the transition superficial gas velocity, but currently there is no comprehensive understanding of the influence of column diameter. The current study does not aim to assess the overall impact of column diameter, but does examine variation of the BSD with two different column diameters (D = 63 and 102 mm). Results in Figure 5-12 show no significant deviation for either bubble size measurements between the two column diameters.

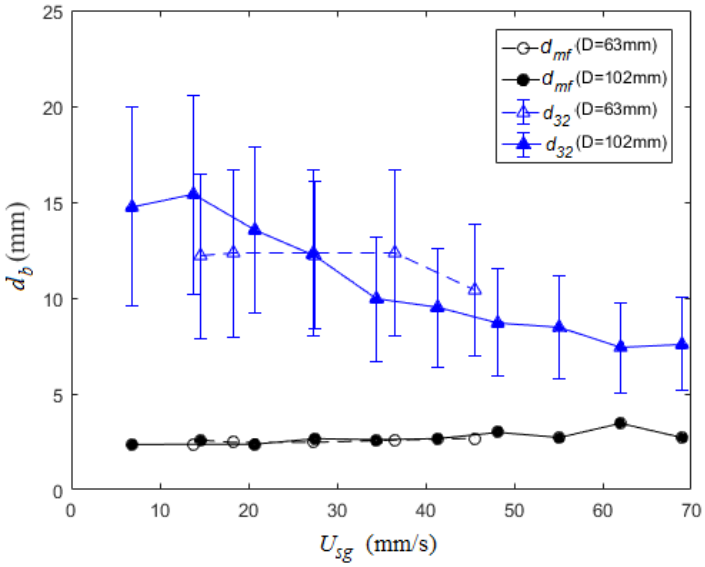

Figure 5-12. Bubble sizes (d_{mf} and d_{32}) plotted versus the superficial gas velocity with different column diameters (d_{inj} = 0.8 mm; P_{me} = 600 kPa).

5.2.6 Higher order statistics

While the parameter space of the current study is insufficient to provide a detailed analysis of higher order statistics (i.e., standard deviation σ, skewness S and kurtosis κ), the available results are provided in Figure 5-13 given the dearth of available data in the literature. Based on the previous observations/discussion, there are a few expected trends in the higher order statistics. In particular, increasing the injector diameter is expected to increase the

skewness given that larger injection tubes generate larger maximum bubbles, which will result in a longer tail in the PDF. This is observed in Figure 5-13c, noting that the open symbols are d_{inj} = 0.8 mm and the closed symbols are d_{inj} = 1.6 mm. Thus focusing on the large column (D = 102 mm) and P_{me} = 600 kPa, the smaller injector tube diameter results in a smaller skewness at a given U_{SG}. The kurtosis (a measure of "tailedness" of a distribution) is provided in Figure 5-13d, which for all conditions the kurtosis is greater than that of a normal distribution (κ = 3). The relatively high kurtosis values indicate the presence of infrequent excessive deviations from the mean. Furthermore, use of the skewness and kurtosis can provide a quantitative measure of the bimodality of the distribution (e.g., Sarle's bimodality coefficient). There is a peak in this bimodality coefficient at a Reynolds number based on the d_{mf} at ~1000. This supports the previous observations that the bimodality could be the product of the transition from the unsteady flow-field between 500 < Re < 1000 and the turbulent far-wake with Strouhal shedding above 1000. Thus, the higher order statistics are a potential means for identifying regime transitions within the column.

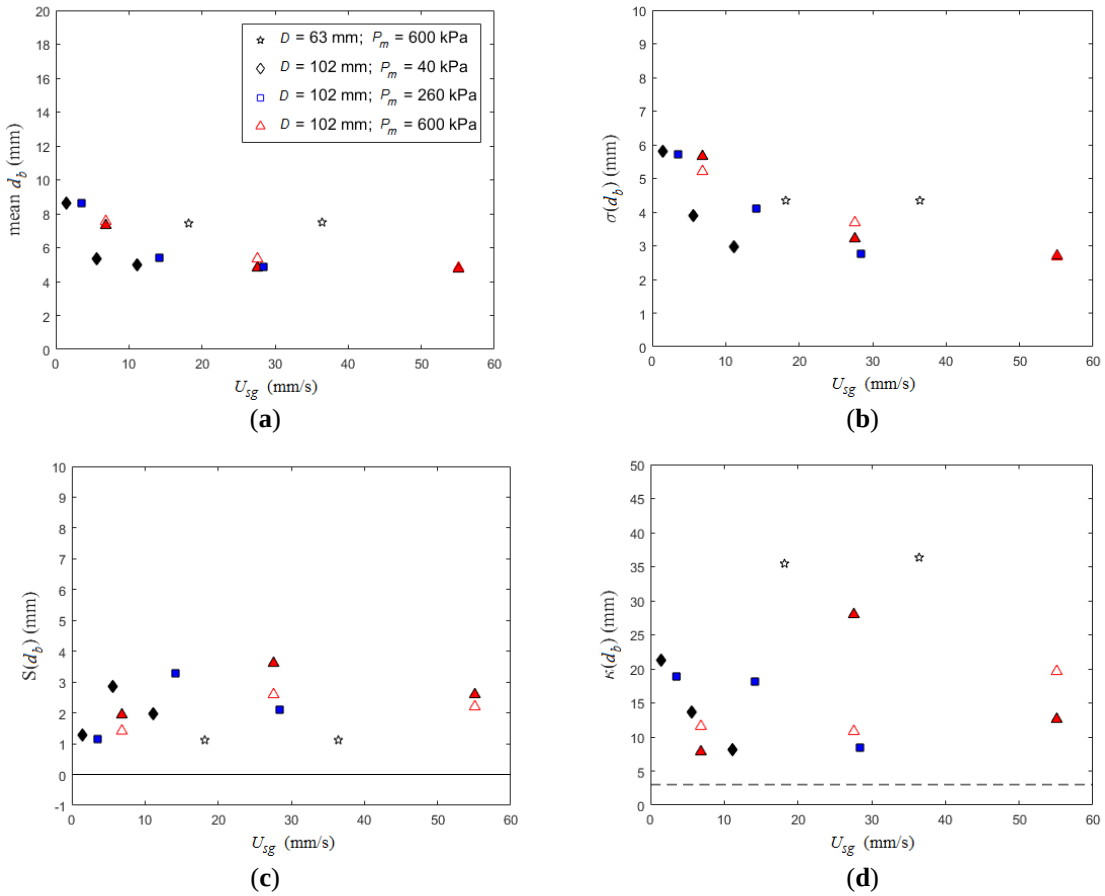

Figure 5-13. Higher order statistics from the PDFs including (a) unweighted mean, (b) standard deviation σ, (c) skewness S and (d) kurtosis κ of the bubble diameter. Dashed line on the kurtosis plot at $\kappa(d_b) = 3$ corresponds to the kurtosis value of a normal distribution. The same legend is used for all plots. Open and closed symbols correspond to $d_{inj} = 0.8$ and 1.6 mm, respectively.

5.3 Vibrating Bubble Column

5.3.1 Bubble size measurement, scaling and statistics

In a static column multiphase parameters are virtually independent of column dimensions when the column aspect ratio is $H/D > 5$ (Wilkinson et al., 1992), where H is the height of liquid (water) in the column. Under vibration, Budzyński et al. (2017) recommends

H/D > 8 to minimized the impact of the liquid surface deformation on void fraction measurements. In this work bubble size distribution was measured within a vibrating bubble column with *H/D* = 8.5 (*H* ≈ 0.85m). Still (2012) used the current experimental setup to study the bubble size, void fraction and mass transfer under vibration. Still (2012) has verified the experimental measurement of bubble size, void fraction, and mass transfer against Waghmare et al. (2007) for validation of the experimental setup. Here the bubble size as well as void fraction data from Still (2012) are used for verification of the proposed models. The bubble size under vibration was measured at gas superficial velocities of U_{SG} = 6.9, 20.7, and 34.5mm/s. Vibration frequency was set to 7.5, 10, or 12.5 Hz, while vibration amplitude was varied between 1, 3, 6, 8 and 10 mm.

Bubble imaging shows that vibration improves the interfacial area by manipulating the bubble size distribution from a poly-dispersed large bubble population to a more uniform distribution. It is worth mentioning that unless stated, the bubble size measurement was conducted 6*D* downstream of the injector tube to eliminate any influence from the injection condition (Mohagheghian & Elbing, 2018a; Mohagheghian & Elbing, 2018b; Mohagheghian & Elbing, 2016). Prior to analyzing the mean statistics, the temporal evolution of the bubble size was examined to determine the steady state conditions. Figure 5-14 shows a time trace of d_{32} under vibration (*A* = 6 mm, *f* = 10 Hz) with U_{SG} = 6.9 mm/s, which shows that the bubble size becomes nearly constant after ~10 seconds. The bubble size distribution is examined in Figure 5-15 with a probability density function (PDF) of bubble size. For this condition, vibration modifies the bubble size distribution (see Figure 5-15a) from a bimodal distribution (corresponding to pseudo-homogenous bubbly regime) in static column to a unimodal distribution (corresponding to mono-dispersed homogenous bubbly regime) due to bubble

breakage. The phase-averaged results for the vibration condition can be produced by combining the known time history given the sample rate and tracking a reference point located on the column wall (Hedrick, 2008). It is interesting that while under vibration the shape of the distribution appears independent of phase, the largest observed bubble sizes appear to have a significant phase dependence.

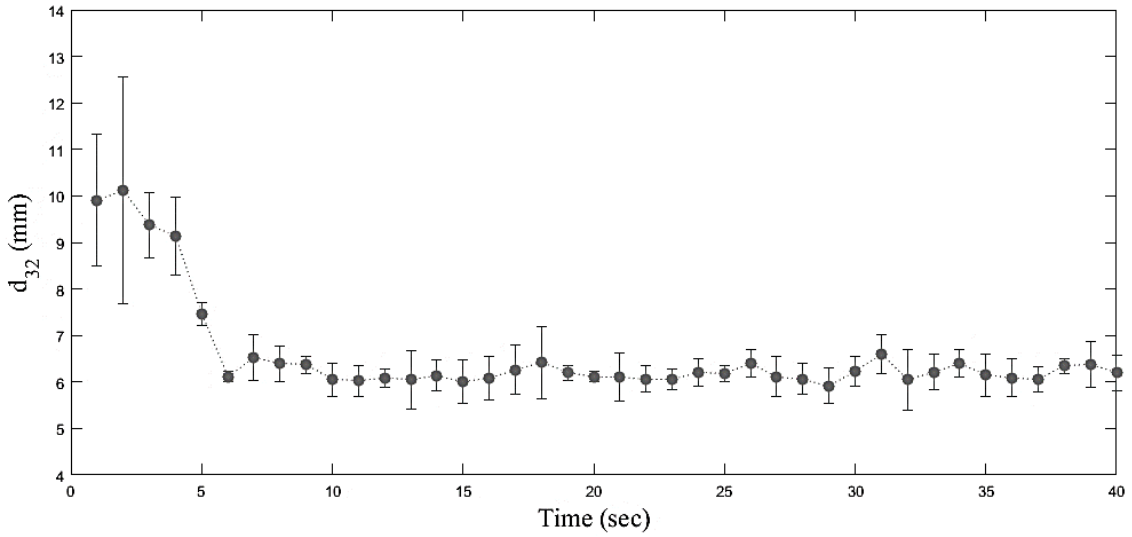

Figure 5-14. Temporal response of the bubble size (d_{32}) with vibration (f = 10 Hz, A = 6 mm) starting at time equals zero. (H_0 = 85 cm, U_{SG} = 6.9 mm/s, P_0 = 1 atm).

Figure 5-16 illustrates the bubble breakage along the column height and its dependence on the vibration amplitude. The vibration input power increases with increasing amplitude, which results in a reduction in the bubble size. Figure 5-16 also shows that at lower vibration amplitudes (i.e. A = 1 and 2 mm) the size distribution remains significantly poly-dispersed. Another interesting finding from Figure 5-16 is that increasing the amplitude has a significant effect on bubble shape as well as hydrodynamic behavior of the system (operation regime). In the current work, at lower vibration amplitudes the bubble column operates at a pseudo-

homogenous regime (Besagni et al., 2017b; Guédon et al., 2017) with cap shape bubbles of various sizes (see Figure 5-16, A = 1-2mm). Increasing the vibration amplitude breaks the aforementioned bubbles into smaller oblate spheroids (Figure 5-16, A = 6-10mm) and shifts the operation regime from pseudo-homogenous to mono-dispersed homogenous regime (Besagni et al., 2017b; Guédon et al., 2017). Unlike the static case that had a bubble size distribution partially resembling a Gaussian distribution, the vibration case is better approximated as a log-normal distribution (Still, 2012). These results are similar to the size distribution observed with 4-point optical probes in stationary columns (Xue et al., 2008).

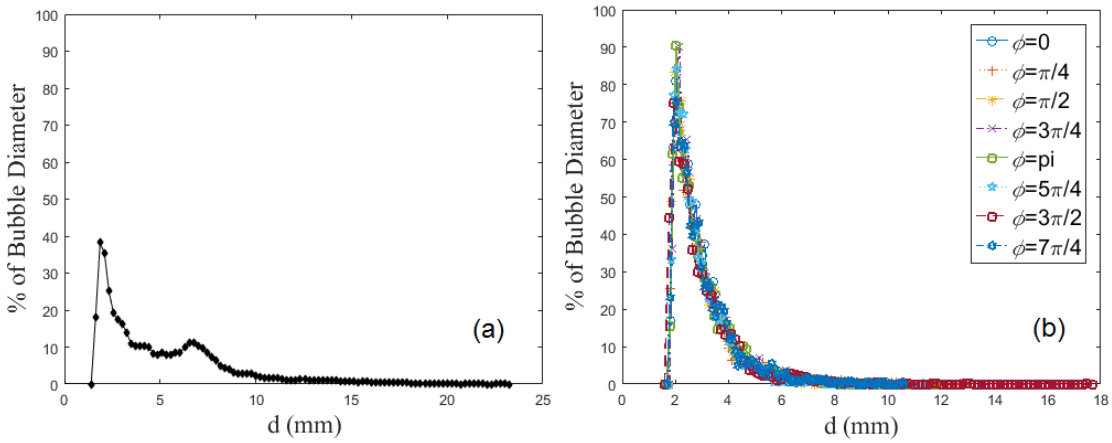

Figure 5-15. Probability density function of bubble sizes (U_{SG} = 6.9mm/s, P_0 = 1 atm) for the (a) static column and (b) column vibrating at f = 10 Hz with A = 6 mm. Symbols for the vibration phase (ϕ) in radians is provided in the legend.

Waghmare et al. (2007) proposed a correlation following the work of Hinze (1955) to predict the maximum stable bubble size as a function of specific power input and the properties of the continuous phase (i.e. surface tension, viscosity, and density). Equation 4-2 for scaling the bubble size under vibration was used here, where specific power input (P_m) was modeled as the sum of the input from gas injection (gU_{SG}) and the time averaged vibration input power

($0.5A^2\omega^3$). Hinze (1955) suggest that proportionality coefficient in Equation 4-3 is a function of critical Weber number ($We = \rho_L U_b^2 d/\sigma$) and depends on the bubble breakup mechanism (Waghmare et al., 2008). The proportionality constant has been reported as k = 0.725 for isotropic turbulent (Hinze, 1955), k = 1.67 for shear bubble breakup (Lewis & Davidson, 1982), k = 1.7 for bubble breakage in a pulsing bubble column (Waghmare et al., 2007, 2008) and k = 1.73 in a (piston) pulsing bubble column (Miyauchi & Oya, 1965). Waghmare et al. (2007) used a pulsing column that produced an oscillating shear flow by means of an oscillating membrane, which could explain the reported proportionality constant closely matching that of the shear breakup mechanism. The fit of Waghmare et al. (2007) is compared with the current vibrating column results in Figure 5-17. Vibrating the whole column produces an oscillatory pressure field with negligible shear, which is distinctly different from the shear breakup mechanisms. The current results in Figure 5-17 demonstrate a minimum input power (P_m ~ 0.54 W/kg) for the onset of breakage, which below this threshold the bubble size remains nearly constant nominally at the static bubble column value. Once the threshold is exceeded, there is a decrease in bubble size with increasing input power consistent with Equation 4-3 when k = 3.4. Note that close to the threshold level there is evidence that the vibration produces a slight increase in bubble size relative to the static case (d_0), which is consistent with data from Waghmare et al. (2007). Figure 5-18 uses all of the experimental data (Sauter mean diameter) from Figure 5-4 and Figure 5-17 to validate Equation 5-1, results show that in both the static and vibrating scenario all of the data collapse on the power-law correlation between the scaled bubble size and scaled specific input power. To the author's knowledge, the scaled specific power input has not been presented in bubbly flow literature prior to this date. For simplicity, we refer to this term as the breakage budget.

Figure 5-19 was produced to depict the effect of vibration amplitude on bubble velocity. Here d_{32} was used to produce a scaled amplitude. Froude number ($Fr = \frac{U_{SG}}{\varepsilon\sqrt{g d_{32}}}$) decreases as A/d_{32} increases, showing that as vibration amplitude increases the bubble velocity (U_{SG}/ε) decays more rapidly than d_{32}. It is interesting to see two distinctly different behaviors with the critical Froude number of approximately 1.

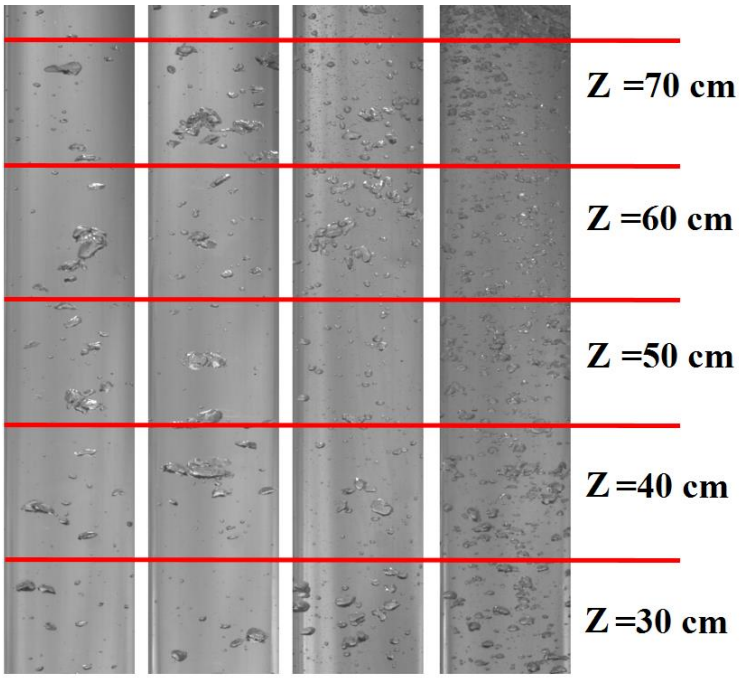

Figure 5-16. Instantaneous images illustrating the bubble size distribution along the column height at f = 10 Hz and (from left to right) A = 1 mm, 2 mm, 6 mm and 10 mm. (H_0 = 85 cm, U_{SG} = 5.0mm/s, P_0 = 1 atm).

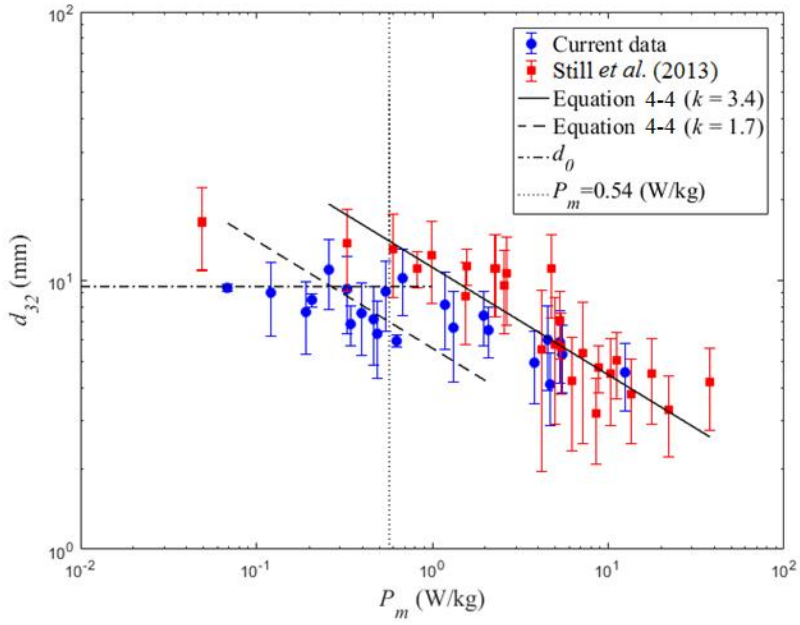

Figure 5-17. Sauter mean diameter (d_{32}) under vibration versus the input power (see Equation 4-3). Results are compared against bubble size in static condition (d_o).

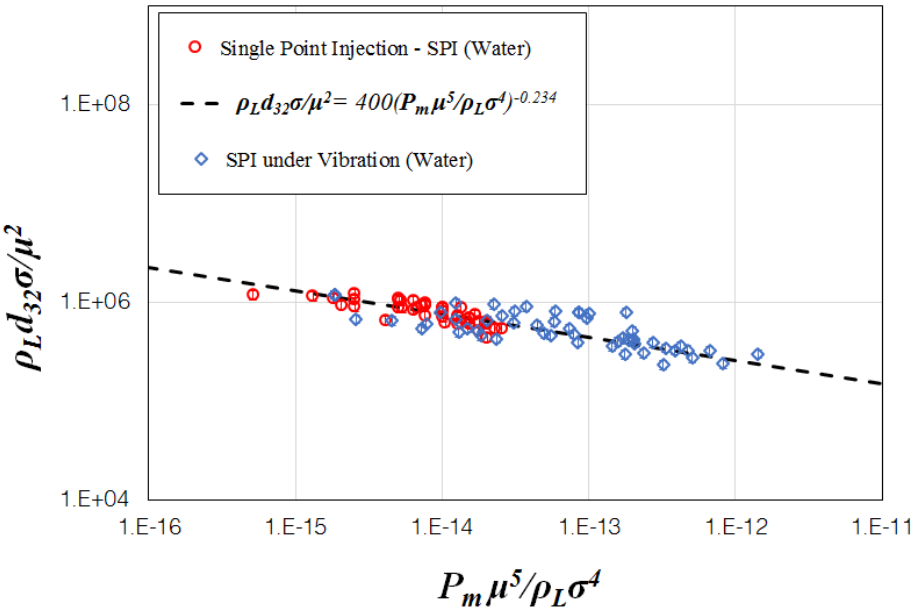

Figure 5-18. A power-law correlation between scaled bubble size and scaled specific input power (see Equation 5-1) in static and vibrating test conditions.

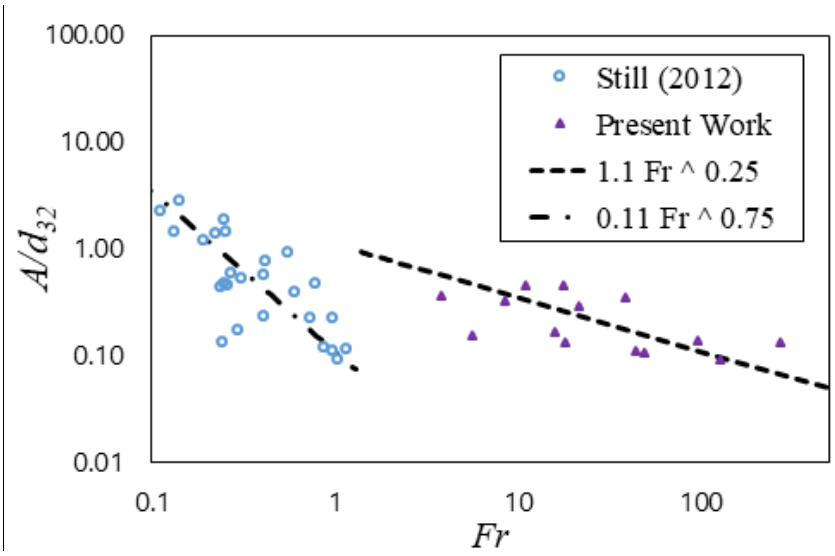

Figure 5-19. Effect of vibration amplitude on bubble velocity.

5.3.2 Void fraction modeling

Most of the pioneering work on vibrating bubble columns was conducted between 1960 and the late 1980s. More recently there has been a renewed interest in the study of vibrating bubble columns (Krishna et al., 2000; Krishna & Ellenberger 2002; Ellenberger & Krishna, 2003; Ellenberger et al., 2005; Ellenberger & Krishna 2007a; Ellenberger & Krishna 2007b; Knopf et al. 2006a; Knopf et al. 2006b; Waghmare et al. 2007; Waghmare et al. 2008; Waghmare et al. 2009). These recent efforts have developed theoretical physics-based models to predict mass transfer and void fraction in bubble column reactor (BCR) systems undergoing vibration (Waghmare et al. 2007; Waghmare et al. 2008; Waghmare et al. 2009). These models were tested in a limited range of data, but have yet to be fully understood or validated against a broad range of experimental data. Therefore, additional work is required to gain a fundamental understanding of the multiphase flow (including bubble size distribution and void

fraction) to enable scale-up and improving the operation of BCRs. The current work aims expand the available parameter space and test current models.

Historically the instantaneous upward force on a bubble has been formulated by neglecting the radial motion of the bubble and surrounding liquid. The assumption of isothermal expansion and contraction justifies the application of Boyle's law to calculate the average gas volume fluctuations (Houghton, 1963; Jameson & Davidson, 1966; Jameson, 1966; Waghmare et al., 2007, 2008, 2009; Still et al., 2013). The validity of this approach, especially near levitation conditions is questionable given that the levitation condition exhibits strong Reynolds number dependency (Jameson, 1966). It is important to note here that the work of Waghmare et al. (2007) examined void fraction and mass transfer within a pulsed bubble column. They proposed a void fraction model based on balancing the buoyancy and drag force on a single bubble. In addition, Waghmare et al. (2007) used this void fraction model and the definition of mass transfer coefficient from penetration theory to propose a mass transfer model. These models were successfully tested against experimental measurements, but over a relatively narrow range. It is noteworthy that vibration makes it extremely challenging to control the test conditions due to unintended surface entrainment and resonance characteristics of the vibration facility. Furthermore, a complete body of experimental data is not available to test the previous models. Hence the current work will examine them over a broader range of conditions as well as propose new models.

This section presents physics-based models for the prediction of void fraction in a vibrating bubble column. Here subscripts L and G distinguish the properties of the liquid and gas phase, respectively. The transient pressure field at a particular distance (h) from the liquid

free surface is given in Equation 5-2. Here A is the vibration amplitude, ω is the vibration angular velocity, ρ_L is the liquid density, and g is gravitational acceleration. The first term on the right hand side (P_0) is the external pressure, which is atmospheric unless pressurized. The second term represents the hydrostatic pressure, and the remaining term is the influence that the vibrations have on the pressure field $P(t)$. The transient response of the bubble radius (R) to the vibration can be formulated using the Rayleigh-Plesset equation (Equation 5-3). Here ν_L is liquid kinematic viscosity, σ is surface tension, R_0 is the reference (stationary) bubble size, P_v is the liquid vapor partial pressure inside of the bubble and κ is the gas heat capacity.

$$P = P_0 + \rho_L g h - \rho_L h A \omega^2 \sin(\omega t), \qquad \text{Equation 5-2}$$

$$R R'' + \frac{3}{2} R'^2 + \frac{4\nu_L R'}{R} + \frac{2\sigma}{\rho_L R} = \frac{1}{\rho_L}\left[\left(P_0 + \frac{2\sigma}{R_0} - P_v\right)\left(\frac{R_0}{R}\right)^{3\kappa} - P_0 - P(t)\right] \qquad \text{Equation 5-3}$$

The amplitude of oscillations (r) from the bubble radius R_o can be obtained from Equation 5-3 with the following assumptions:

- bubble expansion and contraction is adiabatic,
- liquid temperature is uniform and no significant thermal effect takes place,
- the bubbles contain a negligible amount of liquid vapor ($P_v << P_o$),
- bubble resonant frequency (f_N) is significantly larger than the vibration frequency,

- bubble radial oscillations are sinusoidal and in phase with the liquid pressure field $\left(R = R_0 + r\sin\omega t\right)$,
- bubble initial/stationary radius is significantly larger than the oscillation amplitude $(R_o \gg r)$ and
- standing acoustic wavelength is much larger than the bubble radius.

In addition, order of magnitude analysis shows that the second and third terms from the left hand side of Equation 5-3 (corresponding to convective acceleration and viscous effects) are significantly smaller than the fluctuating pressure and transient acceleration terms. Applying these assumptions, a relationship can be formed for the scaled bubble radius oscillation amplitude under vertical vibration (Equation 5-4). Given the bubble size, the instantaneous upward force (buoyancy) acting on a bubble is given in Equation 5-5. Here *F(t)* and *V(t)* are the instantaneous buoyancy force and bubble volume, respectively. The net upward force (i.e. time-average of Equation 5-5 over one period) is then found from Equation 5-6 with *M(h)* defined in Equation 5-7.

$$\frac{r}{R_0} = \frac{\rho_L A\omega^2 h}{3\kappa\left(P_0 + 2\sigma/R_0\right)}. \qquad \text{Equation 5-4}$$

$$F(t) = \rho_L V(t)\left(g - A\omega^2\sin(\omega t)\right) \qquad \text{Equation 5-5}$$

$$\bar{F} = \rho_L V_0 g\left(1 - M(h)\right) \qquad \text{Equation 5-6}$$

$$M(h) = \frac{1}{2\kappa}\frac{A\omega^2}{g}\frac{\rho_L A\omega^2 h}{P_0 + \frac{2\sigma}{R_0}}$$ Equation 5-7

Here V_0 is the static bubble volume and $M(h)$ is the transient buoyancy (Bjerknes) number, which is the product of the scaled vibration acceleration amplitude $(A\omega^2/g)$, the scaled vibration pressure amplitude $(\rho_L A\omega^2 h/[P_o + 2\sigma/R_o])$, and $(1/2\kappa)$. It is noteworthy that for an air-water system at thermal equilibrium ($\kappa = 1$), in the absence of significant (ambient) vacuum or micro-bubbles ($P_0 >> 2\sigma/R_0$) the expression of $M(h)$ simplifies to the Bjerknes number (Bj) given in Equation 5-8. The Bjerknes number (Bj) has been widely used in vibrating bubble column literature (Jameson & Davidson, 1966; Jameson, 1966; Rubin, 1986; Waghmare et al., 2007; Waghmare et al., 2008; Still et al., 2013).

$$Bj(h) = \frac{1}{2}\frac{\rho_L A\omega^2 h}{P_0}\frac{A\omega^2}{g}.$$ Equation 5-8

Given the buoyancy force from Equation 5-6, an expression for the void fraction in a vibrating bubble column can be formulated. Assuming the bubbles are at terminal velocity, the buoyancy force on average must be balanced by the drag force as shown in Equation 5-9. Here C_D is the drag coefficient and U_b is the bubble rise (terminal) velocity. The relationship between the drag coefficient on a single isolated bubble ($C_{D,\infty}$) and a bubble within a swarm (C_D) is given in Equation 5-10 (Simmonet et al., 2007).

$$\rho_L V g(1 - M(h)) = \frac{1}{2}\rho_L U_b^2 C_D \pi R^2.$$ Equation 5-9

$$C_D = \frac{C_{D,\infty}}{1-\varepsilon}$$ Equation 5-10

Given the definition of the superficial gas velocity $U_{SG} = Q_G / A_{CS}$ and void fraction combined with control volume analysis shows that the bubble rise velocity (U_b) is given in Equation 5-11. Here Q_G is the gas volumetric flux and A_{cs} is the bubble column cross-sectional area. Combining and rearranging Equation 5-9 to Equation 5-11 provides a relationship for the void fraction (Equation 5-12). Here d is the bubble diameter ($d = 2R$). Equation 5-12 is limited to low void fractions (ε < 10%) since in the simplification an ε^3 term was neglected. Alternatively, Hinze (1955) theory can be used to predict the bubble size under vibration (Equation 5-13). Here k is a proportionality coefficient and P_m is the time averaged input power per unit mass (Equation 5-14). The input power pet unit mass is the sum of contributions from the gas injection and vibration. Note that transient vibration power is expressed by $P'_m(t) = gU_{SG} - A^2\omega^3 \sin(\omega t)\cos(\omega t)$.

$$U_b = \frac{U_{SG}}{\varepsilon}.$$ Equation 5-11

$$\varepsilon = U_{SG}\sqrt{\frac{C_{D,\infty}}{\frac{4}{3}dg(1-M(h))}}$$ Equation 5-12

$$d = k\frac{\left(\frac{\sigma}{\rho_L}\right)^{3/5}}{P_m^{2/5}}.$$ Equation 5-13

$$P_m = gU_{SG} + \frac{A^2\omega^3}{2}.$$ Equation 5-14

The magnitude of the proportionality coefficient is dependent on the flow breakup mechanism, which for a turbulent jet (shear breakage) $k = 1.67$ based on the maximum-stable bubble size (Lewis & Davidson, 1982). Waghmare et al. (2007) determined $k = 1.70$ and thus concluded that bubble breakup under vibration was due to shear force and not eddy viscosity. Equation 5-12 can be modified incorporating the Hinze theory based prediction of bubble size (Equation 5-13) to give Equation 5-15. Note that $M(H) \geq 1$ corresponds to a nonphysical scenario where bubbles experience no buoyancy effect at the injector. Therefore, Equation 5-15 should only be considered when $M(H) < 1$.

$$\varepsilon(h) = U_{SG} \sqrt{\frac{C_{D,\infty}}{k(1 - M(h))g\left(\frac{\sigma}{\rho_L}\right)^{3/5} \Big/ P_m}} \qquad \text{Equation 5-15}$$

The average void fraction within the column can be obtained via integration through the column height, as shown in Equation 5-16. The void fraction measurements from Still (2012) are plotted versus $M(H)$ and P_m in Figure 5-20 with a power-law fit for each plot. These results are consistent with Waghmare et al. (2007). Also, Figure 5-20 demonstrates that the void fraction is dependent on both of these parameters; however it shows a stronger dependency on $M(H)$. The correlation between $\varepsilon/\varepsilon_0$ and $M(H)$ supports the theory in Equation 5-12 that $M(H)$ is a primary factor in scaling the void fraction.

$$\langle \varepsilon \rangle = \frac{1}{H}\int_0^H \varepsilon(h)dh = \sqrt{\frac{3C_{D,\infty}}{kg\left(\frac{\sigma}{\rho_L}\right)^{3/5} \Big/ P_m}} \left(\frac{U_{SG}}{M(H)} \left(1 - \sqrt{1 - M(H)}\right) \right) \qquad \text{Equation 5-16}$$

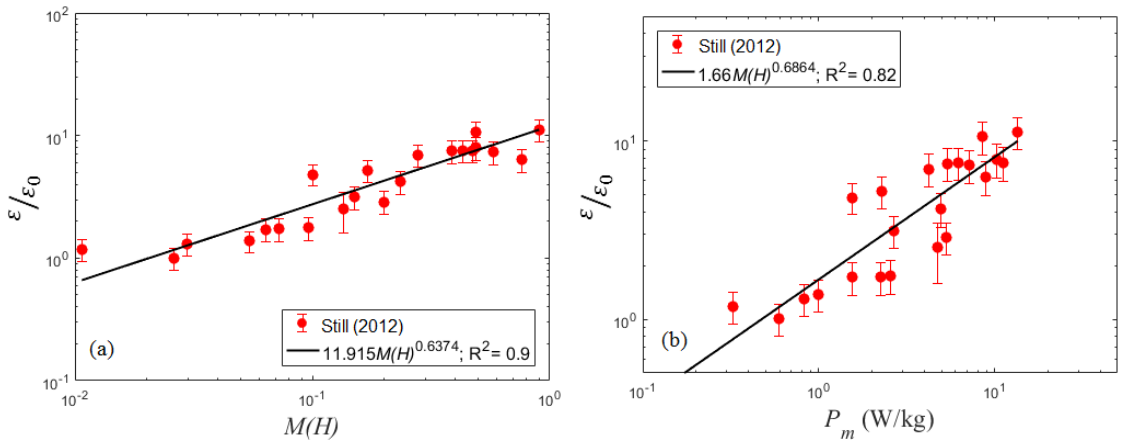

Figure 5-20. (a) void fraction versus *M(H)*, (b) void fraction versus the specific power input (P_m). Plot produced by data from Still (2012).

The void fraction results from Still (2012) are compared with the predictive models proposed in the current work as well as Waghmare et al. (2007) in Figure 5-21. Detailed investigations revealed that water has a low Morton number ($Mo=g\mu_L^4/\rho_L\sigma^3$ ~ 2.6E-10) (Brennen, 2005). Low Morton number liquids are characterized by a minimum in $C_{D,\infty}$ vs. Re_b (Reynolds number) trend. Bubble Reynolds number ($Re_b=U_bd/\nu_L$; is based on bubble size (d), rise velocity and, kinematic viscosity of the liquid (ν_L)) in this work ranges from 125 to 7000. Within the aforementioned range of Reynolds number and system properties (Mo ~ 2.6E-10) the drag coefficient exhibits a minimum $C_{D,\infty}$ = 0.15 at Re = 440 and levels off when Re > 4000 at $C_{D,\infty}$ = 2.74. Therefore, using a proper Reynolds number based correlations to predict the drag coefficient is vital to produce an accurate model to predict void fraction. In the present work, experimental measurements of $C_{D,\infty}$ from Brennen (2005) were used instead of using a correlation to calculate the drag coefficient on a single bubble. Figure 5-21 illustrates the predictions of $\varepsilon/\varepsilon_0$ from this work as well as that of Waghmare et al. (2007) in comparison

with experimental measurements at various *M(H)*'s. Figure 5-21 shows that Equation 5-16 does a poor job predicting $\varepsilon/\varepsilon_0$.

Trial and error approach was used to find an alternative model that scales the void fraction over the entire test range of *M(H)*. Starting with Equation 5-9 with $C_{D,\omega}=24/Re_b$ a new model for the void fraction was produced and given in Equation 5-17. K_ε is assumed to be a constant related to the experimental setup (here $K_\varepsilon = 50$). Figure 5-21 shows that Equation 5-17 offers an improvement in the prediction of $\varepsilon/\varepsilon_0$ within the range tested. It is noteworthy that Equation 5-17 is only valid within the current test range and any extrapolation beyond the current parameter space must be verified against appropriate experimental data. The uncertainty in the predicted void fraction is less than ±10% of the prediction.

$$\langle \varepsilon \rangle = K_\varepsilon \frac{36 U_{SG} \nu_L}{g} \left[\frac{\left(g U_{SG} + \frac{A^2 \omega^3}{2} \right)^{2/5}}{k \left(\frac{\sigma}{\rho_L} \right)^{3/5}} \right]^2 \left[\frac{1}{M(H)} \ln \left(\frac{1}{1 - M(H)} \right) \right]. \qquad \text{Equation 5-17}$$

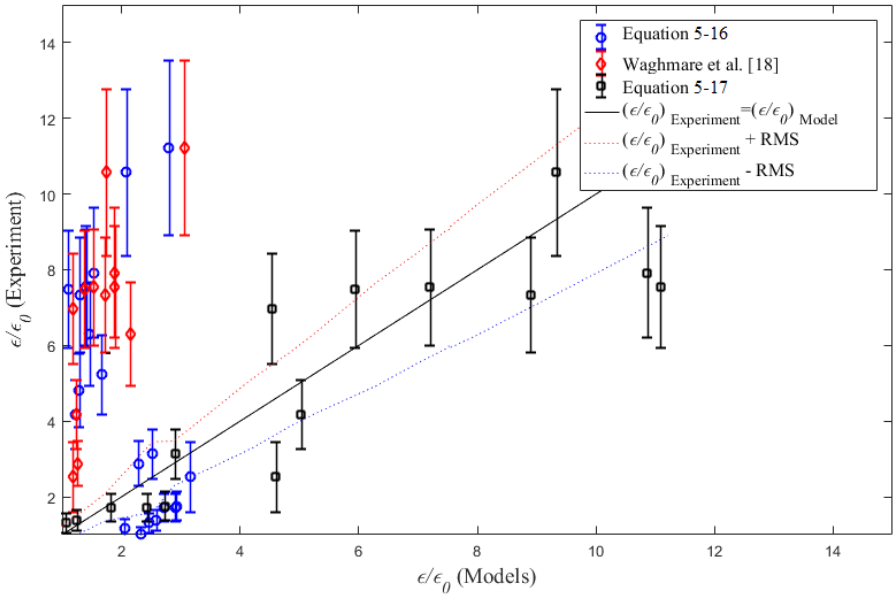

Figure 5-21. Comparison of the experimental data from Still (2012) with the predicted void fraction by models from this work and Waghmare et al. (2007). RMS is the root mean square of $\varepsilon/\varepsilon_0$.

5.3.3 Free surface disintegration

Example images from the recording of the free surface from Still et al. (2013) are shown in Figure 5-22. Examination of these images from the current work and Still (2012) reveal that the onset of air entrainment at the free surface occurs nominally at $M(H) \sim 0.3$. The chaotic oscillation of the liquid free surface captures large pockets of air, this phenomenon introduces an artificial increase in the measured void fraction. Surface entrainment is due to surface disintegration and free surface over turn at the wall (Majumder, 2016). Surface disintegration happens at a wavy free surface when the wave crests evolve into a narrow bottle neck fountain, which ultimately breaks into drop(s). Hashimoto & Sudo (1980) argued that the column aspect ratio (H/D) and vibration amplitude set the onset of surface disintegration. Air bubbles enter the column at the surface due to impact of the disintegrated drops. Note that on one hand increasing the vibration frequency reduces the size of the disintegrated drops (Hashimoto &

Sudo, 1984). On the other hand, the size of entrained air bubbles are proportional to the size of the drops and the wavelength of surface waves (Hashimoto & Sudo, 1984). Over turn of the wave crests at the column wall produces a thin film at the wall that also captures air bubbles into the column. Surface entrainment elevates the free surface and increase the measured void fraction. Thus models that do not consider the effect of surface entrainment will be unable to accurately predict the void fraction within the column when $M(H) > \sim 0.3$.

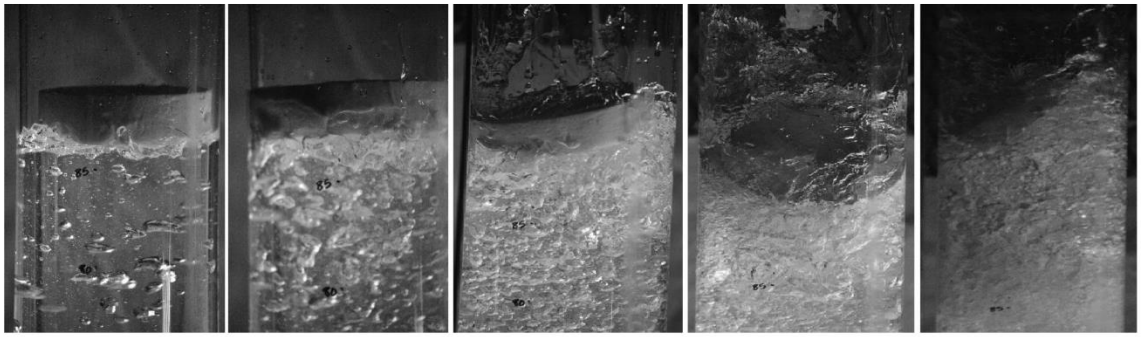

Figure 5-22. Air-Water interface at f = 12.5 Hz, H_0 = 85 cm and (from left to right) (a) A = 1.5 mm ($M(H)$=0.035), (b) A = 2.5 mm ($M(H)$=0.098), (c) A = 4.5 mm ($M(H)$=0.317), (d) A = 6.5 mm ($M(H)$=0.661) and (e) A = 9.5 mm ($M(H)$=1.41) (adopted from Still et al., 2013).

5.4 Conclusions and Remarks

The current study analyzed the BSD within a bubble column using high-speed imaging of a large population of bubbles. The effect of gas superficial velocity, column diameter, injector needle diameter, and external vertical vibration was investigated on the physical behavior of the system as well as the bubble size. The large sampling of bubbles was used to generate PDFs for each test condition. The maximum peak in the PDFs was used to identify a new bubble length scale, which was termed the most frequent bubble size (d_{mf}). This bubble

length scale was compared with the traditional Sauter mean diameter (d_{32}). Results showed, Sauter mean diameter is more sensitive to the largest bubbles within the flow while d_{mf} is related to the turbulent structures created in the bubble wakes. Consequently, the difference between d_{32} and d_{mf} represents the nominal range of bubble sizes expected within a given flow.

The Sauter mean diameter was sensitive to the injection tube angle and diameter, gas injection rate, and column diameter. Sauter mean diameter did exhibit a sensitivity to tube angle with misalignment between the tube and gravity resulting in a ~25% decrease in bubble size. Furthermore, doubling the injector tube diameter produced ~33% increase in the Sauter mean diameter. This dependence is expected based on previous work that noted that the detachment bubble size is of the same order of magnitude as the injector tube, and the detachment bubble size is directly related to the largest bubbles.

Conversely, the most frequent bubble size was relatively insensitive to gas injection rate, injection tube diameter, tube angle and column diameter. The insensitivity to most parameters is due to the minimum bubble diameter based Reynolds number tested being greater than 500 and most bubbles greater than 1000. In this range, coherent structures shed from the bubbles produce turbulent far-wakes. It is known that turbulent flow-fields produce relatively uniform bubble distributions, which is consistent with the observations of d_{mf}.

Higher order statistics (standard deviation, skewness and kurtosis) were also reported for the test conditions. While the range of test conditions limited the insights from these results, they were reported due to the dearth of available data in the literature. The limited data were consistent with some expected behavior given conclusions drawn from the parametric study assessing the behavior of the Sauter mean diameter and the most frequent bubble diameter.

These conclusions are (i) skewness increases with increasing injection tube diameter due to the longer tail in the PDF, (ii) high kurtosis values indicate the presence of infrequent excessive deviations from the mean, and (iii) higher order statistics could be used as an indicator for a regime change since a bimodal coefficient peaked at $Re \sim 1000$. The overall evaluation is that the combination of Sauter mean diameter and most frequent bubble diameter provides a more comprehensive assessment of the flow behavior.

BSD was measured under external vertical vibration to investigate the effect of vibration frequency and amplitude, respectively. As expected, increasing the vibration frequency and amplitude decreased the Sauter mean diameter (d_{32}). The PDF of bubble size under vibration exhibits a constant shape at different phases; however, vibration phase modifies the right leg of the distribution and consequently d_{32}. The smallest bubble sizes ($d_{32} \sim 2$ mm) were obtained at high frequency/amplitude combinations. At higher amplitudes d_{32} decayed to a minimum at lower frequencies. The measured d_{32} was successfully tested against Hinze (1955) correlation. The proportionality coefficient in the present work (k=3.4) is different from those reported in shear bubble breakage and pulsing column literature (k=1.67 and 1.7, respectively). The current k attributes to the difference in the physics of bubble breakup in the present work (shaking-column) and those reported in the literature (pulsing-column). Dimensional analysis was employed to produce a model to predict the bubble size by correlating the scaled bubble size with scaled specific power input (breakage budget). Liquid properties were used along with bubble size and specific input power to comprise the parameter space for dimensional analysis. Bubble size from both static and vibration test conditions collapsed on a power-law correlation between non-dimensional bubble size and the breakage budget. Dimensional analysis was also used to investigate the effect of vibration amplitude on

bubble velocity. Froude number (Fr) was calculated based on bubble size (d_{32}) and bubble velocity (U_{SG}/ε). Results shows that the scaled vibration amplitude (A/d_{32}) has an inverse correlation with Froude number; in other words, bubble velocity decays faster than d_{32} as vibration amplitude increases. Results also shows that the trend between scaled amplitude and Froude number exhibits significant changes when Fr~1; more experimental data is required to interpret this phenomenon as a regime change.

Void fraction data from Still (2012) shows strong dependency on *M(H)*. A physics-based model was proposed to predict the void fraction under vibration by using the reported experimental data of the drag coefficient on a rising bubble. Results shows that the current model (Equation 5-17) presents an improved prediction of void fraction; however, at the onset of surface entrainment the current model is not able to provide accurate prediction of void fraction. A correlation was presented to predict the void fraction with acceptable accuracy within the range tested.

CHAPTER VI

MIXING OF PASSIVE SCALAR IN VIBRATING BUBBLE COLUMN

6.1 Introduction

There are numerous applications where a chemical reaction (or process) takes place in a bubble column. To improve the efficiency of bubble columns in industrial processes one requires a fundamental understanding of multiphase parameters, including mixing characteristics of this gas-liquid system. Studies in batch bubble columns working within the homogenous operation regime identified two mechanisms for mixing (Besnaci et al., 2010), turbulence transport via wake interactions and bubble induced fluctuations in the liquid phase. Both wake transport and bubble interaction mechanisms are illustrated in Figure 6-1. It is worth mentioning that within a uniform bubble swarm there is no mean liquid flow; therefore, mixing is not due to shear induced mixing. Previous studies (Bouche et al., 2013; Bouche et al., 2014; Alméras et al., 2015; Alméras et al., 2016a; Alméras et al., 2016b; Alméras et al., 2018) are mainly focused on the mixing mechanism in simplified geometries (2D bubble columns). However, studies on large scale mixing (i.e. mixing time) are scarce. Furthermore, due to the complexity of gas liquid interactions at the interface, physics based models for prediction of multiphase parameters are rare in the literature. This chapter explores mixing characteristics of a batch bubble column and provides insights into the effect of vibration on mixing of a passive scalar under bubble induced diffusion.

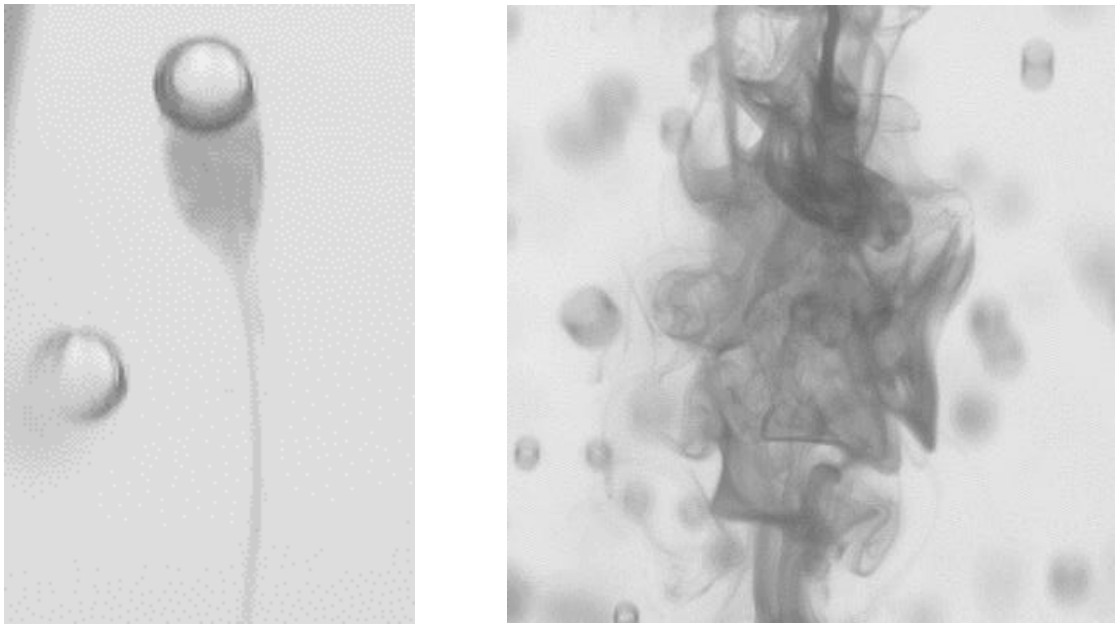

(a) (b)

Figure 6-1. Diffusion of a passive scalar under bubble induced mixing via (a) turbulent wake transport and (b) bubble interaction.

In the heterogeneous regime, void fraction gradients produce large scale recirculation regions. Considering a mixing experiment in the heterogeneous regime, the mixing takes place via shear within the aforementioned recirculation regions. Therefore, study of bubble induced mixing requires an experimental setup capable of producing a uniform swarm of mono-dispersed bubbles. A mono-dispersed homogenous bubble swarm produces no global recirculation in a batch bubble column; hence, guarantee that mixing takes place only via bubble wake and velocity agitations at the bubble surface. To study the bubble induced mixing a uniform swarm of bubbles was produced using the porous sparger disk. Using quantitative flow visualization, the mixing of a passive scalar was quantified by means of tracking the grayscale value in bubble images. For a detailed description of the setup, instrumentation, and measurement method please refer to Chapter 3. This chapter has been organized to provide a

comprehensive characterization of mixing time in the static column to investigate the effect of gas superficial velocity. In addition, over a series of experiments, the effect of vibration on mixing time of a passive scalar was studied and results were compared to those from static tests. Analysis of the mixing time was carried out by incorporating the bubble size and void fraction to explain the physics of the bubble induced mixing.

6.2 Results and Discussion

6.2.1 Static bubble column

In order to characterize the mixing time, the effect of gas superficial velocity (U_{SG}) on mixing time was investigated in a static column. Alméras et al. (2015) shows that the diffusion coefficient is a function of void fraction when $\varepsilon < 13\%$. It is also clear that increasing the void fraction increases the number of bubble interactions, which ultimately accelerates the mixing process. In a static column operating in the homogenous regime, the void fraction is a linear function of gas superficial velocity. To study the effect of void fraction on mixing time, a series of experiments were carried out to investigate the temporal evolution of the passive scalar with a homogenous bubble swarm, Table 6-1 gives the details of each tested condition, in these experiments tap water was used as the continuous phase. The void fraction was measured with a differential pressure transducer (section 3.1.3). Mixing time was measured by tracking the concentration of a blue dye at the center of the column. The dye was injected using a 0.6mm inner diameter tube. The tube was mounted on the column wall and introduces the dye at center of the column (see Figure 6-2). The dye was injected with a very low volumetric flow rate (0.4 ml/min) in order to prevent the premature mixing due to the formation of a turbulent plume of the dye. The Reynolds number ($Re_{ps}=4Q_{ps}/\pi d_{ps}^2 \nu_{ps}$) based on dye properties (i.e. ν_{ps}), dye

volumetric flow rate (Q_{ps}), and injector tube diameter (d_{ps}) was calculated to be $Re_{ps} \sim 20$ in all of the experiments.

Table 6-1. A test matrix for mixing time measurements in a static column

#	U_{SG} (mm/s)	P_m (W/kg)	ε (--)	d_{32} (mm)	d_{10} (mm)	$\sigma(d_b)$ (mm)	$S(d_b)$ (--)	$\kappa(d_b)$ (--)
1	13.8	0.14	2.56%	2.35	2.23	0.19	0.85	3.6
2	27.6	0.27	3.39%	2.51	2.37	0.20	0.9	3.32
3	41.4	0.41	4.21%	2.56	2.42	0.20	1.14	4.06
4	55.2	0.54	5.04%	2.69	2.54	0.22	0.56	2.64
5	69.0	0.68	5.87%	2.86	2.69	0.23	0.65	2.71

In all of the experiments, at the end of dye injection a batch of dye forms at the bottom of the column near the sparger; mixing begin as soon as bubbles reach the dye cloud. The evolution of the dye concentration was traced with respect to time from the beginning of bubbling. All of the measurements were conducted across the column section at the column mid-height, where the refractive-index matching (water-) box was located. When the dye reached the measurement section due to bubble diffusion it obstructs the light and reduces the grayscale in the background of the bubble images. When the dye was fully mixed no further change in grayscale occurred, therefore bubble-mixing time (t_∞) was quantified by tracking the background grayscale level in the bubble images.

It was shown (section 3.1.4) that a linear calibration between the mixed dye concentration and the background grayscale level of the bubble images can be used to characterize the dye local evolution of the dye concentration due to bubble induced diffusion. The accuracy of this technique is highly depended on the range of grayscale variations over the mixing process. To improve the accuracy of concentration measurements using the grayscale level an optimum mass of dye and backlight intensity were selected by careful

inspection. An LED panel was used to produce constant uniform backlighting of the measurement section (see Figure 6-2). Figure 6-3 shows the measurement section (a) before injection, (b) during dye injection, (c) before bubble mixing, and (d) after bubble mixing. Figure 6-3 shows the that during dye injection no mixing occurs, also the change in grayscale from mixing is significant, providing an acceptable measurement range for characterizing the evolution of dye concentration. Grayscale value ranged from 0 to 255; in the present work the grayscale level during mixing typically changed from 206 to 152. Here an EOS70D Canon DSLR camera took 14-bit images.

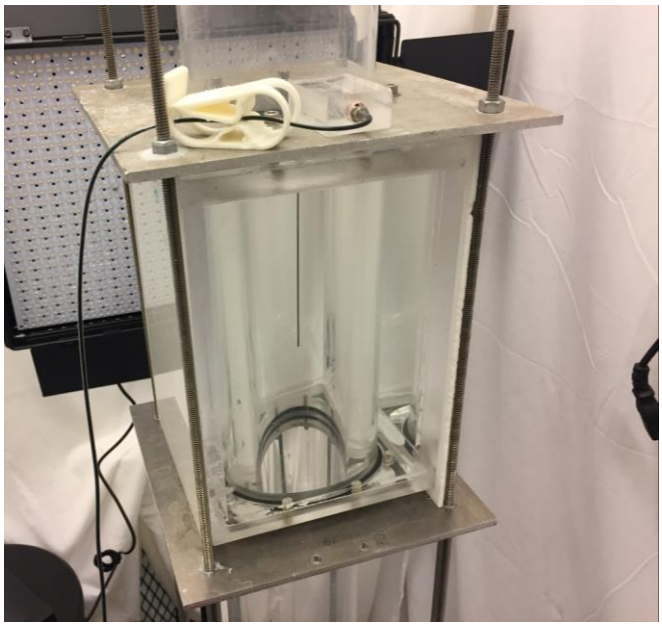

Figure 6-2. Measurement section of bubble column, the waterbox mitigated optical distortions due to refractive index mismatch. The dye injector needle was mounted on the wall, centered, and pointed downward in the column.

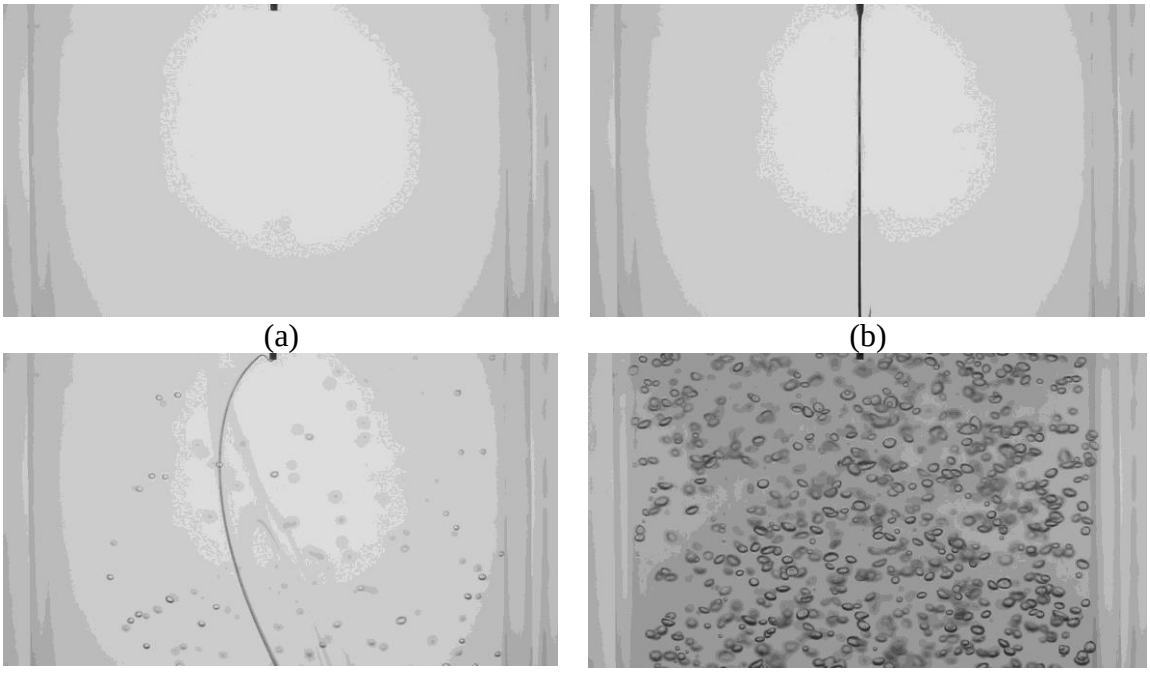

Figure 6-3. Measurement section (a) before and (b) during dye injection as well as (c) before and (d) after bubble mixing.

The effect of gas superficial velocity on bubble induced mixing was tested by tracking the temporal evolution of the normalized concentration at the measurement location. To assure that the present approach provides consistent results, a series of experiments were conducted to investigate the repeatability of the results. Five different gas velocities were selected and each test was repeated ten times. The temporal evolution of the normalized concentration was measured in each test. Figure 6-4 shows the average of all ten repetitions for each gas superficial velocity tested. Here C is the concentration of the dye as a function of time (t) and C_∞ is the concentration of the dye when it was fully mixed. It is worth mentioning that the mixing time (t_∞) was determined as the time when the normalized concentration C/C_∞ exceeds 0.95 and remains steady. In all of the experiments the reference time ($t=0$) corresponds to the beginning of airflow into the column. Figure 6-4 shows that increasing the superficial velocity has a direct impact on accelerating the bubble induced mixing. However, it is also apparent in

Figure 6-4 that the onset of mixing was not concurrent in all of the experiments. This is due to the fact that at lower flow rates it takes a longer time for air to activate the pores on the sparger to initiate bubbling. Therefore, the first few seconds of the experiment at lower gas flow rates are eventless. Figure 6-5 was produced by shifting the time reference for all of the data point so that the t=0 corresponds to the beginning of mixing instead of bubbling. Figure 6-5 shows that for all conditions the data collapse on a single curve when using normalized concentration and normalized time. It is worth mentioning that for all data in Figure 6-5, t_{∞} = 16 sec.

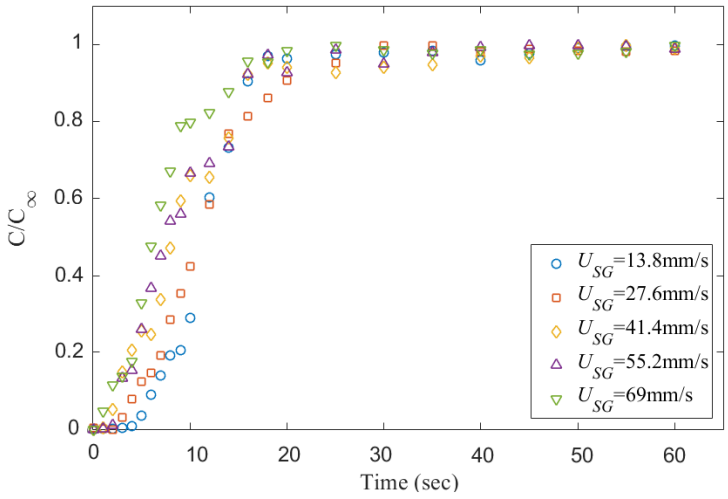

Figure 6-4. Time evolution of the normal concentration of a passive scalar under bubble induced mixing at the column mid-point. The initial time was based on the supply of air to the system.

Bubble images were manually inspected to verify that the mixing rate was constant and independent of gas superficial velocity within the range tested. Figure 6-6 shows representative images of bubble mixing exactly at t= 8sec after mixing. Noting that all these experiments were conducted in water, it can be seen that increasing the gas superficial velocity increases the void fraction, number of the bubbles, and bubble size. However, no significant change can

be seen in the background grayscale level. Bubble images were inspected carefully for identifying the dominant mixing mechanism. No sign of wake capture was observed; therefore, in the absence of liquid circulation one could conclude that bubble mixing due to induced liquid velocity fluctuations was independent of void fraction within the range tested (2% < ε < 6%). Results from Bouche et al. (2013) are consistent with this finding. A generalized correlation was formulated to provide a mathematical model for the temporal evolution of dye concentration under bubble induced diffusion. It was found that an error-function (*erf*) provides a reasonable fit to the data. Figure 6-7 demonstrates the correlation (Equation 6-1) between the normalized concentration and time. It can be seen that the experimental data is well represented by the error-function curve fit.

$$\frac{C}{C_\infty} = 0.55 erf\left(2.7\frac{t}{t_\infty} - 1\right) + 0.45 \qquad \text{Equation 6-1}$$

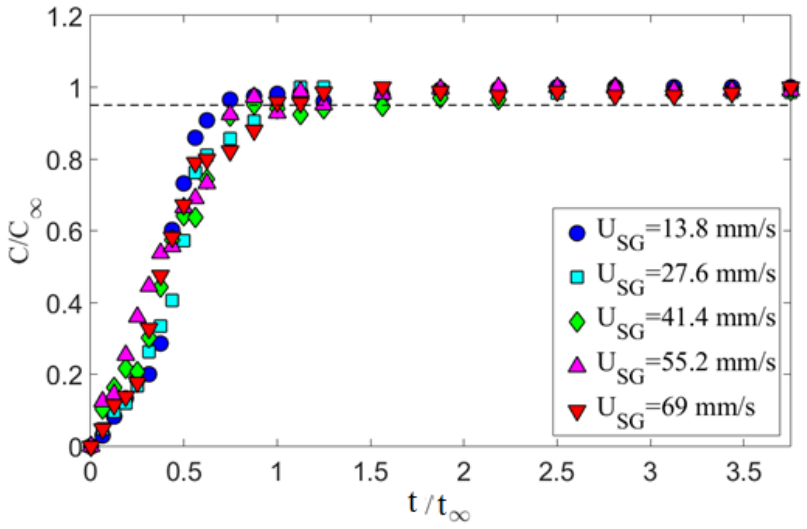

Figure 6-5. Temporal evolution of the normalized concentration and the effect of gas superficial velocity on mixing time in a bubble swarm. Here the time has been adjusted to account for the system delay between the start of air injection and mixing.

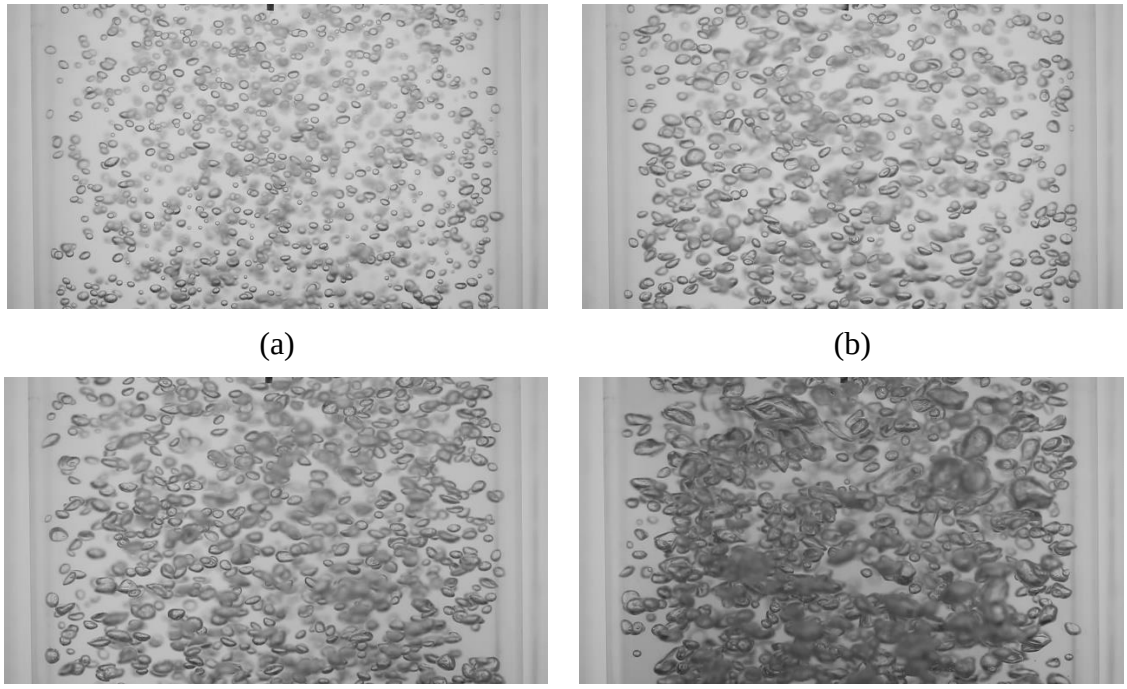

(a) (b)

(c) (d)

Figure 6-6. Instantaneous images of bubble mixing at t = 8 sec and (a) U_{SG}=13.8mm/s, ε = 2.5%; (b) U_{SG}=27.6mm/s, ε = 3.3%; (c) U_{SG}=41.4mm/s, ε = 4.2%; and (d) U_{SG}=55.2mm/s, ε = 5.9%.

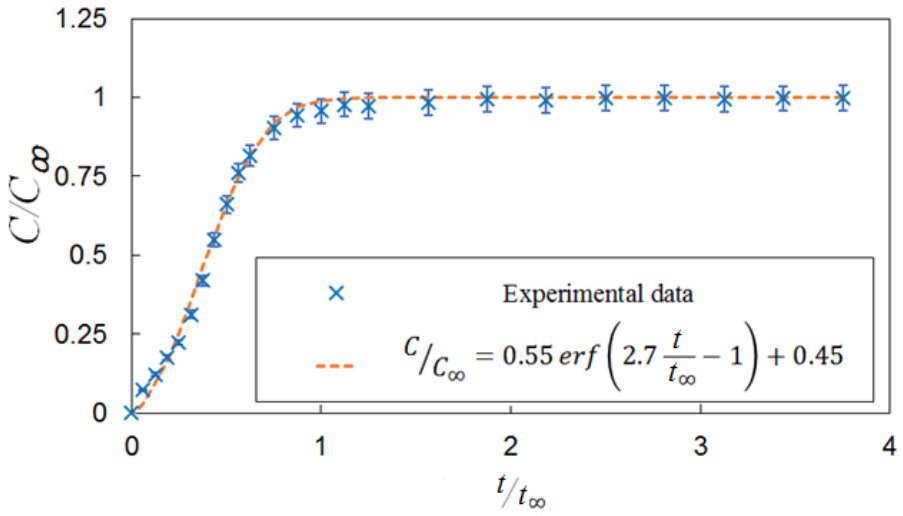

Figure 6-7. A correlation for temporal evaluation of dye concentration under bubble induced mixing.

The effect of viscosity on the mixing time under bubble induced diffusion was tested by fixing the gas superficial velocity (U_{SG}=27.6mm/s) and testing with an aqueous solution of glycerin (85% glycerin – 15% water), which significantly increased the viscosity relative to water (by two orders of magnitude). Figure 6-8 shows the comparison between bubble induced mixing in water and the glycerin solution (85% glycerin – 15% water). Results show that, although the gas superficial velocity was matched and increasing, the bubble size, void fraction, and mixing time increased with increasing viscosity. In a more viscous medium the bubble induced velocity agitations (in liquid) dissipates quicker; therefore, increasing the viscosity suppresses the main mixing mechanism and consequently increases the mixing time. Figure 6-8 supports the hypothesis that bubble mixing in the current study primarily occurs via bubble induced velocity agitations and not wake capture.

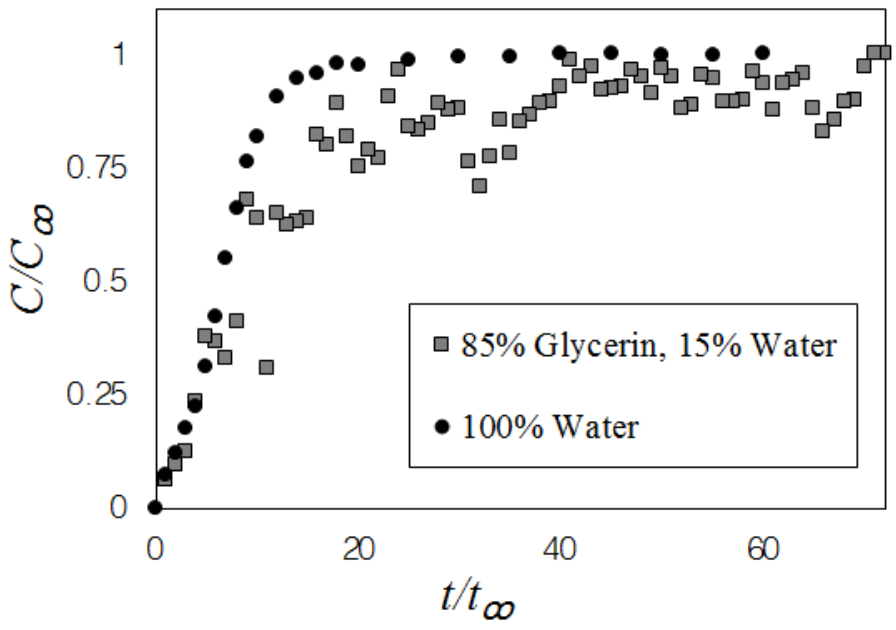

Figure 6-8. A comparison between the mixing time in water (U_{SG}=27.6mm/s, ε=3.4%) and aqueous solution of glycerin (85% glycerin – 15% water) (U_{SG}=27.6mm/s, ε=4.4%).

6.2.2 Vibrating bubble column

A systematic study of mixing in a vibrating bubble column was performed. Table 6-2 provides the test matrix used to study the effect of vibration condition on mixing time in a vibrating bubble column. In each test, bubble size distribution and void fraction were measured along with the mixing time. Figure 6-9 presents the Sauter mean diameter measured from the test conditions. It is interesting to see that the Sauter mean diameter was insensitive to the vibration condition. This is due to the act that the initial bubble size (d_0) from the porous sparger in water was so small that vibration input power was not able to achieve the onset of bubble breakage. In a study of bubble size and shape under vertical vibrations Cano et al. (2014) suggests that a correlation between Froude number ($Fr_d = \frac{U_{SG}}{\varepsilon\sqrt{g d_{32}}}$) and scaled vibration amplitude (A/d_{32}) can predict the bubble velocity ($U_b=U_{SG}/\varepsilon$). Figure 6-10 shows that within the range tested a sparged bubble column exhibits a minimum in void fraction (maximum in Fr_d) when the scaled vibration amplitude is near unity. Since the bubble size and gas superficial velocity were constant, in Figure 6-10 the rise in Froude number is only due to a drop in void fraction. This can be attributed to the presence of a standing acoustic wave that causes the void fraction to exhibit modal behavior at certain vibration conditions. In the rest of this section, the effect of vibration on mixing of a passive scalar will be discussed using experimental measurements of mixing time.

Table 6-2. Summary of all test conditions for bubble size and void fraction measurement.

U_{SG} (mm/s)	A (mm)	f (Hz)	P_m (W/kg)	ε	d_{32} (mm)	d_{10} (mm)	t_{∞}(sec)
11.0	0.6	8.2	0.14	2.56%	2.35	2.23	25
11.0	0.6	15.2	0.27	3.39%	2.51	2.37	25
11.0	0.6	18.5	0.41	4.21%	2.56	2.42	25
11.0	0.6	21	0.54	5.04%	2.69	2.54	20
11.0	0.6	23	0.68	5.87%	2.86	2.69	25
11.0	1.2	9.5	0.26	1.08%	2.45	2.25	25
11.0	1.2	11.5	0.38	1.01%	2.64	2.23	35
11.0	1.2	13.1	0.51	1.06%	2.88	2.27	25
11.0	1.2	14.3	0.63	1.23%	2.60	2.16	30
11.0	1.6	7.9	0.26	1.45%	2.35	2.31	25
11.0	1.6	9.6	0.39	1.10%	2.02	1.79	25
11.0	1.6	11	0.53	1.70%	2.02	1.79	25
11.0	1.6	12	0.66	1.32%	2.77	2.37	20
11.0	1.6	14	0.98	1.73%	3.04	2.42	25
11.0	1.9	8.7	0.40	1.55%	2.94	2.29	17
11.0	1.9	9.9	0.54	1.78%	2.47	2.22	16
11.0	1.9	10.8	0.67	1.55%	2.70	2.36	17
11.0	1.9	12.7	1.03	1.35%	3.09	2.67	17
11.0	1.9	14	1.34	1.35%	3.15	2.60	18
11.0	3.3	8.8	1.03	2.52%	2.32	2.12	13
11.0	3.3	9.7	1.34	2.89%	1.74	1.61	10
11.0	3.3	10.6	1.72	2.12%	2.76	2.36	15
11.0	3.3	11.5	2.16	2.10%	2.54	2.14	13
11.0	3.3	12.5	2.75	2.22%	2.76	2.19	13
11.0	5.7	8	2.17	2.50%	2.73	2.15	11
11.0	5.7	8.7	2.76	2.95%	3.08	2.34	12
11.0	5.7	9.5	3.56	1.91%	3.13	2.40	11
11.0	5.7	10.5	4.77	2.01%	3.08	2.13	10

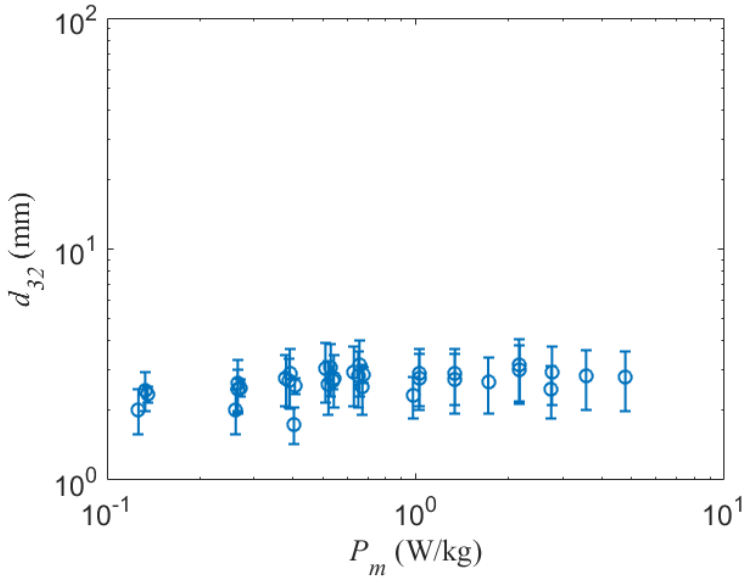

Figure 6-9. Sauter mean diameter from the conditions tested as given in Table 6-2.

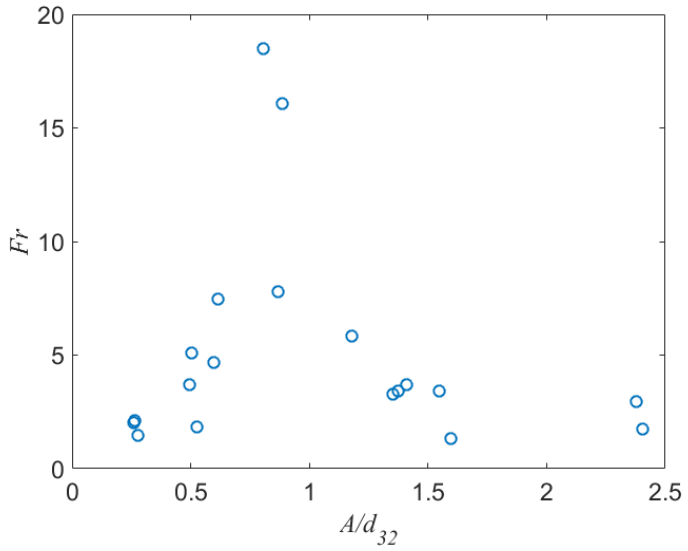

Figure 6-10. Effect of vibration amplitude on bubble size and velocity using the scaled amplitude and Froude number.

To investigate the effect of vibration on mixing performance of the bubble column, four vibrating test conditions were selected and the mixing in these conditions were compared to mixing in static cases at the same specific input power. Table 6-3 presents a test matrix to assess the effect of vibration on bubble induced mixing with respect to the specific input power.

Figure 6-11 presents the temporal evolution of the normalized dye concentration for comparison between static and vibrating cases at matching specific input power. It is worth mentioning that to match the specific input power in the vibration cases the gas superficial velocity was reduced to compensate for power input from vibration. From Figure 6-11 and mixing times (given in Table 6-3) it is apparent that over the range of test conditions with matching specific input power, vibration decelerates the mixing of a passive scalar under bubble induced diffusion. Under vibration, bubble terminal velocity experiences significant retardation, which in turn suppresses the liquid velocity agitations and increases the mixing time. Detailed observations show that increasing the vibration input power enhances the bubble mixing by means of aggregated bubble clouds that produce significant gradients of void fraction and a mean flow in the bubble column; however, high power vibration produces unintended surface entrainment and surface sloshing producing an uncontrolled test environment. Figure 6-12 and Figure 6-13 compare the bubble size and void fraction between static and vibrating vases. These figures show that in a static column with matching specific input power the average bubble size and void fraction was larger than those in a vibrating bubble column; in other words, in a static bubble column more bubbles with higher velocity and larger size will provide a faster mixing and better diffusion.

From the above it is concluded that the present cases support the hypothesis that by matching the specific input power, vibration does not cause a synergic effect to accelerate the mixing of a passive scalar. One should note that the shaker table apparatus is expensive and cumbersome in maintenance; therefore, from the cost effectiveness point of view only when vibration provides significant improvement justifies the use of vibrating bubble column for mixing purposes.

Table 6-3. Operation settings employed to study the effect of specific power input on mixing time.

#	Q_c (lpm)	U_{SG} (m/s)	g (m/s^2)	A (mm)	f (Hz)	ω (rad/s)	P (W/kg)	t_{∞} (s)
1	0.70	0.01	9.81	0.6	9.7	61	0.136	25
2	1.00	0.01	9.81	0.6	0	0	0.135	16
3	0.90	0.01	9.81	0.6	14.5	91	0.258	25
4	1.90	0.03	9.81	0.6	0	0	0.257	16
5	2.00	0.03	9.81	0.6	14.5	91	0.407	25
6	3.00	0.04	9.81	0.6	0	0	0.406	16
7	2.30	0.03	9.81	0.6	20.1	126	0.674	20
8	5.00	0.07	9.81	0.6	0	0	0.677	16

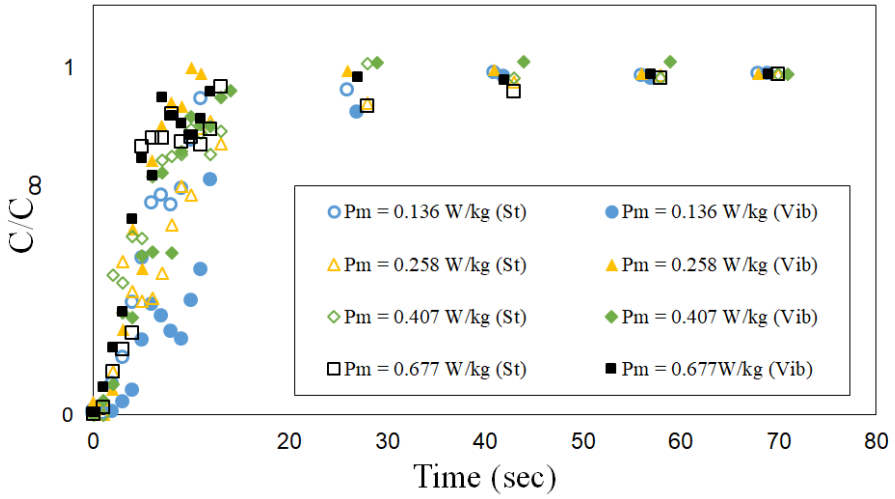

Figure 6-11. Mixing time of the dye in static and vibrating scenarios with matching specific power input ($P_m = gU_{SG} + 0.5A^2\omega^3$).

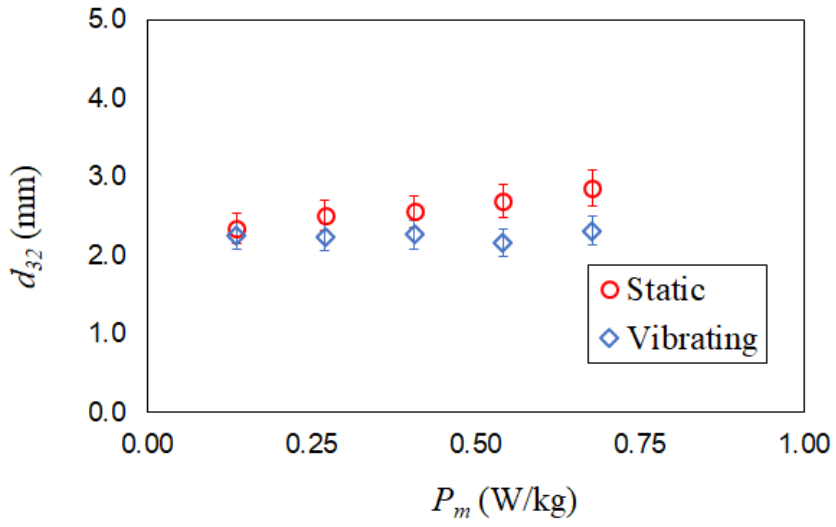

Figure 6-12. Sauter mean diameter from the tested conditions in Figure 6-11.

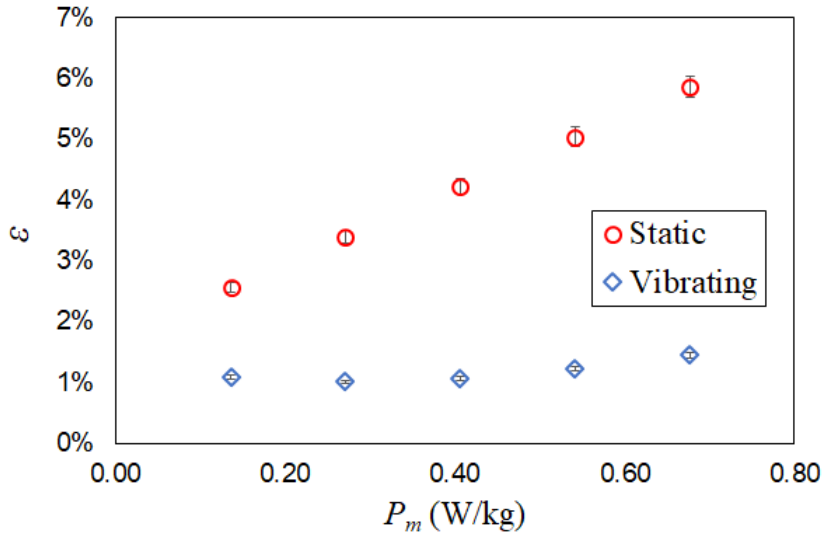

Figure 6-13. Sauter mean diameter from the conditions tested (see Figure 6-11).

Figure 6-14 shows the temporal evolution of the dye concentration in static and vibrating cases (P_m = 0.136 W/kg) and shows a faster mixing in the static case, this is due to bubble retardation from vibration. Under vibration bubble terminal velocity decreases, which means that the bubble induced velocity fluctuations as well as bubble wake contributions to mixing are suppressed compared to the static case; therefore, mixing occurs at a slower rate.

An interesting finding from Figure 6-14 is that vibration improves the uniformity of mixing. In the static cases a region of high dye concentration can be seen in the right half of the test section; however, under vibration this effect has been suppressed. Figure 6-15 shows instantaneous images of dye mixing in static and vibrating cases at a higher input power (P_m = 0.667 W/kg). The bubble breakup and deformation from the oscillating pressure field under vibration enhances the intensity of the bubble induced velocity fluctuations and compensates for the retardation effect. One should note that at the highest tested power the vibration mixing was still slightly slower bubble mixing than the static condition.

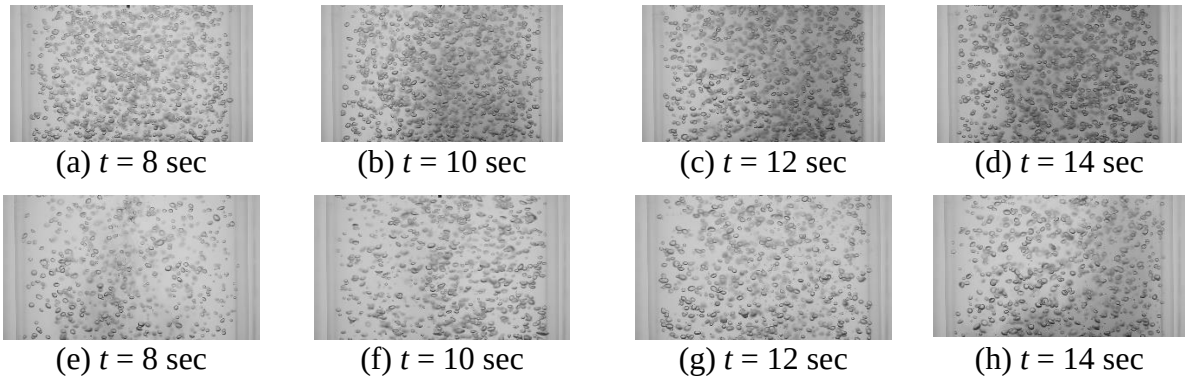

(a) t = 8 sec (b) t = 10 sec (c) t = 12 sec (d) t = 14 sec

(e) t = 8 sec (f) t = 10 sec (g) t = 12 sec (h) t = 14 sec

Figure 6-14. Instantaneous images of mixing in (top row) static and (bottom row) vibrating bubble column (P_m = 0.136 W/kg).

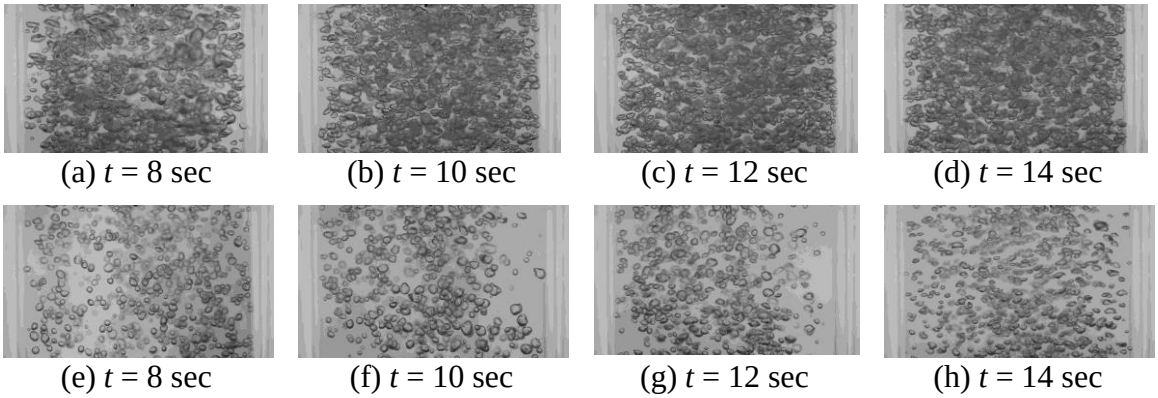

(a) t = 8 sec (b) t = 10 sec (c) t = 12 sec (d) t = 14 sec

(e) t = 8 sec (f) t = 10 sec (g) t = 12 sec (h) t = 14 sec

Figure 6-15. Instantaneous images of mixing in (top row) static and (bottom row) vibrating bubble column (P_m = 0.667 W/kg).

Effect of vertical vibration on mixing of a passive scalar under bubble diffusion was further studied in the current work by investigating the effect of vibration frequency and amplitude independently. In the first set of tests the vibration amplitude was held constant at A = 0.6mm and the effect of frequency was tested at f = 8, 15, 18.8 and 23.3 Hz. The gas superficial velocity was also held constant at U_{SG} = 11mm/s. Table 6-4 summarizes the mixing time as well as the operation settings for this investigation. It is worth mentioning that the specific power input in all of the test conditions in Table 6-4 closely matches those in Table 6-3. Figure 6-16 shows the results, which illustrate the effect of vibration frequency on the mixing time. Assuming that increasing the vibration frequency would increase the mixing time due to a built up retardation effect is not supported. A consistent deceleration trend in mixing is not seen in Figure 6-16. In other words, the mixing time is consistent within the range tested of vibration frequencies. Manual inspection of the bubble images reveals that in addition to retardation, vibration modifies the bubble size and shape. Figure 6-17 shows instantaneous images of the bubbles mixing under vibration at various frequencies. It can be seen that increasing the vibration frequency produces is larger bubbles, which can produce different mixing rates depending on their wake characteristics. Furthermore, increasing the vibration frequency from f = 8 Hz causes the bubble to migrate towards the column wall.

Table 6-4. Operation settings employed to study the effect of vibration frequency on mixing time.

#	U_{SG} (mm/s)	A (mm)	f (Hz)	P (W/kg)	t_{∞} (s)
1	11	0.6	8	0.131	25
2	11	0.6	15	0.259	25
3	11	0.6	18.8	0.405	25
4	11	0.6	23.3	0.673	25

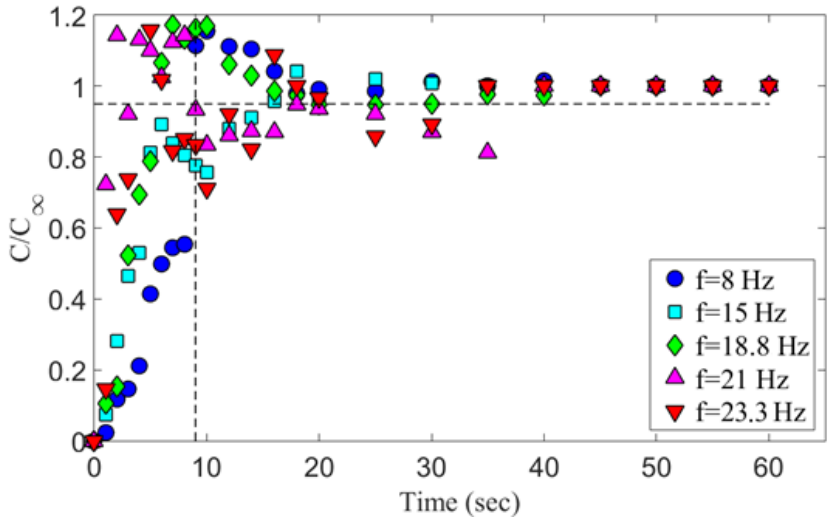

Figure 6-16. Effect of vibration frequency on mixing time, A = 0.6mm and U_{SG} = 11mm/s.

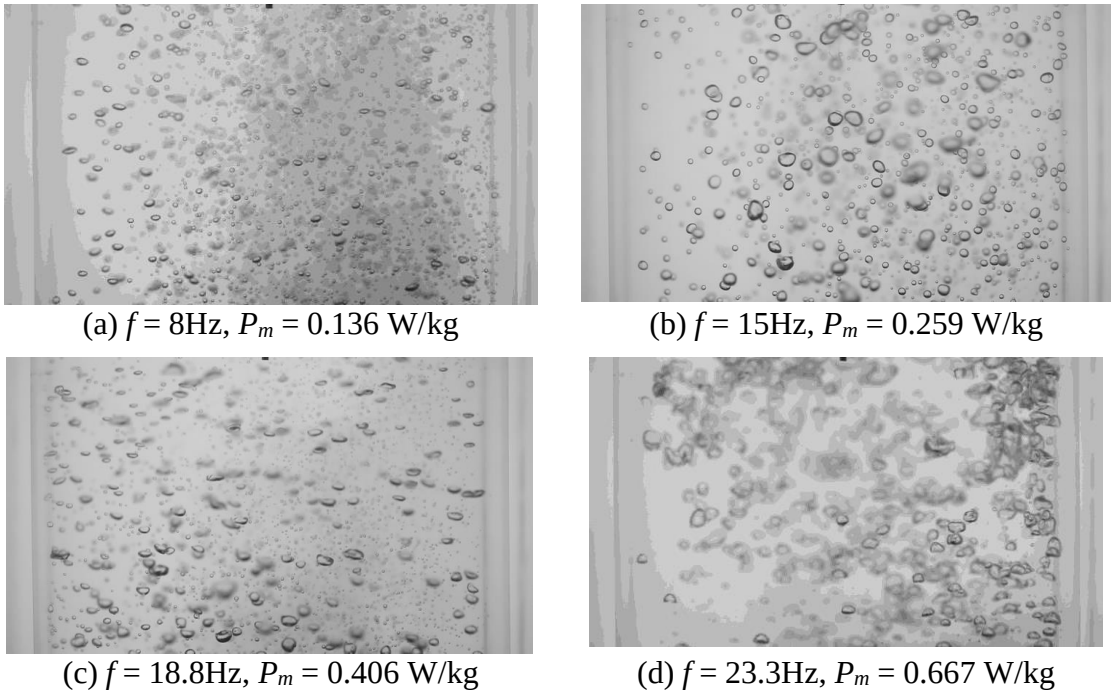

(a) f = 8Hz, P_m = 0.136 W/kg (b) f = 15Hz, P_m = 0.259 W/kg

(c) f = 18.8Hz, P_m = 0.406 W/kg (d) f = 23.3Hz, P_m = 0.667 W/kg

Figure 6-17. Instantaneous images of mixing at t = 8 sec (A= 0.68mm, U_{SG} = 11 mm/s).

Table 6-5 presents the mixing time as well as the operation settings to investigate the effect of vibration amplitude on mixing time scale. Figure 6-18 shows the time evolution results of this investigation. When considering the mixing enhancement from vibrating the bubble column, increasing the vibration power via increasing the amplitude exhibits a weak

trend, especially within the first 5 seconds. Investigating the images from bubble mixing shows that increasing the amplitude has a significant effect on bubble size and shape. Figure 6-19 shows instantaneous images of the bubble mixing under vibration at various tested amplitudes at t = 10 sec. Figure 6-19 also shows that increasing the amplitude produces smaller bubbles. It is also very interesting to see that increasing the vibration amplitude from A = 1.4 mm to A = 2.4 mm causes the high concentration region to shift from the left to the right side of the column in all tests. A mean flow inside of the column will transport the dye faster than the velocity agitations from bubbles wake and deceleration of the mixing process under vibration shows that a mean flow is not present in the vibrating bubble column. This refutes the hypothesis that the mean flow in the column is produced from non-uniformities in bubble swarm production at the sparger.

Table 6-5. Operation settings employed to study the effect of vibration amplitude on mixing time.

#	U_{SG} (mm/s)	A (mm)	f (Hz)	P (W/kg)	t_{∞} (s)
1	9.6	0.06	9.5	0.139	25
2	9.6	1.4	9.5	0.338	25
3	9.6	2.8	9.5	1.076	16
4	9.6	3.6	9.5	1.702	10

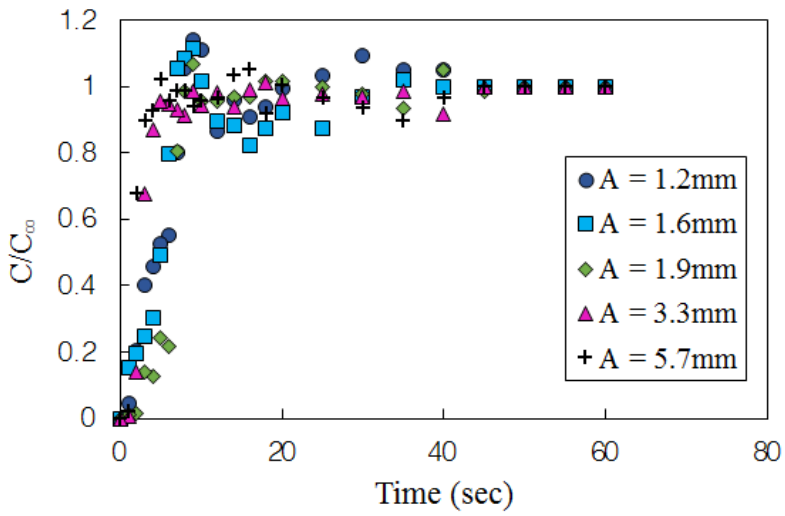

Figure 6-18. Effect of vibration amplitude on mixing time, f = 10 Hz and U_{SG} = 9.6mm/s.

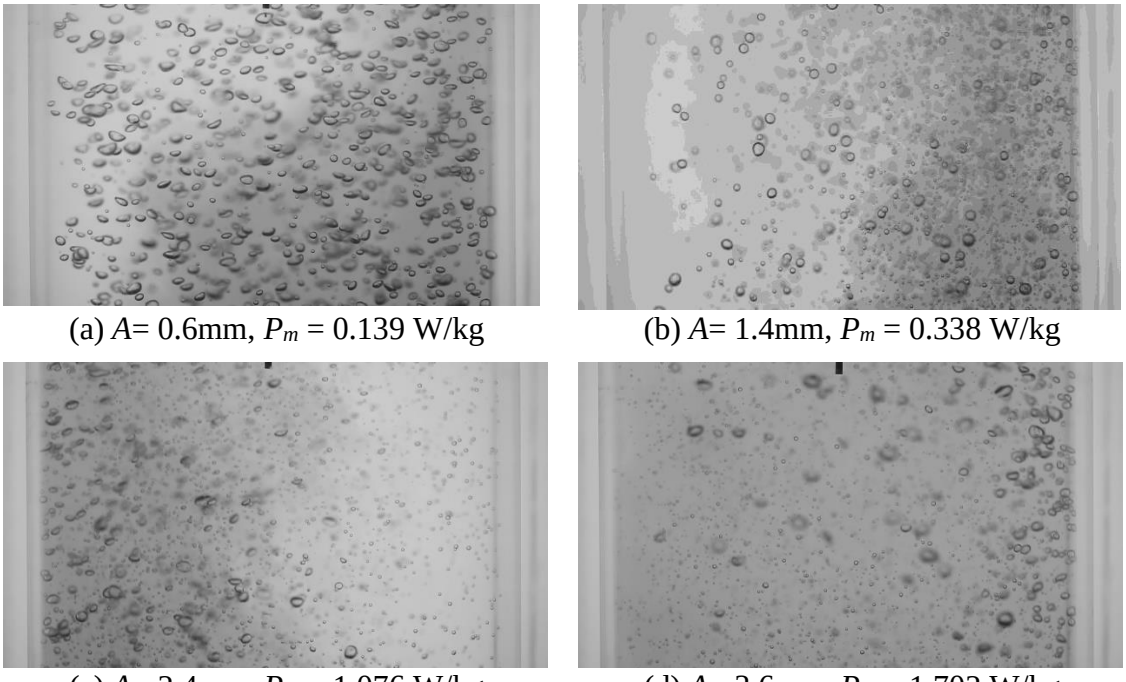

(a) A= 0.6mm, P_m = 0.139 W/kg

(b) A= 1.4mm, P_m = 0.338 W/kg

(c) A= 2.4mm, P_m = 1.076 W/kg

(d) A= 3.6mm, P_m = 1.702 W/kg

Figure 6-19. Instantaneous images of mixing at t = 10 sec (f= 10Hz, U_{SG} = 9.6mm/s).

6.3 Analysis

This section presents an analysis of the measured mixing time of a passive scalar under vibration. It was argued that when the specific input power is lower than 0.6 W/kg, vibration is not able to enhance the mixing time. Table 6-2 presents the mixing time measured over all test conditions, results shows that in low specific input power the mixing time exhibit inconsistencies; however, increasing the input power clearly improve the mixing under bubble diffusion. When the input power is larger than 1.0 W/kg a consistent trend between the power input and mixing time can be seen. From an engineering-application point-of-view, it is desirable to predict the mixing time. Dimensional analysis was employed to produce a correlation between non-dimensional mixing time ($t_\infty U_{SG}/d_{32}$) and non-dimensional specific input power. Radl et al. (2010) recommends that the phase interfacial area ($a_i=6\varepsilon/d_{32}$) be used in addition to the liquid properties to make a scaled specific input power. Equation 6-2 correlates the scaled mixing time and specific input power. Equation 6-2 also confirms that increasing the liquid viscosity increases the mixing time, this can be seen in Figure 6-8. Figure 6-20 shows the experimental results against the correlation for the prediction of the mixing time of a passive scalar, although the experimental data is scattered an acceptable agreement between Equation 6-2 and the experimental data can be seen.

$$\frac{t_\infty U_{SG}}{d_{32}} = 295\left[\left(\frac{P_m}{a_i}\right)\left(\frac{\sigma}{\rho\mu^3}\right)^{3/5}\right]^{-0.489} \qquad \text{Equation 6-2}$$

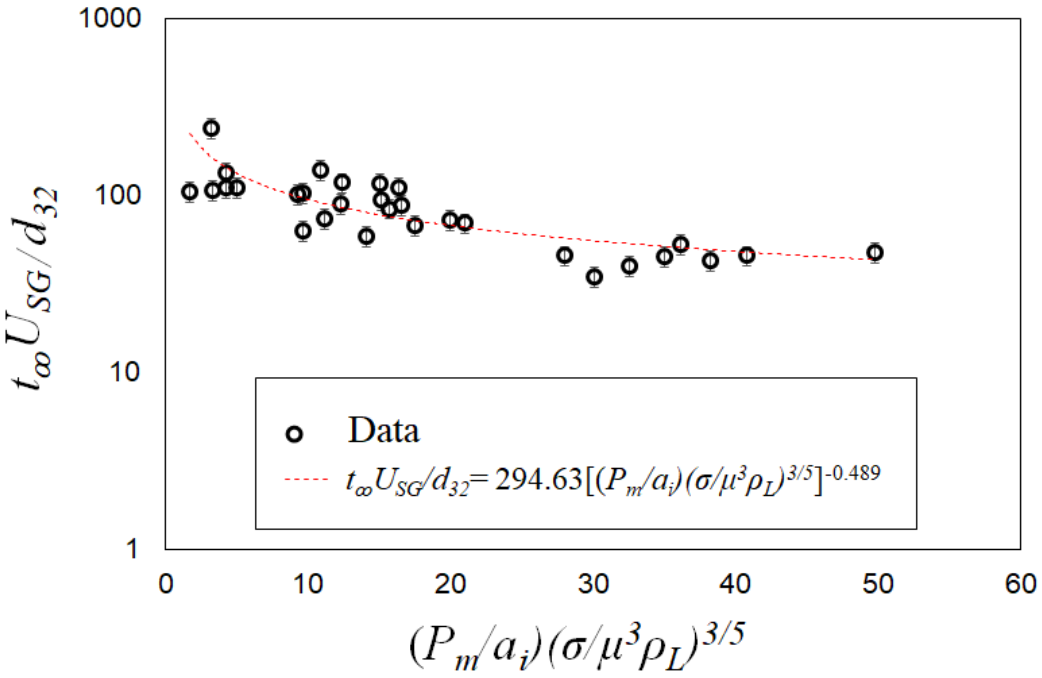

Figure 6-20. Scaled mixing time versus scaled specific input power, with the experimental data compared against a dimensionally reasoned curve fit.

6.4 Conclusions

This chapter presents a characterization of mixing time of a passive scalar under bubble induced diffusion in a vertically vibrated bubble column. Bubble size and void fraction were measured in addition to the mixing time to study the effect of multiphase parameters on the mixing time. In diffusion tests a passive scalar was introduced into the column using a volumetric pump forming a static cloud (batch) of dye, mixing was initiated by bubbling the column in a timely fashion. The temporal evolution of the mixing was characterized by tracking of the background grayscale level in the bubble images. A series of image processing tools were developed for this task to filter the bubbles from each image and track the grayscale value in liquid phase.

In the static tests, increasing the gas superficial velocity did not accelerate the bubble induced mixing process significantly. Detailed study of the temporal evolution of dye concentration shows that normalized concentration of the dye is a function of time (normalized time), and an error-function curve fit provides a good representation of the data. It was found that vibration has a dual effect on mixing time. In lower input powers, vibration decelerates the mixing due to bubble retardation; however, bubble aggregation in higher power inputs provides a slightly faster mixing performance. It should be noted that a vibrating bubble column is an expensive facility, which requires regular maintenance with associate safety requirements and consequently, without a reasonable enhancement in the mixing performance, vibrating a bubble column is not recommended for mixing operations. Dimensional analysis was employed to find a correlation between the non-dimensional mixing time and the non-dimensional input power, results shows the mixing time has an inverse power-law correlation with the specific input power.

CHAPTER VII

DEPENDENCE OF INCLINATION ANGEL ON ANNULAR FLOW LIQUID FILM THICKNESS

7.1 Introduction

This chapter presents an experimental study for characterization of film thickness in gas-liquid annular flow. Contrary to bubbly flow where the gas phase is dispersed within liquid, in annular flow the dispersed phase is liquid. The absence of a sound understanding of the effect of pipe inclination (gravity) on the physical structure of annular flow is an opportunity for experimental initiatives to fill the gap in annular flow research. Thus, further experimental investigation of two-phase flow parameters in annular flow at inclined pipe orientation will contribute to the fundamental understanding of the gas liquid two-phase flow physics. Previously, studies on liquid film thickness in inclined annular flow has been carried out using intrusive instrumentation. The present work aims to explore the problem of film thickness in annular flow using planar laser induced fluorescent (PLIF) a non-intrusive method.

The annular flow regime occurs in numerous industrial practices, including boiling and condensing heat transfer apparatuses, refrigeration and power cycles, boilers, and steam generators. In annular flow, the liquid flows partly as a thin film on the wall(s) and partly as entrained droplets travelling in the turbulent gas core. The central bulk of the gas travels significantly faster than the liquid phase. Gravity tends to descend the liquid film to the bottom region of the pipe. The circumferential drag from the secondary gas-flow, rolling of the liquid

on the wall, and drop deposition on random circumferential locations act synergically to maintain the liquid circumferential distribution uniform. The liquid film is comprised of two regions, the base film and a wavy interface (disturbance waves). The base film is relatively smooth and occupies most of the gas-liquid interface. Shedd & Newell (2004) argue that the base film is similar to a single-phase turbulent boundary layer that extents well into the buffer layer. Above the base film are the disturbance waves, in this region momentum transfer from the gas core is at a higher rate; therefore, the interface is wavy and travels faster than the base film. Similar to other gas-liquid systems, the physics of the interface is very complex. Schubring et al. (2010a,b) argue that increasing the gas flow rate reduces the amplitude (height) of the disturbance waves; in contrast, increasing the liquid flow rate initiates larger waves that stretch longer in the stream-wise direction. For the purpose of clarity in this document *liquid film* refers to the thickness of liquid from the wall up to the gas-liquid interface. The disturbance waves are also the source for liquid drops to be entrained within the gas core. The entrained drops then deposit into the liquid film again. Characterization of entrainment within annular flow regime is utmost demanding due to the nature of the arrangement of phases as well as the rate at which phases travel.

Modeling of annular flow for the most part has been carried out using two concepts namely, *excess liquid* and the *triangular relationship* (Bhagwat, 2015). The excess liquid concept is based on conservation of liquid mass and gives the entrainment fraction by comparing the base film thickness to an ideal case where no entrainment occurs. However, the liquid excess concept is not able to distinguish between the entrained drops from the disturbance wave; therefore, is not able to provide an accurate entrainment fraction, especially in high liquid flow rates where disturbance waves occupy most of the gas-liquid interface. The

triangular relationship is a more sophisticated approach for modeling annular flow. This model is attributed to Hewitt & Hall-Tylor (1970) and establishes two closure relationships between interfacial shear (from pressure drop), liquid film thickness, and liquid film mass flow rate. One closure relationship (Equation 7-1), also known as the film roughness concept, gives the interfacial shear (τ_i) as a function of film thickness (δ) and the film flow rate ($\dot{m}_{film}$). The film roughness concept hypothesizes that the film thickness can be modeled similar to solid-wall roughness in a single-phase confined flow. Note that in Equation 7-1, the interfacial shear (τ_i) and δ can be switched. It is also worth mentioning that the interfacial shear can be calculated from pressure drop (ΔP) measurements using Equation 7-2, where D_p is the pipe diameter and L is the length over which the pressure drop has been measured. The second closure is a relationship that gives the film flow rate ($\dot{m}_{film}$) by integrating the inner variable scaled velocity ($u^+ = u/(\tau_i/\rho_L)^{1/2}$) across the film height. One should note that experimental measurements of the film velocity profile are utterly scares, most of the approaches to the second closure have been carried using Hewitt & Hall-Tylor (1970) recommendation on using the turbulent velocity profile in channel flow for the film velocity profile.

$$\tau_i = F\left(\dot{m}_{film}, \delta\right) \qquad \text{Equation 7-1}$$

$$\tau_i = \frac{\Delta P}{L}\frac{D_p}{4} \qquad \text{Equation 7-2}$$

This chapter aims to study the liquid film thickness in inclined annular flow to improve our understanding of the effect of gravity on film descend towards the bottom section of the pipe. A variable inclination angle pipe setup in the OSU Multiphase Lab, along with the components of a state-of-the-art PIV system from the Experimental Flow Physics Lab (EFPL)

were employed for the current study. The following section (§7.2) gives a summary of the work in the OSU Multiphase Lab in preparation for the measurements as well as details of the instrumentation for the measurements in this chapter. The next section (§7.3) elaborates on the measurement method with a detailed discussion of the experimental setup, instrumentation, and calibration process. A comparison of the current measurements with experimental data from literature at similar conditions will be presented in section 7.4 to validate the current measurements. Then an investigation of the effect of inclination angle as well as phase flow rates on the film thickness (§7.5). Finally, section 7.6 presents the conclusions and remarks for the current chapter.

7.2 Planar Laser Induced Fluorescent (PLIF) Setup

Characterization of liquid film thickness in annular flow is the chief goal of this chapter. Planar laser induced fluorescent (PLIF) technique was selected for film thickness measurements due to its non-invasive nature. Details of the experimental setup and flow control instruments are given in Chapter 3 (section 3.2). The measurements were conducted in the flow visualization and void fraction branch of the setup. The 12.7mm ID polycarbonate transparent pipe provides optical access for visualization of the annular film. See Figure 3-18 for an illustration of the setup, which the PLIF measurement location was a couple diameters upstream of the end of the polycarbonate section. The measurement section was located $187D_p$ downstream of the pipe inlet (gas-liquid spiral mixer). It is worth mentioning that Schubring et al. (2010) and Bhagwat (2015) recommended a development length of $150D_p$ or more for measurements in annular flow regime. In the current work, all of film thickness measurements were carried out at $187D_p$ from the pipe inlet. Figure 7-1 presents the regime map specifically

developed for the current experimental setup (Bhagwat, 2015). All of the test conditions were compared against this map to ensure that measurements were conducted in the annular flow regime.

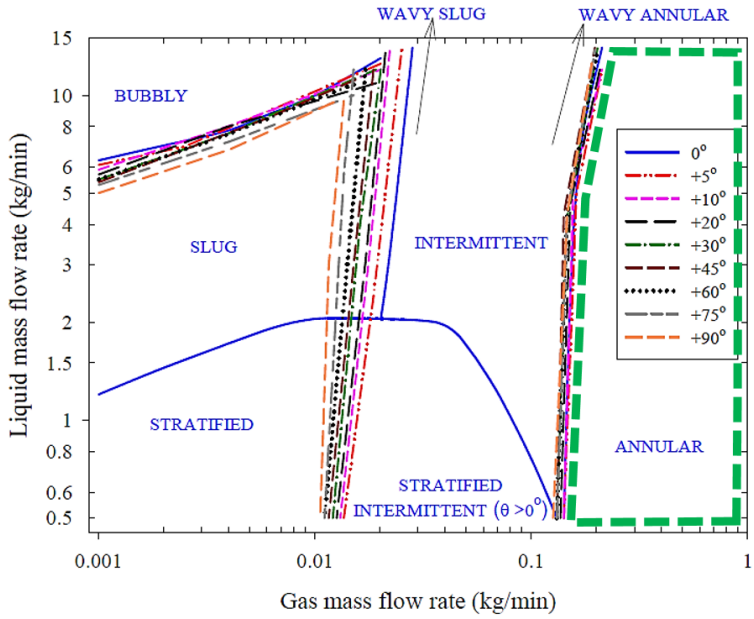

Figure 7-1. Flow pattern map for upward inclined pipe orientations, adapted from Bhagwat (2015). The annular flow regime is demarcated by the region outlined with the thick, green dashed line.

A monochromic pulsing laser light provided excitation to the fluorescent material and a camera recorded the event simultaneously. Laser pulses with 532nm wavelength from a double pulse, single-cavity Nd:YAG laser (Gemini 100-15, New Wave Research, Fermont, CA, USA) provided the excitations with a maximum pulse of 15Hz and a pulse width in the range of 3-5 ns. An articulated (mirror) arm (Laserpulse^{TM} light arm 610015, TSI, Minneapolis, MN, USA) provided flexibility in delivering the laser beam for PLIF measurements. Using T-slotted aluminum rails, a mounting structure was built around the pipe test section for rigidly mounting the camera (see Figure 7-2) as well as the articulated arm and laser optics. This structure ensured that the camera spatial calibration and laser position was consistent

throughout the PLIF tests. The test section was also enforced against flow-induced vibrations using wooden mounts. The unsteady large gas-liquid structures can produce violent vibrations of the pipe; these vibrations can alter the position of the wall by around 30±10μm.

Figure 3-20 provides a schematic of the test section that shows that the thickness of the laser sheet (W) has a direct effect on the uncertainty associated with the film thickness measurement (Ξ_δ) due to the curvature of the pipe. This error was calculated based on the assumption that the film thickness is approximately 200 μm. Table 7-1 shows the resulting bias error in film thickness measurements due to the laser sheet thickness. The target laser sheet thickness in the current work was 0.7 mm or thinner, which results in a bias error of less than 4 μm. This is sufficiently small that it is within the spatially resolution of the current setup.

Figure 7-2. Laser and camera positioning on the variable inclination multiphase pipe flow setup, green dashed lines represent the laser beam path used to reach the test section.

Table 7-1. Estimation of the PLIF measurement error due to thickness of the laser sheet.

D_p (mm)	W (mm)	δ (mm)	Ξ_δ (mm)	Ξ_δ / δ (%)
12.7	5	0.2	0.513	10%
12.7	4	0.2	0.323	8%
12.7	3	0.2	0.180	6%
12.7	2	0.2	0.0792	4%
12.7	1	0.2	0.0197	2%
12.7	0.7	0.2	9.65E-03	1%
12.7	0.1	0.2	1.97E-04	0.2%
12.7	0.05	0.2	4.92E-05	0.1%

Producing a laser sheet of 1mm or lower thickness from a laser beam with ~5mm diameter requires a suite of optical lenses. A custom made optical setup was employed to produce a thin laser sheet with a thickness of ~0.7mm at the measurement location as illustrated in the schematic shown in Figure 7-3. Later a beam collimator (LaVision Inc, Ypsilanti, MI, USA) and an apperature was used to produce a thin beam and spreaded into sheet via a glass rode. PLIF images were recorded using a sCMOS camera (Imager sCMOS, LaVision Inc, Ypsilanti, MI, USA) with spatial resolution of 2600 × 2200 pixels, maximum frame rate of 100 Hz, and a maximum pixel size of 6.5μm. The camera was equipped with a NAVITAR Zoom 7000 optical lens at a nominal working distance of 127mm the field-of-view was 9.5mm × 8mm. A programmable time unit (PTU X, LaVision Inc, Ypsilanti, MI, USA) was used for synchronizing the laser and the camera under the control of a PIV software package (Davis, LaVision Inc, Ypsilanti, MI, USA). In all of the experiments, the camera field-of-view was kept fixed at the bottom wall of the polycarbonate pipe. A home-made calibration target was employed for spatial calibration of the images. The calibration target in the present work was

made of an aluminum rod with a half-circle cross-section, a squared-mesh grid (1mm × 1mm in mesh size) was added on the rod for providing spatial reference for calibration. The optical distortions due to the change of refractive index and the NAVITAR Zoom 7000 optical lens was corrected using a 3rd order polynomial fit mapping scheme for spatial calibration. The spatial calibration and mapping processes was carried out using PIV software Davis v8.0 (LaVision Inc, Ypsilanti, MI, USA). Figure 7-4 shows images of the calibration target before (Figure 7-4a) and after (Figure 7-4b) the spatial calibration and mapping.

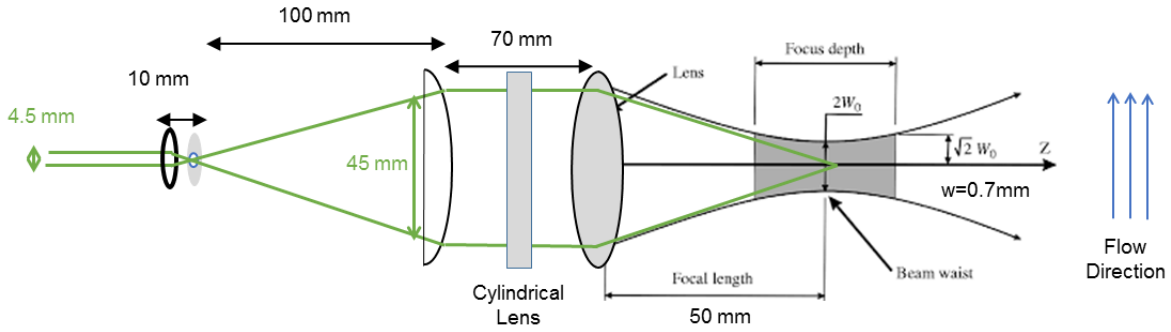

Figure 7-3. Schematics of the custom made optical setup for producing a thin laser sheet.

Rhodamine-6G fluorescent dye (Sigma-Aldrich, St Louis, MO, USA) was introduced into the liquid for PLIF visualization of the liquid film. The dye gives a red color to water, in the present work a 10wppm concentration of dye was selected based on manual inspection of the PLIF images. In a methanol solution, Rhodamine-6G absorbs light maximally at 528 nm and emits light maximally at 551 nm. Care was given to assure that the fluorescent dye does not alter properties of the liquid phase (i.e. surface tension). A long pass optical filter was mounted on the NAVITAR Zoom 7000 to attenuate the 532 nm laser light and pass only the

Stokes-shifted light (~551 nm). Figure 7-5 shows a sample of flow visualization in annular flow demonstrating the liquid film at the walls and an entrained drop of liquid.

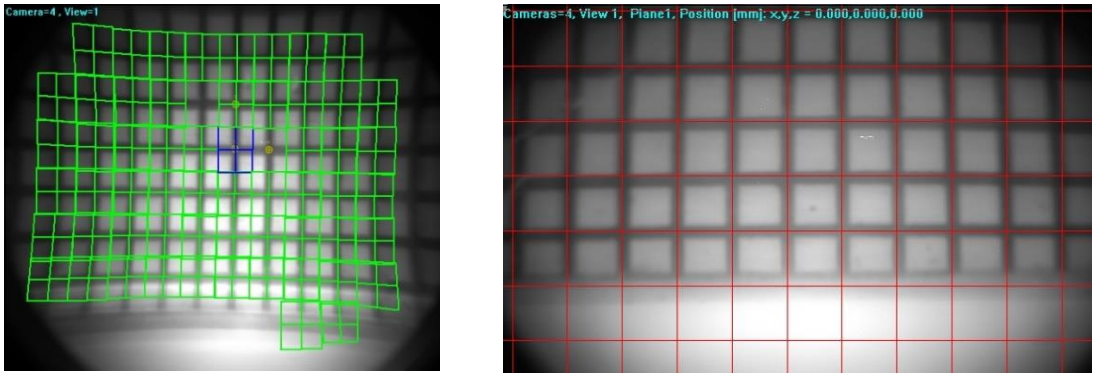

(a) (b)

Figure 7-4. Spatial calibration for mapping the PLIF images to correct for the effects of refractive index and optical distortions from the NAVITAR Zoom 7000 lens.

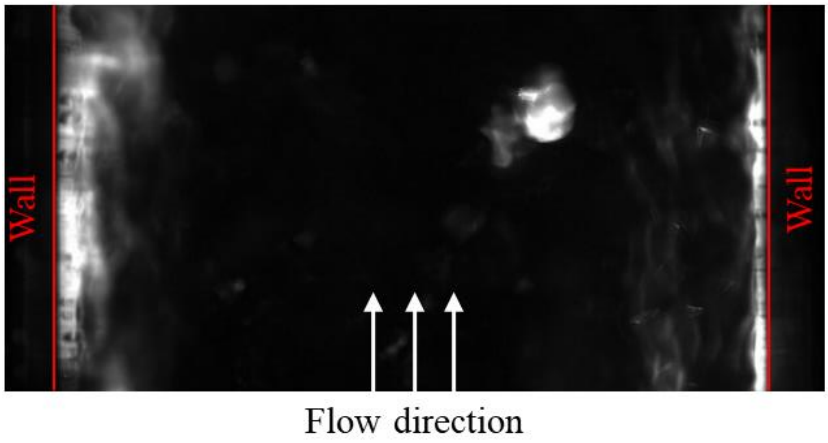

Figure 7-5. Flow visualization of horizontal annular flow using PLIF with $\dot{m_G}$ = 0.48kg/min and $\dot{m_L}$ = 1.8kg/min.

7.3 PLIF Processing

Raw images of the annular film were taken using DaVis and stored on an external hard drive. Images were then manually inspected for non-interfacial features such as bubbles in the film, and drops near the film, as well as large scale turbulent clouds. The aforementioned features corrupt the measurement; therefore, care was taken to manually omit images with such

features from the measurement samples. ImageJ was the primary image processing tool for the film thickness measurements. A series of image processing steps were devised for the film thickness measurement.

The calibrated (mapped and spatially scaled) Images were exported from DaVis for film thickness measurement using ImageJ, here JPEG format was employed for exporting. Prior to data collection, the flow visualization section of the setup was filled with liquid phase (containing 10wppm Rhodamine-6G) and images were taken, these images were then compared to those of annular film to confirm the consistency of the wall location throughout the experiments. The background was first removed from each image to enhance the edges of the film; the background natural color was set to black. The out of focus portions and unintended reflections were eliminated by using a threshold and the *Max* function to produce binary images. *Max* function allows pixels in the film region with a high grayscale value to be replaced by a given constant; while other pixels (with lower grayscale value) will drop to zero (black). At this point, every pixel in the image is either black (background) or has a constant grayscale (film region). By switching the background points to white and film region to black a binary image was produced that can be used for film thickness measurement. At this point, *Despeckle* function eliminates the noise without changing the film and the image is ready for *Analyze Particles* function, which gives the size and geometrical characteristics of the film region. The threshold in this work was set to 105 and changing the threshold by ±10 did not change the measurements more than ± 2.5%. It is worth mentioning that the maximum grayscale level within the film region is a good criterion to find a proper threshold iteratively. This means that depending on the laser intensity and concentration of the fluorescent dye, the threshold must be adjusted. In the present work, the laser intensity and Rhodamine-6G

concentration were kept constant, therefore all images were processed using a consistent code. The mean film thickness, as well as standard deviation of the film thickness, was measured from the PLIF images. It is worth mentioning that the standard deviation of the film thickness was then used as error bars for plotting the film thickness measurements. This does not represent the measurement uncertainty, but rather the temporal variation of the film thickness. Figure 7-6 shows a sample of raw PLIF image before the processing (Figure 7-6a) and a processed imaged (Figure 7-6b) there the film has been detected and picked up by the processing scheme.

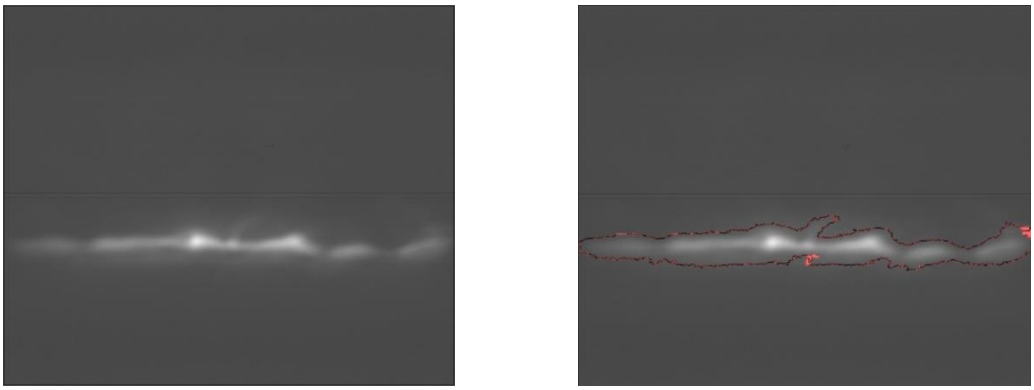

(a) (b)

Figure 7-6. (a) Raw PLIF image exported from DaVis and (b) processed PLIF image with the film boundaries detected and marked with red contour.

The present method gives the liquid film thickness (i.e. base film and the disturbance wave); however, without an accurate estimation of the base film thickness, characterization of the waves is not possible. Rodriguez (2004) shows that the ratio of the liquid film thickness to that of base film thickness is approximately 2, which Schubring (2010a, b) supported this finding with a refined ratio of 1.85.

7.4 Test Setup Validation

The accuracy of the measurement in the current work was validated against the experimental data from the literature. Film thickness measurements were carried out in horizontal orientation for a range of air and water mass flow rates (Reynolds numbers) that closely match the work of Shedd & Newell (2004). Therefore, no extrapolation from graphical data of other works was needed. The data from Shedd & Newell (2004) is the only data, to author's knowledge that matches the features of the present experimental setup (i.e. pipe diameter and gas and liquid Reynolds numbers based on pipe diameter and mass flow rates).

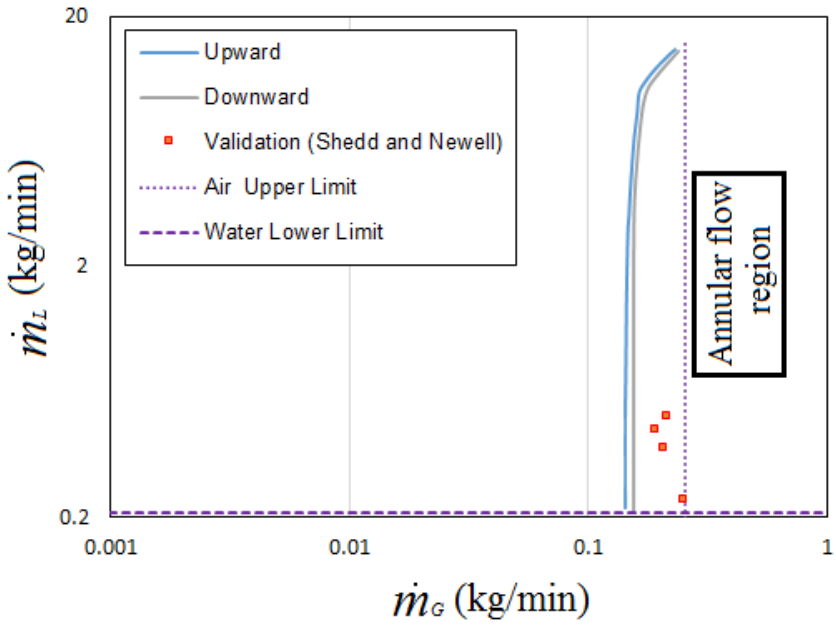

Figure 7-7. Validation test conditions (red square-dots) against the boundaries of annular flow (reproduced from Bhawgat, 2015). The blue and gray lines are the boundaries of the annular flow in upward and downward vertical pipe orientation.

With regard to the setup's ability to produce test conditions in terms of flow rates, four test conditions were reproduced from Shedd & Newell (2004) to validate the liquid film thickness measurements. Figure 7-7 shows the selected test conditions from Shedd & Newell

(2004) against the boundary for annular flow. The interested reader can refer to Bhagwat (2015) for a detailed regime map produced specifically for the current experimental setup. Table 7-2 presents the validation test conditions in terms of the liquid and gas mass flow rates and the corresponding Reynolds number. It is worth mentioning that care was given to match the Reynolds numbers within 5% of the target values.

Table 7-2. Flow conditions for the data obtained for validation of the test setup.

$\dot{m}_G$ (kg/min)	$\dot{m}_L$ (kg/min)	Re_{SL} (--)	Re_{SG} (--)
0.192	0.444	740	17,800
0.210	0.378	630	19,500
0.216	0.504	840	20,000
0.252	0.234	390	23,400

Figure 7-8 shows the estimated base film thickness for the test conditions given in Table 7-2. Comparison of the current data with that of Shedd & Newell (2004) validates the current setup. It is worth mentioning that the PLIF measurements in the current study directly measure the entire film height (i.e. base film height and disturbance wave height). Experimental results based on statistical analysis of annular film thickness (Schubring et al., 2010a) shows that the ratio of the film height to base film is 1.85. Using the aforementioned ratio between the film thickness and base film, the base film was calculated; Figure 7-8 shows that the base film measurement in the current study is in excellent agreement with that of Shedd & Newell (2004). In addition, results from Figure 7-8 show that gas and liquid flow rates effect the base film height. However, this effect is not significant. In most film roughness models, the standard deviation of the film thickness $\sigma(\delta)$ divided by the mean film thickness (δ) is used to find the interfacial shear. This ratio for the current study is provided in Figure 7-9. The

current work shows that the ratio of the standard deviation of the film thickness to the mean film thickness was sensitive to gas and liquid flow rates, which is consistent with Schubring et al. (2010a). Furthermore, experimental data from Schubring (2009) over a wide range of gas and liquid flow rates, shows the ratio of $\sigma(\delta)/\delta$ increases as a result of both increasing the liquid flow rate and decreasing the gas flow rates. Figure 7-9 shows that with a constant gas superficial velocity, increasing the liquid superficial velocity increases $\sigma(\delta)/\delta$. Consequently, in the current conditions tested (Figure 7-9) the interfacial shear increases, which results in a greater pressure drop.

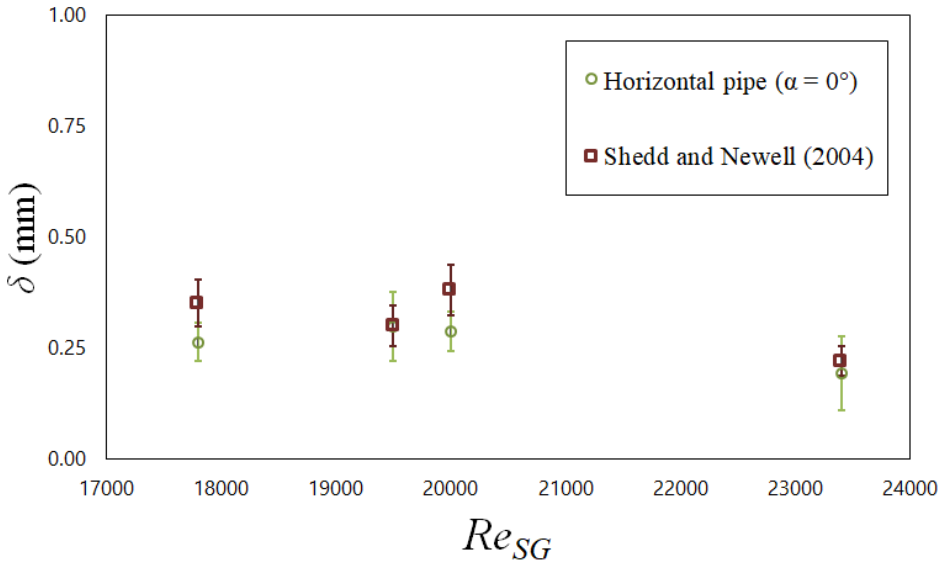

Figure 7-8. Comparison of the base film height from the current work to that of Shedd & Newell (2004).

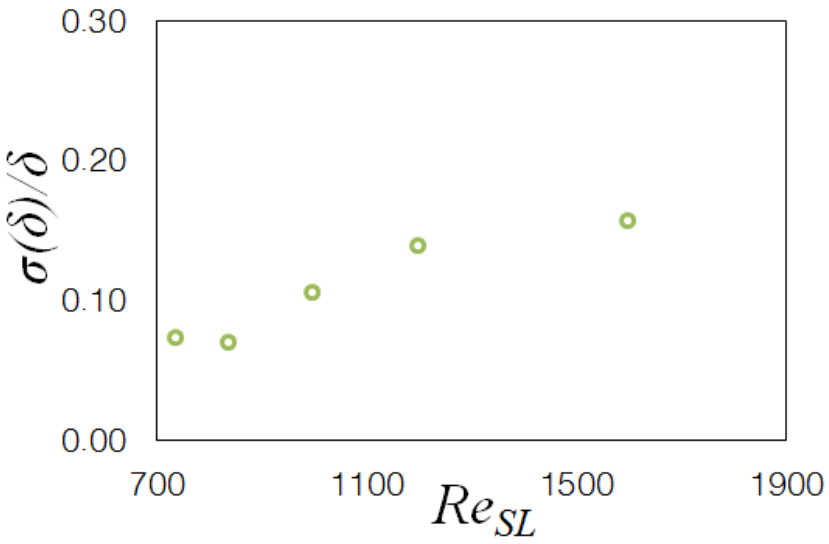

Figure 7-9. Ratio of the standard deviation of the film thickness (film roughness) to the film thickness plotted versus the Reynolds number of superficial liquid velocity ($Re_{SG} \approx 20{,}000$).

7.5 Sensitivity to Inclination Angle

This section presents the results of film thickness measurements in the inclined pipe configuration to study the effect of gravity on film thickness. Figure 7-10 presents the annular film thickness in downward orientations (i.e. $\alpha = -5°$ and $-20°$) in comparison with the film thickness in the horizontal pipe. Figure 7-10 shows a constant decreasing trend in annular film thickness with increasing inclination angle. It is worth mentioning that except in vertical downward annular flow, the circumferential distribution of the film thickness is asymmetric due to the effect of gravity. It is interesting to see that in downward tests the change of pipe orientation has a more significant effect on the liquid film thickness in comparison with the change of flow rates. It is worth mentioning that the test conditions in Figure 7-10 are the same ones from Table 7-2, here the liquid superficial velocity (so as Re_{SL}) does not change significantly. From Figure 7-10 and detail inspection of the flow behavior, increasing the

downward pipe inclination angles attributes to enhancing the uniformity of the circumferential film thickness distribution by decreasing the effect of gravity.

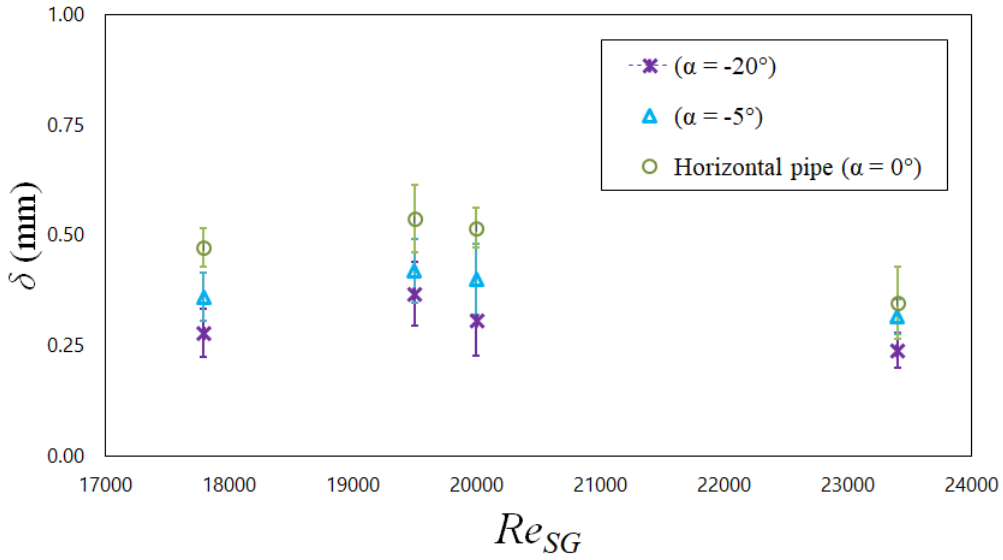

Figure 7-10. Annular liquid film thickness in downward orientations; effect of gas superficial velocity.

Figure 7-11 presents the film thicknesses in upward pipe orientations (α = +5°, +20°, +45°, and +60°), and Table 7-2 provides the corresponding flow rates. From Figure 7-11 it can be seen that increasing the inclination from horizontal to upward inclinations results in a dual effect on film thickness. It was expected to see a constant decreasing trend in annular film thickness; however, some test conditions (e.g. +45°) deviate from this general decreasing trend. It is known that in upward test conditions if the pipe inclination is steep enough the liquid film drifts backward. This phenomenon is known as flow (film) reversal and could be either local or global depending on pipe orientation (inclination angle) and interfacial shear. Bhawgat (2015) argues that film reversal occurs when the gas phase is not able to carry the liquid along due to lack of interfacial shear at the slip boundary at high gas flow rates. Hewitt et al. (1985) and Mao & Dukker (1993) identified the onset of flow reversal when the frictional pressure

drop decays to zero. Bhawgat (2015) argues that in the current experimental setup the frictional pressure drop that corresponds to flow reversal occurs when the scaled gas velocity is in the range of 0.2< Fr_{SG} <0.35. The scaled gas superficial and non-dimensional liquid superficial velocity are defined in Equation 7-3 and Equation 7-4, respectively, as Froude numbers.

$$Fr_{SG} = U_{SG}\sqrt{\frac{\rho_G}{gD_P(\rho_L - \rho_G)}} \qquad \text{Equation 7-3}$$

$$Fr_{SL} = U_{SL}\sqrt{\frac{\rho_L}{gD_P(\rho_L - \rho_G)}} \qquad \text{Equation 7-4}$$

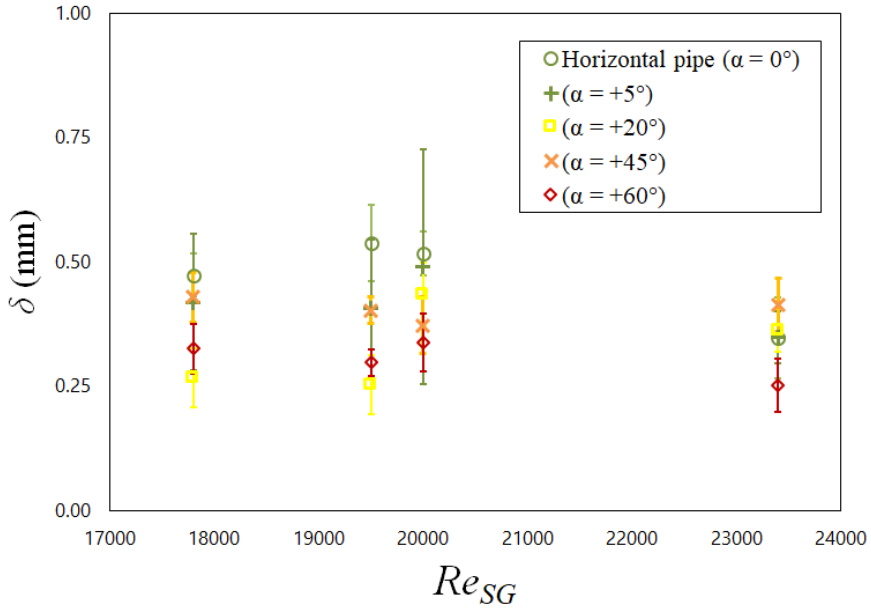

Figure 7-11. Annular liquid film thickness in upward orientations; effect of gas superficial velocity.

Bhawgat (2015) also provides experimental measurements of the frictional pressure drop and argues that Fr_{SG} ~ 0.4 corresponds to a local maximum in frictional pressure drop when the inclination is α > +10°. The increasing roughness in this region is due to significant

waviness of the gas-liquid interface. Figure 7-11 shows that the standard deviation of the film thickness (error bars) increases in the upward conditions. Furthermore, similar to downward flow scenarios, the inclination angle produces a more acute effect on film thickness in comparison with gas flow rate.

Table 7-3. Flow conditions for the study of liquid flow rate on annular film thickness.

$\dot{m}_G$ (kg/min)	$\dot{m}_L$ (kg/min)	Re_{SL} (--)	Re_{SG} (--)
0.212	0.38	630	19600
0.212	0.42	700	19600
0.212	0.60	1000	19600
0.212	0.78	1200	19600
0.212	0.95	1600	19600

Following the investigation of the effect of gas flow rate, a series of tests were conducted to study the effect of liquid flow rate on the thickness of annular liquid film, these test conditions are given in Table 7-3. In these tests the gas superficial velocity was held constant (0.121 kg/min) and the liquid mass flow rate was tested in the range of $0.38 < \dot{m}_L <$ 0.95 kg/min. The effect of pipe inclination was tested in two downward (i.e. $\alpha = -5°$ and $-20°$) and four upward (i.e. $\alpha = +5°$, $+20°$, $+45°$, and $+60°$) orientations and were compared to the horizontal data. Figure 7-12 shows the effect of increasing the liquid superficial velocity on the annular film thickness in downward orientations. Results are showing that the annular film thickness is insensitive to liquid superficial velocity. However, the film thickness in downward pipe orientations is consistently smaller than that of the horizontal pipe. This film thickness reduction may be the result of an increased rate of drop entrainment followed by the random deposition of the drop back into the film. This process improves the uniformity of the circumferential film thickness distribution.

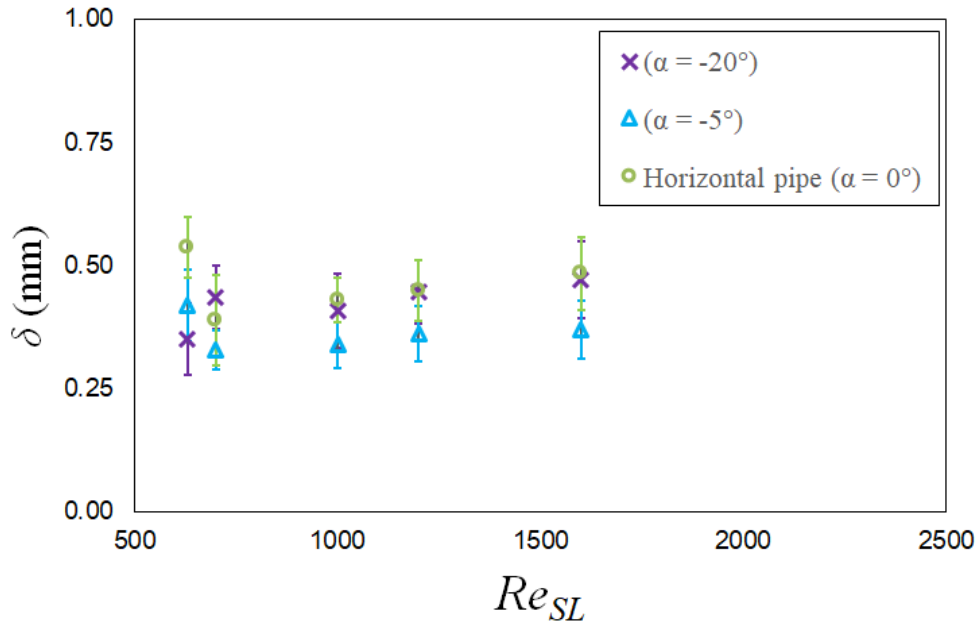

Figure 7-12. Annular liquid film thickness in downward orientations; effect of liquid superficial velocity.

Figure 7-13 shows the annular film thickness at different liquid superficial velocities in downward orientations. Here the annular film is not sensitive to increasing the liquid superficial velocity. As it was previously mentioned, the current test conditions in the upward orientations was not subjected to flow reversal, therefore the film thickness does not exhibit a significant change with inclination angle. However, it can be seen from Figure 7-13 that increasing the inclination angle in upward orientations tend to decrease the film thickness. In addition, results in Figure 7-13 show that increasing the inclination angle reduces the standard deviation of the film thickness (error bars); thus, the film surface becomes smoother with increasing inclination angle.

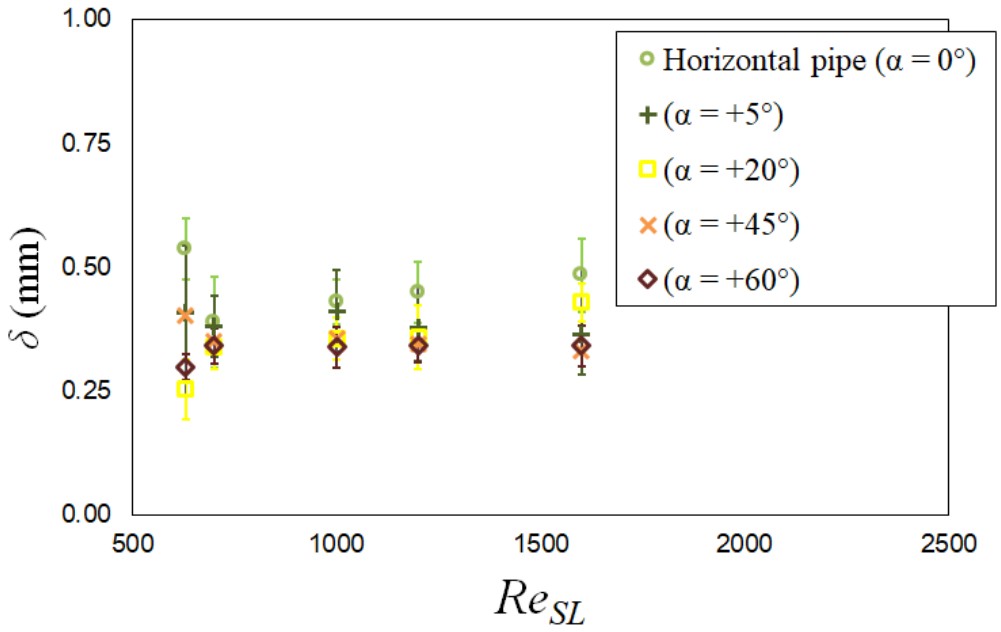

Figure 7-13. Annular liquid film thickness in upward orientations; effect of liquid superficial velocity.

Figure 7-14 shows the ratio of the standard deviation to the mean of the film thickness, which is commonly referred to as the average roughness (Schubring, 2009), for all conditions tested. The majority of test conditions have an average roughness of approximately 0.22, this could be due to the limited range of gas and liquid flow rates in the current study. Experimental data from Geraci et al. (2007) shows that at 45° inclination angle the liquid film thickness decreases in comparison with the horizontal pipe orientation, this is in agreement with the current measurements (see Figure 7-13). Figure 7-14 shows that the average roughness at the higher gas superficial velocities exhibits a significant rise; this implies that the liquid film surface at 45° of pipe inclination angle exhibits larger fluctuations at higher gas flow rates tested. Additionally, current data shows both average roughness (see Figure 7-14) and average film thickness (see Figure 7-13) at 5° of pipe inclination angle are relatively scattered. Since

the data does not exhibit a consistent trend, the source of this scatter is not obvious and a more detailed investigation is required.

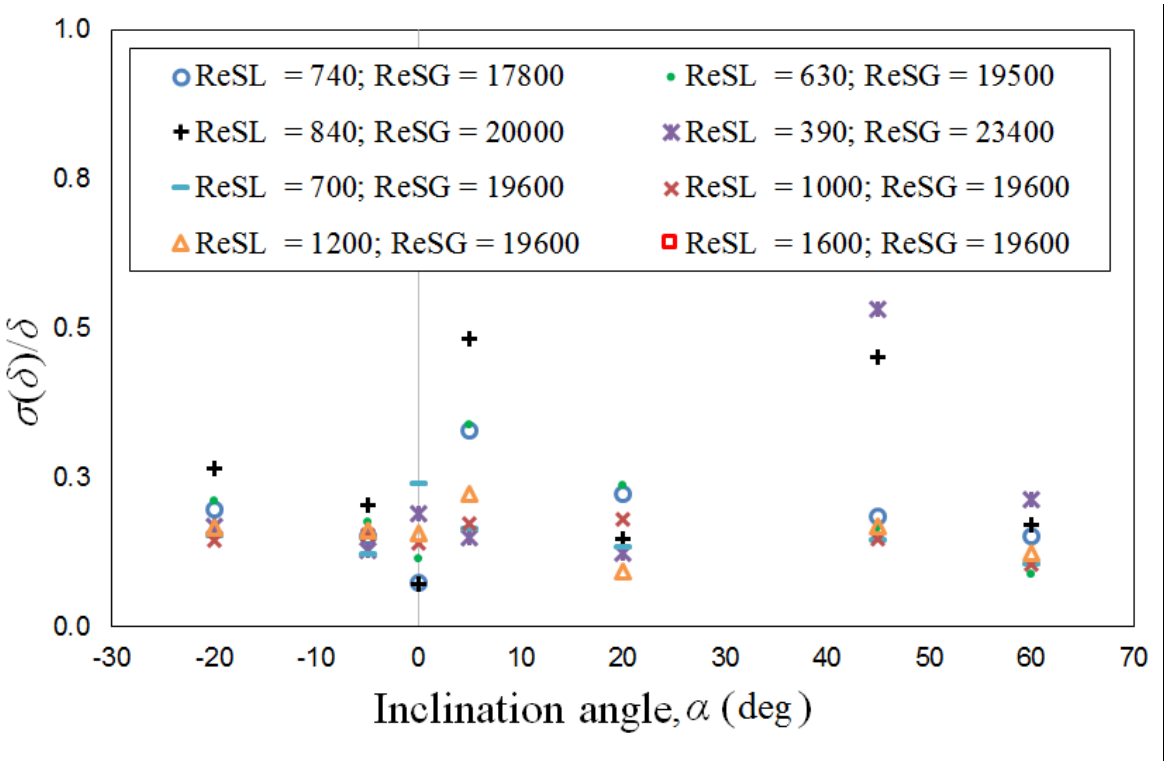

Figure 7-14. Film average roughness (ratio of film thickness standard deviation to the average film thickness).

7.6 Conclusions and Remarks

This chapter presents an experimental study on liquid film thickness in the annular flow regime. The main objective of this work was to establish a non-intrusive method for accurate film thickness measurement. Planar laser induced fluorescent (PLIF) was selected to meet the requirements of the current work. A PIV system was used for collecting the PLIF images of the liquid film. Trace amounts of Rhodamine-6G were used for visualization of the annular liquid film. An automated image-processing scheme was developed in ImageJ for measuring the film thickness. The accuracy of the film thickness measurement was validated against

experimental data from the literature at matching test conditions (Shedd & Newell, 2004). The current experimental setup was the first of its kind variable inclination angle for a multiphase flow loop, which allows the pipe orientation to be varied from vertical upward flow (α = +90°) to vertical downward (α = –90°). The current work explores the effect of gravity on annular liquid film thickness in two downward (α = –5° and –20°), a horizontal (α = 0°), and four upward (α = +5°, +20°, +45° and +60°) inclination angles. For each inclination angle a total of eight flow conditions were tested, results show that the average film thickness was almost insensitive to the change of flow rate. However, changing of inclination angle had a distinct effect on the liquid film thickness. In downward orientations the circumferential distribution of the film thickness becomes more uniform and a reduction of film thickness at the lower wall was observed. In upward cases, the film thickness exhibits fluctuations due to increases in the interfacial roughness due to the selected range of gas and liquid flow rates.

CHAPTER VIII

CONCLUSIONS AND RECOMMENDATIONS

8.1 Conclusions

The current work studied bubbly and annular flow by exploring the multiphase parameter space via flow visualization. Bubble size and void fraction in bubbly flow were investigated in a vibrating bubble column setup with a parametric study of the effect of the injection method, liquid properties, gas superficial velocity, vibration characteristics, and bubble column geometry. Annular flow was investigated in a variable inclination angle, two-phase flow setup with the objective of understanding the effect of inclination angle on annular liquid film thickness. Addressing the research objectives of the current study in Chapter 1, the following is a brief summary of the achievements, key results, and proposed models.

Bubble size and Void fraction in a Static Sparged Bubble Column in the Homogenous and Heterogeneous Regimes

1. Increasing the viscosity within the range tested facilitated the regime transition from homogenous bubbly to churn-turbulent. Regime transition was mark with two distinct behaviors. First a drastic change in the PDF of BSD from near Gaussian to a “spike” shaped distribution. Second, the deviation from the linear trend between void fraction and gas superficial velocity.

2. Dimensional analysis was used to produce a correlation between the scaled specific input power (P_m) and the scaled bubble size (d_{32}). This correlation (Equation 4-4) was validated against experimental data from a parametric study that tested the effect of liquid properties as well as gas superficial velocity. Further validations were carried out using experimental data from the literature.

Bubble size from Single Point Injection in a Static Bubble Column

1. The maximum peak in the PDFs of BSD was used to identify a new bubble length scale, termed the most frequent bubble size (d_{mf}). The most frequent bubble size (d_{mf}) is related to the size of turbulent structures created in the bubble wakes. Therefore, the difference between d_{32} and d_{mf} provides a nominal range of bubble sizes expected within a given flow.
2. Sauter mean diameter (d_{32}) was scaled with the specific input power using experimental measurement of bubble size from a parametric study. This scaling law (Equation 5-1) is in agreement with the findings of Hinze (1955) for shear breakage.

Bubble size and Void Fraction from Single Point Injection in a Vibrating Bubble Column

1. Under vertical vibration, the Sauter mean diameter scaled with the specific input power (Equation 5-1).
2. Measured bubble sizes were consistent with the prediction by the Hinze (1955) correlation that predicts the maximum stable bubble size. The proportionality coefficient in the present work (k = 3.4) is different from those reported in shear bubble breakage and pulsing column literature (k = 1.67 and 1.7, respectively).

3. A physics-based model (Figure 5-17) was proposed to predict the void fraction under vibration. The model was validated against experimental data from Waghmare et al. (2007) and Still (2012). This model successfully predicts the void fraction under vertical vibration until the onset of sloshed-induced surface entrainment (*M(H)=0.3*).

Mixing of a Passive Scalar in a Sparged Injection Vibrating Bubble Column

1. Experimental results show that the temporal change of the normalized concentration of a passive scalar under bubble-induced diffusion is well approximated with an *error-function*.
2. Vibration exhibited a dual effect on mixing time of the passive scalar. In comparison with a static column at matching specific input powers, vibration decelerates the mixing due to bubble retardation at lower specific input powers. However, bubble aggregation at higher power inputs provides a slightly faster mixing performance.

Annular Liquid Film Thickness at Variable Inclination Angles

1. Experimental results showed that the annular liquid film thickness was relatively insensitive to gas and liquid flow rates. However, the inclination angle has a distinct effect on the liquid film thickness.
2. In downward orientations, the film circumferential distribution becomes more uniform and a reduction of film thickness at the lower wall was observed. Increasing the inclination angle towards vertical downward flow improves the uniformity of film thickness.

3. In upward cases the film thickness exhibits larger fluctuations due to an increase in the interfacial roughness for the selected range of gas and liquid flow rates.

8.2 Recommendations

Based on the experimental work from the current study, certain limitations and shortcomings of the two-phase flow knowledge have been identified to address as recommendations for future work. These recommendations consider the limitation of the current research facilities and instrumentation.

1. Experimentally investigate the effect of injector characteristic length scale and column diameter on bubble size for further validation of Equation 4-2.
2. Experimentally investigate the effect of liquid density and surface tension on bubble size for further validation of Equation 4-2.
3. Experimentally investigate the mixing of a passive scalar under bubble-induced diffusion using PLIF imaging and study the diffusion at different locations along the bubble column.
4. Experimentally characterize the liquid velocity agitations from a bubble swarm in non-Newtonian liquids using a dual probe (hot-film and optical probe).
5. Experimentally study the bubble formation mechanism as well as experimentally measured the bubble size distribution in a shear-thinning non-Newtonian liquid and study the regime transition.

6. Experimentally measure the velocity profile within the annular liquid film and produce a non-dimensional velocity profile using the universal boundary layer scaling coordinates.
7. High quality imaging of the annular liquid film to characterize the ripple and disturbance waves

REFERENCES

Abbas, M., Billet, A. M., & Roig, V. (2009). Experiments on mass transfer and mixing in a homogeneous bubbly flow. In *ICHMT Digital Library Online*. Begel House Inc.

Abràmoff, M. D., Magalhães, P. J., & Ram, S. J. (2004). Image processing with ImageJ. *Biophotonics International*, 11(7), 36-42.

Akita, K., & Yoshida, F. (1974). Bubble size, interfacial area, and liquid-phase mass transfer coefficient in bubble columns. *Industrial & Engineering Chemistry Process Design and Development*, 13(1), 84-91.

Alamu, M. B. (2010). Investigation of periodic structures in gas-liquid flow (Doctoral dissertation, University of Nottingham).

Alekseenko, S. V., Antipin, V. A., Cherdantsev, A. V., Kharlamov, S. M., & Markovich, D. M. (2008). Investigation of waves interaction in annular gas–liquid flow using high-speed fluorescent visualization technique. *Microgravity Science and Technology*, 20(3-4), 271-275.

Alekseenko, S., Antipin, V., Cherdantsev, A., Kharlamov, S., & Markovich, D. (2009). Two-wave structure of liquid film and wave interrelation in annular gas-liquid flow with and without entrainment. *Physics of Fluids*, 21(6), 061701.

Alméras, E., Risso, F., Roig, V., Cazin, S., Plais, C., & Augier, F. (2015). Mixing by bubble-induced turbulence. *Journal of Fluid Mechanics*, 776, 458-474.

Alméras, E., Cazin, S., Roig, V., Risso, F., Augier, F., & Plais, C. (2016a). Time-resolved measurement of concentration fluctuations in a confined bubbly flow by LIF. *International Journal of Multiphase Flow*, 83, 153-161.

Alméras, E., Plais, C., Euzenat, F., Risso, F., Roig, V., & Augier, F. (2016b). Scalar mixing in bubbly flows: Experimental investigation and diffusivity modelling. *Chemical Engineering Science*, 140, 114-122.

Alméras, E., Plais, C., Roig, V., Risso, F., & Augier, F. (2018). Mixing mechanisms in a low-sheared inhomogeneous bubble column. *Chemical Engineering Science*, 186, 52-61.

Al-Sarkhi, A., Sarica, C., & Magrini, K. (2012). Inclination effects on wave characteristics in annular gas–liquid flows. *AIChE Journal*, *58*(4), 1018-1029.

Anastasiou, A. D., Kazakis, N. A., Mouza, A. A., & Paras, S. V. (2010). Effect of organic surfactant additives on gas holdup in the pseudo-homogeneous regime in bubble columns equipped with fine pore sparger. *Chemical Engineering Science*, 65(22), 5872-5880.

Andreussi, P., Asali, J. C., & Hanratty, T. J. (1985). Initiation of roll waves in gas-liquid flows. *AIChE Journal*, 31(1), 119-126.

Asali, J. C., & Hanratty, T. J. (1993). Ripples generated on a liquid film at high gas velocities. *International Journal of Multiphase Flow*, 19(2), 229-243.

Asali, J. C., Hanratty, T. T., & Andreussi, P. (1985). Interfacial drag and film height for vertical annular flow. *AIChE Journal*, 31(6), 895-902.

Baird, M. H. I. (1963). Resonant bubbles in a vertically vibrating liquid column. *The Canadian Journal of Chemical Engineering*, 41(2), 52-55.

Baird, M. H. I. & Davidson, J. F. (1962). Gas absorption by large rising bubbles. *Chemical Engineering Science*, 17(2), 87-93.

Baird, M. H. I. & Garstang, J. H. (1972). Gas absorption in a pulsed bubble column. *Chemical Engineering Science*, 27(4), 823-833.

Basha, O. M., Sehabiague, L., Abdel-Wahab, A., & Morsi, B. I. (2015). Fischer–Tropsch synthesis in slurry bubble column reactors: experimental investigations and modeling–a review. *International Journal of Chemical Reactor Engineering*, 13(3), 201-288.

Belt, R. J. (2007). On the liquid film in inclined annular flow. (Doctoral dissertation, Delft University of Technology).

Berna, C., Escrivá, A., Muñoz-Cobo, J. L., & Herranz, L. E. (2014). Review of droplet entrainment in annular flow: Interfacial waves and onset of entrainment. *Progress in Nuclear Energy*, 74, 14-43.

Besagni, G., Di Pasquali, A., Gallazzini, L., Gottardi, E., Colombo, L. P. M., & Inzoli, F. (2017a). The effect of aspect ratio in counter-current gas-liquid bubble columns: Experimental results and gas holdup correlations. *International Journal of Multiphase Flow*, 94, 53-78.

Besagni, G., Inzoli, F., Ziegenhein, T., & Lucas, D. (2017b). Computational Fluid-Dynamic modeling of the pseudo-homogeneous flow regime in large-scale bubble columns. *Chemical Engineering Science*, 160, 144-160.

Besagni, G., Inzoli, F., & Ziegenhein, T. (2018). Two-Phase Bubble Columns: A Comprehensive Review. *ChemEngineering*, 2(2), 13.

Besnaci, C., Roig, V., & Risso, F. (2010). Mixing induced by a random dispersion at high particulate Reynolds number. In *Proceedings of 7th International Conference on Multiphase Flow*, Tampa.

Bhagwat, S. M. (2015). Experimental measurements and modeling of void fraction and pressure drop in upward and downward inclined non-boiling gas-liquid two phase flow (Doctoral dissertation, Oklahoma State University).

Bhagwat, S. M., & Ghajar, A. J. (2012a). Similarities and differences in the flow patterns and void fraction in vertical upward and downward two phase flow. *Experimental Thermal and Fluid Science*, 39, 213-227.

Bhagwat, S. M., & Ghajar, A. J. (2012b). Flow pattern and pipe orientation independent semi-empirical void fraction correlation for a gas-liquid two phase flow based on the concept of drift flux model. In *ASME 2012 Heat Transfer Summer Conference collocated with the ASME 2012 Fluids Engineering Division Summer Meeting and the ASME 2012 10th International Conference on Nanochannels, Microchannels, and Minichannels* (327-336). American Society of Mechanical Engineers.

Bhagwat, S. M., & Ghajar, A. J. (2014). A flow pattern independent drift flux model based void fraction correlation for a wide range of gas–liquid two phase flow. *International Journal of Multiphase Flow*, 59, 186-205.

Bhagwat, S. M., & Ghajar, A. J. (2015a). An Empirical Model to Predict the Transition Between Stratified and Nonstratified Gas–Liquid Two-Phase Flow in Horizontal and Downward Inclined Pipes. *Heat Transfer Engineering*, 36(18), 1485-1494.

Bhagwat, S. M., & Ghajar, A. J. (2015b). Modified liquid entrainment fraction correlation for varying pipe orientation and system pressure. *International Journal of Multiphase Flow*, 74, 1-4.

Bhagwat, S. M., & Ghajar, A. J. (2016a). Experimental investigation of non-boiling gas-liquid two phase flow in upward inclined pipes. *Experimental Thermal and Fluid Science*, 79, 301-318.

Bhagwat, S., & Ghajar, A. J. (2016b). Measurements of Void Fraction, Pressure Drop and Heat Transfer in Horizontal and Downward Inclined Gas-Liquid Stratified Flow. In *9th International Conference on Multiphase Flow*

Bhagwat, S. M., & Ghajar, A. J. (2017). Experimental investigation of non-boiling gas-liquid two phase flow in downward inclined pipes. *Experimental Thermal and Fluid Science*, 89, 219-237.

Bhagwat, S. M., Mollamahmutoglu, M., & Ghajar, A. J. (2012a). Experimental investigation and empirical analysis of non-boiling gas-liquid two phase heat transfer in vertical downward pipe orientation. In *ASME 2012 Heat Transfer Summer Conference collocated with the ASME 2012 Fluids Engineering Division Summer Meeting and the ASME 2012 10th International Conference on Nanochannels, Microchannels, and Minichannels* (349-359). American Society of Mechanical Engineers.

Bhagwat, S. M., Mollamahmutoglu, M., & Ghajar, A. J. (2012b). Experimental investigation and performance evaluation of isothermal frictional two phase pressure drop correlations in vertical downward gas-liquid two phase flow. In *ASME 2012 Heat Transfer Summer Conference collocated with the ASME 2012 Fluids Engineering Division Summer Meeting and the ASME 2012 10th International Conference on Nanochannels, Microchannels, and Minichannels* (337-348). American Society of Mechanical Engineers.

Bouche, E., Cazin, S., Roig, V., & Risso, F. (2013). Mixing in a swarm of bubbles rising in a confined cell measured by mean of PLIF with two different dyes. *Experiments in Fluids*, *54*(6), 1552.

Bouche, E., Roig, V., Risso, F., & Billet, A. M. (2014). Homogeneous swarm of high-Reynolds-number bubbles rising within a thin gap. Part 2. Liquid dynamics. *Journal of Fluid Mechanics*, *758*, 508-521.

Brennen, C. E., (2005). *Fundamentals of Multiphase Flow*. Cambridge University Press.

Bretsznajder, S. (1963). Increasing the rate of certain industrial chemical processes by the use of vibration. *Industrial Chemical Engineering*, *3*, 496-502.

Buchanan, R. H., Jameson, G., & Oedjoe, D. (1962). Cyclic migration of bubbles in vertically vibrating liquid columns. *Industrial & Engineering Chemistry Fundamentals*, 1(2), 82-86.

Budzyński, P., Gwiazda, A., & Dziubiński, M. (2017). Intensification of mass transfer in a pulsed bubble column. *Chemical Engineering and Processing: Process Intensification*, 112, 18-30.

Cano-Pleite, E., Hernández-Jiménez, F., de Vega, M., & Acosta-Iborra, A. (2014). Experimental study on the motion of isolated bubbles in a vertically vibrated fluidized bed. *Chemical Engineering Journal*, 255, 114-125.

Cheng, H., Hills, J. H., & Azzopardi, B. J. (2002). Effects of initial bubble size on flow pattern transition in a 28.9 mm diameter column. *International Journal of Multiphase Flow*, 28(6), 1047-1062.

Cioncolini, A., & Thome, J. R. (2012). Entrained liquid fraction prediction in adiabatic and evaporating annular two-phase flow. *Nuclear Engineering and Design*, 243, 200-213.

Clark, N. N., & Turton, R. (1988). Chord length distributions related to bubble size distributions in multiphase flows. *International Journal of Multiphase Flow*, 14(4), 413-424.

Collier, J. G., & Thome, J. R. (1994). *Convective Boiling and Condensation*. Clarendon Press.

Cook, W. L. (2008). An experimental apparatus for measurement of pressure drop, void fraction, and non-boiling two-phase heat transfer and flow visualization in pipes for all inclinations (Master thesis, Oklahoma State University).

Crowe, C. T. (Ed.). (2005). *Multiphase Flow Handbook* (Vol. 59). CRC press.

Daly, J. G., Patel, S. A., & Bukur, D. B. (1992). Measurement of gas holdups and sauter mean bubble diameters in bubble column reactors by dynamics gas disengagement method. *Chemical Engineering Science*, 47(13-14), 3647-3654.

Elbing, B. R., Dowling, D. R., Perlin, M., & Ceccio, S. L. (2010). Diffusion of drag-reducing polymer solutions within a rough-walled turbulent boundary layer. *Physics of Fluids*, 22(4), 045102.

Elbing, B. R., Still, A. L., & Ghajar, A. J. (2015). Review of bubble column reactors with vibration. *Industrial & Engineering Chemistry Research*, 55(2), 385-403.

Ellenberger, J., & Krishna, R. (2003). Shaken, not stirred, bubble column reactors: Enhancement of mass transfer by vibration excitement. *Chemical Engineering Science*, 58(3-6), 705-710.

Ellenberger, J., & Krishna, R. (2007a). Levitation of air bubbles in liquid under low frequency vibration excitement. *Chemical Engineering Science*, *62*(18-20), 5669-5673.

Ellenberger, J., & Krishna, R. (2007b). Levitation of air bubbles and slugs in liquids under low-frequency vibration excitement. *Chemical Engineering Science*, *62*(24), 7548-7553.

Ellenberger, J., Van Baten, J. M., & Krishna, R. (2005). Exploiting the Bjerknes force in bubble column reactors. *Chemical Engineering Science*, 60(22), 5962-5970.

Foster, J. M., Botts, J. A., Barbin, A. R., & Vachon, R. I. (1968). Bubble trajectories and equilibrium levels in vibrated liquid columns. *Journal of Basic Engineering*, 90(1), 125-132.

Fukano, T., & Furukawa, T. (1989). Prediction of the circumferential distribution of film thickness in horizontal and near-horizontal gas-liquid annular flows. *International Journal of Multiphase Flow*, 15(3), 403-419.

Fukuma, M., Muroyama, K., & Yasunishi, A. (1987). Properties of bubble swarm in a slurry bubble column. *Journal of Chemical Engineering of Japan*, 20(1), 28-33.

Gaddis, E. S., & Vogelpohl, A. (1986). Bubble formation in quiescent liquids under constant flow conditions. *Chemical Engineering Science*, 41(1), 97-105.

George, D. L., Torczynski, J. R., Shollenberger, K. A., O'Hern, T. J., & Ceccio, S. L. (2000). Validation of electrical-impedance tomography for measurements of material distribution in two-phase flows. *International Journal of Multiphase Flow*, *26*(4), 549-581.

Geraci, G., Azzopardi, B. J., & Van Maanen, H. R. E. (2007). Effect of inclination on circumferential film thickness variation in annular gas/liquid flow. *Chemical Engineering Science*, 62(11), 3032-3042.

Ghajar, A. J., & Bhagwat, S. M. (2013). Effect of void fraction and two-phase dynamic viscosity models on prediction of hydrostatic and frictional pressure drop in vertical upward gas–liquid two-phase flow. *Heat Transfer Engineering*, 34(13), 1044-1059.

Ghajar, A. J., & Bhagwat, S. M. (2014a). Flow patterns, void fraction and pressure drop in gas-liquid two phase flow at different pipe orientations. *Frontiers and Progress in Multiphase Flow* (157-212). Springer, Cham.

Ghajar, A. J., & Bhagwat, S. M. (2014b). Gas-liquid two phase flow phenomenon in near horizontal upward and downward inclined pipe orientations. *International Journal of Mechanical, Aerospace, Industrial and Mechatronics Engineering*, 8(6), 1039-1053.

Govier, G. W., & Aziz, K. (1972). *The flow of complex mixtures in pipes* (Vol. 469). New York: Van Nostrand Reinhold.

Guédon, G. R., Besagni, G., & Inzoli, F. (2017). Prediction of gas–liquid flow in an annular gap bubble column using a bi-dispersed Eulerian model. *Chemical Engineering Science*, 161, 138-150.

Hanratty, T. J., & Hershman, A. (1961). Initiation of roll waves. *AIChE Journal*, *7*(3), 488-497.

Harbaum, K. L., & Houghton, G. (1960). Effects of sonic vibrations on the rate of absorption of gases from bubble beds. *Chemical Engineering Science*, 13(2), 90-92.

Harbaum, K. L., & Houghton, G. (1962). Effects of sonic vibrations on the rate of absorption of carbon dioxide in gas bubble-beds. *Journal of Chemical Technology and Biotechnology*, 12(5), 234-240.

Hashimoto, H., & Sudo, S. (1980). Surface disintegration and bubble formation in vertically vibrated liquid column. *AIAA Journal*, 18(4), 442-449.

Hashimoto, H., & Sudo, S. (1984). Dynamic behavior of liquid free surface in a cylindrical container subject to vertical vibration. *Bulletin of JSME*, 27(227), 923-930.

Hecht, K., Bey, O., Ettmüller, J., Graefen, P., Friehmelt, R., & Nilles, M. (2015). Effect of gas density on gas holdup in bubble columns. *Chemie Ingenieur Technik*, 87(6), 762-772.

Hedrick, T. L. (2008). Software techniques for two-and three-dimensional kinematic measurements of biological and biomimetic systems. *Bioinspiration & Biomimetics*, 3(3), 034001.

Helmig, R. (1997). *Multiphase Flow and Transport Processes in the Subsurface: A Contribution to the Modeling of Hydrosystems.* Springer-Verlag.

Henstock, W. H., & Hanratty, T. J. (1976). The interfacial drag and the height of the wall layer in annular flows. *AIChE Journal*, 22(6), 990-1000.

Hewitt, G.F., Martin, C.J., Wilkes, N.S. (1985). Experimental and Modeling Studies of Churn-Annular Flow in the Region Between Flow Reversal and the Pressure Drop Minimum. *Physicochemical Hydrodynamics* 6, 69–86.

Hewitt, G. F., & Govan, A. H. (1990). Phenomenological modelling of non-equilibrium flows with phase change. *International Journal of Heat and Mass Transfer*, 33(2), 229-242.

Hewitt, G. F., & Hall Taylor, N. S. (1970) *Annular Two-Phase Flow*, Pergamon Press.

Hewitt, G. F., & Lovegrove, P. C. (1969). Frequency and velocity measurements of disturbance waves in annular two-phase flow (No. AERE-R—4304). *Atomic Energy Research Establishment*, Harwell (England).

Hewitt, G. F., Jayanti, S., & Hope, C. B. (1990). Structure of thin liquid films in gas-liquid horizontal flow. *International Journal of Multiphase Flow*, 16(6), 951-957.

Hinze, J. O. (1955). Fundamentals of the hydrodynamic mechanism of splitting in dispersion processes. *AIChE Journal*, 1(3), 289-295.

Hori, K., Nakasamomi, M., Nishikawa, K., & Sekoguchi, K. (1978). Study of ripple region in annular two-phase flow (Third report, effect of liquid viscosity on gas-liquid interfacial character and friction factor). *Transactions of the Japan Society of Mechanical Engineers* 44(387), 3847-56.

Houghton, G. (1963). The behaviour of particles in a sinusoidal velocity field. *Proceedings of the Royal Society A*, 272(1348), 33-43.

Houghton, G. (1966). Particle trajectories and terminal velocities in vertically oscillating fluids. *The Canadian Journal of Chemical Engineering*, 44(2), 90-95.

Houghton, G., McLean, A. M., & Ritchie, P. D. (1957). Mechanism of formation of gas bubble-beds. *Chemical Engineering Science*, 7(1-2), 40-50.

Hur, Y. G., Yang, J. H., Jung, H., & Park, S. B. (2013). Origin of regime transition to turbulent flow in bubble column: Orifice-and column-induced transitions. *International Journal of Multiphase Flow*, 50, 89-97.

Hurlburt, E. T., Fore, L. B., & Bauer, R. C. (2006, January). A two zone interfacial shear stress and liquid film velocity model for vertical annular two-phase flow. In *ASME 2006 2nd Joint US-European Fluids Engineering Summer Meeting Collocated with the 14th International Conference on Nuclear Engineering* (677-684). American Society of Mechanical Engineers.

Ishii, M., & Grolmes, M. A. (1975). Inception criteria for droplet entrainment in two-phase concurrent film flow. *AIChE Journal*, 21(2), 308-318.

Jacowitz, L. A., & Brodkey, R. S. (1964). An analysis of geometry and pressure drop for the horizontal, annular, two-phase flow of water and air in the entrance region of a pipe. *Chemical Engineering Science*, 19(4), 261-274.

Jameson, G. J. (1966). The motion of a bubble in a vertically oscillating viscous liquid. *Chemical Engineering Science*, 21(1), 35-48.

Jameson, G. J., & Davidson, J. F. (1966). The motion of a bubble in a vertically oscillating liquid: theory for an inviscid liquid, and experimental results. *Chemical Engineering Science*, 21(1), 29-34.

John, T. J., Bhagwat, S. M., & Ghajar, A. J. (2015). Heat transfer measuremetns and correlations assessment for downward inclined gas-liquid two phase flow. *ASTFE Digital Library*. Begel House Inc.

Kantarci, N., Borak, F., & Ulgen, K. O. (2005). Bubble column reactors. *Process Biochemistry*, 40(7), 2263-2283.

Kazakis, N. A., Mouza, A. A., & Paras, S. V. (2008). Experimental study of bubble formation at metal porous spargers: effect of liquid properties and sparger characteristics on the initial bubble size distribution. *Chemical Engineering Journal*, 137(2), 265-281.

Kazakis, N. A., Papadopoulos, I. D., & Mouza, A. A. (2007). Bubble columns with fine pore sparger operating in the pseudo-homogeneous regime: gas hold up prediction and a criterion for the transition to the heterogeneous regime. *Chemical Engineering Science*, 62(12), 3092-3103.

Knopf, F. C., Ma, J., Rice, R. G., & Nikitopoulos, D. (2006a). Pulsing to improve bubble column performance: I. Low gas rates. *AIChE Journal*, 52(3), 1103-1115.

Knopf, F. C., Waghmare, Y., Ma, J., & Rice, R. G. (2006b). Pulsing to improve bubble column performance: II. Jetting gas rates. *AIChE Journal*, 52(3), 1116-1126.

Koide, K., Morooka, S., Ueyama, K., Matsuura, A., Yamashita, F., Iwamoto, S., ... & Akehata, T. (1979). Behavior of bubbles in large scale bubble column. *Journal of Chemical Engineering of Japan*, 12(2), 98-104.

Krishna, R., Ellenberger, J., Urseanu, M. I., & Keil, F. J. (2000). Utilisation of bubble resonance phenomena to improve gas–liquid contact. *Naturwissenschaften*, 87(10), 455-459.

Krishna, R., & Ellenberger, J. (2002). Improving gas–liquid contacting in bubble columns by vibration excitement. *International Journal of Multiphase Flow*, 28(7), 1223-1234.

Krishna, R., & Ellenberger, J. (2003). Influence of low-frequency vibrations on bubble and drop sizes formed at a single orifice. *Chemical Engineering and Processing: Process Intensification*, 42(1), 15-21.

Kulkarni, A. A., & Joshi, J. B. (2005). Bubble formation and bubble rise velocity in gas− liquid systems: a review. *Industrial & Engineering Chemistry Research*, 44(16), 5873-5931.

Lamb, H. (1975). *Hydrodynamics*, 585/587.

Lance, M., & Bataille, J. (1991). Turbulence in the liquid phase of a uniform bubbly air–water flow. *Journal of Fluid Mechanics*, 222, 95-118.

Lares, E. I. L. (2014). Design of an Experimental Setup for Two Phase Flow Studies in near Horizontal Upward and Downward Pipe Orientations (Master thesis, Oklahoma State University).

Levich, V. G. (1962). *Physicochemical hydrodynamics*, Prentice Hall.

Levy, S. (1999). *Two-Phase Flow in Complex Systems*. John Wiley & Sons.

Lewis, D. A. (1982). Bubble splitting in shear flow. *Transactions of the Institution of Chemical Engineers*, 60, 283-291.

Liow, J. L. (2000). Quasi-equilibrium bubble formation during top-submerged gas injection. *Chemical Engineering Science*, 55(20), 4515-4524.

Loisy, A. (2016). Direct numerical simulation of bubbly flows: coupling with scalar transport and turbulence (Doctoral dissertation, Université de Lyon).

Majumder, S. K. (2016). *Hydrodynamics and Transport Processes of Inverse Bubbly Flow*. Elsevier.

Mäkiharju, S. A., Elbing, B. R., Wiggins, A., Schinasi, S., Vanden-Broeck, J. M., Perlin, Dowling, D. R. & Ceccio, S. L. (2013). On the scaling of air entrainment from a ventilated partial cavity. *Journal of Fluid Mechanics*, 732, 47-76.

Manera, A., Prasser, H. M., Lucas, D., & Van Der Hagen, T. H. J. J. (2006). Three-dimensional flow pattern visualization and bubble size distributions in stationary and transient upward flashing flow. *International Journal of Multiphase Flow*, 32(8), 996-1016.

Mao, Z. S., & Dukler, A. E. (1993). The myth of churn flow?. *International Journal of Multiphase Flow*, 19(2), 377-383.

Mareuge, I., & Lance, M. (1995). Bubble-induced dispersion of a passive scalar in bubbly flows. In *Proceedings of the 2nd International Conference on Multiphase Flow, Kyoto, Japan, PT1-3–8*.

Marmur, A., & Rubin, E. (1976). Viscous effect on stagnation depth of bubbles in a vertically oscillating liquid column. *The Canadian Journal of Chemical Engineering*, *54*(6), 509-514.

Martínez-Mercado, J., Palacios-Morales, C. A., & Zenit, R. (2007). Measurement of pseudoturbulence intensity in monodispersed bubbly liquids for 10< Re< 500. *Physics of Fluids*, 19(10), 103302.

Mercado, J. M., Gomez, D. C., Van Gils, D., Sun, C., & Lohse, D. (2010). On bubble clustering and energy spectra in pseudo-turbulence. *Journal of Fluid Mechanics*, *650*, 287-306.

Mendez-Diaz, S., Serrano-Garcia, J. C., Zenit, R., & Hernandez-Cordero, J. A. (2013). Power spectral distributions of pseudo-turbulent bubbly flows. *Physics of Fluids*, *25*(4), 043303.

Mercado, J. M., Gomez, D. C., Van Gils, D., Sun, C., & Lohse, D. (2010). On bubble clustering and energy spectra in pseudo-turbulence. *Journal of Fluid Mechanics*, *650*, 287-306.

Miyauchi, T., & Oya, H. (1965). Longitudinal dispersion in pulsed perforated-plate columns. *AIChE Journal*, *11*(3), 395-402.

Mohagheghian, S., & Elbing, B. R. (2016, July). Study of bubble size and velocity in a vibrating bubble column. In *ASME 2016 Fluids Engineering Division Summer Meeting collocated with the ASME 2016 Heat Transfer Summer Conference and the ASME 2016 14th International Conference on Nanochannels, Microchannels, and Minichannels* (pp. V01BT33A012-V01BT33A012). American Society of Mechanical Engineers.

Mohagheghian, S., & Elbing, B. R. (2018a). Characterization of Bubble Size Distributions within a Bubble Column. *Fluids*, 3(1), 13.

Mohagheghian, S., Still, A., Elbing, B., & Ghajar, A. (2018b). Study of bubble size, void fraction, and mass transport in a bubble column under high amplitude vibration. *ChemEngineering*, 2(2), 16.

Mouza, A. A., Dalakoglou, G. K., & Paras, S. V. (2005). Effect of liquid properties on the performance of bubble column reactors with fine pore spargers. *Chemical Engineering Science*, 60(5), 1465-1475.

Okawa, T., Kitahara, T., Yoshida, K., Matsumoto, T., & Kataoka, I. (2002). New entrainment rate correlation in annular two-phase flow applicable to wide range of flow condition. *International Journal of Heat and Mass Transfer*, 45(1), 87-98.

Oliveira, M. S. N., & Ni, X. (2001). Gas hold-up and bubble diameters in a gassed oscillatory baffled column. *Chemical Engineering Science*, 56(21-22), 6143-6148.

Omebere-Iyari, N. K., Azzopardi, B. J., Lucas, D., Beyer, M., & Prasser, H. M. (2008). The characteristics of gas/liquid flow in large risers at high pressures. *International Journal of Multiphase Flow*, 34(5), 461-476.

Owen, D. (1987). An improved annular two-phase flow model. In *Third International Symposium on Multiphase Flow, The Hague*, BHRA.

Oyewole, A. L. (2013). Study of flow patterns and void fraction in inclined two phase flow (Master thesis, Oklahoma State University).

Paras, S. V., & Karabelas, A. J. (1991). Properties of the liquid layer in horizontal annular flow. *International Journal of Multiphase Flow*, 17(4), 439-454.

Peters, R., Rasband, W. S. (2012) ImageJ, US National Institutes of Health, Bethesda, Maryland, USA.

Radl, S., & Khinast, J. G. (2010). Multiphase flow and mixing in dilute bubble swarms. *AIChE Journal*, 56(9), 2421-2445.

Rasband, W.S. ImageJ. U.S. *National Institutes of Health, Bethesda, MD, USA*, 1997–2016. Available online: http://imagej.nih.gov/ij (accessed on 16 April 2013).

Riboux, G., Risso, F., & Legendre, D. (2010). Experimental characterization of the agitation generated by bubbles rising at high Reynolds number. *Journal of Fluid Mechanics*, 643, 509-539.

Risso, F. (2011). Theoretical model for k− 3 spectra in dispersed multiphase flows. *Physics of Fluids*, 23(1), 011701.

Rodríguez, D. J. (2004). Characterization of bubble entrainment, interfacial roughness and the sliding bubble mechanism in horizontal annular flow (Doctoral dissertation, University of Wisconsin-Madison).

Rodriguez, J. M. (2009). Numerical simulation of two-phase annular flow (Doctoral dissertation, Rensselaer Polytechnic Institute).

Rubin, E. (1968). Behavior of gas bubbles in vertically vibrating liquid columns. *The Canadian Journal of Chemical Engineering*, 46(3), 145-149.

Ruzicka, M. C., Drahoš, J., Fialova, M., & Thomas, N. H. (2001). Effect of bubble column dimensions on flow regime transition. *Chemical Engineering Science*, 56(21-22), 6117-6124.

Sarrafi, A., Müller-Steinhagen, H., Smith, J. M., & Jamialahmadi, M. (1999). Gas holdup in homogeneous and heterogeneous gas—liquid bubble column reactors. *The Canadian Journal of Chemical Engineering*, *77*(1), 11-21.

Sasaki, S., Uchida, K., Hayashi, K., & Tomiyama, A. (2017). Effects of column diameter and liquid height on gas holdup in air-water bubble columns. *Experimental Thermal and Fluid Science*, 82, 359-366.

Saxena, S. C., Rao, N. S., & Saxena, A. C. (1990). Heat-transfer and gas-holdup studies in a bubble column: air-water-glass bead system. *Chemical Engineering Communications*, 96(1), 31-55.

Schadel, S. A. (1988). Atomization and deposition rates in vertical annular two-phase flow. Illinois Univ., Urbana, IL (USA).

Schneider, C. A., Rasband, W. S., & Eliceiri, K. W. (2012). NIH Image to ImageJ: 25 years of image analysis. *Nature Methods*, 9(7), 671.

Schubring, D., & Shedd, T. A. (2008). Wave behavior in horizontal annular air–water flow. *International Journal of Multiphase Flow*, 34(7), 636-646.

Schubring, D. (2009). Behavior interrelationships in annular flow (Doctoral dissertation, University of Wisconsin).

Schubring, D., Ashwood, A. C., Shedd, T. A., & Hurlburt, E. T. (2010a). Planar laser-induced fluorescence (PLIF) measurements of liquid film thickness in annular flow. Part I: Methods and data. *International Journal of Multiphase Flow*, 36(10), 815-824.

Schubring, D., Shedd, T. A., & Hurlburt, E. T. (2010b). Planar laser-induced fluorescence (PLIF) measurements of liquid film thickness in annular flow. Part II: Analysis and comparison to models. *International Journal of Multiphase Flow*, 36(10), 825-835.

Sekoguchi, K. (1985). Interfacial structure in vertical upward annular flow. *PCH Physico Chemical Hydrodynamics*, 6(1), 239-255.

Shedd, T. A., & Newell, T. A. (1998). Automated optical liquid film thickness measurement method. *Review of Scientific Instruments*, 69(12), 4205-4213.

Shedd, T. A., & Newell, T. A. (2004). Characteristics of the liquid film and pressure drop in horizontal, annular, two-phase flow through round, square and triangular tubes. *Journal of Fluids Engineering*, 126(5), 807-817.

Simonnet, M., Gentric, C., Olmos, E., & Midoux, N. (2007). Experimental determination of the drag coefficient in a swarm of bubbles. *Chemical Engineering Science*, 62(3), 858-866.

Still, A. (2010). Multiphase phenomena in a vibrating bubble column reactor (Master thesis, Mechanical & Aerospace Engineering, Oklahoma State University, Stillwater, OK, USA).

Still, A. L., Ghajar, A. J., & O'Hern, T. J. (2013, July). Effect of amplitude on mass transport, void fraction and bubble size in a vertically vibrating liquid-gas bubble column reactor.

In *Proceedings of the ASME Fluids Engineering Summer Meeting-FEDSM2013-16116, Incline Village, NV, USA* (7-11).

Taitel, Y., & Dukler, A. E. (1976). A model for predicting flow regime transitions in horizontal and near horizontal gas-liquid flow. *AIChE Journal*, 22(1), 47-55.

Tatterson, D. F., Dallman, J. C., & Hanratty, T. J. (1977). Drop sizes in annular gas-liquid flows. *AIChE Journal*, 23(1), 68-76.

Turner, J. M., & Wallis, G. B. (1965). The separate-cylinders model of two-phase flow, paper no. *Paper No. NYO-3114-6, Thayer's School Engineering, Dartmouth College, Hanover, NH, USA*.

Turner, J.M., Wallis, G.B., 1965. The Separate Cylinders Model of Two Phase flow. Technical Report, No. NYO-3114-6 (Thayer's School of Engineering, Dartmouth College).

Van der Welle, R. (1985). Void fraction, bubble velocity and bubble size in two-phase flow. *International Journal of Multiphase Flow*, 11(3), 317-345.

Vogelaar, Rob (2010), Lufthansa and Airbus Launch Worlds First Passenger Bio-Fuel Flights, aviationnews.eu, http://www.aviationnews.eu/2010/11/29/lufthansa-and-airbus launch-worlds-first-passenger-bio-fuel-flights.

Waghmare, Y. G., Knopf, F. C., & Rice, R. G. (2007). The Bjerknes effect: Explaining pulsed-flow behavior in bubble columns. *AIChE Journal*, 53(7), 1678-1686.

Waghmare, Y. G., Rice, R. G., & Knopf, F. C. (2008). Mass transfer in a viscous bubble column with forced oscillations. *Industrial & Engineering Chemistry Research*, 47(15), 5386-5394.

Waghmare, Y. G., Dorao, C. A., Jakobsen, H. A., Knopf, F. C., & Rice, R. G. (2009). Bubble size distribution for a bubble column reactor undergoing forced oscillations. *Industrial & Engineering Chemistry Research*, 48(4), 1786-1796.

Wiemann, D., & Mewes, D. (2005). Prediction of backmixing and mass transfer in bubble columns using a multifluid model. *Industrial & Engineering Chemistry Research*, 44(14), 4959-4967.

Wilkinson, P. M., Spek, A. P., & van Dierendonck, L. L. (1992). Design parameters estimation for scale-up of high-pressure bubble columns. *AIChE Journal*, 38(4), 544-554.

Wu, C., Suddard, K., & Al-dahhan, M. H. (2008). Bubble dynamics investigation in a slurry bubble column. *AIChE Journal*, 54(5), 1203-1212.

Xue, J., Al-Dahhan, M., Dudukovic, M. P., & Mudde, R. F. (2008). Four-point optical probe for measurement of bubble dynamics: Validation of the technique. *Flow Measurement and Instrumentation*, 19(5), 293-300.

Xue, J., Al-Dahhan, M., Dudukovic, M. P., & Mudde, R. F. (2008). Bubble velocity, size, and interfacial area measurements in a bubble column by four-point optical probe. *AIChE Journal*, 54(2), 350-363.

Youssef, A. A., & Al-Dahhan, M. H. (2009). Impact of internals on the gas holdup and bubble properties of a bubble column. *Industrial & Engineering Chemistry Research*, 48(17), 8007-8013.

Zahradnik, J., Fialova, M., Ru, M., Drahos, J., Kastanek, F., & Thomas, N. H. (1997). Duality of the gas-liquid flow regimes in bubble column reactors. *Chemical Engineering Science*, 52(21-22), 3811-3826.

APPENDICES

Appendix A: Calculations and Derivations

Image Macro for Analyzing Bubble Size Distribution

```
macro "Macro 9_30 [v]"

{run("Subtract Background...", "rolling=80 light");

run("Find Edges");

setAutoThreshold("Default dark");

//run("Threshold...");

//run("Close");

setOption("BlackBackground", false);

run("Make Binary", "thresholded remaining black");

run("Fill Holes");

run("Despeckle");

run("Analyze Particles...", "size=150-2500 circularity=0.87-1.00 show=[Overlay Outlines]
display exclude include in_situ");

run("Revert");}

macro "close [n]"
```

```
{close();}
```

Image Macro for Analyzing the Dye Concentration

```
macro "Mixing [v]"

{run("Min...", "value=120");

//setTool("line");

makeLine(85, 360, 1160, 360);

run("Plot Profile");}

close();
```

Appendix B: Uncertainty Analysis

Analysis of uncertainties associated with measurements in the current study was carried out to assess the validity of the measurements approach. After characterization of the error associated with each measurement, error propagation was calculated for the measured parameters.

Vibration frequency and amplitude

By individual measurement of vibration frequency and amplitude, the associated uncertainty was quantified. Vibration frequency was set and monitored at a variable frequency drive (VFD) with ±0.1 Hz accuracy, this was also confirmed by manual inspection during the experiments. Vibration amplitude was measured before and after each experiments by tracing a fix point from high-speed videos. Hedrick (2008) was employed for digitization of the vibration motion profile and from the spatial calibration the associated error was 0.1mm. The uncertainty in the calculated (peak) acceleration was quantified by error propagation method given by Equation B-1. Table B-1 presents the calculated vibration power error for all measurement conditions.

$$\frac{\Xi_{P_m}}{|A^2\omega^3|} = \pm\sqrt{\left(\frac{3\Xi_{frequency}}{|2\pi f|}\right)^2 + \left(\frac{2\Xi_{amplitude}}{|A|}\right)^2} \qquad \text{Equation B-1}$$

Table B-1. Summary of acceleration error for all possible test conditions

Frequency (Hz)	Amplitude (mm)									
	0.6	1.2	1.6	1.9	2.5	3.3	4	6	8	10
	Ξ_{P_m}									
7.5	33.3%	16.7%	12.5%	10.6%	8.1%	6.1%	5.1%	3.5%	2.7%	2.2%
9	33.3%	16.7%	12.5%	10.6%	8.0%	6.1%	5.1%	3.4%	2.6%	2.2%
10	33.3%	16.7%	12.5%	10.6%	8.0%	6.1%	5.1%	3.4%	2.6%	2.1%
11	33.3%	16.7%	12.5%	10.5%	8.0%	6.1%	5.0%	3.4%	2.6%	2.1%
12	33.3%	16.7%	12.5%	10.5%	8.0%	6.1%	5.0%	3.4%	2.6%	2.1%
13	33.3%	16.7%	12.5%	10.5%	8.0%	6.1%	5.0%	3.4%	2.6%	2.1%
14	33.3%	16.7%	12.5%	10.5%	8.0%	6.1%	5.0%	3.4%	2.6%	2.1%
15	33.3%	16.7%	12.5%	10.5%	8.0%	6.1%	5.0%	3.4%	2.5%	2.1%
20	33.3%	16.7%	12.5%	10.5%	8.0%	6.1%	5.0%	3.4%	2.5%	2.0%
21	33.3%	16.7%	12.5%	10.5%	8.0%	6.1%	5.0%	3.4%	2.5%	2.0%
23	33.3%	16.7%	12.5%	10.5%	8.0%	6.1%	5.0%	3.3%	2.5%	2.0%

Gas superficial velocity

In the current study the gas superficial velocity is the most tested independent variable, and effect of gas superficial velocity was investigated on every multiphase parameter measured. Superficial gas velocity is the ratio of volumetric flow rate of compressed air to the cross sectional area of the column/pipe. The gas superficial velocity was calculated from the readings from a pressure gage, rotameter, and thermocouple. Ideal gas law was employed to calculated the volumetric rate at which compressed air was sent into the column according to Equation B-2.

$$Q_c = \frac{P_{mani}}{P_{atm}} Q_{mani}$$ Equation B-2

The error associate with reading the pressure gage and rotameter was considered 0.02 bar and 0.05 lit/min respectively. The uncertainty associated with Q_c was calculated from Equation B-3, in the worst case scenario this uncertainty was 10% and the lowest uncertainty is 1%; Table B-2 presents the calculated air flow rate error for all measurement conditions.

$$\frac{\Xi_{Q_c}}{Q_c} = \sqrt{\left(\frac{\Xi_{Q_{mani}}}{Q_{mani}}\right)^2 + \left(\frac{\Xi_{p_{mani}}}{p_{mani}}\right)^2}$$ Equation B-3

Table B-2. Summary of the air flow rate error for all possible test conditions

		Q_{mani} (lit/min)									
		0.5	1	1.5	2	2.5	3	3.5	4	4.5	5
		Ξ_{Q_c}									
P_{mani} (bar)	0.4	11.2%	7.1%	6.0%	5.6%	5.4%	5.3%	5.2%	5.2%	5.1%	5.1%
	2.6	10.0%	5.1%	3.4%	2.6%	2.1%	1.8%	1.6%	1.5%	1.4%	1.3%
	4	10.0%	5.0%	3.4%	2.5%	2.1%	1.7%	1.5%	1.3%	1.2%	1.1%
	6	10.0%	5.0%	3.3%	2.5%	2.0%	1.7%	1.5%	1.3%	1.2%	1.1%

Bubble Size

Bubble size measurement was discussed in §3.1.2. Since the bubble size distribution was calculated from image processing using ImageJ, determining an accurate measurement uncertainty from a theoretical perspective is a cumbersome task. Therefore, the uncertainty of measurements was obtained via an experimental approach. Effect of column curvature (causing distortions in the bubble images), image depth, and image processing scheme (sensitivity to threshold) was considered in estimation of bubble size error. The error associated

with Sauter mean diameter was discussed in §3.1.2. and calculated by assuming the worst case scenario to be 8.5%.

Void fraction

Void fraction was measured using two different methods namely, optical tracking of the free surface and differential pressure measurements along 70% of liquid height in the column. The uncertainty associated with void fraction measurements was determined based on the standard deviation of the amplitude of surface fluctuations in optical measurements. The standard deviation of the differential pressure measured by the pressure transducer was used to calculate the uncertainty of void fraction in associated tests.

Annular liquid film thickness

The annular liquid film thickness measurement was described in §3.1.2. Similar to bubble size uncertainty, the film thickness uncertainty was determined experimentally. The standard deviation of the measured film thickness as well as processing uncertainty due to sensitivity to the binary threshold was considered to calculate the film thickness error. Manual inspections shows that the sensitivity to the binary threshold produces a negligible error (2.5% in the worst case scenario); therefore, Standard deviation of the film thickness from the measurement samples was used to determine the film thickness error.

VITA

Shahrouz Mohagheghian

Candidate for the Degree of

Doctor of Philosophy

Dissertation: STUDY OF BUBBLY AND ANNULAR FLOW USING QUANTITATIVE FLOW VISUALIZATION

Major Field: MECHANICAL AND AEROSPACE ENGINEERING

Biographical:

Education:

Completed the requirements for the Doctor of Philosophy in Mechanical Engineering Oklahoma State University, Stillwater, Oklahoma in May, 2019.

Completed the requirements for the Master of Science in Mechanical Engineering at Yazd University, Yazd, Iran in 2012.

Completed the requirements for the Bachelor of Science Mechanical Engineering at Shahrekord University, Shahrekord, Iran in 2009.

Experience: Graduate Teaching/Research Assistant at the School of Mechanical and Aerospace Engineering, Oklahoma State University, Stillwater from 2014-2019.

Professional Memberships: American society of Mechanical Engineers (ASME) and Division of Fluid Dynamics of American Physical Society (APS-DFD).